

Dissertation zur Erlangung des akademischen Grades
Doctor rerum naturalium (Dr. rer. nat.)

From electronic correlations to higher-order
topology in nodal Fermi liquids

vorgelegt von

András László Szabó

geboren am 8. August 1991 in Budapest

Fakultät Physik

Technische Universität Dresden

und

Max-Planck-Institut für Physik komplexer Systeme

wissenschaftlicher Betreuer:

Prof. Dr. Bitan Roy

Betreuer:	Prof. Dr. Bitan Roy
Erstgutachter:	Prof. Dr. Roderich Moessner
Zweitgutachter:	Prof. Dr. Fakher Assaad
Drittgutachter:	Prof. Dr. Matthias Vojta
Abgabedatum:	6. Oktober 2021
Datum der Disputation:	

Abstract

In this thesis we study a variety of two- and three-dimensional (2D and 3D, respectively) nodal semimetals, subjected to local electronic interactions or disorder. Such systems constitute a minimal model for various real materials and capture a plethora of interesting physical phenomena therein. Our methodology includes an unbiased renormalization group analysis controlled by ϵ expansions about the appropriate lower critical dimension, mean-field analysis, as well as complementary numerical analyses.

First, we focus on emergent symmetries at various infrared unstable quantum critical points, appearing in a renormalization group flow of interaction couplings. We investigate a 3D chiral Dirac semimetal, which in a noninteracting system enjoys a microscopic $U(1)\otimes SU(2)$ global symmetry. Though the chiral symmetry is absent in the interacting model, it gets restored (partially or fully) at various fixed points as emergent phenomena. Subsequently, we study a collection of 3D interacting effective spin-3/2 biquadratic Luttinger fermions, and demonstrate the emergence of full rotational symmetry between the distinct nematic sectors (namely E_g and T_{2g}) of the corresponding octahedral group.

We then investigate the effects of electronic interactions at zero and finite temperature and chemical doping in a collection of (i) 2D Dirac and Luttinger fermions, constituting the linearly and quadratically dispersing low-energy excitations in monolayer and bilayer graphene, respectively, and (ii) 3D Luttinger fermions, describing a biquadratic touching of Kramers degenerate conduction and valence bands, relevant in the normal state of 227 pyrochlore iridates, and half-Heusler compounds, for example. These systems exhibit a plethora of competing broken symmetry phases (both magnetic and superconducting) when tuning the strength of interactions, temperature, and chemical doping. In this context we propose the selection rules, identifying the broken symmetry phases promoted by a given interaction channel, and the organizing principle, ordering these preselected phases along the temperature axis based on a generalized energy-entropy argument.

Finally, we explore topological aspects of nodal Fermi liquids. We propose an experimentally feasible way to engineer higher-order topological phases via the application of uniaxial strain on a 3D Luttinger semimetal. Favoring a direction, strain explicitly breaks cubic symmetry. We show that the corresponding nematic orderings of Luttinger fermions result in a topological insulator or Dirac semimetal, depending on the sign (compressive or tensile, respectively) of the strain. We show that both of these phases host 1D hinge modes, localized along the edges parallel to the direction of strain, that are therefore second-order topological in nature. We then investigate the effects of disorder on such a second-order Dirac semimetal, and show its stability for weak enough disorder. At a critical disorder strength the system goes through a quantum phase transition into a diffusive metal phase and the topological hinge states melt into the bulk. The methodology presented in this thesis can be extended to a large family of correlated multiband systems, such as Weyl and nodal-loop semimetal.

List of sources

This thesis is based on the author's own publications as follows.

Chapter 3:

A. S., B. Roy, Emergent chiral symmetry in a three-dimensional interacting Dirac liquid, *Journal of High Energy Physics* **2021**, 4 (2021)

Chapters 4 and 7:

A. S., R. Moessner, B. Roy, Interacting spin-3/2 fermions in a Luttinger semimetal: Competing phases and their selection in the global phase diagram, *Phys. Rev. B* **103**, 165139 (2021)

Chapters 5 and 6:

A. S., B. Roy, Extended Hubbard model in undoped and doped monolayer and bilayer graphene: Selection rules and organizing principle among competing orders, *Phys. Rev. B* **103**, 205135 (2021)

Chapter 8:

A. S., R. Moessner, B. Roy, Strain-engineered higher-order topological phases for spin-3/2 Luttinger fermions, *Phys. Rev. B* **101**, 121301(R) (2020)

Chapter 9:

A. S., B. Roy, Dirty higher-order Dirac semimetal: Quantum criticality and bulk-boundary correspondence, *Phys. Rev. Research* **2**, 043197 (2020)

Contents

1	Introduction	1
2	Methodology	9
2.1	Coherent state path integral	9
2.1.1	Fermionic coherent states	10
2.1.2	Path integral formulation of partition function	11
2.1.2.1	Matsubara frequencies	12
2.1.3	Euclidean action	12
2.2	Wilsonian momentum-shell renormalization	14
2.2.1	Fierz reduction of quartic terms	15
2.2.2	Zero temperature and chemical doping	16
2.2.2.1	Fixed point analysis	17
2.2.2.2	Order parameters	18
2.2.3	Finite temperature and chemical doping	20
I	Emergent symmetries	23
3	Three-dimensional Dirac liquid	25
3.1	Noninteracting models: continuum and lattice	25
3.1.1	Continuum model	25
3.1.2	Lattice model	27
3.2	Electron-electron interactions	30
3.2.1	Renormalization group analysis	31
3.2.2	Fixed points and critical exponents	33
3.2.3	Nambu doubling and ordered phases	33
3.2.4	Emergent chiral symmetry	37
3.2.5	Phase diagram	38
3.2.6	Anisotropic Dirac semimetal	41
3.3	Summary and Discussion	42
4	Three-dimensional Luttinger semimetal	45
4.1	Luttinger model	46

4.1.1	Hamiltonian and Symmetries	46
4.1.2	Lagrangian and Scaling	48
4.2	Electron-electron interactions	49
4.2.1	Nambu doubling and Broken symmetry phases	50
4.2.1.1	Particle-hole or excitonic orders	50
4.2.1.2	Particle-particle or superconducting orders	51
4.2.2	Renormalization group analysis	52
4.2.3	Quantum criticality in Luttinger semimetal	53
4.2.3.1	Isotropic Luttinger semimetal ($\alpha = \frac{\pi}{4}$)	54
4.2.3.2	Anisotropic Luttinger semimetal: $\alpha \rightarrow \frac{\pi}{2}$	55
4.2.3.3	Anisotropic Luttinger semimetal: $\alpha \rightarrow 0$	56
4.2.4	Universality class and critical exponents	57
4.2.5	Scaling of the transition temperature	57
4.3	Summary and discussion	59

II Competing orders and selection rules 61

5 Selection rules and organizing principle 63

6 Monolayer and bilayer graphene 67

6.1	Lattice models	68
6.1.1	Monolayer graphene	69
6.1.2	Bilayer graphene	70
6.2	Low-energy effective theory	71
6.2.1	Non-interacting models	72
6.2.2	Symmetries and action	73
6.2.3	Electron-electron interactions	75
6.2.4	Broken symmetry phases	79
6.2.4.1	Particle-hole or excitonic orders	82
6.2.4.2	Particle-particle or superconducting orders	83
6.3	Phase diagrams	84
6.3.1	Quartic interactions: Mass channels	85
6.3.2	Quartic interactions: Nematic channels	89
6.3.3	Quartic interactions: Smectic channels	92
6.3.4	Quartic interactions: Kekulé channels	93
6.4	Extended honeycomb Hubbard model	96
6.4.1	On site repulsion (U)	97
6.4.2	Nearest neighbor repulsion (V_1)	99
6.4.3	Next-nearest neighbor repulsion (V_2)	101
6.5	Summary and discussion	103

7	Three dimensional Luttinger (semi)metal	107
7.1	Energy, entropy, and topology	108
7.1.1	Reconstructed band structure and emergent topology	109
7.1.2	Energy and Entropy Inside Ordered Phases	113
7.2	Electron-electron interactions	115
7.2.1	Mean-field susceptibility	116
7.2.1.1	Isotropic Luttinger Semimetal ($\alpha = \frac{\pi}{4}$)	116
7.2.1.2	Anisotropic Luttinger Semimetal near $\alpha = \frac{\pi}{2}$	117
7.2.1.3	Anisotropic Luttinger Semimetal near $\alpha = 0$	119
7.2.2	Renormalization group analysis	120
7.2.2.1	Phase diagrams at finite temperature	120
7.2.3	RG analysis in Luttinger metal ($\mu \neq 0$)	122
7.2.4	Selection rules: Examples	125
7.3	Summary and Discussions	127
III	Higher-order topology in nodal semimetals	129
8	Strain-engineered HOT phases in a Luttinger semimetal	133
8.1	Toy model	135
8.2	Lattice models	136
8.3	Luttinger model	138
8.4	E_g strain	139
8.5	T_{2g} strain	142
8.6	Summary and discussion	143
9	Disordered higher-order Dirac semimetal	145
9.1	Lattice model and symmetries	146
9.2	Numerical analysis of density of states	148
9.3	Renormalization group analysis	152
9.4	Summary and Discussion	155
	Conclusions	157
	Appendices	161
A.1	Three-dimensional chiral Dirac semimetal	163
A.1.1	Symmetry classification of four-fermion interaction	163
A.1.2	Fierz reduction of four-fermion interaction	164
A.1.2.1	Isotropic Dirac semimetal	165
A.1.2.2	Anisotropic Dirac semimetals	166
B.2	Three-dimensional Luttinger (semi)metal	167
B.2.1	Specific heat and compressibility	167

B.2.2	Dynamic conductivity	169
B.2.3	Details of Luttinger model	170
B.2.4	Fierz Identity	171
B.2.5	Details of RG flow equations	172
B.2.6	Stability matrix analysis	174
C.3	Two-dimensional Dirac and Luttinger liquids	175
C.3.1	Diagrammatic contributions to order parameter fields	176
C.3.2	Fierz reduction of local interaction terms	178
C.3.3	Renormalization group (RG) flow equations	180
C.3.3.1	Monolayer graphene	182
C.3.3.2	Bilayer graphene	185
D.4	Strain-engineered higher order topology	188
D.4.1	Effects of external strain along y axis and $\langle 111 \rangle$ directions	188
D.4.2	Luttinger Hamiltonian in the $k_z = 0$ plane	190
E.5	Disordered higher order topological Dirac semimetal	191
E.5.1	Renormalization group analysis	191
E.5.1.1	Fermionic self energy	192
E.5.1.2	Vertex correction	194
E.5.1.3	RG flow equations	194

Chapter 1

Introduction

Semimetals are a class of material where the bands around the Fermi level have little overlap in energy, resulting in small and equal density of electron- and hole-like charge carriers. In the conventional meaning of the term, the top of the valence band does not necessarily coincide with the bottom of the conduction band in their position in the Brillouin zone. This results in disjoint electron and hole-like pockets for example as in Bi, As, or Sb [1,2]. This scenario is depicted in Fig. 1.1(a). Recently, the notion of a semimetal more often than not refers to a family of systems where the valence and conduction bands touch at one or more distinct, typically high-symmetry points in momentum space. If the Fermi energy lies exactly at the band degeneracy, then the previously extended Fermi surface shrinks to just a pointlike Fermi point, as shown in Fig. 1.1(b), with still equal number of electron- and hole-like excitations. Such nodal semimetals can also be named nodal Fermi liquid.

We classify nodal semimetals based on their electronic dispersion in the vicinity of the Fermi points. Linearly dispersing quasiparticles are found in Dirac (in two and three dimensions, or 2D and 3D respectively) and Weyl semimetals (in 3D). Such linear band structure is depicted in Fig. 1.2(a). On the other hand, quadratic band touching can be found in Luttinger semimetals, both in 2D [see Fig. 1.2(b)] and 3D. In the scope of this thesis we study multiple examples featuring such band dispersions, which can also be found in real materials. It is worth noting that nodal semimetals extend beyond purely linear and quadratic band touching points. For example, bicubic dispersion can be realized by stacking three sheets of honeycomb lattice (also known as trilayer graphene) [3], whereas various 3D systems exhibit a mixed band structure; linear along one momentum direction and quadratic or cubic along the remaining two, constituting a multi-Weyl semimetal [4,5], see Fig. 1.2(c).

Owing to their band structure, nodal Fermi liquids are germane for many interesting physical phenomena. The nodes act as topological defects, resulting in a diverse family of topological systems, and stabilizing the band degeneracy points. At the same time, due to the available gapless excitations, electronic interactions and/or disorder often have a dramatic influence therein. These phenomena constitute the central theme of this thesis.

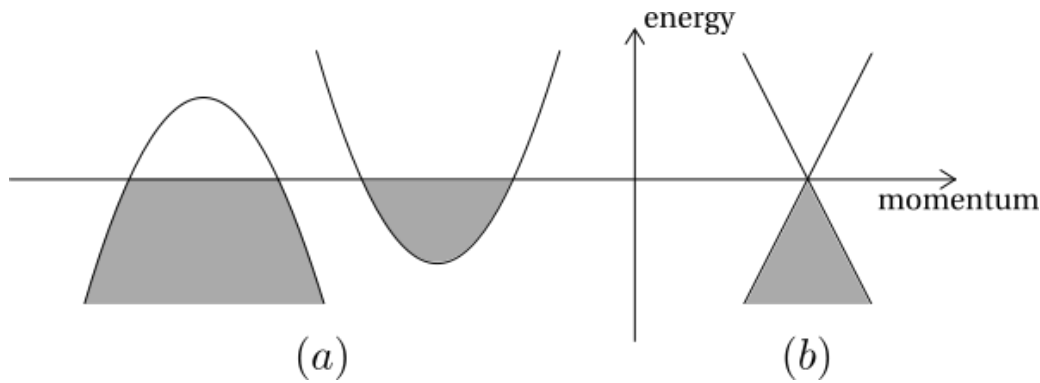


Figure 1.1: Schematic band structure of two types of semimetal. The horizontal line indicates the Fermi level, up to which all states are filled (shaded region). In (a) there is a finite overlap between valence and conduction bands, while (b) represents a zero-gap semimetal with a linear band degeneracy point.

A system exhibiting linear band touching points in the presence (absence) of Kramers degeneracy is coined Dirac (Weyl) semimetal. This is in analogy with the Dirac equation from electrodynamics, where the equations for the left and right chiral Weyl spinors decouple in the massless limit, and yield two independent Weyl equations [6]. In condensed matter systems, a band composed of half-integer spin quasiparticles is two-fold degenerate for each spin projection, which is the so-called Kramers degeneracy [7]. In the presence of this degeneracy, two Weyl fermions that form a Kramers doublet constitute a Dirac fermion. Among two-dimensional (2D) systems, a paradigmatic example of a Dirac semimetal is monolayer graphene [8, 9]. The honeycomb structure of graphene is constituted by two interpenetrating triangular lattices, and the resulting unit cell contains two atoms, see Fig. 6.2(a). The corresponding Brillouin zone is itself a hexagonal structure, where the band degeneracy points are located at the six corners [10]. In a carbon-based honeycomb lattice we often neglect spin-orbit coupling, due to the low atomic number of carbon. Spin is then a good quantum number and the two-fold Kramers degeneracy of the valence and conduction bands results in a collection of Dirac fermions as low-energy excitations in monolayer graphene. At the same time, inequivalent valleys in the Brillouin zone give rise to isospin degrees of freedom.

Electronic correlations in graphene result in a rich phase diagram under the tuning of various experimental parameters (such as chemical doping, temperature, etc). Even though there is an innate stability of the 2D Dirac fermions against weak local interactions (see Sec. 6.2.3) due to linearly vanishing density of states (DoS) $\rho(E) \sim |E|$, strong enough interactions destabilize the linear band touching toward the formation of broken symmetry phases [11, 12], that set in via quantum phase transitions. At low temperatures the resulting phase diagram is dominated by mass orders, as a uniform gap is energetically favorable compared to the gapless spectrum [13]. At zero chemical doping and for net repulsive interactions, excitonic phases are the most prominent orderings. They include the charge-density-wave [14] and antiferromagnet [15] phases, describing charge and spin polarization of the two sublattices, respectively [Figs 1.3(a) and 1.3(d)]. Nucleation of

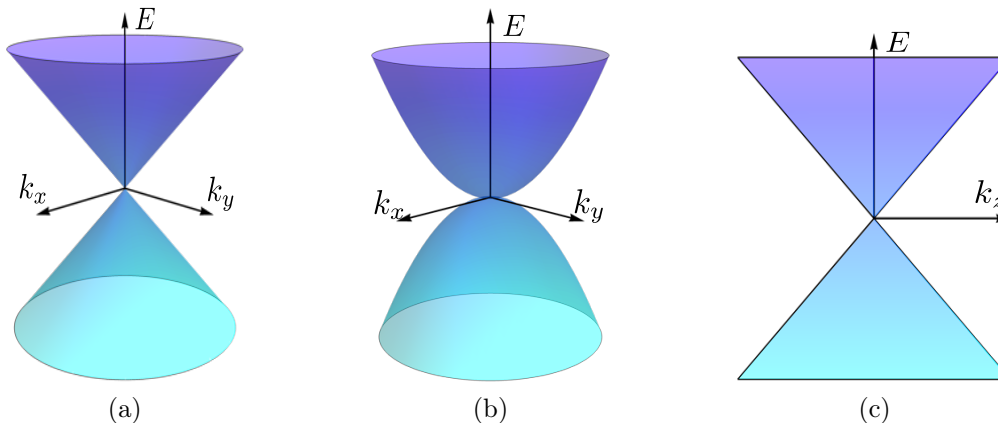


Figure 1.2: (a) linear and (b) quadratic band touching point in two dimensions, characterized by vorticity 1 and 2, found for example in 2D Dirac and Luttinger semimetals, respectively. A 3D extension of such band structures can be constructed by adding linear dispersion along the k_z axis, as shown in (c). The resulting system is then characterized by its monopole charge $n = 1$ and 2 for (a) and (b), found respectively in Weyl and double-Weyl semimetals [4, 5].

the Haldane mass results in a quantum anomalous or spin Hall insulator, characterized by topological edge states [16] [Figs 1.3(b) and 1.3(e)]. Furthermore, the translation symmetry breaking Kekulé valence bond solid phase features an enlarged unit cell, due to dimerization of the nearest-neighbor electronic hopping in the Kekulé pattern [Figs 1.3(c) and 1.3(f)] [17]. Hence, there are many available gapped excitonic phases in graphene-like systems, also known as Dirac masses.

The notion of nodal semimetals extends beyond linearly dispersing Dirac fermions. For example, quadratic band touching in 2D systems can be engineered by e.g. coupling two sheets of graphene in the so-called AB stacking, yielding the Bernal bilayer graphene. The interlayer coupling modifies the resulting band structure and the dispersion around the band degeneracy points becomes quadratic [18, 19]. Since both the conduction and valence bands display quadratic scaling at low energies, we also call such band dispersion biquadratic. In contrast to linear fermions in two-dimensions, the quadratic dispersion results in local electronic interactions being marginally relevant due to the constant DoS at low energies. Therefore, such two-dimensional systems are unstable in the presence of infinitesimal Hubbardlike interactions. Otherwise, bilayer graphene is endowed with the same microscopic symmetries as its monolayer counterpart. We present a simultaneous analysis of the effects of electronic interaction in monolayer and bilayer graphene in Chapter 6. Alternatively, one can achieve such a biquadratic band touching by tuning the hopping amplitudes in the checkerboard or Kagome lattices [20].

Dirac semimetals in both two and three dimensions can be found at the quantum critical point separating two time-reversal symmetric, topologically distinct insulators [21, 22]. Even though such massless Dirac fermions appear at infrared unstable fixed points, their imprint on thermodynamic and transport properties extends to a wide quantum critical fan, exposed by either temperature or frequency. Furthermore, 3D topological Weyl

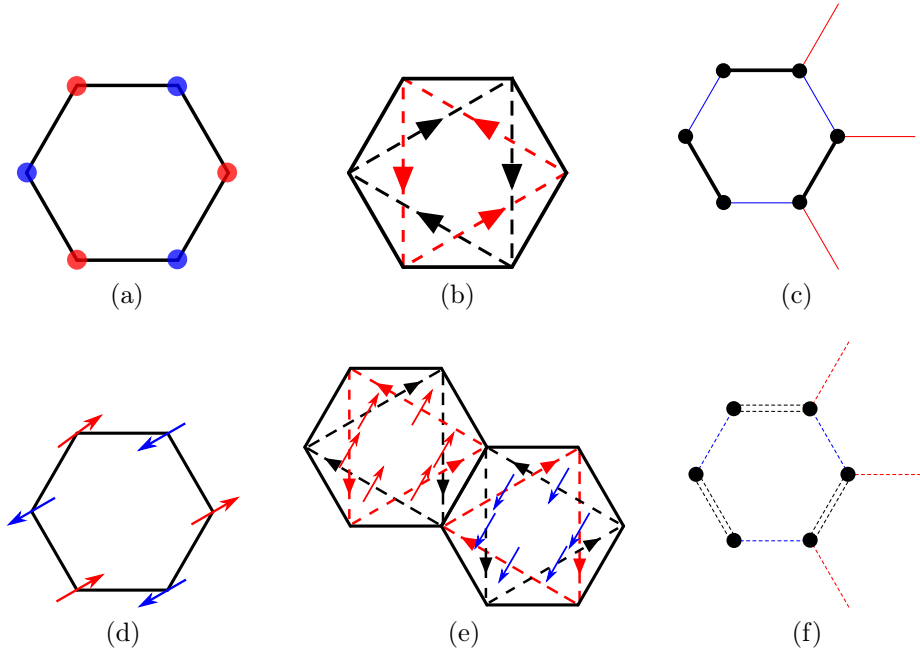


Figure 1.3: Schematic depictions of excitonic mass orders on the honeycomb lattice, without (with) spin ordering for the top (bottom) row. (a) Charge density wave ordering, accompanied by polarization of local electronic density between two sublattices (red and blue sites). (b) Topological quantum anomalous Hall insulator, resulting from Haldane’s time reversal symmetry breaking intrasublattice imaginary hoppings (red and black arrows). (c) Kekulé valence bond solid order and dimerization of nearest-neighbor electronic hopping in the Kekulé pattern, resulting in an enlarged unit cell. Here the hopping amplitudes are $\Delta \cos \alpha$ along red lines, and $\Delta \cos(\alpha \pm 2\pi/3)$ along black and blue lines, respectively, where α is the U(1) internal phase. (d) Staggered spin polarization of sublattices, leading to antiferromagnetic ordering. (e) Quantum spin Hall insulator, with opposite Haldane hoppings for the two spin polarizations. (f) Spin Kekulé solid order, with spin \uparrow displaying the same hopping amplitudes as in (c), whereas spin \downarrow are associated with hopping amplitudes exactly opposite in magnitude.

and Dirac semimetals can be achieved by stacking layers of quantum anomalous Hall and spin Hall insulators in momentum space, respectively. While the 2D constituents of these stacked systems are (as the name suggests) gapped, the resulting 3D systems host a topological semimetal sandwiched between a trivial and a topological insulator as we tune the interlayer coupling [23, 24]. Experimentally Weyl semimetals have been successfully realized using noncentrosymmetric materials (where inversion symmetry is broken), including TaAs [25, 26], NbAs [27], TaP and NbP [28]. Though time reversal symmetry breaking magnetic Weyl semimetals have been more illusive, recent years witnessed an increasing number of related discoveries, for example in YbMnBi₂ [29], Co₃Sn₂S₂ [30], and strained Pr₂Ir₂O₇ [31]. On the other hand, 3D topological Dirac semimetals have been observed using compounds for example Na₃Bi [32] or Cd₃As₂ [33, 34]. In Chapter 3 we study the effect of electronic interactions on a collection of 3D Dirac fermions, that in the noninteracting limit enjoy a microscopic global $U(1) \otimes SU(2)$ chiral symmetry. Without imposing this symmetry on the interacting theory, we observe the restoration of it (either

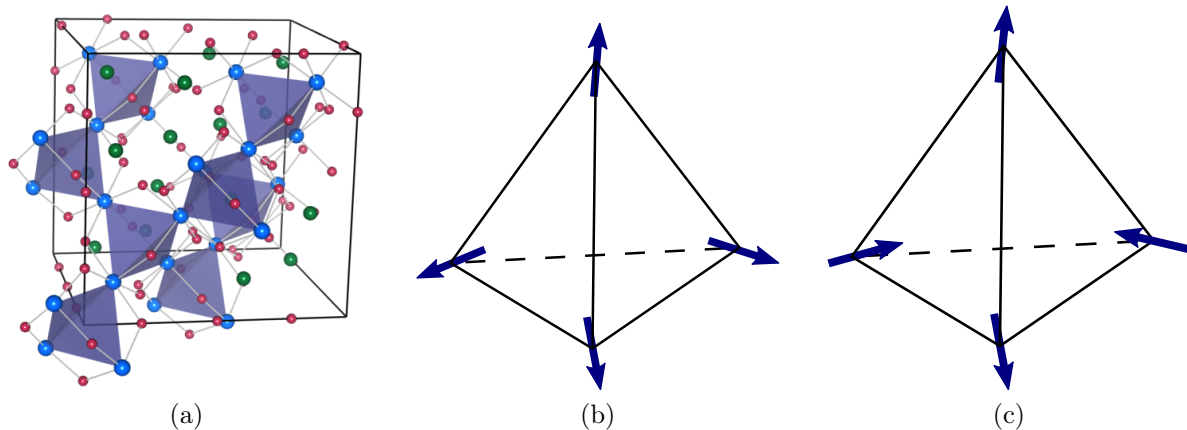


Figure 1.4: (a) Crystal structure of 227 pyrochlore iridates. Both the Ir (blue) and rare earth Ln (green) atoms span a network of corner-sharing tetrahedra, highlighted for the Ir atoms. The electronic properties are largely determined by the Ir $5d$ electrons. Each Ir sits in a trigonally compressed octahedron of oxygen atoms (red). Republished with permission of Annual Reviews, Inc., from Ref. [35]; permission conveyed through Copyright Clearance Center, Inc. (b) all-in-all-out (AIAO) arrangement of electronic spin, yielding Weyl semimetal or antiferromagnetic insulator phase [36–40]. (c) two-in-two-out or spin-ice arrangement of electronic spin, supporting a large anomalous Hall effect due to resulting dipolar Weyl fermions [41–44].

partial or full) at various renormalization group fixed points.

Finally, biquadratic band touching in three spatial dimensions has been observed in numerous compounds. Such quasiparticle excitations have been found in HgTe [45, 46] and gray-Sn [47, 48], which however do not show signatures of significant electronic correlations. On the other hand, band structure calculations suggest several members of the 227 pyrochlore iridates ($\text{Ln}_2\text{Ir}_2\text{O}_7$, where Ln is a lanthanide or rare-earth element) exhibit quadratic band touching in their normal state [35, 49]. Most prominently this has been confirmed in $\text{Nd}_2\text{Ir}_2\text{O}_7$ and $\text{Pr}_2\text{Ir}_2\text{O}_7$ using angle-resolved photoemission spectroscopy (ARPES) and terahertz spectroscopy [50–52]. These materials feature comparable spin-orbit coupling and electronic correlations, which is germane for a confluence of competing exotic phases and emergent topology [35]. The electronic properties of these compounds are largely determined by the itinerant Ir $5d$ electrons, which form a network of corner-sharing tetrahedra, see Fig. 1.4(a). The majority of 227 pyrochlore iridates exhibit antiferromagnetic (insulating) order at low temperatures, possibly resulting from an all-in-all-out (AIAO) arrangement of electron spin [36–40] as depicted in Fig. 1.4(b). An exception is $\text{Pr}_2\text{Ir}_2\text{O}_7$, which remains metallic to the lowest accessible temperatures and exhibits large anomalous Hall conductivity, despite the apparent absence of magnetic ordering even at low temperature [41–44]. This peculiar behavior is possibly due to a two-in two-out or spin-ice ordering of electron spin [see Fig 1.4(c)] [43]. Quadratic band touching in 3D can also be found in the family of half-Heusler compounds (such as LnPtBi or LnPdBi) [53–55]. In contrast to the iridates, where the Fermi surface is prohibitively small for pairing orders to nucleate, half-Heuslers exhibit an interplay of

antiferromagnetism and unconventional superconductivity [56–65].

In this thesis we study 3D biquadratic band touching in the framework of the Luttinger model, constituted by strong spin-orbit coupled, effective spin-3/2 fermions, interacting via short-range Coulomb repulsion. In Chapter 4 we study the effects of electronic interaction on the quantum critical properties of such system. We show that, so long we do not introduce cubic deformations explicitly, full rotational symmetry emerges at the quantum critical point between disordered and ordered phase. The emergent spherical symmetry connects the otherwise distinct E_g and T_{2g} nematic sectors of the corresponding octahedral group. In Chapter 7 we then investigate the effect of finite temperature and chemical doping on the competition among broken symmetry phases in the Luttinger semimetal. We show that this model can successfully capture the semimetal-itinerant magnetic order quantum phase transition, observed in the 227 iridates, as well as the competition of magnetic orders and d -wave pairing, which is consistent with the experimental observations in LnPdBi [57].

Due to the fine balance between electron and hole-like excitations, nodal systems lack the bias of normal Fermi liquids toward pairing orders, which promotes a rich landscape of excitonic phases [66]. Nevertheless, these systems host a number of exotic superconductors as well. Besides the aforementioned d -wave pairing in the Luttinger materials, the prominent pairing orders in monolayer and bilayer graphene (apart from mundane s -wave pairing) are the f -wave and Kekulé superconductors or pair-density-wave [13, 14, 19, 67–70]. However, owing to the nodal structure of the bands around the Fermi energy, particle-particle orders often cannot nucleate at the lowest available temperatures at zero or low carrier densities for repulsive interactions. The question then naturally arises; how can we realize these interesting, unconventional pairing orders? Adding attractive net interactions by hand naturally gives rise to superconductivity. However, this is very much a theoretical tool. On the other hand, increasing the number of charge carriers is often feasible experimentally, either via applying gate voltage (like in the case of graphene [71]), or by chemical doping. According to the Kohn-Luttinger mechanism, in the presence of a Fermi surface, a net attractive interaction channel can be generated between time reversal partner electronic degrees of freedom [72, 73]. This is ultimately conducive for the condensation of electrons into Cooper pairs.

Interfacing theoretical work with experimental or numerical results requires a fine balance between capturing the essential microscopic physics and casting it into a tractable model. One of the simplest microscopic descriptions of correlated electrons in solids is the (extended) Hubbard model. It describes electrons hopping on a lattice and interacting via finite range components of Coulomb repulsion. The simplest incarnation of the Hubbard model only considers on site repulsion, while in its extended form further terms, such as nearest neighbor, next-nearest neighbor, etc., are also taken into account. This extension is necessary for example for spinless electrons, where the on site interaction is not viable due to the Pauli principle. We deploy the extended Hubbard model in the context of

monolayer and bilayer graphene in Chapter 6. Our analysis predicts the appearance of various excitonic masses (such as antiferromagnet, charge-density-wave, and quantum spin Hall insulator) at zero doping, as well as the onset of pairing phases (such as s -wave and f -wave pairing, as well as nematic and Kekulé superconductors) at finite doping. Our results are consistent with numerical simulations using functional renormalization group [14] and Monte Carlo [16] methods, which will be discussed in details later.

Besides hosting correlated electrons, nodal systems are also interesting from a topological point of view. As mentioned before, three-dimensional topological Weyl and Dirac semimetals can be constructed theoretically by stacking two-dimensional quantum anomalous and spin Hall insulators (respectively) in momentum space. The resulting 3D system hosts topologically protected nodes that act as sources and sinks of Abelian Berry curvature, separated along the axis of stacking. A hallmark of these systems are the so-called Fermi arcs, which are a collection of surface states, connecting the bulk nodes in momentum space. The Fermi arcs have been observed in noncentrosymmetric Weyl semimetals TaAs, NbAs, and TaP [25–27, 74], and in the magnetic Weyl semimetal compound YbMnBi₂ [29]. On the other hand, topological Dirac nodes have been captured in the compounds Cd₃As₂ [33, 34, 75] and Na₃Bi [32]. ARPES measurements also successfully showed the Fermi arcs in Na₃Bi [76].

Conventionally, the notion of topological states concerns edge modes living on surfaces of one less dimension than the host system. In 2D, this includes 1D edge modes of Chern insulators, while in 3D we can find 2D Fermi arc states of topological Weyl and Dirac semimetals, as well as surface states of topological insulators, for example. If we define the codimension as

$$d_c = \text{dimension of system} - \text{dimension of surface state}, \quad (1.1)$$

the above mentioned examples fall into the $d_c = 1$ or “first-order” topological category [21, 22, 77, 78]. The generalization of this idea leads us to higher order topology, where we study systems that host surface states for which $d_c > 1$ (integer) [79–84]. In this thesis we are primarily concerned with hinge states in 3D topological Dirac semimetals, that are localized along certain (1D) edges of the sample, and therefore $d_c = 3 - 1 = 2$. In principle, (zero dimensional) topological corner states of two- and three-dimensional systems ($d_c = 2$ and 3) represent second- and third-order topological phases of matter, respectively.

Despite numerous theoretical proposals, experimental observation of higher order topology is still sparse, with a few notable examples being elemental Bi [85], Bi_{0.92}Sb_{0.08} [86], and possibly WTe₂ [87]. In Chapter 8 we elicit higher order topological states via engineering nematic phases in a Luttinger semimetal by the application of uniaxial strain. Recent experiments suggest this approach might be germane for strained HgTe [88]. Subsequently, in Chapter 9 we examine the fate of the resulting hinge modes in the presence of random potential disorder. The stability of first order Dirac semimetal against

weak enough potential disorder (up to rare region effects) is well established in the literature [89–91]. However, at some critical disorder strength, the system undergoes a quantum phase transition into a diffusive metal phase. We study the effects of disorder in a higher-order topological Dirac semimetal and establish the existence of a region of stability, not unlike the one in its first order relative. We also scrutinize the universality class of the corresponding quantum phase transition into a diffusive metal.

Nodal Fermi liquids therefore exhibit a rich landscape of exotic phenomena. One primary objective of this thesis is identifying the pattern of symmetry breaking in various prototypical systems in the presence of electronic interactions. Besides the nature of interactions, we consider the influence of finite temperature and chemical doping. As an attempt to capture these effects within a unified framework, we pronounce the selection rules and organizing principle in Chapter 5. The role of the selection rules is to provide a set of ordered phases that are promoted in a given interaction channel. The organizing principle then orders these preselected phases along the temperature axis, based on a generalized energy-entropy principle. In the chapters that follow we anchor these expectations in a variety of nodal Fermi liquids in two and three dimensions.

Chapter 2

Methodology

This thesis focuses on the role of electronic interactions and the emergent quantum critical behavior in two- and three-dimensional nodal semimetals. The present chapter is devoted to outline some of the key methods, which can be applied in general to this new emerging family of materials. Much of what follows can be found in multiple textbooks, other parts are specific to the research presented in this thesis. Nevertheless, setting the cornerstones of the applied formalism should facilitate a more fluent discussion later on.

2.1 Coherent state path integral

Systems with a large (or even variable) number of particles challenge the formalism of single-particle quantum mechanics. While solving the Schrödinger equation for a small number of constituents (for example in case of the hydrogen atom) is manageable, in condensed matter systems the number of degrees of freedom quickly reaches the order of the Avogadro number. For this reason, we use the second quantized formalism, where all operators are cast in terms of creation and annihilation operators, that act on the generalized Fock space. In this section we review the key ideas behind the partition function for a system of fermions using the basis of coherent states. This formalism is tailored to deal with quantum many particle systems with fixed or variable particle number $\sim 10^{23}$. For a pedantic description we refer the reader to Ref. [92]. A presentation of the analogous problem for bosons can be found in Ref. [93].

The partition function Z constitutes the backbone of equilibrium statistical physics. In case of the canonical and grand canonical ensembles (latter one being particularly useful for many particle systems), the probability of a state occurring is a function of how energetically expensive it is in the environment where the energy scale is set by the temperature T via $k_{\text{B}}T$, where k_{B} is the Boltzmann constant. This manifests through the exponential functions

$$\exp[-\beta\hat{H}], \quad \exp[-\beta(\hat{H} - \mu\hat{N})], \quad (2.1)$$

appearing respectively in the partition function for the canonical and grand canonical ensembles, where $\beta = 1/(k_B T)$, \hat{H} is the Hamiltonian, μ is the chemical potential and \hat{N} is the number operator. The path integral formulation of such partition function happens via considering the cyclic evolution of a system through imaginary time $\tau = it$. In this section we outline the cornerstones of this derivation. However, to do this we first introduce our basis of fermion coherent states.

2.1.1 Fermionic coherent states

For our construction of the path integral we use the basis of coherent states, which are the eigenstates of annihilation operators [92]. Denoting the creation and annihilation operators for the state α respectively with a_α^\dagger and a_α , the pertinent eigenvalue condition reads

$$a_\alpha|\psi\rangle = \psi_\alpha|\psi\rangle, \quad (2.2)$$

where $|\psi\rangle$ is a vector in the generalized Fock space, about which more shortly. The anticommutation of fermionic annihilation and creation operators demand that distinct eigenvalues satisfy

$$\{\psi_\alpha, \psi_\beta\} = 0, \quad \text{and} \quad \{\psi_\alpha^*, \psi_\beta^*\} = 0, \quad (2.3)$$

where the curly bracket denotes anticommutation. This property necessitates the introduction of Grassmann variables, that satisfy the anticommutation in Eq. (2.3). To close this algebra we introduce the adjoint of Eq. (2.2)

$$\langle\psi|a_\alpha^\dagger = \langle\psi|\psi_\alpha^*, \quad (2.4)$$

where ψ_α^* is the conjugate but independent variable to ψ_α . These variables square to zero, mutually anticommute, and anticommute with the fermionic creation and annihilation operators. These properties can be summarized as

$$\begin{aligned} \psi^2 = (\psi^*)^2 &= 0, & \{\psi, \psi^*\} &= 0, \\ \{\psi, a\} &= 0, & \{\psi, a^\dagger\} &= 0, \\ \{\psi^*, a\} &= 0, & \{\psi^*, a^\dagger\} &= 0, \end{aligned} \quad (2.5)$$

where we suppressed the α index. A fermionic coherent state that fulfills the above algebraic requirements is constructed as

$$|\psi\rangle = e^{-\sum_\alpha \psi_\alpha a_\alpha^\dagger} |0\rangle, \quad (2.6)$$

where $|0\rangle$ is the vacuum. This way the state $|\psi\rangle$ is a linear combination of Grassmann numbers and vectors in the Fock space, and such linear combinations span the generalized Fock space.

2.1.2 Path integral formulation of partition function

The grand canonical partition function may be written as

$$Z = \text{Tr} e^{-\beta(\hat{H}-\mu\hat{N})}, \quad (2.7)$$

where Tr denotes the trace, \hat{H} is the second quantized Hamiltonian, $\hat{N} = \sum_{\alpha} a_{\alpha}^{\dagger} a_{\alpha}$ is the number operator and $\beta = 1/(k_{\text{B}}T)$. The partition function can be thought of as the trace of the imaginary time ($\tau = it$) evolution operator, or in other words the sum over all *periodic* trajectories with period β . At the same time, the trace of an operator between fermionic coherent states requires antiperiodic boundary conditions, yielding

$$Z = \int \prod_{\alpha} d\psi_{\alpha}^{*} d\psi_{\alpha} e^{-\sum_{\alpha} \psi_{\alpha}^{*} \psi_{\alpha}} \langle -\psi_{\alpha} | e^{-\beta(\hat{H}-\mu\hat{N})} | \psi_{\alpha} \rangle. \quad (2.8)$$

One can then divide the imaginary time interval $\tau = [0, \beta]$ into M slices so that $\Delta\tau = \beta/M$ and insert the $e^{-\Delta\tau(\hat{H}-\mu\hat{N})}$ operator M times. Furthermore, between each ‘‘time slice’’ we insert the resolution of unity

$$1 = \int \prod_{\alpha} d\psi_{\alpha}^{*} d\psi_{\alpha} e^{-\sum_{\alpha} \psi_{\alpha}^{*} \psi_{\alpha}} | \psi_{\alpha} \rangle \langle \psi_{\alpha} |, \quad (2.9)$$

to obtain

$$\begin{aligned} Z = & \int \prod_k \prod_{\alpha} d\psi_{\alpha,k}^{*} d\psi_{\alpha,k} \langle -\psi_{\alpha,1} | e^{-\Delta\tau(\hat{H}-\mu\hat{N})} | \psi_{\alpha,M} \rangle \langle \psi_{\alpha,M} | e^{-\Delta\tau(\hat{H}-\mu\hat{N})} | \psi_{\alpha,M-1} \rangle \\ & \times \dots \times \langle \psi_{\alpha,2} | e^{-\Delta\tau(\hat{H}-\mu\hat{N})} | \psi_{\alpha,1} \rangle. \end{aligned} \quad (2.10)$$

So long as the expression in the exponential is normal ordered¹, the individual time slices can be evaluated using Eqs. (2.2) and (2.4). Upon sending $M \rightarrow \infty$ we take $\psi_{\alpha,k+1} - \psi_{\alpha,k} \rightarrow \dot{\psi}_{\alpha}(\tau)\Delta\tau$ and introduce the functional integral notation

$$\lim_{M \rightarrow \infty} \int \prod_k \prod_{\alpha} d\psi_{\alpha,k}^{*} d\psi_{\alpha,k} \rightarrow \int_{\psi_{\alpha}(0)=-\psi_{\alpha}(\beta)} \mathcal{D}\psi_{\alpha}^{*}(\tau) \mathcal{D}\psi_{\alpha}(\tau), \quad (2.11)$$

¹Normal ordering means all creation operators are to the left of all annihilation operators. Matrix elements of normal ordered operators between coherent states can be evaluated in a straightforward manner, using Eqs. (2.2) and (2.4).

and the partition function becomes

$$Z = \int' \mathcal{D}\psi_\alpha^*(\tau) \mathcal{D}\psi_\alpha(\tau) \exp \left[- \int_0^\beta d\tau \left\{ \sum_\alpha \psi_\alpha^*(\tau) (\partial_\tau - \mu) \psi_\alpha(\tau) + H[\psi_\alpha^*(\tau), \psi_\alpha(\tau)] \right\} \right], \quad (2.12)$$

where \int' indicates the integration limits are to be taken as $\psi_\alpha(0) = -\psi_\alpha(\beta)$. The integral in the exponential is also referred to as *Euclidean action*, which facilitates for the partition function the compact form

$$Z = \int' \mathcal{D}\psi_\alpha^*(\tau) \mathcal{D}\psi_\alpha(\tau) e^{-S[\psi_\alpha^*(\tau), \psi_\alpha(\tau)]}. \quad (2.13)$$

2.1.2.1 Matsubara frequencies

It is worthwhile at this stage to point out a subtlety in the imaginary time formalism when it comes to finite temperatures. Often when a space-time variable is homogeneous, it is useful to work in the associated Fourier space. For example, when spatial translations are a symmetry, then wave-number (continuous or discrete) is a good quantum number. In the scope of this thesis, our primary tool for addressing electron-electron interactions is the Wilsonian momentum shell renormalization group (RG) analysis, for which we consider an effective low energy continuum theory of some underlying lattice system. Therefore, our momentum variable is typically continuous and the magnitude of it runs from zero to some nonuniversal ultraviolet cutoff Λ .

On the other hand, the integration in imaginary time τ is restricted to the interval $\tau \in [0, \beta)$. Hence, when $T \rightarrow 0$, and consequently $\beta \rightarrow \infty$, the associated frequency ω runs from $-\infty$ to ∞ and for a coherent state $\psi(\tau)$ we can write

$$\psi(\tau) = \int_{-\infty}^{\infty} \frac{d\omega}{2\pi} \psi(i\omega) e^{i\omega\tau}. \quad (2.14)$$

However, at finite temperature β also becomes finite. The fermionic fields in the partition function are periodic in τ with antiperiodic boundary conditions, and therefore contain only a discrete set of Fourier components, that are given by the fermionic Matsubara frequencies, $\omega_n = (2n + 1)/\beta$. Eq. (2.14) then becomes

$$\psi(\tau) = \frac{1}{\beta} \sum_{n=-\infty}^{\infty} \psi(i\omega_n) e^{i\omega_n\tau}. \quad (2.15)$$

2.1.3 Euclidean action

Now that we arrived to the expression of the partition function, let us focus on the quantity in the exponential, which is a Wick-rotated action, conventionally called Euclidean action.

Let us write it as the sum

$$S = S_0 + S_{\text{int}}, \quad (2.16)$$

where S_0 is the noninteracting part, and S_{int} encompasses the terms describing electronic interaction. The noninteracting action is generally of the form

$$S_0 = \int d\tau d^d \mathbf{r} \Psi^\dagger [\partial_\tau + \hat{h}(\mathbf{k} \rightarrow -i\nabla) - \mu] \Psi, \quad (2.17)$$

where d is the spatial dimensionality and the spinors Ψ^\dagger and Ψ are independent Grassmann variables, describing internal degrees of freedom such as spin, sublattice, etc. The operator $\hat{h}(-i\nabla)$ is a first quantized object and it is often obtained from an underlying lattice Hamiltonian via Taylor expansion around some wave-vector. As in this thesis we mostly study nodal Fermi liquids, the Hamiltonian usually describes one or more band degeneracy points. Hence, after expanding around one of these band touching points $\hat{h}(\mathbf{k}) \sim |\mathbf{k}|^z$, where z is the dynamical critical exponent. Furthermore, the Hamiltonian \hat{h} typically contains some matrix structure, that operates on the components of Ψ^\dagger and Ψ . Finally, μ is a chemical potential term, that allows for deviations of electron filling from the band touching point. In this context $\mu = 0$ suggests the chemical potential is fine tuned to the degeneracy point, and the Fermi surface is replaced by a zero dimensional or pointlike Fermi point.

Let us now turn our focus to the interacting action. In the scope of this work we only consider short-range or local electron-electron interactions. In general, Thomas-Fermi screening renders the Coulomb interaction short ranged in the presence of a Fermi surface. Our renormalization scheme is aware of the chemical potential term, which is in fact a relevant perturbation at the noninteracting fixed point (more of that later), and therefore a finite bare value of μ already results in the screening of the long range tail of the Coulomb potential. Similarly, since the density of states (DoS) at low energies in a d dimensional system scales as

$$\rho(E) \sim |E|^{\frac{d-z}{z}}, \quad (2.18)$$

in e.g. a two-dimensional quadratic band touching system ($d = z = 2$) the low-energy DoS is constant, which also results in screening. Moreover, at finite temperatures thermal screening kicks in, yielding a finite thermal mass to the photon [94]. Admittedly, with vanishing $\rho(E)$ at zero temperature and chemical potential, long-range interactions can in principle play an important role. In this case one has to rely on complementary theoretical computations or experiments, and assess whether the results obtained considering only short-range interactions are consistent with these. The schematic form of S_{int} containing

only local (momentum-independent) quartic terms reads

$$S_{\text{int}} = \int d\tau d^d \mathbf{r} \sum_{M,N} \lambda_{MN} (\Psi^\dagger M \Psi) (\Psi^\dagger N \Psi), \quad (2.19)$$

where M and N are Hermitian matrices of the same dimensionality as Ψ^\dagger and Ψ , and g_{MN} is the coupling constant of the interaction. In our convention positive values of λ_{MN} correspond to repulsive interactions.

Before we proceed, let us make a few remarks on the role of symmetries. In general, the underlying physical system can be endowed with various discrete symmetries, e.g. time reversal, parity, or charge conjugation symmetry. Further symmetries might be imposed by the point group (or space group) of the lattice. When deriving the corresponding continuum descriptions, these microscopic symmetries must be preserved. Note that some of these might become continuous instead of discrete, for example the Dirac cones in graphene at low energies are endowed with full rotational symmetry, even though the honeycomb lattice only possesses discrete C_3 lattice rotational invariance. When proceeding to write down the interacting action S_{int} , one has to again preserve all operative symmetries. This typically severely restricts the terms allowed in Eq. (2.19).

2.2 Wilsonian momentum-shell renormalization

To study the quantum critical properties of a system we examine its low-energy and long-wavelength behavior under the tuning of nonthermal parameters, such as the strength of the local interactions λ_{MN} . To do this we apply the momentum shell renormalization scheme, where we gradually coarse grain the degrees of freedom of the given system, thus constructing an effective theory at low energies. To proceed we introduce a hard ultraviolet momentum cutoff $\Lambda \sim 2\pi/a$, which replaces the cubic Brillouin zone by a spherical one. Here a bears the dimension of the lattice constant. In the renormalization group (RG) procedure we then gradually decrease Λ by repeatedly integrating out a thin Wilsonian momentum shell defined as $\Lambda e^{-\ell} < |\mathbf{k}| < \Lambda$, where $\ell > 0$ is the logarithm of the RG scale (also called RG time). Finally, we restore the Euclidean action ($S_0 + S_{\text{int}}$) into its original form, but in terms of the renormalized quantities. The so-called RG flow acquired this way is cast in terms of differential equations of various parameters appearing in S with respect to ℓ , describing the change in some quantity during the above procedure. These are also called β -functions.

The scaling of various quantities appearing in the action relative to \mathbf{k} is of crucial importance as we gradually lower the ultraviolet cutoff. When a quantity Q appearing in the Euclidean action is invariant under

$$Q \rightarrow Q e^{-s\ell}, \quad (2.20)$$

then its *scaling dimension* is $[Q] = s$. The scaling dimensions of momentum and frequency are respectively $[k] = 1$ and $[\omega] = z$. This is exactly the role of the dynamical critical exponent, it tells us the relative scaling between space and imaginary time (or momentum and Matsubara frequency). The scale-invariance of S_0 requires that $[\Psi] = d/2$, from which we obtain the scaling dimension of the quartic coupling constants to be $[\lambda_{MN}] = z - d$. For linearly or quadratically dispersing fermions in two or three dimensions this leaves only two possibilities at tree level. Local interactions are *marginal* if $[\lambda_{MN}] = 0$, e.g. in the case of Bernal bilayer graphene ($d = z = 2$). In this case leading loop corrections scale as $\mathcal{O}(\lambda_{MN}^2)$, and the system is unstable in the presence of already infinitesimal interactions. On the other hand, if $[\lambda_{MN}] < 0$ then local interactions are *irrelevant*, e.g. in the case of Dirac fermions in graphene ($d = 2$ but $z = 1$). This results in the system being stable in the presence of weak enough electronic interactions. However, above some critical value of the bare couplings it undergoes a quantum phase transition into some broken symmetry phase.

The scaling dimension $[\lambda_{MN}]$ also pins the lower critical dimension at $d_c = z$, where short-range interactions are marginal, which facilitates a controlled ϵ expansion about $d = d_c$, with $\epsilon = d - d_c$. Note the question of relevance or marginality of interactions can also be appreciated from the point of view of DoS. Namely, $[\lambda_{MN}] = d - z > 0$ suggests $\rho(E \approx 0)$ vanishes as power law, whereas $[\lambda_{MN}] = d - z = 0$ means the $\rho(E \approx 0)$ is constant.

2.2.1 Fierz reduction of quartic terms

Before we go on to utilize the above outlined formalism let us point out a source of simplification in the interacting action S_{int} . To write down all symmetry-allowed local four fermion terms, we first classify all Hermitian matrices of the corresponding dimension according to their transformation properties under the operative symmetries. In a system with N internal degrees of freedom there are N^2 such matrices. The following Fierz identity reveals a level of redundancy on the level of four fermion terms.

The Fierz identity for D -dimensional Hermitian matrices reads [11, 18]

$$[\Psi^\dagger(x)M\Psi(x)][\Psi^\dagger(y)N\Psi(y)] = -\frac{1}{D^2} \sum_{a,b} \text{Tr}(M\Gamma^a N\Gamma^b)[\Psi^\dagger(x)\Gamma^b\Psi(y)][\Psi^\dagger(y)\Gamma^a\Psi(x)], \quad (2.21)$$

where Γ^a span a basis in the space of such matrices. This allows us to express each local quartic term with $x = y$ as the linear combination of the remaining ones. If we arrange the interaction terms in an array \mathbf{X} , this linear connection can be written as

$$\mathbf{X} = A\mathbf{X}, \quad (\mathbb{I} - A)\mathbf{X} \equiv F\mathbf{X} = 0, \quad (2.22)$$

where A is a quadratic matrix of the same dimension as \mathbf{X} , and in the second equation

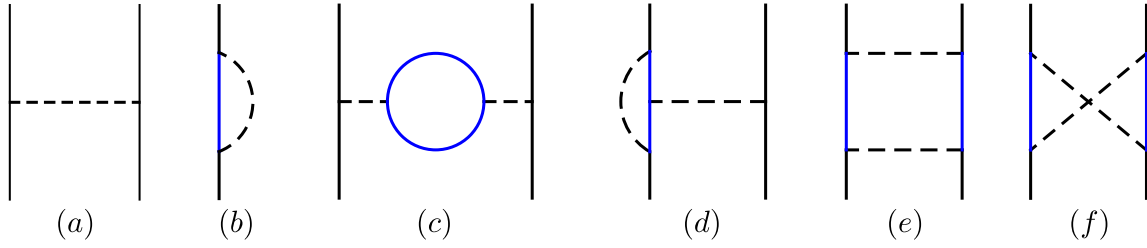


Figure 2.1: (a) Bare four-fermion interaction vertex and (b) the self-energy correction due to four-fermion interaction. The contribution from Feynman diagram (b) is finite only when the chemical potential (μ) is finite, and renormalizes μ . Feynman diagrams (c)-(f) yield corrections to the bare interaction vertex to the leading order in the ϵ expansion, where $\epsilon = d - z$. Here, solid lines represent fermions, while blue lines in (b)-(f) correspond to the fast modes living within a thin Wilsonian momentum shell $\Lambda e^{-l} < |\mathbf{k}| < \Lambda$, where Λ is the ultraviolet momentum cut-off and l is the logarithm of the renormalization group scale. The black lines are the slow modes with $|\mathbf{k}| < \Lambda e^{-l}$. Figure adapted from Ref. [13].

we introduced the Fierz matrix F . The number of independent quartic terms equals (dimension of F) - (rank of F). The linear relations among various four fermion terms can be extracted from F using row reduction, for example.

2.2.2 Zero temperature and chemical doping

Let us dive into a simple example of zero temperature (T) and chemical doping (μ). The relevant Feynman diagrams are displayed in Fig. 2.1. At $T = \mu = 0$ the contribution of fermionic self energy [Fig. 2.1(b)] vanishes. In fact, even though for $\mu > 0$ this diagram renormalizes the chemical potential, this correction is neglected on the basis of the leading order ϵ expansion. This is so, because the chemical potential enters via the loop corrections to the interaction couplings, which themselves are already leading order in ϵ . The one-loop corrections to the coupling constant λ_{MN} come from the λ_{MN}^2 term after evaluating the diagrams from Fig. 2.1(c)-(f). The flow of the coupling constants is described by flow equations (or β -functions), which generally constitute a system of coupled differential equations.

For simplicity's sake, we first consider a simple example with a single independent coupling constant λ . In our RG and ϵ expansion scheme the flow equation of λ takes the form

$$\beta_\lambda \equiv \frac{d\lambda}{d\ell} = -\epsilon\lambda + c \frac{\Lambda^d}{\epsilon_\Lambda} \lambda^2, \quad (2.23)$$

where c is some constant prefactor coming from the loop integrals. Typically $c > 0$. We have yet to cast β_λ into a dimensionless form, for which we introduce

$$g = c \frac{\Lambda^d}{\epsilon_\Lambda} \lambda, \quad (2.24)$$

where g is the dimensionless coupling constant, ϵ_Λ is the quasiparticle energy $\epsilon_{\mathbf{k}}$ evaluated

at $|\mathbf{k}| = \Lambda$, meaning $\epsilon_\Lambda \sim \Lambda^z$. Notice therefore $g \sim \Lambda^\epsilon$, and the cutoff cancels at the lower critical dimension. In terms of the dimensionless coupling constant g , Eq. (2.23) becomes

$$\beta_g = -\epsilon g + g^2. \quad (2.25)$$

The differential equation β_g has two *fixed points* (FPs), where $\beta_g = 0$. The trivial or *Gaussian* FP is at $g = 0$, which is stable for any $\epsilon > 0$. Besides, an unstable FP can be found at $g = \epsilon$, which represents a *quantum critical point* (QCP). For a bare value of interactions strength $g(0) < \epsilon$ the renormalized coupling $g(\ell)$ flows back to the noninteracting Gaussian FP. On the other hand, $g(0) > \epsilon$ means $g(\ell)$ grows with the RG time indefinitely. The meaning of this divergence is that interactions grow stronger under coarse graining, and it indicates an instability towards some broken symmetry phase (BSP), that sets in via a *quantum phase transition* (QPT). Notice when the physical value of $\epsilon = d - z = 0$, this corresponds to the case when local interactions are marginal, and the system becomes unstable towards the formation of a BSP for infinitesimal interaction coupling when $c > 0$.

2.2.2.1 Fixed point analysis

Let us now generalize the above scenario to multiple running couplings g_i at once, where $i = 1, \dots, N$ and N is the number of independent coupling constants. Then the system of flow equations up to leading order takes the form

$$\beta_{g_i} = -\epsilon g_i + \sum_{j,k} H_{jk}^{(i)} g_j g_k, \quad (2.26)$$

where the prefactors $H_{jk}^{(i)}$ again come from the loop integrals. Here β_{g_i} describe the flow in the N dimensional space of the coupling constants and the FPs are located where $\beta_{g_i} = 0$, $\forall i$. Let us denote such a point in the space of coupling constants by \mathbf{g}_a^* , which is an N -component array and a indexes the various FPs. To analyze each \mathbf{g}_a^* we linearize the flow around it and construct the *stability matrix* M^a , the components of which are

$$M_{ij}^a = \left. \frac{d\beta_{g_i}}{dg_j} \right|_{\mathbf{g}_a^*}. \quad (2.27)$$

The number of positive eigenvalues of M^a classifies each FP as follows. All eigenvalues being negative correspond to a fully attractive FP, for example the Gaussian FP in a Gross-Neveu-like model with only four fermion interactions, as in our previous example of only one such coupling constant. One positive eigenvalue constitutes a QCP, endowed with one repulsive direction (like the one at $g = \epsilon$ in our model with one coupling). To the leading order in the ϵ -expansion the positive eigenvalue at all QCPs is exactly ϵ , which in

turn determines the *correlation length exponent* (ν) according to

$$\nu^{-1} = \epsilon + \mathcal{O}(\epsilon^2). \quad (2.28)$$

The fact that ν is the same at all QCPs is however an artifact of the leading order ϵ expansion. To the leading order in the ϵ -expansion local interactions do not yield any correction to the fermion self energy, and hence to the dynamic scaling exponent (z). Two positive eigenvalues (and therefore two repulsive directions) indicate a bicritical point (BCP) in the flow of the coupling constants. Such points are necessary for a continuous flow and they separate the basins of attraction of different QCPs. In principle one can encounter more than two positive eigenvalues, however in this thesis we do not include such points into our analysis.

The above analysis allows us to reconstruct the structure of the RG flow in the space of coupling constants and identify the instabilities in terms of runaway directions, indicated by the positive eigenvalue of some QCP. In what follows we seek to establish the nature of symmetry breaking at each QCP by incorporating order parameters into the action, and ultimately into the RG scheme. Next we describe this methodology.

2.2.2.2 Order parameters

In the previous section we renormalized a set of interaction couplings appearing in the the Euclidean action S , see Eqs. (2.16), (2.17), and (2.19). The existence of runaway directions in their flow indicates instabilities of the interacting system toward some BSP, that sets in via QPTs. Here we introduce order parameters in the action in order to probe the nature of symmetry breaking at each QCP in an unbiased fashion.

To facilitate the forthcoming discussion we introduce the Nambu-doubled spinor basis, suitable to capture both excitonic and superconducting orders within a unified framework, according to

$$\Psi_{\text{Nam}} = \begin{bmatrix} \Psi_{\mathbf{k}} \\ U\Psi_{-\mathbf{k}}^* \end{bmatrix}, \quad (2.29)$$

where U is the unitary part of the time reversal operator. A time reversal symmetric noninteracting Hamiltonian \hat{h}_0 under this change of basis becomes

$$\hat{h}_0^{\text{Nam}}(\mathbf{k}) = \eta_3 \otimes \hat{h}_0(\mathbf{k}), \quad (2.30)$$

where \otimes indicates tensor product and η_μ is a set of Pauli matrices with $\mu = \{0, 1, 2, 3\}$ (η_0 is the unit matrix) that act on the newly introduced particle-hole degree of freedom. The above extension of the Hilbert space allows for the addition of particle-particle (or hole-hole) terms to the Hamiltonian, which will appear as off-diagonal elements in the Hamiltonian, and capture the condensation of electrons into Cooper pairs. We utilize this

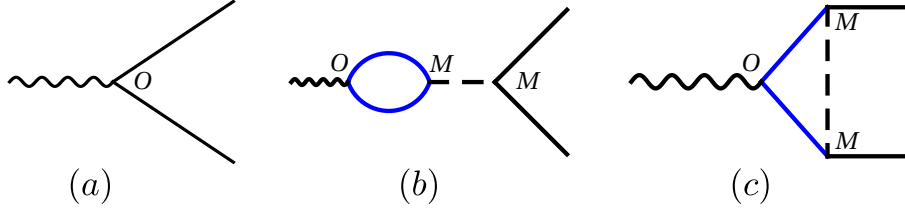


Figure 2.2: (a) The bare vertex associated with the source term $\Psi^\dagger O \Psi$. The leading order renormalization of such vertices arises from Feynman diagrams (b) and (c), yielding the RG flow of the source terms or conjugate fields, see Eq. (2.33). Here, wavy lines stand for the conjugate field, while solid lines for fermions, and the dashed lines for the interaction vertex. The black (blue) solid lines represent slow (fast) modes. Figure adapted from Ref. [13].

basis for the renormalization of order parameters throughout this thesis.

We now proceed by adding to the action fermion bilinears of the form

$$\sum_{i=1}^N \Delta_i \Psi_{\text{Nam}}^\dagger O_i \Psi_{\text{Nam}}, \quad (2.31)$$

where $O_i = \eta_0 \otimes A_i$ or $\eta_3 \otimes A_i$ for excitonic orders and $O_i = (\eta_1 \cos \phi + \eta_2 \sin \phi) \otimes A_i$ for pairing orders, where ϕ is the superconducting U(1) angle. Here A_i transform under an N dimensional representation of an operative symmetry and Δ_i are the corresponding conjugate fields. To determine the pattern of symmetry breaking happening through QCPs in an unbiased fashion, besides the interaction couplings g_i we also renormalize the conjugate fields. Since the RG transformation does not break any symmetries, each component of Δ_i acquires the same correction, which is also called *anomalous dimension*. Only once the symmetry breaking happens the system picks an orientation in the internal space of the nucleating order parameters (also called phase locking). However, the RG strictly speaking loses its jurisdiction as soon as a coupling constant diverges, and any information from inside the ordered phase has to be extracted using different methods (for example mean field theory).

Let us now allow for multiple running couplings and write down the action in a schematic form, containing all independent interaction couplings, and all local (excitonic and superconducting) order parameters

$$S = S_0 + \int d\tau d^d \mathbf{r} \left[\left\{ g_1 \sum_{i=1}^{m_1} (\Psi_{\text{Nam}}^\dagger M_i^{(1)} \Psi_{\text{Nam}})^2 + g_2 \sum_{i=1}^{m_2} (\Psi_{\text{Nam}}^\dagger M_i^{(2)} \Psi_{\text{Nam}})^2 + \dots \right\} + \left\{ \Delta_1 \sum_{i=1}^{n_1} \Psi_{\text{Nam}}^\dagger O_i^{(1)} \Psi_{\text{Nam}} + \Delta_2 \sum_{i=1}^{n_2} \Psi_{\text{Nam}}^\dagger O_i^{(2)} \Psi_{\text{Nam}} + \dots \right\} \right], \quad (2.32)$$

where, in factoring out the conjugate field Δ_i , we exploited the fact that the components of the same order parameter renormalize together. The first order parameter is then $O(n_1)$ symmetric, the second is $O(n_2)$ symmetric, and so on. The renormalization of conjugate

fields happens through the Feynman diagrams displayed in Fig. 2.2. For technical details on diagram contributions consult Appendix C.3.1.

Note that writing the interactions in the particle-hole basis means we can renormalize all independent couplings without utilizing the Nambu basis. However, in order to remain unbiased between excitonic and pairing orders, we have to carry out the renormalization of order parameters in the Nambu doubled formalism. Schematically the β -functions for the conjugate fields read

$$\beta_{\Delta_i} - z = \sum_j F_j^{(i)} g_j, \quad (2.33)$$

where the prefactors $F_j^{(i)}$ are analogous to $H_{jk}^{(i)}$ in Eq. (2.26), and we separated the scaling dimension (z) of Δ_i to the left hand side. Since β_{Δ_i} only depend on the coupling constants, they can be evaluated at the locations of the fixed points \mathbf{g}_a^* . The dominant instability at each FP is then indicated by the largest (positive) anomalous dimension [right hand side of Eq. (2.33)]. Note that to the leading order in the ϵ -expansion all FPs $|\mathbf{g}_a^*| \sim \epsilon$, therefore the anomalous dimensions acquired by supplying these values in Eq. (2.33) are also in units of ϵ .

2.2.3 Finite temperature and chemical doping

The general spirit of the RG analysis at finite temperature and chemical doping is the same as outlined in the previous section, with one important distinction. Namely, as both T and μ are *relevant* perturbations, they grow with RG time, and provide a natural infrared cutoff in the following way. Let us introduce the dimensionless temperature and chemical doping respectively as

$$t = \frac{T}{\epsilon_\Lambda}, \quad \text{and} \quad \tilde{\mu} = \frac{\mu}{\epsilon_\Lambda}. \quad (2.34)$$

Then these quantities scale according to $[t] = [\tilde{\mu}] = z$, and their flow equations read

$$\frac{dt}{d\ell} = zt, \quad \text{and} \quad \frac{d\tilde{\mu}}{d\ell} = z\tilde{\mu}. \quad (2.35)$$

Due to the simple form of these β -functions we can immediately write

$$t(\ell) = t(0)e^{z\ell}, \quad \text{and} \quad \tilde{\mu}(\ell) = \tilde{\mu}(0)e^{z\ell} \quad (2.36)$$

and from now on we suppress the tilde from the dimensionless chemical potential and take $\tilde{\mu} \rightarrow \mu$. The infrared cutoff introduced this way corresponds to a scenario when the renormalized temperature $t(\ell)$ or chemical doping $\mu(\ell)$ become comparable to the ultraviolet energy ϵ_Λ , beyond which the notion of the original quasiparticles becomes moot and the flow equations lose their jurisdiction.

On a technical note, temperature enters the RG analysis via the discrete sum over the Matsubara frequencies in Eq. (2.15), whereas the chemical potential term results from Eq. (2.7) when setting $\mu \neq 0$. Then, the coefficients in the flow equations in Eqs. (2.26) and (2.33) become

$$H_{jk}^{(i)} \rightarrow H_{jk}^{(i)}(t, \mu), \quad F_j^{(i)} \rightarrow F_j^{(i)}(t, \mu). \quad (2.37)$$

Our computation of phase diagram then involves the following steps.

(1) We set the value $\zeta \sim \mathcal{O}(1)$ up to which either t and/or μ is allowed to grow. Equation (2.36) then determines an upper bound ℓ^* to the RG time according to

$$\ell^* = \min(\ell_t^*, \ell_\mu^*), \quad (2.38)$$

where

$$\ell_t^* = \frac{1}{z} \ln \left(\frac{\zeta}{t(0)} \right), \quad \ell_\mu^* = \frac{1}{z} \ln \left(\frac{\zeta}{\mu(0)} \right). \quad (2.39)$$

(2) We set the bare values of interaction couplings $g_i(0)$ and temperature $t(0)$, as well as that of the chemical potential $\mu(0)$. All order parameter conjugate fields are initialized to zero, $\Delta_i(0) = 0$.

(3) We numerically iterate the flow equations from Eqs. (2.26) and (2.33) together with Eq. (2.36) between $0 < \ell < \ell^*$. A broken symmetry phase is indicated when at least one coupling constant diverges, $g_j(\ell_d) \sim \mathcal{O}(1)$, $\ell_d < \ell^*$. The first point in parameter space for which a divergence is detected contributes a data point $(\mu, t, \mathbf{g}, \dots)$, where \dots indicates other possible parameters in the theory. The phase boundary is strictly between disordered and ordered phases.

(4) The nature of symmetry breaking is determined by the largest positive anomalous or scaling dimension $\Delta_i(\ell_d)$.

It is important to emphasize that the RG analysis breaks down once a coupling constant diverges, and as such is only equipped to detect a phase boundary between disordered and ordered phases, as well as the pattern of the corresponding symmetry breaking. For this reason, we always start out in the disordered phase, and slowly increase the bare interaction couplings until we detect a divergence in the renormalized interactions. Any information from inside the ordered phase (e.g. coexistence) has to be extracted using different methods, for example mean field theory.

Note at zero temperature and chemical doping the system is devoid of any natural infrared cutoff. Here we simply set $\ell^* \sim \mathcal{O}(10)$ large enough for a coupling constant to

diverge if the conditions are right. Admittedly, the above outlined methodology bears a level of arbitrariness in terms of the upper bound ζ to which t and μ are allowed to grow, and the value that constitutes a divergent coupling constant. However, the interplay of these parameters only affects nonuniversal quantities, such as the requisite strength of interactions.

Having the basic building blocks in place, we now dive into the venture of studying various nodal Fermi liquids. In the next part we focus on the quantum critical properties of some paradigmatic models, constituted by three-dimensional Dirac fermions (Chapter 3), as well as the three-dimensional effective spin-3/2 Luttinger fermions (Chapter 4).

Part I

Emergent symmetries

We start our journey by examining the quantum critical properties of various nodal Fermi liquids, with special focus on the emergence of enlarged symmetries at certain QCPs. Microscopic symmetries of a physical system are present on all energy and length scales, and accordingly they have to be imposed in its description, both in the lattice model and the low-energy continuum theory. In contrast, emergent symmetries arise only on certain scales, and in our context they appear in the deep infrared regime, described by infrared FPs of a renormalization group flow.

In practice, the order parameters breaking distinct symmetries generally renormalize separately, and the conjugate fields have distinct β -functions, in other words generally $\beta_{\Delta_i} \neq \beta_{\Delta_j}$ when $i \neq j$. Note that these flow equations are functions of the interaction couplings and hence can be evaluated at the various FPs, providing the anomalous dimension of the OP at a FP. Symmetry enlargement of a certain FP, say \mathbf{g}^* , means, that order parameters breaking *different microscopic symmetries* acquire *identical anomalous or scaling dimensions* at the given FP, in other words

$$\beta_{\Delta_i}|_{\mathbf{g}^*} = \beta_{\Delta_j}|_{\mathbf{g}^*}, \quad i \neq j. \quad (2.40)$$

Then, the given FP (in our case QCP or BCP) is said to possess an enlarged symmetry, in comparison to the original symmetries of the action. For example, if Δ_j and Δ_k respectively possess distinct $O(n_1)$ and $O(n_2)$ symmetries, the QCP fulfilling Eq. (2.40) enjoys an enlarged $O(n_1 + n_2)$ symmetry, that is absent at the microscopic level, but emerges at the infrared unstable QCP.

In what follows we start the investigation in three spatial dimensions and examine the symmetry enlargement at the interacting QCPs in linearly dispersing Dirac fermions in Chapter 3. Subsequently, in Chapter 4 we study a collection of spin-3/2 fermions in a Luttinger semimetal, a strong spin-orbit coupled, quadratically dispersing system.

Chapter 3

Three-dimensional Dirac liquid

In this chapter we focus on a three-dimensional strong spin-orbit coupled gapless Dirac liquid, constituted by four-component massless Dirac fermions. Relevant material examples are, for example, strong spin-orbit coupled Cd_3As_2 [75] and Na_3Bi [32]. Our model, besides the fundamental discrete parity (\mathcal{P}), time-reversal (\mathcal{T}) and charge-conjugation (\mathcal{C}) symmetries, also enjoys a *microscopic* continuous $\text{U}(1)\otimes\text{SU}(2)$ global chiral symmetry. The following discussion unfolds the role of strong momentum-independent Hubbardlike or local electronic interactions among such massless chiral Dirac fermions.

3.1 Noninteracting models: continuum and lattice

We start by introducing a noninteracting gapless Dirac system, endowed with genuine *microscopic* continuous chiral symmetry. We first present the effective low-energy description of such system, and discuss its invariance under various discrete and continuous symmetries. Subsequently, we propose a lattice realization of a genuine chiral Dirac semimetal.

3.1.1 Continuum model

The minimal model for three-dimensional massless chiral Dirac fermions is captured by the Hamiltonian

$$\hat{h}(\mathbf{k}) = \sum_{j=1}^3 v_j \Gamma_j k_j, \quad (3.1)$$

where k_j are the components of momentum and v_j are the Fermi velocities along the principal axes. Here $j = 1, 2$ and 3 correspond to x, y , and z , respectively. The mutually anticommuting four-component Hermitian Γ matrices satisfy the Clifford algebra $\{\Gamma_i, \Gamma_j\} = 2\delta_{ij}$. Our results only depend on the internal algebra of these matrices, and are independent of the spinor representation. Nevertheless, picking a representation is informative as it captures some underlying physics. We organize the four-component spinor basis as $\Psi_{\mathbf{k}} = (c_{+\uparrow}, c_{+\downarrow}, c_{-\uparrow}, c_{-\downarrow})^\top(\mathbf{k})$, where $c_{ps}(\mathbf{k})$ are the fermion annihilation

operators with parity $p = \pm$, spin projections $s = \uparrow, \downarrow$, and momentum \mathbf{k} . The Γ matrices are then given by $\Gamma_j = \Gamma_{1j}$ for $j = 1, 2, 3$, with $\Gamma_{\mu\nu} \equiv \tau_\mu \otimes \sigma_\nu$, where \otimes denotes the Kronecker product. Two sets of Pauli matrices $\{\tau_\mu\}$ and $\{\sigma_\nu\}$ operate on parity and spin indices, respectively, and τ_0 and σ_0 are the two-dimensional identity matrices. The model in Eq. (3.1) then describes the mixing of different parity states with unit angular momentum difference. To close the anticommuting Clifford algebra, which contains five elements in the space of four-dimensional Hermitian matrices, we define $\Gamma_4 = \Gamma_{30}$ and $\Gamma_5 = \Gamma_{20}$.

For now we set $v_x = v_y = v_z = v$, which brings Eq. (3.1) into a fully rotationally symmetric form $\hat{h}(\mathbf{k}) = v\Gamma_{1j}k_j$, where the summation over the repeated spatial indices is assumed, and $\hat{h}(\mathbf{k})$ describes an isotropic, doubly Kramers degenerate Dirac cone centered at the $\Gamma = (0, 0, 0)$ point of the cubic Brillouin zone [see Sec. 3.1.2]. The generators of rotations about the x -, y - and z -axis are respectively Γ_{01}, Γ_{02} , and Γ_{03} . For example, a rotation by an angle θ about the j th axis is generated by $R_j(\theta) = \exp[i\theta\Gamma_{0j}/2]$. Specifically, when $\theta = \pi/2$ and $j = z$, $\mathbf{k} \rightarrow (k_y, -k_x, k_z)$, such that $R_z(\pi/2)\hat{h}(\mathbf{k})R_z^{-1}(\pi/2) = \hat{h}(\mathbf{k})$ in an isotropic system. Therefore, the noninteracting Hamiltonian remains invariant under the four-fold (C_4) rotation about the z axis. Similarly, under the C_4 rotations about the x and y axes $\mathbf{k} \rightarrow (k_x, k_z, -k_y)$ and $(-k_z, k_y, k_x)$, respectively. It is then straightforward to show that $\hat{h}(\mathbf{k})$ remains invariant under $O(3)$ rotations.

The $O(3)$ rotational symmetry of the low-energy model is only plausible when the underlying lattice structure possesses a cubic symmetry. The isotropic Fermi velocity in a low-energy theory is then $v \sim ta$, where t is the hopping amplitude and a is the lattice constant. However, known Dirac materials often exhibit tetragonal symmetry [32, 75], with elongated (or shortened) lattice constant along one of the three principle axes, for example. In a tetragonal environment this results in the breakdown of the $O(3)$ rotational symmetry down to an in-plane $O(2)$ one about the z -axis. In other words, $v_x = v_y \neq v_z$ in a tetragonal Dirac material. In Sec. 3.2.6 we discuss the effects of *weak* rotational symmetry breaking on interacting chiral Dirac fermions in a perturbative manner.

The gapless chiral Dirac system is invariant under the discrete parity transformation (\mathcal{P}), reversal of time (\mathcal{T}), and charge conjugation (\mathcal{C}). In our representation of the four-component spinor $\Psi_{\mathbf{k}}$ and the Γ matrices, the above transformations are realized as $\mathcal{P}\Psi_{\mathbf{k}}\mathcal{P} = \Gamma_{30}\Psi_{-\mathbf{k}}$, $\mathcal{T}\Psi_{\mathbf{k}}^*\mathcal{T} = -\Gamma_{02}\Psi_{-\mathbf{k}}$ and $\mathcal{C}\Psi_{\mathbf{k}}\mathcal{C} = -i\Gamma_{12}\Psi_{\mathbf{k}}^*$ [6]. The time-reversal operator is *antiunitary* and can be written as $\mathcal{T} = UK$, where $U = \Gamma_{02}$ is the unitary part and K is complex conjugation, such that $\mathcal{T}^2 = -1$, yielding Kramers degenerate Dirac bands.

The noninteracting system remains invariant also under a continuous global $U(1)$ chiral rotation (θ_{ch}), under which $\Psi_{\mathbf{k}} \rightarrow \exp[i\theta_{\text{ch}}\Gamma_{10}]\Psi_{\mathbf{k}}$, where the matrix $C = \Gamma_{10}$ is the generator of the chiral rotation. We note that two mass matrices, namely Γ_4 and Γ_5 , that anticommute with $\hat{h}(\mathbf{k})$, break the global $U(1)$ chiral symmetry of the massless Dirac Hamiltonian. While the scalar mass (Γ_4) only breaks the continuous chiral symmetry, the

pseudoscalar mass (Γ_5) in addition breaks the discrete \mathcal{P} and \mathcal{T} symmetries. Furthermore, the noninteracting Hamiltonian $\hat{h}(\mathbf{k})$ possesses a *pseudospin* $SU(2)$ chiral symmetry, which only becomes visible once we Nambu double the spinor basis, as shown in Sec. 3.2.3. Therefore, the noninteracting gapless chiral Dirac system enjoys a $U(1) \otimes SU(2)$ chiral symmetry.

The imaginary time (τ) Euclidean action for such a collection of noninteracting chiral Dirac fermions reads

$$S_0 = \int d\tau \int d^d \mathbf{x} \Psi_{\tau, \mathbf{x}}^\dagger \left[\partial_\tau + \hat{h}(\mathbf{k} \rightarrow -i\nabla) \right] \Psi_{\tau, \mathbf{x}}, \quad (3.2)$$

where d is the number of spatial dimensions. The absence of a chemical potential term implies the fine tuning of the Fermi energy to the band touching Dirac point, whereby the Fermi surface shrinks to just one point at the center of the Brillouin zone (see, however, Ref. [95]). While constructing the interacting theory, besides the spatial rotational symmetry, we impose \mathcal{P} , \mathcal{T} and \mathcal{C} symmetries separately. But, we do not enforce invariance under $U(1)$ chiral rotations or pseudospin $SU(2)$ rotations explicitly at the microscopic level. Instead, we demonstrate restoration of the chiral symmetry as an emergent phenomena at various RG fixed points that can be accessed by tuning the strength of interactions among Dirac fermions, as we also witnessed on a relativistic flatland, namely graphene, in the previous chapter. For the time being however our noninteracting single-flavor model is chiral symmetric, which at first glance seems to be at odds with the Nielsen-Ninomiya “no-go” theorem [96], when it comes to constructing a corresponding lattice model. We proceed with pointing at a possible way out of this conundrum. Nevertheless, given that two-dimensional genuine chiral Dirac-Hubbard model on a square lattice [97], and three-dimensional Dirac-Hubbard on a cubic lattice [98] have been studied recently using quantum Monte Carlo simulations, a concrete lattice realization of three-dimensional massless chiral Dirac fermions should facilitate future numerical investigations of this system, where our results can be scrutinized.

3.1.2 Lattice model

In this section we consider a single flavor of four-component massless chiral Dirac fermions in a continuum theory, the translation of which to a lattice model is, however, a nontrivial task. The challenge originates from constructing a lattice version of the derivative operator while taking $\mathbf{k} \rightarrow -i\nabla$ in Eq. (3.1). Nevertheless, symmetrizing the derivative from basic calculus as

$$\frac{df(x)}{dx} = \lim_{a \rightarrow 0} \frac{f(x+a) - f(x-a)}{2a} \quad (3.3)$$

proffers a tempting lattice version, in which one treats a as the lattice constant, and arrives at the nearest neighbor description, where in one dimension the eigenenergies are $\epsilon_k \sim t \sin(ka)$, the blue squares in Fig. 3.1. Here k is the discrete valued lattice momentum and t is a hopping amplitude, setting the energy scale. However, this construction results

in so-called fermion doublers at the edges of the one-dimensional Brillouin zone ($k = \pm\pi/a$). In fact in d dimensions one finds 2^d number of low-energy Dirac points compared to the continuum theory [99]. A common remedy to this problem is the introduction of a momentum-dependent Wilson mass, which gaps the doublers, but vanishes at the desired Γ point [100,101]. But, such a construction comes with its own intricacies. As such adding another discrete symmetry (\mathcal{P} , \mathcal{T} , \mathcal{C}) preserving anticommuting mass matrix (Γ_4) spoils the genuine microscopic chiral symmetry of Dirac fermions. Even though the resulting higher order in momentum ($\propto k^2$) terms are *irrelevant* in the RG framework, yielding an emergent chiral U(1) symmetry, the nucleation of \mathcal{P} , \mathcal{T} and \mathcal{C} symmetric, but chiral U(1) symmetry breaking scalar mass (Γ_4) at strong coupling then takes place through a *fluctuation driven first-order transition*, as it does not break any bonafide microscopic symmetry [102]. So, we seek for a lattice realization of single flavored massless Dirac fermions with genuine microscopic chiral symmetry.

The doubler problem can also be overcome by extending the nearest neighbor derivative to next nearest neighbor [99], with hopping parameters $t_1 = (1 + \mu)/(2\mu)$ and $t_2 = (\mu - 1)/(4\mu)$ between the first and second neighbors, respectively. Here μ is a tuning parameter that recovers the nearest neighbor limit for $\mu = 1$. The corresponding spectrum is then given by

$$\epsilon_k = t_1 \sin(ka) + t_2 \sin(2ka). \quad (3.4)$$

Upon sending $\mu \rightarrow 0$, the Fermi velocity of the doublers gets pushed to *infinity*, and due to the finite sampling of the k axis there will be no additional low-energy mode in the Brillouin zone, see orange diamonds in Fig. 3.1. However, this construction results in much of the spectral weight being pushed to high energies $\epsilon_k \gg \pi t$.

The aforementioned complications are solved by using the Stanford Linear Accelerator (SLAC) lattice derivative [104], a pedagogic construction of which is provided in Ref. [105]. The three main ingredients of the SLAC construction are the following. (i) Identifying the (continuum) derivative operation with convolving a function $f(x)$ with the negative derivative of the Dirac delta function $f'(x) = -\delta'(x) \star f(x)$. (ii) Applying a low-pass filter to the continuum formalism to restrict it in momentum space to the first Brillouin zone. (iii) Finally, sampling the resulting operator on a lattice. Since the Fourier transform of the Dirac delta function is unity, and the ideal low-pass filter in position space is $\sin(\pi x/a)/(\pi x)$, steps (i) and (ii) can be summarized as

$$-[\delta^{\text{filt}}(x)]' = \frac{a \sin\left(\frac{\pi x}{a}\right) - \pi x \cos\left(\frac{\pi x}{a}\right)}{a\pi x^2}, \quad (3.5)$$

where $\delta^{\text{filt}}(x)$ is the *filtered* Dirac delta operator that has Fourier components only in the first Brillouin zone. By performing the Taylor expansion we find that $\delta^{\text{filt}}(x)'$ vanishes linearly around $x = 0$, and the SLAC construction does not have an on site component. The ideal lattice derivative is then obtained by sampling the expression from Eq. (3.5) at

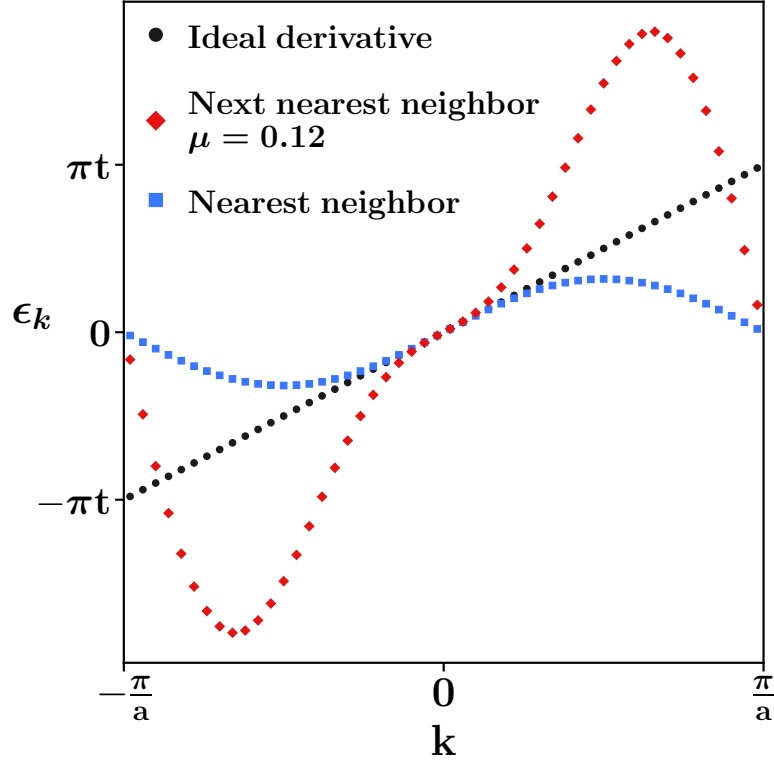


Figure 3.1: Spectrum of the one-dimensional Hamiltonian $\hat{h}_{1D} = -i(ta)d/(dx)$ for three different choices for the lattice derivative. The blue squares show the simplest, nearest neighbor approach [see Eq. (3.3)], which results in doublers around $k = \pm\pi/a$. The orange diamonds correspond to the next nearest neighbor spectrum from Eq. (3.4) for $\mu = 0.12$. Notice that the Fermi velocity of the doubler around $k = \pm\pi/a$ in this case is greater than that near the center of the Brillouin zone ($k = 0$). This effect is exacerbated by further decreasing μ , which eventually gets rid of the doublers, but pushes much of the spectral weight to high energies ($\epsilon_k \gg \pi t$). The gray dots represent the ideal derivative, the spectrum of which is devoid of doublers and remains linear in the entire Brillouin zone, thereby yielding a genuine chiral symmetry at the microscopic level. Notice that around $k \approx 0$ all three constructions recover k -linear dispersion. This construction can be generalized to realize three-dimensional massless Dirac fermions with microscopic chiral symmetry, see Eq. (3.7). Figure adapted from Ref. [103].

the lattice points $x = na$, multiplied by the lattice spacing (a), yielding

$$\Delta(n) = \begin{cases} 0, & \text{if } n = 0 \\ -\frac{(-1)^n}{na}, & \text{otherwise.} \end{cases} \quad (3.6)$$

By identifying the position space derivative with convolution from Eq. (3.6), we get rid of the doublers, but pay the price of our operator now being *non-local*, albeit only along the principal axes.

The resulting tight binding Hamiltonian which corresponds to Eq. (3.1) on a three-

dimensional cubic lattice with linear dimension $L = 2N + 1$ in each direction reads

$$h_{\text{latt}} = -i \sum_{\mathbf{R}} \sum_{j=1}^3 \sum_{n=-N}^N \Delta(n) \Psi_{\mathbf{R}}^\dagger \Gamma_j \Psi_{\mathbf{R}+n\hat{\mathbf{e}}^{(j)}}, \quad (3.7)$$

where \mathbf{R} denotes the position of the lattice sites and $\hat{\mathbf{e}}^{(j)}$ is a vector of length a in the j th principal direction. While the locality of the SLAC derivative on a conceptual level can be subject to debate, the long-range nature of it is certainly unwieldy from a practical point of view. Nevertheless, in exchange we obtain spectra that reflect the “true” momentum operator on a lattice, namely $\epsilon_{\mathbf{k}} = (ta)\mathbf{k}$, where $v = ta$ is the isotropic Fermi velocity. See the gray dots in Fig. 3.1.

3.2 Electron-electron interactions

In what follows we seek to unveil the structure of the RG fixed points (including both QCPs and BCPs) and emergent symmetries therein starting from an interacting model for three-dimensional massless chiral Dirac fermions, similar to two-dimensional Dirac fermions in the previous chapter. To capture interaction-induced spontaneous symmetry breaking in this system we construct the symmetry-allowed four-fermion or quartic terms. Throughout this thesis we only take the Hubbardlike short-range (momentum-independent) interactions into account. On the other hand, the long-range tail of the Coulomb interaction in Dirac materials only provide logarithmic correction to the Fermi velocity [106–116], without causing any transition to ordered states [109, 111, 113]. When simultaneously present with the short-range interactions, it can only cause non-universal shifts of the phase boundaries [112, 114], without altering the underlying quantum critical behavior [111, 113].

The most general local four-fermion term is of the schematic form

$$g_{\mu\nu\rho\lambda} (\Psi^\dagger \Gamma_{\mu\nu} \Psi) (\Psi^\dagger \Gamma_{\rho\lambda} \Psi),$$

where $\mu, \nu, \rho, \lambda = 0, 1, 2, 3$, $g_{\mu\nu\rho\lambda}$ is the coupling constant, and $\Psi^\dagger \equiv \Psi_{\tau, \mathbf{x}}^\dagger$ and $\Psi \equiv \Psi_{\tau, \mathbf{x}}$ are two independent Grassmann variables in the path integral or action formalism. Before imposing any symmetry constraint on the quartic terms, altogether there are 136 of them. Namely, 16 (the number of Hermitian matrices, constituting the basis for all four-dimensional matrices) of them are obtained for $\mu\nu = \rho\lambda$, while $\mu\nu \neq \rho\lambda$ in the remaining 120 quartic terms. However, this number gets drastically reduced first by imposing the discrete symmetries, namely parity (\mathcal{P}), time-reversal (\mathcal{T}) and charge conjugation (\mathcal{C}). These three discrete symmetries permit only 12 terms with $\mu\nu \neq \rho\lambda$ and 16 quartic terms with $\mu\nu = \rho\lambda$. The spatial $O(3)$ rotational symmetry eliminates the former set of quartic terms, and organizes remaining 16 terms of the form $(\Psi^\dagger \Gamma_{\mu\nu} \Psi)^2$ into eight distinct interac-

tion channels. For a detailed derivation see Appendix A.1.1. The interacting Lagrangian containing all symmetry allowed local quartic terms is then given by

$$L_{\text{int}} = \sum_{\mu=0}^3 g_{\mu}^s (\Psi^{\dagger} \Gamma_{\mu 0} \Psi)^2 + \sum_{\mu=0}^3 g_{\mu}^t \left[\sum_{j=1}^3 (\Psi^{\dagger} \Gamma_{\mu j} \Psi)^2 \right]. \quad (3.8)$$

The four-fermion interactions with coupling constants g_j^s (g_j^t) for $j = 1, 2, 3$ correspond to spin-independent (spin-dependent) mixing of even and odd parity states. By contrast, g_0^s (g_0^t) corresponds to short-range density-density (ferromagnetic) interaction. Notice that we did not enforce chiral U(1) symmetry on L_{int} at the bare level. Consequently, the components of chiral U(1) vectors appear as independent quartic terms in Eq. (3.8). Namely, two quartic terms containing Γ_{20} and Γ_{30} (Γ_{2j} and Γ_{3j}) acquire two separate coupling constants g_2^s and g_3^s (g_2^t and g_3^t), respectively, at the microscopic level. On other hand, in Weyl semimetals the chiral U(1) symmetry is associated with the translational symmetry in the continuum limit [117, 118]. Therefore, the interacting theory must preserve the chiral U(1) symmetry in Weyl semimetals.

However, the number of linearly independent four-fermion terms is only *four* due to the existence of the Fierz identity [11] (see Appendix A.1.2). We choose them to be the ones appearing with the coupling constants $\{g_{\mu}^s\}$. The corresponding interacting Euclidean action reads

$$S_{\text{int}} = \int d\tau \int d^d \mathbf{x} \left(\sum_{\mu=0}^3 g_{\mu}^s (\Psi^{\dagger} \Gamma_{\mu 0} \Psi)^2 \right). \quad (3.9)$$

Notice that eight quartic terms appearing in L_{int} can be decomposed into two sectors, the ones transforming as scalars (three-component vectors) under spatial O(3) rotations and appearing with coupling constants g_{μ}^s (g_{μ}^t), for $\mu = 0, \dots, 3$. Consequently, we can choose four quartic terms in the singlet channel as the independent ones. Next we study the interacting model $S_0 + S_{\text{int}}$ within the framework of Wilsonian momentum-shell RG analysis.

3.2.1 Renormalization group analysis

Our methodology for the zero temperature renormalization group (RG) analysis is as outlined in Chapter 2. We start by establishing the scaling of various quantities relative to momentum, the scaling of which is by definition $[k] = 1$. The relative scaling between momentum and frequency is given by the dynamic scaling exponent z , hence $[\omega] = z$. For linearly dispersing Dirac fermions $z = 1$. The scale-invariance of S_0 requires that $[\Psi] = d/2$, from which we obtain the scaling dimension of the quartic coupling constants to be $[g_{\mu}^s] = z - d = -1$. Therefore, local interactions in three-dimensional Dirac systems are *irrelevant* in the RG sense and the Dirac cone remains stable as long as they are sufficiently *weak*. On the other hand, strong enough local interactions can drive the system through quantum phase transitions into various broken symmetry phases. The scaling

coupling	C1	C2	C3	C4	B1	B2	B3	B4
g_0^s	-0.042	0.062	0.062	-2/3	0	0	-0.895	-0.895
g_1^s	-1/8	0.136	0.136	0	0	0	0.614	0.614
g_2^s	1/6	0.215	-0.153	-1/3	0	1/3	-0.056	-0.840
g_3^s	1/6	-0.153	0.215	-1/3	1/3	0	-0.840	-0.056

Table 3.1: Locations of four quantum critical points (QCPs) [C1, \dots , C4] and four bicritical points (BCPs) [B1, \dots , B4] in the four-dimensional space of coupling constants, measured in units of ϵ , where $\epsilon = d - 1$ and d is the spatial dimension of the system. Each QCP (BCP) possesses *one* (*two*) unstable direction(s). Note C1 and C4 are chiral U(1) symmetric QCPs, since $g_2^s = g_3^s$ therein. On the other hand, C2 and C3 are chiral U(1) partners, as their locations transform into each other under U(1) chiral rotation $g_2^s \leftrightarrow g_3^s$. Similarly, two pairs of BCPs, namely (1) (B1,B2), and (2) (B3,B4) are chiral U(1) partners. In addition, three QCPs C2, C3 and C4, and two BCPs B3 and B4 individually possess pseudospin SU(2) chiral symmetry. The emergent chiral symmetries can be anchored by comparing the scaling dimensions of fermion bilinears, tabulated in Table 3.2, at various fixed points, see Table 3.3. In particular, the scaling dimensions of fermion bilinears that are related to each other by chiral U(1) [pseudospin SU(2) chiral] rotations are identical at the U(1) [pseudospin SU(2)] symmetric fixed points. By contrast, the scaling dimensions of two fermion bilinears that form a U(1) vector under the chiral U(1) rotations, are interchanged between two fixed points that are chiral partners of each other. Finally, the scaling dimension of chiral U(1) scalar fermion bilinears remain unchanged between two chiral partner fixed points. Only the fully U(1) \otimes SU(2) symmetric QCP C4 becomes unstable even against weak rotational symmetry breaking, see Sec. 3.2.6.

dimension [g_μ^s] pins the lower critical dimension at $d = 1$, where short-range interactions are marginal, which facilitates a controlled ϵ expansion about one spatial dimension, with $\epsilon = d - 1$. Note that vanishing density of states, namely $\rho(E) \sim |E|^2$ indicates stability of the Dirac node against sufficiently weak interactions in $d = 3$, whereas interactions become marginal when $d = z = 1$, yielding a constant density of states.

Evaluating the Feynmann diagrams from Fig. 2.1 up to one-loop order [119], we arrive at the following leading-order RG flow equations for the coupling constants

$$\begin{aligned}
\frac{dg_0^s}{d\ell} &= -\epsilon g_0^s - (g_0^s g_3^s + g_0^s g_2^s + 2g_3^s g_2^s), \\
\frac{dg_1^s}{d\ell} &= -\epsilon g_1^s + g_0^s g_3^s + g_0^s g_2^s - 4g_3^s g_2^s, \\
\frac{dg_2^s}{d\ell} &= -\epsilon g_2^s + 3(g_2^s)^2 - 2(g_0^s g_3^s + g_0^s g_2^s - g_3^s g_2^s) + 3g_1^s (g_2^s - g_3^s), \\
\frac{dg_3^s}{d\ell} &= -\epsilon g_3^s + 3(g_3^s)^2 - 2(g_0^s g_3^s + g_0^s g_2^s - g_3^s g_2^s) + 3g_1^s (g_3^s - g_2^s). \quad (3.10)
\end{aligned}$$

Here we made the substitution $\frac{\Lambda^\epsilon}{3v\pi^2} g_\mu^s \rightarrow g_\mu^s$, such that the flow equations are expressed in terms of dimensionless couplings. Note that the flow equations are symmetric under the exchange of g_2^s and g_3^s , manifesting the chiral U(1) symmetry of the noninteracting system.

3.2.2 Fixed points and critical exponents

We examine the quantum critical phenomena by analyzing the fixed point (FP) structure of the RG flow equations from Eq. (3.10), following the methodology outlined in Sec. 2.2.2.1. We adapt the notation $\beta_{g_\mu^s} \equiv dg_\mu^s/d\ell$, and denote a FP location (a solution to $\beta_{g_\mu^s} = 0$, $\mu = 0, \dots, 3$) by \mathbf{g}^* . With that the components of the stability matrix at a FP read

$$M_{\mu+1, \nu+1} = \left. \frac{d\beta_{g_\mu^s}}{dg_\nu^s} \right|_{\mathbf{g}^*}, \quad (3.11)$$

where $\mu, \nu = 0, \dots, 3$. A negative (positive) eigenvalue of \mathbf{M} corresponds to a stable (unstable) eigendirection, and the number of unstable directions characterizes a given fixed point. For example, a QCP (BCP) has one (two) unstable direction(s) in the arbitrary multi-dimensional space of coupling constants.

We find altogether nine FPs [113], of which the trivial one at $\mathbf{g}^s = (0, 0, 0, 0)$ is the fully attractive noninteracting Gaussian fixed point. It describes a stable Dirac semimetal for sufficiently weak, but generic short-range interactions. The rest of the eight FPs at nontrivial strength of the coupling constants are reported in Table 3.1. Four of them are QCPs (C1, \dots , C4) and the remaining four are BCPs (B1, \dots , B4). The existence of BCPs is necessary for the continuity of the RG flow trajectories. As such they separate the basins of attraction of various QCPs. All fixed points are located at $\mathbf{g}_*^s \sim \epsilon$, which can be seen from Eq. (3.10).

The dynamic scaling exponent $z = 1$ at all four QCPs. On the other hand, the inverse of the positive eigenvalue of the stability matrix (\mathbf{M}) determines the correlation length exponent (ν) at each QCP. To the leading order in the ϵ expansion we obtain $\nu^{-1} = \epsilon$, and $\nu = 1/2$ in $d = 3$. The mean-field value of the correlation length exponent is an exact result, as the system resides at the upper-critical three spatial dimensions [120, 121].

From the locations of the fixed points we can conclude the following. Two QCPs C1 and C4 are chiral symmetric, where the couplings of the two components of the U(1) chiral vector g_2^s and g_3^s are *identical*. The remaining two QCPs, namely C2 and C3, are chiral partners of each other and their locations transform into one another under the chiral rotation $g_2^s \leftrightarrow g_3^s$. On the other hand, the four BCPs form two such pairs of chiral partners, namely under $g_2^s \leftrightarrow g_3^s$ (1) B1 \leftrightarrow B2 and (2) B3 \leftrightarrow B4. To further anchor the restoration of chiral symmetry at various RG fixed points next we compute the scaling dimension of all symmetry allowed fermion bilinears.

3.2.3 Nambu doubling and ordered phases

Sufficiently strong local electronic interactions destabilize a gapless Dirac liquid and drive the system through quantum phase transitions into various broken symmetry phases. Here we consider all such symmetry allowed particle-hole (or excitonic) and particle-particle (or superconducting or pairing) orders. To bring both sectors under a unified

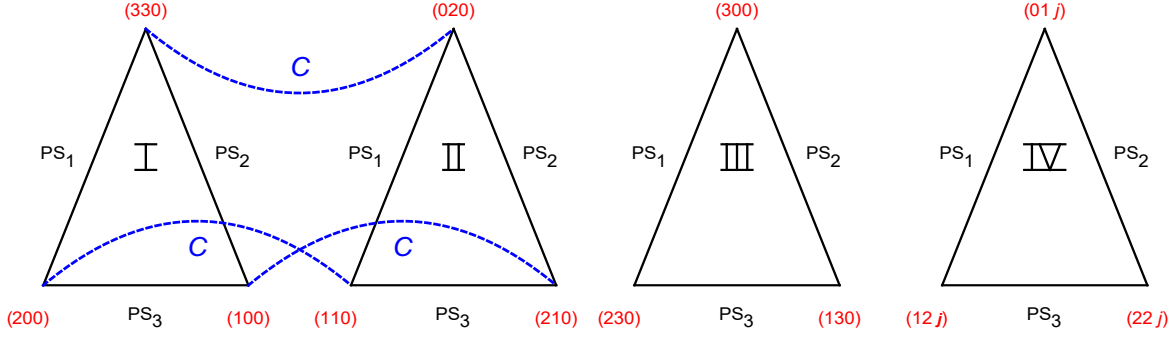


Figure 3.2: Four sets of three mutually anticommuting fermion bilinears in the Nambu doubled basis Ψ_{Nam} [see Eq. (6.10)], denoted by $(\mu\nu\rho) \equiv \Psi_{\text{Nam}}^\dagger \eta_\mu \Gamma_{\nu\rho} \Psi_{\text{Nam}}$, residing at the vertices of four triangles, each representing a pseudospin SU(2) vector. Each triangle demonstrates pseudospin SU(2) chiral rotation among (I) scalar, (II) pseudoscalar excitonic and two components (real and imaginary) of pairing or superconducting masses, (III) fermionic density and two components of temporal vector pairing, and (IV) Abelian current and two components of spatial vector pairing with a specific spin orientation ($\rho \equiv j = 1, 2, 3$). The real and imaginary components of any pairing correspond to $\mu = 1$ and 2, respectively. Three pseudospin generators PS_j with $j = 1, 2, 3$ reside at three vertices of III [see also Eq. (3.14)]. Any arm of the triangle corresponds to the rotation between two fermion bilinears, sitting at its two ends, by a specific generator of pseudospin SU(2) chiral symmetry. Also the identical vertices of triangles I and II are related by the chiral U(1) rotation (the blue dashed lines), generated by $C = \eta_3 \Gamma_{10}$. See also Table 3.2. Figure adapted from Ref. [103].

framework we extend the Dirac spinor following the Nambu doubling

$$\Psi_{\mathbf{k}} \rightarrow \Psi_{\text{Nam}} = \begin{bmatrix} \Psi_{\mathbf{k}} \\ \Gamma_{20} \Psi_{-\mathbf{k}}^* \end{bmatrix}. \quad (3.12)$$

Note that in the lower block we absorb the unitary part of the time-reversal operator (\mathcal{T}), such that Ψ_{Nam} transform as $\Psi_{\mathbf{k}}$ under all symmetry operations [122]. The noninteracting Hamiltonian from Eq. (3.1) in this basis reads

$$\hat{h}_{\text{Nam}}(\mathbf{k}) = \eta_3 \sum_{j=1}^3 v_j \Gamma_j k_j. \quad (3.13)$$

The newly introduced set of Pauli matrices $\{\eta_\mu\}$ operate on the Nambu or particle-hole indices, with $\mu = 0, \dots, 3$. The generator of the chiral U(1) symmetry in this basis becomes $C = \eta_3 \Gamma_{10}$. Furthermore, the Nambu doubling allows us to unveil the *pseudospin* SU(2) chiral symmetry of the noninteracting system, generated by

$$\mathbf{PS} = \{\eta_1 \Gamma_{30}, \eta_2 \Gamma_{30}, \eta_3 \Gamma_{00}\}, \quad (3.14)$$

since $[\hat{h}_{\text{Nam}}(\mathbf{k}), \mathbf{PS}] = 0$. Specifically, $\text{PS}_3 = \eta_3 \Gamma_{00}$ is the number operator. Therefore a collection of noninteracting four-component massless Dirac fermions enjoys $\text{U}(1) \otimes \text{SU}(2)$

chiral symmetry, since $[C, \mathbf{PS}] = 0$. Previously, the pseudospin $SU(2)$ symmetry has been discussed in the context of two-dimensional Hubbard model [123–126]. But, its imprints on three-dimensional interacting systems remained unexplored so far.

To appreciate the imprint of the enlarged chiral symmetry in the presence of interactions, next we consider all symmetry allowed fermion bilinears describing different orders in the Nambu doubled basis. The effective action containing all (excitonic and pairing) symmetry allowed local orders reads as

$$S_{\text{local}} = \int d\tau \int d^d \mathbf{r} \Psi_{\text{Nam}}^\dagger (\hat{h}_{\text{exc}} + \hat{h}_{\text{pair}}) \Psi_{\text{Nam}}, \quad (3.15)$$

where

$$\begin{aligned} \hat{h}_{\text{exc}} = & \Delta_0^s \eta_3 \Gamma_{00} + \Delta_1^s \eta_3 \Gamma_{10} + \Delta_2^s \eta_0 \Gamma_{20} + \Delta_3^s \eta_3 \Gamma_{30} \\ & + \sum_{j=1}^3 \left[\Delta_0^t \eta_0 \Gamma_{0j} + \Delta_1^t \eta_0 \Gamma_{1j} + \Delta_2^t \eta_3 \Gamma_{2j} + \Delta_3^t \eta_0 \Gamma_{3j} \right], \end{aligned} \quad (3.16)$$

and

$$\hat{h}_{\text{pair}} = (\eta_1 \cos \phi + \eta_2 \sin \phi) \times \left[\Delta_0^p \Gamma_{00} + \Delta_1^p \Gamma_{10} + \Delta_2^p \sum_{j=1}^3 \Gamma_{2j} + \Delta_3^p \Gamma_{30} \right], \quad (3.17)$$

with ϕ as the $U(1)$ superconducting phase. The real (imaginary) component of any pairing order corresponds to $\phi = 0$ ($\pi/2$). Here Δ_μ^a is the conjugate field of the corresponding fermion bilinear.

The bilinears, their physical meanings together with the corresponding matrices and their transformations under various symmetry operations (discrete and continuous) are summarized in Table 3.2. The two fully gapped phases in the particle-hole subspace are the scalar and pseudoscalar masses, which form a $U(1)$ vector under the chiral $U(1)$ rotation generated by $C = \eta_3 \Gamma_{10}$. The Nambu basis accommodates two additional massive orders in the particle-particle sector, the scalar s -wave and pseudoscalar p -wave pairings [127, 128]. They form two copies of $U(1)$ chiral vector, where the doubling is due to the gauge redundancy in the internal $U(1)$ degree of freedom associated with the superconducting phase (ϕ). Furthermore, the two tensor bilinears (coupled with the conjugate fields Δ_2^t and Δ_3^t) form other three copies of two-component chiral $U(1)$ vector, where the three-fold redundancy stems from the spatial $O(3)$ symmetry. Additionally, there exist four three-component orders, each of which is a composite of a particle-hole and a particle-particle order and transforms as a vector under the pseudospin $SU(2)$ chiral rotations, generated by \mathbf{PS} [see Eq. (3.14)], as shown in Fig. 3.2.

To extract the scaling dimension of various fermion bilinears, first we compute the RG flow equations for the corresponding source terms or conjugate fields Δ_μ^a , where $\mu = 0, \dots, 3$ and $a = s, t, p$. After evaluating the relevant Feynman diagrams in Fig. [FDiags

CF	Matrix	Physical meaning	\mathcal{P}	\mathcal{T}	\mathcal{C}	CH	PS
Δ_0^s	$\eta_3\Gamma_{00}$	Fermionic density	+	+	-		III
Δ_1^s	$\eta_3\Gamma_{10}$	Chiral density	-	+	+		
Δ_2^s	$\eta_0\Gamma_{20}$	Pseudoscalar mass	-	-	+	i	II
Δ_3^s	$\eta_3\Gamma_{30}$	Scalar mass	+	+	+	i	I
Δ_0^t	$\eta_0\Gamma_{0j}$	Axial current	+	-	+		
Δ_1^t	$\eta_0\Gamma_{1j}$	Abelian current	-	-	-		IV
Δ_2^t	$\eta_3\Gamma_{2j}$	Spatio-temporal tensor	-	+	-	ii	
Δ_3^t	$\eta_0\Gamma_{3j}$	Spatial tensor	+	-	-	ii	
Δ_0^p	$\eta_\alpha\Gamma_{00}$	Scalar s -wave pairing	+	+/-	+	iii	I
Δ_1^p	$\eta_\alpha\Gamma_{10}$	Pseudoscalar p -wave pairing	-	+/-	+	iii	II
Δ_2^p	$\eta_\alpha\Gamma_{2j}$	Spatial vector pairing	-	+/-	+		IV
Δ_3^p	$\eta_\alpha\Gamma_{30}$	Temporal vector pairing	+	+/-	+		III

Table 3.2: Various local (momentum independent) orderings with their conjugate fields (CFs) (first column), the corresponding matrix $\eta_\mu\Gamma_{\nu\rho}$ (second column) associated with the fermion bilinears $\Psi_{\text{Nam}}^\dagger\eta_\mu\Gamma_{\nu\rho}\Psi_{\text{Nam}}$ in the Nambu basis Ψ_{Nam} , defined in Eq. (3.12), and the physical meaning of the orderings (third column). First eight (last four) rows correspond to excitonic (superconducting) orders. In the superconducting channels $\alpha = 1$ and 2, reflecting the U(1) gauge redundancy in the choice of the superconducting phase (ϕ), see Eq. (3.17). Transformation of each fermion bilinear under discrete \mathcal{P} , \mathcal{T} , and \mathcal{C} symmetries are shown in the fourth, fifth and sixth columns, respectively. Here, + and - respectively correspond to even and odd. Fermion bilinears transforming as components of three chiral U(1) vectors under the U(1) chiral (CH) rotation are marked as i, ii, and iii. Rest of the bilinears are scalars under chiral U(1) rotation. Fermion bilinears transforming as components of four pseudospin (PS) SU(2) vectors are marked as I, II, III and IV in the eighth column, see Fig. 3.2. The rest of the fermion bilinears transform as scalars under the pseudospin rotations.

susc] up to the one-loop order [119], we arrive at the following leading-order β functions for Δ_μ^a

$$\begin{aligned}
\bar{\beta}_{\Delta_0^s} &= 0, & \bar{\beta}_{\Delta_1^s} &= 0, \\
\bar{\beta}_{\Delta_2^s} &= -\frac{3}{2}(g_0^s - g_1^s - 3g_2^s - g_3^s), & \bar{\beta}_{\Delta_3^s} &= -\frac{3}{2}(g_0^s - g_1^s - g_2^s - 3g_3^s), \\
\bar{\beta}_{\Delta_0^t} &= -g_0^s - g_1^s - g_2^s - g_3^s, & \bar{\beta}_{\Delta_1^t} &= -g_0^s - g_1^s + g_2^s + g_3^s, \\
\bar{\beta}_{\Delta_2^t} &= \frac{1}{2}(-g_0^s + g_1^s - g_2^s + g_3^s), & \bar{\beta}_{\Delta_3^t} &= \frac{1}{2}(-g_0^s + g_1^s + g_2^s - g_3^s), \\
\bar{\beta}_{\Delta_0^p} &= \frac{3}{2}(g_0^s + g_1^s - g_2^s + g_3^s), & \bar{\beta}_{\Delta_1^p} &= \frac{3}{2}(g_0^s + g_1^s + g_2^s - g_3^s), \\
\bar{\beta}_{\Delta_2^p} &= g_0^s - g_1^s - g_2^s - g_3^s, & \bar{\beta}_{\Delta_3^p} &= 0,
\end{aligned} \tag{3.18}$$

where $\bar{\beta}_{\Delta_\mu^a} = d \ln \Delta_\mu^a / d\ell - 1$. The right hand side of each equation corresponds to the one-loop corrections to the scaling dimension of the corresponding order or fermion bilinear, which we compute at various RG fixed points (see Table 3.1) and their values are reported in Table 3.3.

CF	C1	C2	C3	C4	B1	B2	B3	B4
Δ_0^s	0	0	0	0	0	0	0	0
Δ_1^s	0	0	0	0	0	0	0	0
Δ_2^s	0.875	0.849	-0.256	-1	1/2	4/3	0.754	-1.597
Δ_3^s	0.875	-0.256	0.849	-1	4/3	1/2	-1.597	0.754
Δ_0^t	-0.167	-0.260	-0.260	4/3	-1/3	-1/3	1.176	1.176
Δ_1^t	0.500	-0.136	-0.136	0	1/3	1/3	-0.614	-0.614
Δ_2^t	-0.042	-0.147	0.221	1/3	1/6	-1/6	0.363	1.147
Δ_3^t	-0.042	0.221	-0.147	1/3	-1/6	1/6	1.147	0.363
Δ_0^p	-0.250	-0.256	0.849	-1	1/2	-1/2	-1.597	0.754
Δ_1^p	-0.250	0.849	-0.256	-1	-1/2	1/2	0.754	-1.597
Δ_2^p	-0.250	-0.136	-0.136	0	-1/3	-1/3	-0.614	-0.614
Δ_3^p	0	0	0	0	0	0	0	0

Table 3.3: Scaling dimensions (in units of ϵ) of various particle-hole (first eight rows) and particle-particle (last four rows) order parameters (see Table 3.2) at the eight nontrivial fixed points (see Table 3.1). At the chiral U(1) symmetric fixed point C1 any two orders transforming as chiral U(1) vector (see Table 3.2, seventh column) possess *identical* scaling dimensions. By contrast, their scaling dimensions *switch* between two fixed points that are chiral U(1) partners of each other, namely (1) (C2,C3), (2) (B1,B2), and (3) (B3,B4). At four pseudospin SU(2) chiral symmetric fixed points (C2, C3, B3, B4) all components of each pseudospin SU(2) vector (see Table 3.2, eighth column and Fig. 3.2) possess identical scaling dimension. At the fully U(1) \otimes SU(2) chiral symmetric fixed point C4, all components of chiral U(1) and pseudospin SU(2) vectors acquire equal scaling dimensions. In the phase diagram shown in Fig. 3.3, we highlight the role of these fixed points. At three QCPs (C1, C2, and C3) and two BCPs (B1 and B2) the mass orders possess the largest scaling dimensions (shown in bold). Therefore, C1 controls the transition to scalar and pseudoscalar excitonic mass orders. By contrast, C2 (C3) controls transition to pseudoscalar (scalar) excitonic and superconducting masses. On the other hand, when the role of C1 and C3 (C1 and C2) switches, the continuous transition to the scalar (pseudoscalar) excitonic mass is controlled by the BCP B1 (B2).

3.2.4 Emergent chiral symmetry

Computation of one-loop corrections to the scaling dimensions for all excitonic and pairing orders reveals the emergent chiral symmetry at various RG fixed points. First we note that the bilinears that commute with $\hat{h}_{\text{Nam}}(\mathbf{k})$, the fermionic density, chiral density and temporal vector pairing, do not receive any correction to their bare scaling dimension. The matrices associated with these bilinears are also the generators of U(1) \otimes SU(2) chiral symmetry of the noninteracting system.

One can construct three chiral U(1) vectors by combining (1) the scalar and pseudoscalar excitonic masses, (2) two tensor order parameters, and (3) the scalar s -wave and pseudoscalar p -wave pairing masses, see Table 3.2. Two components of any chiral U(1) vector acquire identical scaling dimensions at C1 and C4, while their scaling dimensions are exchanged between (a) C2 and C3, (b) B1 and B2, and (c) B3 and B4. Therefore, only C1 and C4 are chiral U(1) symmetric. On the other hand, the four-dimensional coupling

constant space accommodates three chiral U(1) partner fixed points, namely (a) (C2,C3), (b) (B1,B2), and (c) (B3,B4), as we previously anticipated from their locations.

Also the possible restoration of the pseudospin SU(2) chiral symmetry can be anchored from the scaling dimensions of fermion bilinears at various RG fixed points. As such one can construct four three-component pseudospin SU(2) vectors by combining (1) the scalar excitonic and pairing masses, (2) the pseudoscalar excitonic and pairing masses, (3) fermion density and temporal vector pairing, and (4) Abelian current and spatial vector pairing, see Fig. 3.2. All components of each pseudospin vector acquire identical scaling dimensions at three QCPs, C2, C3 and C4, and at two BCPs, B3 and B4. Hence, these five fixed points are pseudospin SU(2) chiral symmetric. Therefore, while all the RG fixed points at least partially restore the chiral U(1) \otimes SU(2) symmetry of the noninteracting system, it is fully restored only at the C4 QCP.

Even though the space of independent coupling constants is four-dimensional, the imprint of various chiral symmetric fixed points on the global phase diagram of interacting massless chiral Dirac fermions can be appreciated by focusing on its representative cut on the (g_3^s, g_2^s) plane, as shown in Fig. 3.3, which we discuss next.

3.2.5 Phase diagram

Now we proceed to construct the phase diagram in the (g_3^s, g_2^s) plane by numerically solving the β functions of the coupling constants [see Eq. (3.10)] and the conjugate order parameter fields [see Eq. (3.18)]. We simultaneously run the flow equations for four coupling constants (g_μ^s) and all symmetry allowed source terms (Δ_μ^a) for various choices of the *bare* coupling constants as a function of the RG time (ℓ). Sufficiently weak but generic local interactions are irrelevant perturbation in three-dimensional Dirac semimetals due to the vanishing density of states ($\rho(E) \sim |E|^2$). Therefore, onset of any ordered phase takes place beyond a bare critical strength of interaction, which we identify from the divergence of at least one of the renormalized coupling constants as $\ell \rightarrow \infty$. At the same time at least one of the source terms diverges, which ultimately determines the pattern of the symmetry breaking in the ordered phase in an unbiased fashion. We pursue this approach to construct a representative cut of the global phase diagram for three-dimensional interacting massless chiral Dirac fermions, displayed in Fig. 3.3, which manifests an intriguing confluence of all *four* mass orders (the scalar and pseudoscalar excitonic and pairing masses), and the restoration of chiral U(1) and pseudospin SU(2) symmetries among them. Note that at zero temperature nucleation of mass orders is energetically most favored as they isotropically gap the Dirac point and thereby optimally lower the free-energy (no competition with entropy [119]).

Since the QCPs are not located in the (g_3^s, g_2^s) plane, to unequivocally pin down the critical point governing some segment of the phase boundary between Dirac semimetal and ordered phase, we deploy the following strategy. Note that the coupling constants flow to zero on the disordered side of the phase boundary, while they diverge on the ordered

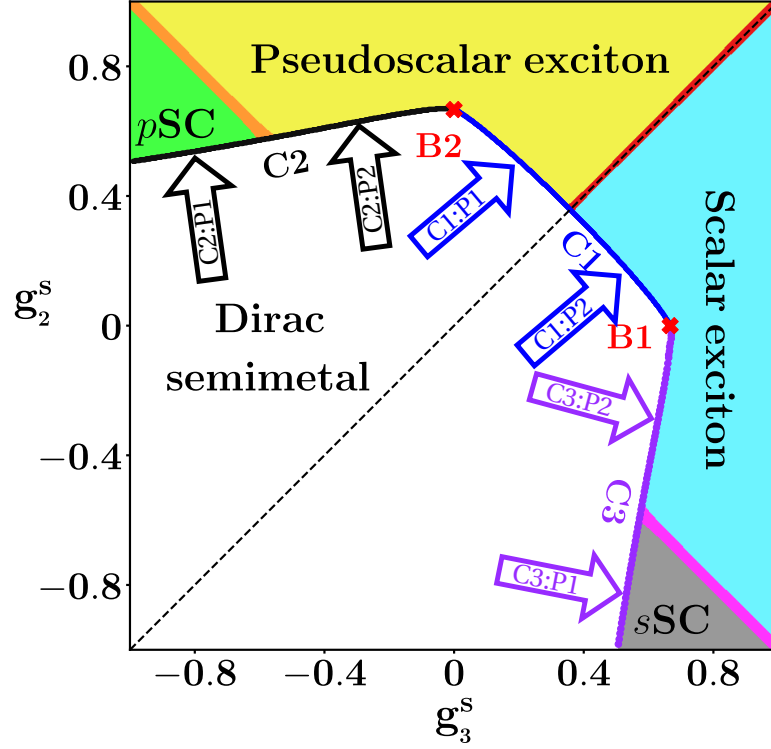


Figure 3.3: A representative phase diagram of a three-dimensional interacting isotropic Dirac semimetal in a two-dimensional subspace of interaction couplings. Here g_3^s and g_2^s are the coupling constants in scalar and pseudoscalar excitonic mass channels, respectively, measured in units of $\epsilon = d - 1$. Their positive (negative) values correspond to repulsive (attractive) interactions. Together, these two masses form a vector under the chiral U(1) rotation. The scalar s -wave and pseudoscalar p -wave superconducting masses (denoted by s SC and p SC, respectively) also constitute a U(1) chiral vector. The emergent chiral symmetry manifests through the *mirror symmetry* of the phase diagram about the $g_3^s = g_2^s$ dashed line. Under the mirror transformation the components of the chiral U(1) mass orders transform into each other. The Dirac semimetal-excitonic mass quantum phase transition (blue boundary) is governed by the U(1) symmetric QCP C1. The scalar and pseudoscalar excitonic masses are degenerate along the red phase boundary between them, where the ordered state represents a \mathcal{P} and \mathcal{T} symmetry breaking *axionic* insulator [129–131]. The phase transitions across the black and purple boundaries are governed by the pseudospin SU(2) symmetric QCPs C2 and C3, respectively. Each excitonic mass is degenerate with the adjacent superconducting mass along the 135° diagonal (orange and pink lines), where they constitute pseudospin SU(2) chiral vectors, see Fig. 3.2. The basins of attraction of C1 and C2 (C1 and C3) are separated by the bicritical point B2 (B1), see Table 3.1. To unambiguously determine the governing QCP, we examine the RG flow initialized to the locations indicated by colored arrows, see Fig. 3.4.

side. This divergence ultimately happens through a QCP, which is to be identified. If we fine tune the bare coupling constants right to the phase boundary, in principle they spend arbitrarily long RG time at the governing critical point. This method is then only limited by numerical rounding. Following this scenario, we now highlight the role of various RG fixed points on different segments of this phase diagram. For the RG flows demonstrating

the governing QCP at various segments of the phase boundary (marked by arrows in Fig. 3.3) see Fig. 3.4.

The chiral U(1) symmetric QCP C1 can be accessed for *purely* repulsive interactions $g_2^s, g_3^s > 0$ and it governs the continuous quantum phase transitions between Dirac semimetal and the two excitonic mass orders (the blue phase boundary in Fig. 3.3). These two excitonic masses are degenerate along the 45° red line, where we realize an axionic insulator [129–131]. A slight deviation from the red line in favor of g_3^s (g_2^s) tips the balance in favor of the nucleation of pure scalar (pseudoscalar) excitonic mass.

The phase transitions out of the Dirac semimetal across the black phase boundary into the pseudoscalar excitonic and pairing (p -wave superconductor) masses is governed by the SU(2) pseudospin symmetric QCP C2. In the absence of a Fermi surface, strong attractive interaction in at least one channel is required for the stability of a superconducting phase, which in this case occurs in the g_3^s channel. These two orderings are degenerate along the 135° (orange) line. The basins of attraction of C1 and C2 are separated by the bicritical point B2, where the pseudoscalar exciton possesses the largest scaling dimension, see Table 3.3. Still the transition to this ordered phase through B2 is continuous as it is accessed by holding one of its unstable directions fixed [123].

The rest of the phase diagram and the role of various fixed points therein can be appreciated by exploiting a *mirror symmetry* of the whole phase diagram, under which $g_2^s \leftrightarrow g_3^s$. Such a mirror symmetry is rooted in the underlying U(1) chiral symmetry and corresponds to a reflection about the 45° diagonal (dashed) line, defined by $g_2^s = g_3^s$, that brings the upper left triangle of the phase diagram onto its chiral partner, the bottom right triangle. Also note that the three-component scalar and pseudoscalar masses, constructed by combining the corresponding excitonic and pairing orders, can be rotated into each other by the generator of the chiral U(1) symmetry $C = \eta_3 \Gamma_{10}$, see Fig. 3.2. Correspondingly, C2 is rotated into C3, which governs the phase transitions between the Dirac semimetal and the scalar excitonic and pairing (s -wave superconductor) mass orders that take place through the purple phase boundary. These two competing orders are degenerate along the 135° (pink) line, as C3 is bestowed with the same pseudospin SU(2) chiral symmetry. In this segment of the phase diagram, the roles of g_2^s and g_3^s are exchanged due to the aforementioned mirror transformation and the requisite strong attractive interaction for the nucleation of the scalar s -wave pairing is now fulfilled by $g_2^s (< 0)$. The basins of attraction of C1 and C3 are separated by B1, where the scalar excitonic mass possesses the largest scaling dimension, see Table 3.3. Still the transition to this phase through B1 is continuous.

The remaining three fixed points, C4, B1 and B2, play no evident role on the phase diagram in the (g_3^s, g_2^s) plane. Moreover, we find that the existence of the QCP C4 is due to the assumed O(3) rotational symmetry and is in general not present in a tetragonal environment. Next we address the effects of *weak* rotational symmetry breaking on various RG fixed points in a perturbative manner.

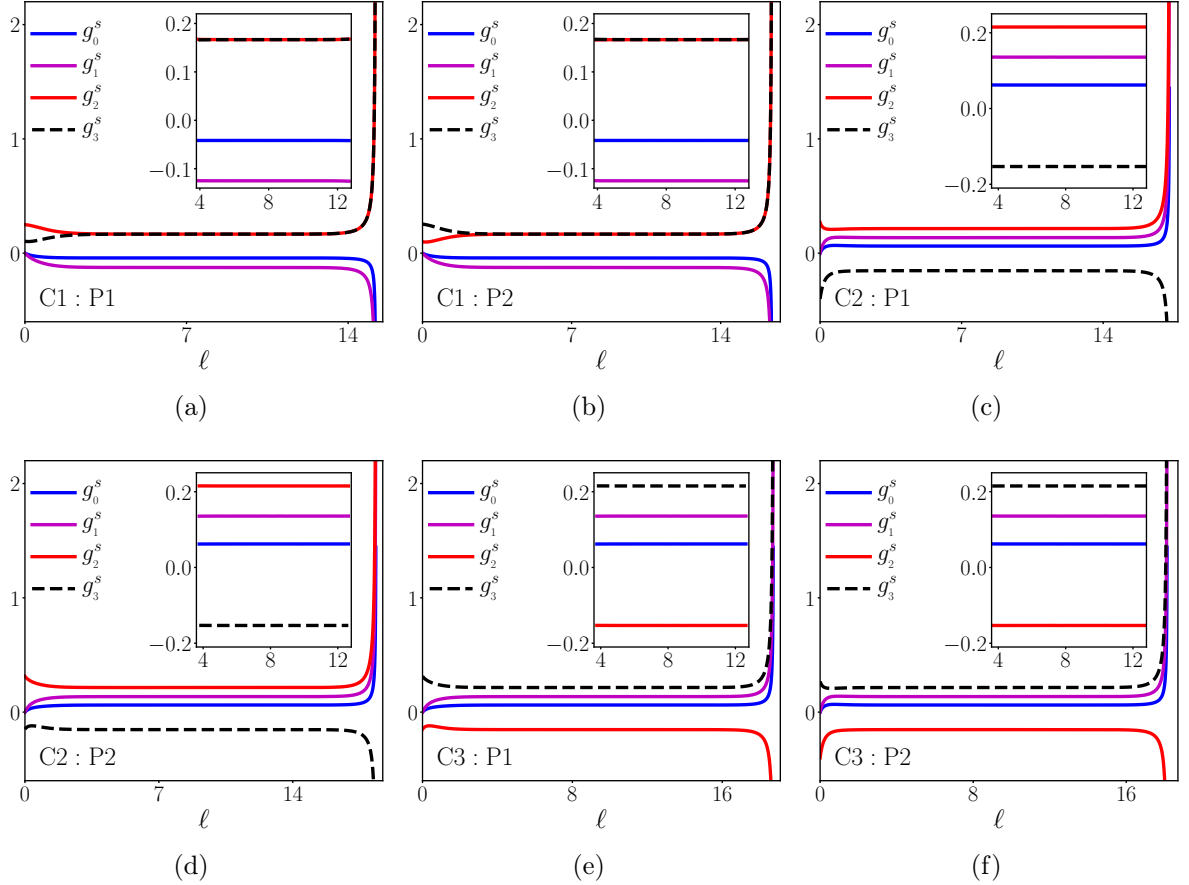


Figure 3.4: RG flows of quartic interaction couplings with the bare values fine tuned to a segment of the phase boundary, see colored arrows in Fig. 3.3. Being fine tuned to the boundary between disordered and ordered phase, the couplings first flow to their fixed point values (see Table 3.1), where they spend arbitrarily long RG time, limited by numerical rounding. We picked the initial conditions such that the interaction couplings ultimately diverge. The flat parts of the flow are also shown in the inset, where the coupling constants are approximately at their fixed point value. Thus, (a) and (b) correspond to C1, (c) and (d) to C2, while (e) and (f) to C3. All coupling constants are measured in units of ϵ .

3.2.6 Anisotropic Dirac semimetal

Finally, we address the breakdown of the $O(3)$ rotational symmetry down to an in-plane $O(2)$ invariance about the z -axis, which manifests through an anisotropy between the perpendicular and the z components of the Fermi velocity, i.e., $v_x = v_y = v_\perp \neq |v_z|$. Due to such a reduced symmetry, all three-component four-fermion terms get split into the perpendicular and z components, namely $g_\mu^t \rightarrow (g_\mu^\perp, g_\mu^z)$, where $\mu = 0, \dots, 3$, see Eq. (3.8). The interacting Lagrangian then contains 12 quartic terms, out of which only *five* are linearly independent due to the Fierz constraint. See Appendix A.1.2 for detailed derivation. To account for the reduced symmetry, we take the fifth independent quartic term to be $g_1^z(\Psi^\dagger \Gamma_{13} \Psi)^2$. Assuming sufficiently *weak* rotational symmetry breaking, we

compute the one-loop renormalization of g_1^z only *up to linear order* in g_1^z , yielding

$$\frac{dg_1^z}{d\ell} = (-\epsilon - g_0^s - 3g_1^s - 2g_2^s - 2g_3^s) g_1^z + \mathcal{O}((g_1^z)^2). \quad (3.19)$$

Since we are interested in capturing the leading order effects of *weak* rotational symmetry breaking, all the Feynman diagrams are computed with isotropic Dirac kernel.

The relevance of the rotational symmetry breaking can be estimated by computing the scaling dimension of g_1^z at all the fixed points reported in Table 3.1 for the isotropic system. Evaluating the right hand side of Eq. (3.19) at the eight fixed points from Table 3.1, we find

$$\begin{aligned} \left. \frac{d \ln g_1^z}{d\ell} \right|_{C1} &= -1.251\epsilon, & \left. \frac{d \ln g_1^z}{d\ell} \right|_{C2/C3} &= -1.594\epsilon, \\ \left. \frac{d \ln g_1^z}{d\ell} \right|_{C4} &= +\epsilon, & \left. \frac{d \ln g_1^z}{d\ell} \right|_{B1/B2} &= -\frac{5}{3}\epsilon, \\ \left. \frac{d \ln g_1^z}{d\ell} \right|_{B3/B4} &= -0.155\epsilon. & & \end{aligned} \quad (3.20)$$

Therefore, slight distortion of the Dirac cone is an *irrelevant* perturbation in the close vicinity of all the fixed points, except C4. In other words, C4 becomes unstable and turns into a BCP even for sufficiently *weak* breaking of the rotational symmetry. Therefore, this QCP cannot be found in general in a three-dimensional interacting Dirac system. We also note that the irrelevance of g_1^z at the BCPs B3 and B4 is *weak*, in comparison to those near C1, C2, C3, B1 and B2. Therefore, it is conceivable that these two BCPs ultimately turn into tricritical points with three relevant directions in a strongly anisotropic Dirac semimetal, this investigation is, however, outside of the scope of this thesis.

3.3 Summary and Discussion

Here we investigate the role of strong momentum-independent local or Hubbardlike electronic interactions among three-dimensional massless Dirac fermions that in the noninteracting system possess a global chiral $U(1) \otimes SU(2)$ symmetry. We provide a lattice realization of such quasiparticle excitations in terms of the SLAC fermions, which should facilitate future numerical investigation of this subject using quantum Monte Carlo simulations [97, 98], for example. We show that an isotropic interacting Dirac semimetal is described in terms of only *four* linearly independent local quartic interactions. Beside studying the possible ordered or broken symmetry phases in this system, which set in through continuous quantum phase transitions, we also pay special attention to the restoration of partial and full chiral symmetry at various interacting fixed points. By performing a leading-order field theoretic RG analysis, controlled by a *small* parameter $\epsilon = d - 1$, about the lower-critical one spatial dimension ($d = 1$), we find that an isotropic interacting chiral Dirac semimetal altogether supports *nine* RG fixed points. One of them

corresponds to the noninteracting trivial Gaussian fixed point, describing a stable Dirac semimetal for sufficiently weak, but generic short-range interactions. On the other hand, the system also supports four quantum critical (Ci) and four bicritical (Bi) fixed points at finite interaction couplings ($\sim \epsilon$), where $i = 1, 2, 3, 4$, see Table 3.1. Note that even though in the physically relevant situation $\epsilon = 2$, none of our results depend on the value of ϵ (so long as $\epsilon > 0$). This is reflected, for example, by the fact that all FP locations are in units of ϵ [see Eq. (3.10)].

Even though we do not impose (partial or full) chiral symmetry on the interacting theory S_{int} at the bare level, two QCPs, namely C1 and C4, transform as chiral U(1) scalars, while the remaining six fixed points (C2,C3), (B1,B2) and (B3,B4) pairwise transform as three two-component vectors under the chiral U(1) rotations. In addition, the pseudospin SU(2) chiral symmetry gets restored at three QCPs (C2, C3 and C4) and two BCPs (B3 and B4). Therefore, only one fixed point, namely C4, enjoys the full chiral U(1) \otimes SU(2) symmetry of the noninteracting systems, see Tables 3.1, 3.2 and 3.3.

The dynamic scaling exponent (z) and correlation length exponent (ν) at all the QCPs are respectively $z = 1$ and $\nu^{-1} = \epsilon$. Together they determine the scaling of the transition temperature $T_c \sim \delta^{\nu z}$ of the ordered states (up to a logarithmic correction due to the breakdown of the hyperscaling hypothesis in $d = 3$), where δ is the reduced distance from a critical point. The value of $\nu = 1/2$ is an exact result as the system resides at the upper critical three spatial dimension [120, 121]. The momentum shell RG procedure although breaks the space-(imaginary)time Lorentz symmetry of the noninteracting system, it does not obscure the restoration of internal chiral symmetry at various RG fixed points.

We also demonstrate the imprints of some of these fixed points and emergent chiral symmetry among competing phases on a representative cut of the zero temperature global phase diagram, shown in Fig. 3.3. This phase diagram displays an intriguing confluence of four competing mass orders, the scalar and pseudoscalar excitonic and superconducting masses, which are the energetically most favored ordered states at zero temperature as they uniformly and isotropically gap the Dirac point. In particular, we find high-symmetry lines in the phase diagram along which the chiral U(1) symmetry between two excitonic (scalar and pseudoscalar) masses and the pseudospin SU(2) symmetry among scalar or pseudoscalar excitonic and superconducting masses get restored. We also note that the phase diagram displays a chiral mirror symmetry about the 45° diagonal across which all the scalar and pseudoscalar mass orders transform into each other.

In Chapter 5 we propose a set of “*selection rules*”, organizing various broken symmetry phases in the phase diagram of correlated multiband systems. It is worth pointing out that the arrangements among the competing and neighboring phases in the phase diagram obtained in this chapter are consistent with these rules. In particular, one can immediately verify the following. (1) A quartic interaction $(\Psi_{\text{Nam}}^\dagger \eta_\mu \Gamma_{\nu\rho} \Psi_{\text{Nam}})^2$, written in the Nambu doubled basis Ψ_{Nam} [see Eq. (3.12)], is conducive for the nucleation of an ordered state, represented by the fermion bilinear $\Psi_{\text{Nam}}^\dagger \text{O} \Psi_{\text{Nam}}$, only if (a) $\text{O} \equiv \eta_\mu \Gamma_{\nu\rho}$ or (b) $\{\text{O}, \eta_\mu \Gamma_{\nu\rho}\} =$

0, see Eq. 5.2. (2) Two ordered phases, represented by the fermion bilinears $\Psi_{\text{Nam}}^\dagger O_1 \Psi_{\text{Nam}}$ and $\Psi_{\text{Nam}}^\dagger O_2 \Psi_{\text{Nam}}$ reside next to each other only when $\{O_1, O_2\} = 0$. We pronounce these rules in details and anchor them in various nodal systems in Part II.

Finally, we show that a weak anisotropy of the Dirac cone leaves the nature of various RG fixed points unchanged, except the fully $U(1) \otimes SU(2)$ chiral symmetric critical point C4. Specifically, this critical point gets converted into a bicritical point even in a *weakly* anisotropic Dirac system. A complete RG analysis, fixed point structure and the phase diagram in a three-dimensional anisotropic chiral Dirac semimetal is, however, left for a future investigation.

We will revisit the world of Dirac fermions in two subsequent chapters. Chapter 6 features a paradigmatic example of linearly dispersing fermions in a flatland, the honeycomb lattice of graphene. In Chapters 8 and 9 we explore the topological properties of a three-dimensional Dirac semimetal. However, for the time being we leave the realm of Dirac fermions and turn our focus to a system exhibiting quadratically dispersing quasiparticles, the Luttinger semimetal [132].

Chapter 4

Three-dimensional Luttinger semimetal

So far in this thesis we encountered condensed matter systems exhibiting linearly dispersing Dirac fermions as their low energy excitations. For such quasiparticles the dynamical scaling exponent $z = 1$, meaning momentum and frequency (and hence space and imaginary time) scale the same way, and these systems are in general germane for (though not necessarily endowed with) an emergent Lorentz symmetry. In what follows we go beyond the landscape of Dirac materials and study a collection of strongly interacting spin-3/2 fermions in three dimensions that in the normal phase display a biquadratic touching of Kramers degenerate valence and conduction bands at an isolated point in the Brillouin zone. This system is also known as Luttinger semimetal [132, 133].

The non-interacting Luttinger semimetal (LSM) can be thought of as a QCP between electron and hole doped Fermi liquids, with the dynamical scaling exponent $z = 2$, reflecting the biquadratic nature of the band degeneracy point, see Fig. 4.1. The crossover temperature as a function of chemical doping from critical Luttinger fermions to Fermi liquid can be estimated as

$$T^* \sim \frac{\hbar^2}{2m} \frac{1}{\xi^2} \sim \frac{\hbar^2}{2m} |n|^{2/3}, \quad (4.1)$$

where m is the effective mass of the quasiparticles, ξ is a characteristic length scale, $|n|$ is the carrier density, and we set $k_B = 1$. $T^*(n)$ then describes the boundaries of the quantum critical fan (the shaded region in Fig. 4.1), where the critical properties are governed by the underlying QCP. For example, the specific heat scales as $C_V \sim T^{3/2}$, whereas the scaling of compressibility is $\kappa \sim \sqrt{T}$. Furthermore, the conductivity $\sigma \sim \sqrt{T}$ or $\sqrt{\omega}$ (see Appendix B.2.2). Therefore, even when the chemical doping is finite there exists a wide quantum critical regime, where the scaling of thermodynamic and transport quantities are essentially governed by $z = 2$ quasiparticles in $d = 3$. Indeed, in the quantum critical fan, chemical potential only contributes subleading corrections to these quantities. For more detailed analysis on the transport properties of LSM we refer the reader to Appendix B.2.

The type of quasiparticle excitations described in the theory of the LSM can be found

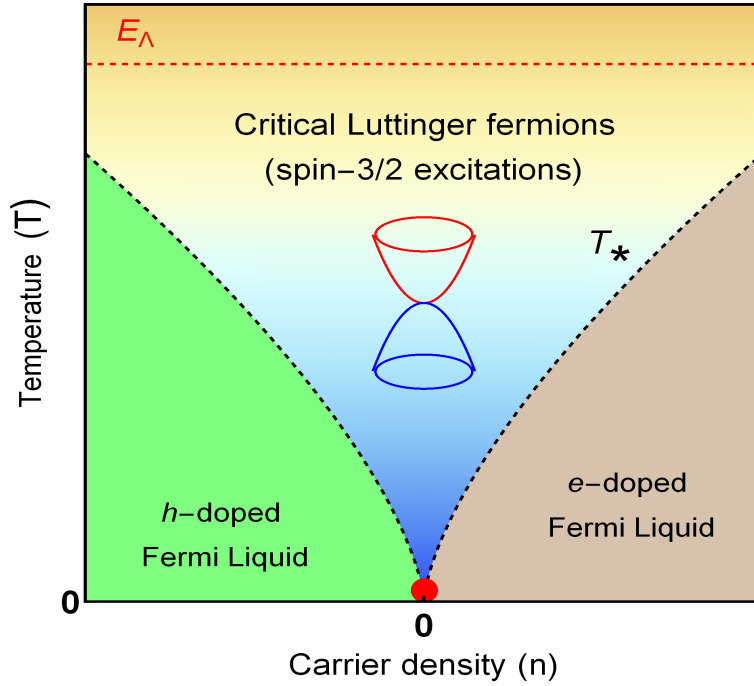


Figure 4.1: A schematic phase diagram of noninteracting Luttinger fermions. The red dot represents the Luttinger semimetal fixed point separating electron- and hole-doped Fermi liquid of spin-3/2 fermions. The shaded sector corresponds to the quantum critical regime associated with the $z = 2$ fixed point in $d = 3$ (the red dot), controlling scaling properties in this regime (see Appendix B.2). Above a nonuniversal high energy cutoff E_Λ (red dashed line), spin-3/2 fermions lose their jurisdiction. The crossover temperature T_* (black dashed lines) above which critical Luttinger fermions are operative is given by $T_* \sim |n|^{z/d}$, with $z = 2$ and $d = 3$, where n is the carrier density measured from the biquadratic band touching point. Figure adapted from Ref. [119].

for example in HgTe [45], gray-Sn [47, 48], 227 pyrochlore iridates ($\text{Ln}_2\text{Ir}_2\text{O}_7$, where Ln is the lanthanide element) [35, 50–52, 134] and half-Heusler compounds (such as LnPtBi, LnPdBi) [53–55]. Besides, biquadratic band touching has recently been observed in the normal state of $\text{Pr}_2\text{Ir}_2\text{O}_7$ [51] and $\text{Nd}_2\text{Ir}_2\text{O}_7$ [50] via angle resolved photo emission spectroscopy (ARPES).

4.1 Luttinger model

In this section we set the stage by introducing the noninteracting Luttinger Hamiltonian. We discuss the operative symmetries, as well as the scaling of various appearing quantities under the RG transformation.

4.1.1 Hamiltonian and Symmetries

The Luttinger model describes a biquadratic touching of Kramers degenerate valence and conduction bands at an isolated point (here chosen to be the $\Gamma = (0, 0, 0)$ point, for

convenience) in the Brillouin zone. The Hamiltonian operator is given by [132, 133]

$$\hat{h}_{\mathbf{L}}(\mathbf{k}) = -k^2 \left[\sum_{j=1}^3 \frac{\hat{d}_j(\hat{\mathbf{k}})}{2m_1} \Gamma_j + \sum_{j=4}^5 \frac{\hat{d}_j(\hat{\mathbf{k}})}{2m_2} \Gamma_j \right] - \mu \Gamma_0, \quad (4.2)$$

where Γ_0 is the four-dimensional identity matrix. Chemical potential μ and momenta \mathbf{k} are measured from the band touching point. Here, $\hat{\mathbf{d}}(\hat{\mathbf{k}})$ is a five-dimensional unit vector that transforms under the $l = 2$ representation under the orbital $SO(3)$ rotations. Hence $\hat{\mathbf{d}}(\hat{\mathbf{k}})$ is constructed from the d -wave form factors or spherical harmonics $Y_{l=2}^m(\theta, \phi)$, as shown in Appendix B.2.3. The corresponding four-component spinor basis is given by

$$\bar{\Psi}_{\mathbf{k}}^{\top} = \left(c_{\mathbf{k}, +\frac{3}{2}}, c_{\mathbf{k}, +\frac{1}{2}}, c_{\mathbf{k}, -\frac{1}{2}}, c_{\mathbf{k}, -\frac{3}{2}} \right), \quad (4.3)$$

where $c_{\mathbf{k}, j}$ is the fermionic annihilation operator with momenta \mathbf{k} and spin projection $j = \pm 3/2$ and $\pm 1/2$. The five mutually anti-commuting Γ matrices are defined as

$$\begin{aligned} \Gamma_1 &= \kappa_3 \otimes \sigma_2, & \Gamma_2 &= \kappa_3 \otimes \sigma_1, & \Gamma_3 &= \kappa_2 \otimes \sigma_0, \\ \Gamma_4 &= \kappa_1 \otimes \sigma_0, & \Gamma_5 &= \kappa_3 \otimes \sigma_3. \end{aligned} \quad (4.4)$$

Two sets of two dimensional Pauli matrices $\{\kappa_{\nu}\}$ and $\{\sigma_{\nu}\}$ respectively operate on the sign ($\text{sgn}[j]$) and magnitude ($|j| \in \{1/2, 3/2\}$) of the spin projections, where $\nu = 0, 1, 2, 3$. To close the Clifford algebra of all four-dimensional Hermitian matrices we also define ten commutators according to $\Gamma_{jk} = [\Gamma_j, \Gamma_k] / (2i)$, with $j > k$ and $j, k = 1, \dots, 5$. All sixteen four-dimensional matrices can be expressed in terms of the products of spin-3/2 matrices (\mathbf{J}), as also shown in Appendix B.2.3.

The energy spectra for Luttinger fermions are given by $\pm E_s(\mathbf{k}) - \mu$, where for $s = \pm 1$

$$E_s(\mathbf{k}) = \frac{k^2}{2m} \sqrt{\cos^2 \alpha \sum_{j=1}^3 \hat{d}_j^2(\hat{\mathbf{k}}) + \sin^2 \alpha \sum_{j=4}^5 \hat{d}_j^2(\hat{\mathbf{k}})}, \quad (4.5)$$

reflecting the quadratic band touching for $\mu = 0$, which is protected by the cubic symmetry. Here α is the mass anisotropy parameter, about which more in a moment.

Notice that the independence of $E_s(\mathbf{k})$ on s manifests the Kramers degeneracy of the valence and conduction bands, ensured by (1) the time-reversal (\mathcal{T}) and (2) the parity or inversion (\mathcal{P}) symmetries. Specifically, under the reversal of time, $\mathbf{k} \rightarrow -\mathbf{k}$ and $\Psi_{\mathbf{k}} \rightarrow \Gamma_1 \Gamma_3 \Psi_{-\mathbf{k}}$ and hence $\mathcal{T} = \Gamma_1 \Gamma_3 \mathcal{K}$, where \mathcal{K} is the complex conjugation, yielding $\mathcal{T}^2 = -1$ (thereby reflecting Kramers degeneracy of bands). Under the inversion $\mathcal{P} : \mathbf{k} \rightarrow -\mathbf{k}$ and $\Psi_{\mathbf{k}} \rightarrow \Psi_{-\mathbf{k}}$.

The ‘‘average’’ mass m and the mass anisotropy parameter α are respectively given by [43]

$$m = \frac{m_1 m_2}{m_1 + m_2}, \quad \alpha = \tan^{-1} \left(\frac{m_2}{m_1} \right). \quad (4.6)$$

Note that $\{\hat{d}_j\}$ for $j = 1, 2, 3$ and $j = 4, 5$ belong to the T_{2g} (three component) and E_g (two component) representations of the cubic or octahedral (O_h) point group, and m_1 and m_2 are effective masses in these two orbitals, respectively. The mass anisotropy parameter α allows us to smoothly interpolate between (1) the $m_1 \rightarrow \infty$ limit when the dispersion of the T_{2g} orbital becomes flat, yielding $\alpha \rightarrow 0$ and (2) $m_2 \rightarrow \infty$ when the E_g orbital becomes non-dispersive, leading to $\alpha \rightarrow \frac{\pi}{2}$. For $\alpha = \frac{\pi}{4}$ or $m_1 = m_2$, the Luttinger model enjoys an enlarged spherical symmetry. Any $\alpha \neq \frac{\pi}{4}$ captures a *quadrupolar distortion* in the system (still preserving the cubic symmetry). In what follows, we treat α as a *non-thermal* tuning parameter to explore the territory of interacting Luttinger fermions.

The connection between the spin projections ($j = \pm 3/2$ and $\pm 1/2$) and the bands can be appreciated most economically by taking $\mathbf{k} = (0, 0, k)$. For such a specific choice of momentum axis, the Luttinger Hamiltonian takes a *diagonal* form, given by

$$\hat{h}_L(k\hat{z}) = \frac{k^2}{2m_2} \text{Diag.} [-1, 1, 1, -1] - \mu. \quad (4.7)$$

From the above expression we can immediately infer that the pseudospin projections on the valence and conduction bands are respectively $|j| = 3/2$ and $1/2$.

4.1.2 Lagrangian and Scaling

The imaginary time (τ) Euclidean action corresponding to the non-interacting Luttinger model is given by

$$S_0 = \int d\tau d^d \mathbf{r} \Psi^\dagger(\tau, \mathbf{x}) \hat{h}_L(\mathbf{k} \rightarrow -i\nabla) \Psi(\tau, \mathbf{r}), \quad (4.8)$$

the invariance of which determines the scaling of space-(imaginary)time coordinates and the fermionic field

$$[\mathbf{x}] = -1, \quad [\tau] = -z, \quad [\Psi] = d/2, \quad (4.9)$$

where z is the dynamic scaling exponent, measuring the relative scaling between energy and momentum according to $E(\mathbf{k}) \sim |\mathbf{k}|^z$. For Luttinger fermions $z = 2$. The scaling dimensions of temperature (T) and chemical potential (μ) are

$$[T] = [\mu] = z. \quad (4.10)$$

Throughout, we use the *natural unit*, in which $\hbar = k_B = 1$. Having the noninteracting description in place, in the next section we proceed to incorporate local electronic interactions.

4.2 Electron-electron interactions

Next we address the effects of *repulsive* (at the bare level) electron-electron interactions in a perturbative manner, using the RG analysis (following the outlined scheme in Sec. 2.2). As mentioned earlier we will focus only on the local or short-range part of Coulomb interaction and neglect its long-range tail. For the sake of concreteness we assume that the local interactions are density-density in nature. Any generic local density-density interaction (such as the ones appearing in an extended Hubbard model, for example) can be captured by *six* quartic terms and the corresponding interacting Hamiltonian reads

$$\begin{aligned}
 H_{\text{int}} = - & \left[\lambda_0 (\Psi^\dagger \Psi)^2 + \lambda_1 \sum_{j=1}^3 (\Psi^\dagger \Gamma_j \Psi)^2 + \lambda_2 \sum_{j=4}^5 (\Psi^\dagger \Gamma_j \Psi)^2 + \lambda_3 (\Psi^\dagger \Gamma_{45} \Psi)^2 \right. \\
 & \left. + \lambda_4 \sum_{j=1}^3 (\Psi^\dagger \Gamma_j \Gamma_{45} \Psi)^2 + \lambda_5 \sum_{j=1}^3 \sum_{k=4}^5 (\Psi^\dagger \Gamma_{jk} \Psi)^2 \right]. \quad (4.11)
 \end{aligned}$$

In this notation $\lambda_j > 0$ corresponds to repulsive interaction. However, all four-fermion interactions are *not* linearly independent due to the existence of *Fierz identity* among sixteen four-dimensional Hermitian matrices, closing a $U(4)$ Clifford algebra [see Appendix B.2.4] and Sec.2.2.1 [11, 113, 118]. It turns out that any generic local interaction can be expressed in terms of only *three* quartic terms, and we conveniently (without any loss of generality) choose them to be λ_0 , λ_1 and λ_2 . Following the Fierz relations we can express local quartic terms proportional to λ_3 , λ_4 and λ_5 as linear combinations of above three, see Eq. (52). Whenever we generate four-fermion interactions proportional to λ_3 , λ_4 or λ_5 during the coarse-graining (discussed in Sec. 4.2.2), they can immediately be expressed in terms of λ_0 , λ_1 , and λ_2 , and the interacting model defined in terms of λ_0 , λ_1 , and λ_2 [see Eq. (4.12) below] always remains closed under the RG procedure to any order in the perturbation theory.

The imaginary time Euclidean action for the interacting system is given by

$$S_{\text{int}} = S_0 - \int d\tau d^d \mathbf{r} \left[\lambda_0 (\Psi^\dagger \Psi)^2 + \lambda_1 \sum_{j=1}^3 (\Psi^\dagger \Gamma_j \Psi)^2 + \lambda_2 \sum_{j=4}^5 (\Psi^\dagger \Gamma_j \Psi)^2 \right], \quad (4.12)$$

where $\Psi \equiv \Psi(\tau, \mathbf{r})$ and $\Psi^\dagger \equiv \Psi^\dagger(\tau, \mathbf{r})$. Under the rescaling of space-time(imaginary) coordinates and the fermionic fields, see Eq. (4.9), the local four-fermion interaction scales as $[\lambda_j] = z - d$. For $z = 2$ and $d = 3$, $[\lambda_j] = -1$, and any weak local interaction is an *irrelevant* perturbation and leaves the Luttinger fermions unaffected. Therefore, any ordering sets in at an intermediate strength of coupling through a quantum phase transition (QPT). In Sec. 4.2.2 we demonstrate appearances of various broken symmetry phases (BSPs) using a RG analysis, controlled via an ϵ -expansion, where $\epsilon = d - 2$, about the *lower-critical* two spatial dimension of this theory. Within the framework of the ϵ expansion, such QPTs take place at a critical interaction strength $\lambda_j^* \sim \epsilon$, and in three

spatial dimensions ($d = 3$) $\epsilon = 1$. Before carrying out the leading order RG analysis, to further set the stage we review the possible broken symmetry phases.

4.2.1 Nambu doubling and Broken symmetry phases

Next we discuss possible BSPs in this system. As before, to address particle-hole and particle-particle orders in a unified formalism, we introduce the eight-component Nambu spinor basis (see Sec. 2.2.2.2) according to

$$\Psi_{\text{Nam}} = \begin{bmatrix} \Psi_{\mathbf{k}} \\ \Gamma_1 \Gamma_3 \left(\Psi_{-\mathbf{k}}^\dagger \right)^\top \end{bmatrix}. \quad (4.13)$$

Again, in the lower block of Ψ_{Nam} we absorb the unitary part of the time-reversal operator \mathcal{T} , ensuring that the eight-component Nambu spinor (Ψ_{Nam}) transforms the same way as the original four component spinor $\Psi_{\mathbf{k}}$ [introduced in Eq. (4.3)] under the $SU(2)$ pseudospin rotation. In this basis the eight-dimensional Luttinger Hamiltonian takes a simple form

$$\hat{h}_{\text{L}}^{\text{Nam}}(\mathbf{k}) = \eta_3 \hat{h}_{\text{L}}(\mathbf{k}), \quad (4.14)$$

and the time-reversal operator becomes $\mathcal{T}_{\text{Nam}} = \eta_0 \Gamma_1 \Gamma_3 \mathcal{K}$. The newly introduced set of Pauli matrices $\{\eta_\nu\}$ operates on the Nambu or particle-hole indices, with $\nu = 0, 1, 2, 3$. The interacting Hamiltonian [Eq. (4.11)] in the Nambu basis becomes

$$\left\{ \begin{array}{l} \sum_{j=1}^3 (\Psi^\dagger \Gamma_j \Psi)^2 \\ \sum_{j=4}^5 (\Psi^\dagger \Gamma_j \Psi)^2 \\ (\Psi^\dagger \Gamma_{45} \Psi)^2 \\ \sum_{j=1}^3 (\Psi^\dagger \Gamma_j \Gamma_{45} \Psi)^2 \end{array} \right\} \rightarrow \frac{1}{2} \left\{ \begin{array}{l} \sum_{j=1}^3 \left(\Psi_{\text{Nam}}^\dagger \eta_3 \Gamma_j \Psi_{\text{Nam}} \right)^2 \\ \sum_{j=4}^5 \left(\Psi_{\text{Nam}}^\dagger \eta_3 \Gamma_j \Psi_{\text{Nam}} \right)^2 \\ \left(\Psi_{\text{Nam}}^\dagger \eta_0 \Gamma_{45} \Psi_{\text{Nam}} \right)^2 \\ \sum_{j=1}^3 \left(\Psi_{\text{Nam}}^\dagger \eta_0 \Gamma_j \Gamma_{45} \Psi_{\text{Nam}} \right)^2 \end{array} \right\} \quad (4.15)$$

where the factor of $1/2$ takes care of the artificial Nambu doubling.

We introduce various possible excitonic and superconducting orders in the Nambu basis (Ψ_{Nam}) in two subsequent sections. Finally, we discuss the reconstructed band structure and emergent topology inside the ordered phases.

4.2.1.1 Particle-hole or excitonic orders

The effective single-particle Hamiltonian in the presence of all possible momentum-independent or local or intra-unit cell excitonic orders is given by

$$H_{\text{local}}^{\text{exc}} = \int d^3 \mathbf{r} \left(\Psi_{\text{Nam}}^\dagger \hat{h}_{\text{local}}^{\text{exc}} \Psi_{\text{Nam}} \right), \quad (4.16)$$

where

$$\hat{h}_{\text{local}}^{\text{exc}} = \underbrace{\Delta_0 \eta_3 \Gamma_0}_{\text{Density}} + \eta_3 \underbrace{\left[\sum_{j=1}^3 \Delta_1^j \Gamma_j + \sum_{j=4}^5 \Delta_2^j \Gamma_j \right]}_{\text{Nematic}} + \eta_0 \underbrace{\left[\Delta_3 \Gamma_{45} + \sum_{j=1}^3 \Delta_4^j \Gamma_{45} \Gamma_j + \sum_{j=1}^3 \sum_{k=4}^5 \Delta_5^{jk} \Gamma_{jk} \right]}_{\text{Magnetic}}. \quad (4.17)$$

The ordered phases can be classified according to their transformation under the cubic (O_h) point group symmetry. Regular fermionic density (Δ_0) does not break any symmetry (hence does not correspond to any ordering) and transforms under the trivial A_{1g} representation. A three-component *nematic* order-parameter, constituted by $\mathbf{\Delta}_1 = (\Delta_1^1, \Delta_1^2, \Delta_1^3)$, transforms under the T_{2g} representation. By contrast, a two-component nematic order transforming under the E_g representation is captured by $\mathbf{\Delta}_2 = (\Delta_2^1, \Delta_2^2)$. Both of them break only the cubic symmetry, but preserve time-reversal and inversion symmetries. The ordered phase represents either a time-reversal invariant insulator or a Dirac semimetal [see Sec. 7.1.1]. As we discuss in Chapter 8, these phases are in fact higher order topological in nature. Since five Γ matrices transform as components of a rank-2 tensor under $\text{SO}(3)$ rotations, the two nematic phases represent *quadrupolar* orders, see Appendix B.2.3.

All ordered phases shown in the second line of Eq. (4.17) break time-reversal symmetry and represent different magnetic orders. For example, Δ_3 corresponds to an *octupolar* order (since $\Gamma_{45} \sim J_x J_y J_z$), transforming under the singlet A_{2u} representation. In a pyrochlore lattice of 227 iridates such an ordered phase represents the “*all-in all-out*” arrangement of electronic spin between two adjacent corner-shared tetrahedra [37, 134]. By contrast, “*two-in two-out*” or “*spin-ice*” magnetic orderings on a pyrochlore lattice are represented by a three-component vector $\mathbf{\Delta}_4 = (\Delta_4^1, \Delta_4^2, \Delta_4^3)$ (accounting for six possible two-in two-out arrangements in a single tetrahedron). Since $\Gamma_{45} \Gamma_j \sim 7J_j - 4J_j^3$ such an ordered phase contains a linear superposition of dipolar and octupolar moments, and transforms under the T_{1u} representation [43]. Finally, the six component vector Δ_5^{jk} with $j = 1, 2, 3$ and $k = 4, 5$ represents coplanar ordering of spins in 227 iridates, and transforms under the T_{2u} representation [135].

4.2.1.2 Particle-particle or superconducting orders

The effective single particle Hamiltonian in the presence of all possible momentum-independent or local or intra-unit cell superconducting orders reads [122, 136–138]

$$H_{\text{local}}^{\text{pair}} = \int d^3 \mathbf{r} \left(\Psi_{\text{Nam}}^\dagger \hat{h}_{\text{local}}^{\text{pair}} \Psi_{\text{Nam}} \right), \quad (4.18)$$

where

$$\hat{h}_{\text{local}}^{\text{pair}} = (\eta_1 \cos \phi + \eta_2 \sin \phi) \left[\overbrace{\Delta_{A_{1g}}^{\text{p}} \Gamma_0}^{\text{s-wave}} + \underbrace{\sum_{j=1}^3 \Delta_{T_{2g}}^{\text{p},j} \Gamma_j + \sum_{j=4}^5 \Delta_{E_g}^{\text{p},j} \Gamma_j}_{\text{d-wave}} \right], \quad (4.19)$$

and ϕ is the global $U(1)$ superconducting phase. Any pairing proportional to $\eta_1(\eta_2)$ preserves (breaks) time-reversal symmetry (recall that the time-reversal operator in the Nambu basis is $\mathcal{T}_{\text{Nam}} = \eta_0 \Gamma_1 \Gamma_3 \mathcal{K}$). Here, $\Delta_{A_{1g}}^{\text{p}}$ is the amplitude of the s -wave pairing, transforming under the A_{1g} representation. The s -wave pairing breaks only the global $U(1)$ symmetry, but preserves the cubic symmetry. On the other hand, $\Delta_{T_{2g}}^{\text{p},j}$ captures the amplitude of three d -wave pairings (for $j = 1, 2, 3$) transforming under the T_{2g} representation, and $\Delta_{E_g}^{\text{p},j}$ for $j = 4, 5$ represents the amplitude of two d -wave pairings belonging to the E_g representation. Notice $\{\Gamma_j, j = 1, \dots, 5\}$ can be expressed in terms of the product of two spin-3/2 matrices, and all five d -wave pairings break the cubic symmetry, while introducing a lattice distortion or electronic nematicity in the system. Hence, they stand as representatives of *quadrupolar nematic superconductors*. Next we seek to investigate the onset of different BSPs in the interacting Luttinger system and the competition among them within the framework of an unbiased RG analysis.

4.2.2 Renormalization group analysis

In what follows we here restrict ourselves to the leading order in the ϵ expansion, where $\epsilon = d - 2$, and account for corrections to the bare interaction vertices (λ_j s) to quadratic order in the coupling constants. Note that we will revisit the system of three-dimensional Luttinger fermions at finite temperature (T) and chemical potential (μ) in Chapter 7. Therefore, we here already consider the general case of $T, \mu \geq 0$, and in this chapter we simply take the limit $\mu \rightarrow 0$ and $T \rightarrow 0$ (in this order).

Our methodology for the perturbative RG analysis is as outlined in Sec. 2.2, and demonstrated in Chapter 3. We start by introducing dimensionless variables, namely

$$g_i = \frac{\lambda_i}{8(2\pi)^3} \frac{\Lambda^d}{\epsilon_\Lambda}, \quad t = \frac{T}{\epsilon_\Lambda}, \quad \tilde{\mu} = \frac{\mu}{\epsilon_\Lambda}, \quad (4.20)$$

where $\epsilon_\Lambda = \Lambda^2/(2m)$, g_i is the dimensionless quartic coupling constant, while t and $\tilde{\mu}$ are respectively the dimensionless temperature and chemical doping. We again suppress the tilde from the dimensionless chemical potential, and from here on we take $\tilde{\mu} \rightarrow \mu$. The RG flow equations of the coupling constants take the schematic form

$$\beta_{g_i} = -\epsilon g_i + \sum_{j,k} H_{jk}^{(i)}(t, \mu, \alpha) g_j g_k, \quad (4.21)$$

for $i = 0, 1, 2$, where $\beta_X \equiv dX/d\ell$, and the functions $H_{jk}^{(i)}(t, \mu, \alpha)$ for $i, j, k = 0, 1, 2$ are shown in Appendix B.2. Temperature and chemical potential also flow under coarse graining as relevant perturbations with bare scaling dimensions $[t] = [\mu] = z$. Therefore, their flow is described by Eq. (2.35), where $z = 2$ for the Luttinger system. The two flow equations can then be solved, respectively yielding

$$t(\ell) = t(0) e^{z\ell}, \quad \mu(\ell) = \mu(0) e^{z\ell}, \quad (4.22)$$

where $t(0)$ and $\mu(0)$ are the bare values of temperature and chemical doping respectively [also see Eq. (2.36)]. We can therefore set $t(0) = \mu(0) = 0$, and take the corresponding limit in the functions $H_{jk}^i(t, \mu, \alpha)$, to obtain the β -functions operative at zero temperature and chemical doping.

While the *divergence* of at least one of the quartic couplings (i.e., $g_i \rightarrow +\infty$) under coarse graining indicates the onset of a BSP, to unambiguously determine the pattern of symmetry breaking we also account for the leading order RG flow of all source terms, associated with different BSPs, discussed in Sec. 4.2.1. The effective action in the presence of all symmetry allowed fermionic bilinears [see Eqs. (4.16)-(4.19)] is given by

$$S_s = \int d\tau d^3\mathbf{r} \Psi_{\text{Nam}}^\dagger \left(\hat{h}_{\text{local}}^{\text{exc}} + \hat{h}_{\text{local}}^{\text{pair}} \right) \Psi_{\text{Nam}}, \quad (4.23)$$

with $\Psi_{\text{Nam}}^\dagger \equiv \Psi_{\text{Nam}}^\dagger(\tau, \mathbf{r})$ and $\Psi_{\text{Nam}} \equiv \Psi_{\text{Nam}}(\tau, \mathbf{r})$ as two independent Grassmann variables. Relevant Feynman diagrams are shown in Fig. 2.2. The resulting RG flow equations take the following schematic form

$$\frac{d \ln \Delta_i}{d\ell} - 2 = \sum_{j=0}^2 F_i^j(\alpha, t, \mu) g_j. \quad (4.24)$$

See Appendix B.2.5 for explicit form of these flow equations. The quantities appearing on the right hand side of each equation, represent the *scaling dimension* of the corresponding order-parameter. In possession of the RG flow equations β_{g_i} and β_{Δ_j} , we now continue with a systematic analysis of the quantum critical behavior of the LSM, and the role of the anisotropy parameter α therein.

4.2.3 Quantum criticality in Luttinger semimetal

The RG flow equations for $\mu = 0$ and $t = 0$ can be derived by taking the limit $\mu \rightarrow 0$ and then $t \rightarrow 0$ in Eq. (4.21), suggesting that weak interactions are irrelevant perturbations and any ordering takes place at finite coupling $g_i \sim \epsilon$ through a QPT. Next we discuss the following three cases separately (i) isotropic Luttinger system ($\alpha = \frac{\pi}{4}$), large mass for (ii) the T_{2g} orbital ($\alpha \rightarrow \frac{\pi}{2}$) and (iii) the E_g orbital ($\alpha \rightarrow 0$). Note at $t = \mu = 0$, the system is devoid of any natural infrared cutoff as $\ell_*^t, \ell_*^\mu \rightarrow \infty$ [for the definition of ℓ_*^t, ℓ_*^μ see Eqs. (2.38) and (2.39)]. Hence, we run the flows of quartic couplings up to a

Coupling	$\alpha = \frac{\pi}{4}$	$\alpha \approx \frac{\pi}{2}$			$\alpha \approx 0$		
	$\text{QCP}_{\frac{\pi}{4}}^1$	$\text{QCP}_{\frac{\pi}{2}}^1$	$\text{QCP}_{\frac{\pi}{2}}^2$	$\text{BCP}_{\frac{\pi}{2}}$	QCP_0^1	QCP_0^2	BCP_0
$g_0^* \times 10^3$	2.24	1.49	-2.93	-1.58	1.95	-5.98	-5.60
$g_1^* \times 10^3$	2.03	1.47	-2.84	-1.33	1.71	4.80	4.97
$g_2^* \times 10^3$	2.03	1.26	3.76	5.54	1.94	-5.87	-5.48

Table 4.1: Locations of quantum critical points (QCPs) possessing one unstable direction and bicritical points (BCPs) possessing two unstable directions for three specific choices of the mass anisotropy parameter α [see Eq. (4.6)]. Note for $\alpha = \frac{\pi}{4}$ the Luttinger model possesses an emergent spherical symmetry, while for $\alpha \rightarrow 0$ ($\frac{\pi}{2}$) the band dispersion in the $E_g(T_{2g})$ orbitals becomes almost flat. For $\alpha = \frac{\pi}{4}$ the coupled RG flow equations support only one QCP, denoted by $\text{QCP}_{\frac{\pi}{4}}^1$, while for $\alpha \rightarrow \frac{\pi}{2}$ and $\alpha \rightarrow 0$ we find two QCPs, respectively denoted by $\text{QCP}_{\frac{\pi}{2}}^j$ and QCP_0^j for $j = 1, 2$, see also Ref. [139]. For these two limiting cases the flow equations also support one BCP, respectively identified as $\text{BCP}_{\frac{\pi}{2}}$ and BCP_0 . Existence of such BCP in the presence of two QCPs is necessary to ensure the continuity of the RG flow trajectories and separate the basins of attraction of two QCPs. All coupling constants at all fixed points are measured in units of ϵ , where $\epsilon = d - 2$ measures the deviation from the lower critical two spatial dimensions, where all local quartic interactions are *marginal*. Note that $\text{QCP}_{\frac{\pi}{4}}^1$, $\text{QCP}_{\frac{\pi}{2}}^1$, QCP_0^1 represent the same QCP, only its location shifts as we tune α . By contrast, $\text{QCP}_{\frac{\pi}{2}}^2$ and QCP_0^2 are solely introduced by mass anisotropy and bear no analog to the fixed points found around $\alpha = \pi/4$. Besides the above QCPs and the BCPs, there always exists a trivial Gaussian fixed point, representing the non-interacting Luttinger semimetal, at $(g_0^*, g_1^*, g_2^*) = (0, 0, 0)$, endowed with three stable directions. See Appendix B.2.6 for details.

sufficiently large fixed RG time (see Section 2.2), to determine the stability of LSM and the flows of the source terms to pin the pattern of symmetry breaking.

4.2.3.1 Isotropic Luttinger semimetal ($\alpha = \frac{\pi}{4}$)

For $\alpha = \frac{\pi}{4}$ the coupled RG flow equations support only one QCP, reported in Table 4.1 and identified as $\text{QCP}_{\frac{\pi}{4}}^1$, besides the trivial (and fully stable) Gaussian fixed point at $g_0^* = g_1^* = g_2^* = 0$ (representing the stable LSM). This QCP controls QPTs from LSM to various BSPs (depending on the interaction channel). To gain insight into the nature of the candidate competing BSPs, we compute the scaling dimensions for all fermion bilinears at this QCP. The results are summarized in Table 4.2. Note that the s -wave pairing has the largest scaling dimension at this QCP, while two nematic orders possess degenerate but second largest (and positive) scaling dimensions. But, the rest of the fermion bilinears possess *negative* scaling dimensions. Consequently, depending on the nature of interactions, an isotropic Luttinger semimetal supports only these three phases at zero temperature, see Fig. 4.2.

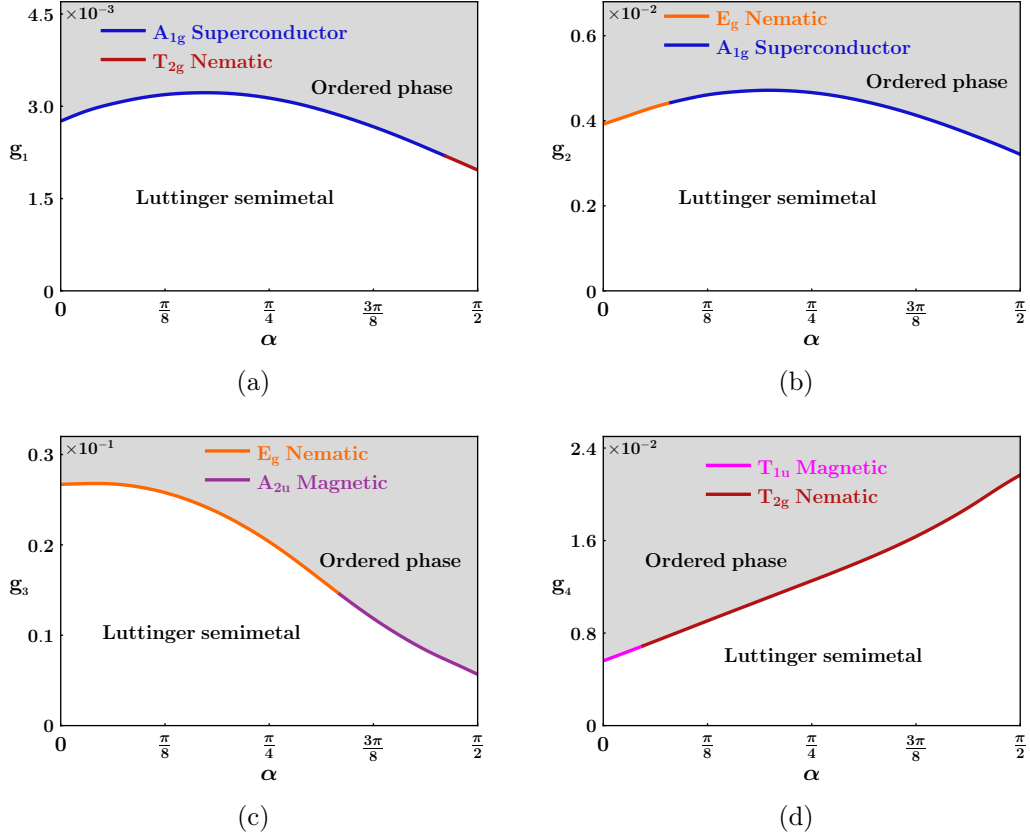


Figure 4.2: Specific cuts of the global phase diagram of an interacting Luttinger semimetal at zero temperature, obtained from an RG analysis [see Sec. 4.2.3]. Here α is the mass anisotropy parameter. For $\alpha = \frac{\pi}{4}$ the system possesses an enlarged spherical symmetry, whereas for $\alpha = 0$ ($\frac{\pi}{2}$) the E_g (T_{2g}) orbital possess *infinite* mass [see Sec. 4.1]. Here g_1 (g_2) captures the strength of repulsive interactions in the T_{2g} (E_g) nematic channels. Magnetic interactions in the A_{2u} (T_{1u}) channel is denoted by g_3 (g_4). Notice that even in the absence of a Fermi surface, pure repulsive nematic interactions are conducive to s -wave pairing among spin-3/2 fermions at zero temperature [see panels (a) and (b)]. In all the panels the coupling constants are measured in units of ϵ . The ordered states correspond to the gray shaded regions, and its boundaries with the Luttinger semimetal (white regions), occupied by distinct broken symmetry phases are identified by different colors. Figure adapted from Ref. [119].

4.2.3.2 Anisotropic Luttinger semimetal: $\alpha \rightarrow \frac{\pi}{2}$

Next we turn our focus to the vicinity of $\alpha = \frac{\pi}{2}$. The coupled flow equations then support *two* QCPs [denoted by $\text{QCP}_{\frac{\pi}{2}}^1$ and $\text{QCP}_{\frac{\pi}{2}}^2$] and *one* bicritical point [denoted by $\text{BCP}_{\frac{\pi}{2}}$], see Table 4.1. The BCP possesses *two* unstable directions. Notice $\text{QCP}_{\frac{\pi}{2}}^1$ is the same as $\text{QCP}_{\frac{\pi}{4}}^1$, only shifted toward weaker coupling, which can be verified from the fact that the signs of the coupling constants and scaling dimensions for all fermion bilinears are *identical* at these two QCPs [see Tables 4.1 and 4.2]. The dominant instability at $\text{QCP}_{\frac{\pi}{2}}^1$ is still the s -wave pairing, but now, due to the cubic deformation, the T_{2g} nematic channel (which becomes “almost mass” in this limit) acquires the second largest anomalous dimension. Correspondingly, the Luttinger semimetal in the $\alpha \rightarrow \frac{\pi}{2}$ limit can support these two

Source field	$\alpha = \frac{\pi}{4}$	$\alpha = 1.5$			$\alpha = 0.04$		
	QCP $^1_{\frac{\pi}{4}}$	QCP $^1_{\frac{\pi}{2}}$	QCP $^2_{\frac{\pi}{2}}$	BCP $_{\frac{\pi}{2}}$	QCP 1_0	QCP 2_0	BCP $_0$
Δ_0	0	0	0	0	0	0	0
Δ_1	<i>0.426</i>	<i>0.531</i>	-0.238	0.378	0.353	<i>0.614</i>	0.656
Δ_2	<i>0.426</i>	0.275	<i>0.325</i>	0.678	<i>0.539</i>	-0.153	-0.070
Δ_3	-0.076	-0.204	1.147	1.006	-0.004	-0.024	-0.024
Δ_4	-0.076	-0.007	-0.021	-0.030	-0.134	0.731	0.699
Δ_5	-0.076	-0.094	0.182	0.092	-0.062	0.020	0.011
$\Delta_{A_{1g}}^p$	0.551	0.545	-0.254	0.355	0.547	-0.166	-0.083
$\Delta_{T_{2g}}^p$	-0.034	-0.004	-0.011	-0.016	-0.059	<u>0.016</u>	0.006
$\Delta_{E_g}^p$	-0.034	-0.088	<u>0.169</u>	0.073	-0.002	-0.012	-0.012

Table 4.2: Scaling dimensions (in units of ϵ) of various source (Sr) terms or fermion bilinears at different fixed points (reported in Table 4.1), obtained by substituting fixed point values of the coupling constants g_0^* , g_1^* and g_2^* on the right-hand side of the corresponding flow equation [see Eq. (4.24)] at $t = 0$ and $\mu = 0$. At each QCP the largest scaling dimension is shown in bold, while the second largest ones are shown in italic. At the two magnetic QCPs (QCP $^2_{\frac{\pi}{2}}$ and QCP 2_0), the largest scaling dimensions for the superconducting channel (namely d -wave pairings) are underlined.

ordered phases, see Fig. 4.2(a), (b), and (d), nucleating through QCP $^1_{\frac{\pi}{2}}$.

On the other hand, QCP $^2_{\frac{\pi}{2}}$ is new and bears no resemblance to any fixed points we found for $\alpha = \frac{\pi}{4}$. This QCP is induced by the mass anisotropy of Luttinger fermions. At this QCP the A_{2u} magnetic (E_g nematic) order possesses the largest (second largest) scaling dimension, see Table 4.2. Among three possible local pairings the E_g d -wave superconductor possesses the *largest* (and positive) scaling dimension at this QCP. However, at zero chemical doping we only observe nucleation of the A_{2u} magnetic order through this QCP, see Fig. 4.2(c).

4.2.3.3 Anisotropic Luttinger semimetal: $\alpha \rightarrow 0$

Finally, we approach the opposite limit, when the mass in the E_g orbital becomes sufficiently large, i.e. $m_2 \gg m_1$ or equivalently $\alpha \rightarrow 0$. In this regime the RG flow equations support two QCPs [denoted by QCP 1_0 and QCP 2_0] and a BCP [denoted by BCP $_0$], see Table 4.1. Note that QCP 1_0 is similar to QCP $^1_{\frac{\pi}{4}}$, only shifted toward weaker coupling. Note that though the s -wave pairing still has the largest anomalous dimension at this QCP, the second leading instability is now the E_g nematic order (which becomes “almost mass” in this limit). We can indeed observe these two orders in the $\alpha \rightarrow 0$ limit, see Fig. 4.2(a), (b), and (c), developing through this QCP.

By contrast, QCP 2_0 is induced by the mass anisotropy. At this QCP, the T_{1u} magnetic (T_{2g} nematic) order possesses the largest (second largest) scaling dimension, see

Table 4.2. Correspondingly, we observe nucleation of T_{1u} magnetic ordering in this limit, see Fig. 4.2(d). Also note that among three local pairings, the d -wave one transforming under the T_{2g} representation possesses the largest (and positive) scaling dimension.

Finally, we comment on the role of the BCPs possessing two unstable directions, see Table 4.1. Note that a BCP can only be found when there exists two QCPs in the three dimensional coupling constant space (g_0, g_1, g_2) . The existence of a BCP separates the basin of attraction of two QCPs and ensures continuity of the RG flow trajectories in coupling constant space.

4.2.4 Universality class and critical exponents

All QCPs, listed in Table 4.1, are characterized by only *one* unstable direction or *positive* eigenvalue of the corresponding stability matrix [see Appendix B.2.6 and Eq. (2.27)], defined as

$$M_{ij}(g_0, g_1, g_2) = \frac{d}{dg_j} \beta_{g_i}. \quad (4.25)$$

To the leading order in the ϵ expansion the positive eigenvalue at all QCPs is exactly ϵ , which in turn determines the *correlation length exponent* (ν) according to

$$\nu^{-1} = \epsilon + \mathcal{O}(\epsilon^2). \quad (4.26)$$

For the physically relevant situation $\epsilon = 1$ and we obtain $\nu = 1$. As mentioned in Sec. 2.2.2.1, ν being the same at all QCPs is, only an artifact of the leading order ϵ -expansion. Generically ν is expected to be distinct at different QCPs, once we account for higher order corrections in ϵ .

Since to the leading order in the ϵ -expansion, local interactions do not yield any correction to fermion self-energy, the dynamic scaling exponent (z) at all interacting QCPs is

$$z = 2 + \mathcal{O}(\epsilon). \quad (4.27)$$

Together the correlation length and dynamic scaling exponents determine the universality class of all continuous QPTs from a LSM to various BSPs. In the next section, we will discuss the imprint of these two exponents on the scaling of the transition temperature (t_c) associated with the finite temperature order-disorder transitions.

4.2.5 Scaling of the transition temperature

Even though our RG analysis in the previous section was performed at zero temperature, one can still find the imprint of various interacting QCPs at finite temperatures. The RG flow equations at finite temperature can be derived from Eqs. (4.21) and (4.24) by taking the $\mu \rightarrow 0$ limit in $H_{jk}^{(i)}(t, \mu, \alpha)$ and $F_i^j(\alpha, t, \mu)$. Recall that temperature introduces a natural *infrared* cutoff for the flow equations ℓ_*^t [see Eqs. (2.38) and (2.39)]. Physically

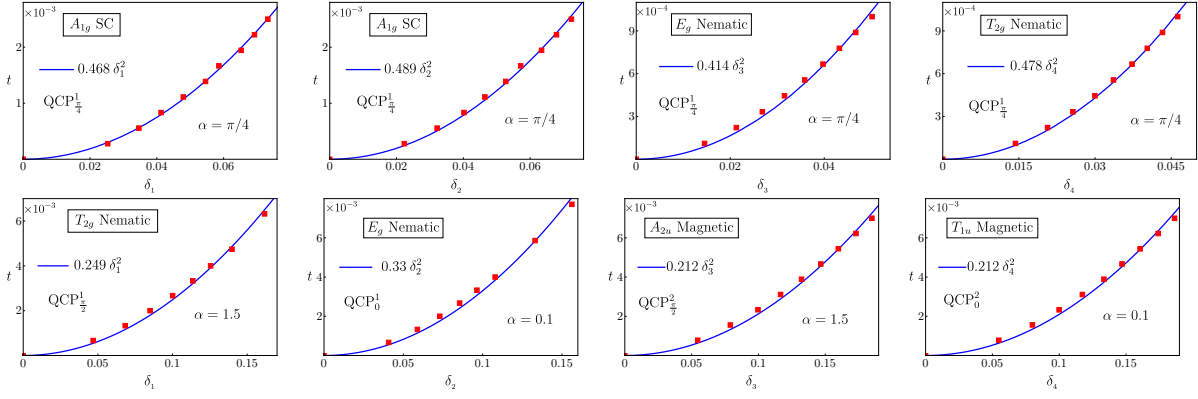


Figure 4.3: Scaling of dimensionless transition temperature (t_c) with the reduced distance ($\delta_j = (g_j - g_j^*)/g_j^*$) from the quantum critical point, located at $g_j = g_j^*$ for $j = 1, 2, 3, 4$, see Sec. 4.2.5. The mass anisotropy parameter α and nature of the ordered phase for $\delta_j > 0$ in each panel are quoted explicitly. Note that $t_c \sim \delta_j^2$ for $\delta \ll 1$, in agreement with field theoretic prediction. The QCPs controlling the Luttinger semimetal to ordered states quantum phase transitions at $t = 0$ are also quoted in each panel. Red dots represent numerically obtained transition temperature and the blue lines correspond to least-square fit of $t_c \sim \delta_j^2$. Figure adapted from Ref. [119].

such an infrared cutoff corresponds to a scenario when the renormalized temperature $t(\ell)$ becomes comparable to the ultraviolet energy $\epsilon_\Lambda = \Lambda^2/(2m)$ [see Fig. 4.1], beyond which the notion of quadratically dispersing fermions becomes moot and the flow equations from Eq. (4.21) lose their validity.

To capture the effects of electronic interactions in a LSM at finite- t , we run three quartic coupling constants up to a scale $\ell \leq \ell_*^t$. Now depending on the bare strength of interactions, two situations arise

$$(a) \quad g(\ell_*^t) < \zeta, \quad \text{or} \quad (b) \quad g(\ell_*^t) > \zeta,$$

respectively representing a disordered LSM (without any long-range ordering) or onset of a BSP at finite temperature. Here ζ is a parameter in the RG analysis (see Sec. 2.2.3), and the universal properties of the system are insensitive to the exact value of it, so long as $\zeta \sim \mathcal{O}(1)$. For a given strength of interaction $g > g_*$, where g_* is the requisite critical strength of interaction for a BSP at $t = 0$, we always find a temperature t_c above (below) which the BSP disappears (appears). We identify t_c as the *critical or transition temperature*. None of the coupling constants diverge for $t > t_c$. All ordered phases can display true long-range order at finite t in three dimensions and t_c corresponds to a genuine transition temperature.

General scaling theory suggests that the transition temperature scales as [140, 141]

$$t_c \sim \delta^{\nu z}, \quad (4.28)$$

for $\delta \ll 1$, where $\delta = (g - g_*)/g_*$ is the *reduced distance* from a QCP, located at $g = g_*$

(say). Hence, for interacting LSM, $t_c \sim \delta^2$ for $\epsilon = 1$ (i.e., the prediction from the leading order ϵ -expansion). The scaling of critical or transition temperature for various choices of coupling constants and resulting BSPs, and different choices of the mass anisotropy parameter α , are shown in Fig. 4.3, showing a fairly good agreement with the field theoretic prediction $t_c \sim \delta^2$ around all QCPs, reported in Table 4.1.

4.3 Summary and discussion

To summarize we have presented an analysis at zero temperature on the role of electron-electron interactions in a three-dimensional Luttinger semimetal, describing a biquadratic touching of Kramers degenerate valence and conduction bands of effective spin-3/2 fermions at an isolated point in the Brillouin zone. This model can succinctly capture the low-energy physics of HgTe [45], gray-Sn [47, 48], 227 pyrochlore iridates [35, 50–52, 134] and half-Heuslers [53–55]. For concreteness, we focused only on the short-range components of the Coulomb interaction (such as the ones appearing in an extended Hubbard model), and neglected its long-range tail. Furthermore, in this chapter we restricted ourselves to zero temperature (mostly) and chemical doping, and focused on the quantum critical properties of the Luttinger semimetal. In Chapter 7 we explore the phase diagram of this system at finite temperature and chemical potential, where thermal fluctuations and the extended Fermi surface profoundly affect the competition among ordered phases.

Due to the vanishing density of states, namely $\varrho(E) \sim \sqrt{E}$, sufficiently weak, but generic local four-fermion interactions are irrelevant perturbations in a system of Luttinger fermions. Consequently, any ordering sets in at an intermediate coupling through quantum phase transitions. We here address the instability of this system at finite coupling within the framework of a renormalization group analysis, controlled by a “*small*” parameter ϵ , where $\epsilon = d-2$. Notice that in two spatial dimensions a biquadratic band touching (similar to the situation in Bernal-stacked bilayer graphene) yields a *constant* density of states, and local four-fermion interactions are *marginal* in $d = 2$. Hence, our renormalization group analysis is performed about the *lower-critical* two spatial dimensions. In this framework all quantum phase transitions from a disordered Luttinger semimetal to any ordered phase take place at $g_j^* \sim \epsilon$, where g_j is the dimensionless coupling constant, and for three dimensions $\epsilon = 1$. We here restrict ourselves to repulsive (at the bare level) electron-electron interactions and compute the anomalous dimensions of various excitonic and pairing order parameters at the occurring QCPs and BCPs, see Table 3.3. This allows us to identify the dominant instabilities in the regions of the phase diagram controlled by certain QCPs.

Using the renormalization group analysis, we show that in an isotropic system an s -wave pairing and two nematic orders are the prominent candidates for a broken symmetry phase, although at zero temperature the s -wave pairing is the dominant instability. While the s -wave pairing only breaks the global $U(1)$ symmetry and produces a uniform mass

gap, two nematic orders, transforming under the T_{2g} and E_g representations, produce lattice distortion along the C_{3v} and C_{4v} axes, respectively. Such ordered phases can describe either time-reversal symmetry preserving insulators or topological Dirac semimetals, hosting one-dimensional hinge-like surface modes, hence exhibiting higher order topology (see Chapter 8). However, a collection of strongly correlated gapless spin-3/2 fermions do not show any noticeable propensity toward the nucleation of any magnetic order or d -wave pairings in an isotropic system at least when $t = 0$. This is so, because the magnetic orders (d -wave pairings) produce gapless Weyl nodes (nodal loops) around which the density of states vanishes as $\rho(E) \sim |E|^2(|E|)$, while the former three orders support gapped spectra. Hence, the magnetic orders and d -wave pairings are energetically inferior to s -wave pairing and electronic nematicities in an isotropic LSM. A detailed discussion on the energy-entropy competition in Luttinger (semi)metal and the role of the low-energy density of states follows in Chapter 7.

We identify that the mass anisotropy (α), measuring the quadrupolar distortion in the Luttinger system, can be a useful non-thermal tuning parameter to further explore the territory of strongly interacting spin-3/2 fermions [43, 139]. In particular, we find that strong quadrupolar distortions can be conducive for various magnetic orderings even at zero temperature. Specifically, when the electronic dispersion along the C_{3v} axes becomes almost flat (realized as $\alpha \rightarrow \frac{\pi}{2}$) the singlet A_{2u} magnetic order stabilizes at $t = 0$ via QCP $_{\frac{\pi}{2}}^2$. On the other hand, when Luttinger fermions are almost non-dispersive along the C_{4v} axes (realized when $\alpha \rightarrow 0$), the system becomes susceptible toward the formation of a triplet T_{1u} magnetic order, the nucleation of which happens through QCP $_0^2$. For these two limiting scenarios the above two magnetic orders become (almost) *mass*, and their nucleation becomes energetically beneficial even at zero temperature. For the anomalous dimensions of order parameters for various values of α consult Table 3.3.

All quantum phase transitions from the Luttinger semimetal to broken symmetry phases are continuous and controlled by various quantum critical points, see Sec. 4.2.3 and Table 4.1. To the leading order in the ϵ -expansion, the universality class of these transitions is characterized by the (a) correlation length exponent $\nu^{-1} = \epsilon$ and (b) dynamic scaling exponent $z = 2$ [see Sec. 4.2.4]. The presence of such quantum critical points manifests itself through the scaling of transition temperature $t_c \sim |\delta|^{\nu z}$, yielding $t_c \sim |\delta|^2$ for $d = 3$ or $\epsilon = 1$, see Fig. 4.3, where δ is the reduced distance from the critical point.

In Part II of this thesis we introduce finite temperature and chemical doping and observe their effect on the competition among broken symmetry phases. Generally speaking, thermal fluctuations allow for less energetically favorable, but more entropic phases to nucleate. At the same time, chemical potential yields an extended Fermi surface instead of the previously present Fermi point, which in turn promotes superconductivity via enhanced carrier density. We follow a similar structure where we consider a few different paradigmatic systems in two and three dimensions, displaying linear and quadratic band degeneracy points in their dispersion.

Part II

Competing orders and selection rules

In Part I we investigated the quantum critical properties of different systems, with special focus on the emergence of enlarged symmetries at various QCPs. Such multiband electronic materials constitute a rich landscape harboring a plethora of competing phases, such as charge- and spin-density-wave orders, or unconventional pairing phases. Indeed, the global phase diagram of strongly correlated electronic materials, such as cuprates, pnictides, iridates, ruthenates, and heavy-fermion compounds, displays a confluence of at least some of these phases. In experiments, these phases can be realized as the temperature, pressure, and chemical doping is tuned in these systems.

Considering the zoo of possible interaction-induced orderings, the following question arises. Can we establish a set of simple directives that ultimately select an ordered state from a soup of incipient phases with respect to the nature of interactions? In the following chapters we attempt to give an affirmative answer to this question. In Chapter 5 we propose a set of *selection rules* that are based solely on the internal algebra of interaction terms, order parameter bilinears and noninteracting Hamiltonian. To further delineate these preselected phases, we then write down the *organizing principle*, that orders various broken symmetry phases along the temperature axis, based on their condensation energy and entropy gain. We then verify the validity of these rules in a diverse set of two- and three-dimensional systems. In Chapter 6, we begin our discussion with monolayer and Bernal bilayer graphene, constituted by two-dimensional honeycomb membranes of carbon atoms, that respectively display linear and quadratic degeneracy points in the low-energy band structure. In these systems, due to the low atomic number of carbon, the spin-orbit coupling is negligibly small. Then, in Chapter 7 we turn our focus again to a three-dimensional strong spin-orbit coupled Luttinger semimetal (introduced in Chapter 4), hosting a collection of quadratically dispersing effective spin-3/2 electrons, and anchor our expectations in this significantly different system.

Chapter 5

Selection rules and organizing principle

Let us begin by spelling out our proposed set of rules, selecting from various symmetry-allowed broken symmetry phases, and organizing them in the phase diagram of generic multiband materials. Consider a band structure described by the Hamiltonian \hat{h} , containing Hermitian matrices H_i . Besides, consider a local interaction channel and an arbitrary but symmetry-allowed local order parameter schematically written as

$$g_M \sum_j (\Psi^\dagger M_j \Psi)^2 \quad \text{and} \quad \Delta_O \sum_k (\Psi^\dagger O_k \Psi),$$

respectively. Here g_M is the coupling constant, and Δ_O is the conjugate field to the fermion bilinears. Moreover, we define the following quantities. Let A_M and C_M respectively be the number of anticommuting and commuting matrix pairs between an order parameter and a four fermion term. Also, let A_H and C_H respectively be the number of anticommuting and commuting matrix pairs between an order parameter and the single-particle Hamiltonian. We can summarize these relations as ¹

$$\begin{aligned} A_H : \{O_k, H_i\} = 0, & & A_M : \{O_k, M_j\} = 0, \\ C_H : [O_k, H_i] = 0, & & C_M : [O_k, M_j] = 0. \end{aligned} \quad (5.1)$$

Then, various cuts of the global phase diagram in the presence of local interactions is organized according to the following two rules.

(I) Among the available ordered phases, the interaction channel coupled by g_M maximally boosts nucleation tendency of the ones satisfying

$$(a) O_i = M_i \quad \text{or} \quad (b) A_M = \text{maximal}. \quad (5.2)$$

(II) Among the phases selected by (I), an ordered phase is energetically (entropically)

¹We write all matrices as Kronecker products of Pauli matrices as $\Gamma_{\mu\nu\dots} = \sigma_\mu \otimes \sigma_\nu \dots$, therefore any two matrices either commute or anticommute.

favorable if

$$A_H - C_H = \text{maximal (minimal)}. \quad (5.3)$$

We name the two “or” conditions in (I) selection rules. They are operative at zero as well as at finite temperature and chemical potential, and only depend on \hat{h} indirectly, in the sense that the interaction terms by construction preserve the microscopic symmetries of the noninteracting Hamiltonian. Of crucial importance is the fact that MLG and BLG are endowed with the same microscopic symmetries. Therefore (I) *cannot distinguish between the two systems*. But (II) can as we show for the extended honeycomb Hubbard model in Sec. 6.4.

Besides (I) having exactly two ways [(a) and (b)] of boosting an ordered phase by a given four-fermion interaction, it leads to the following consequence regarding the adjacent or competing phases. Namely, two broken symmetry phases that reside next to each other in a generic cut of the global phase diagram as we tune the interaction strength, temperature or chemical doping, involving, say, the following two sets of matrices

$$\begin{aligned} \{O_k^{(1)}\}, \quad k = \{1, \dots, K\}, \\ \{O_l^{(2)}\}, \quad l = \{1, \dots, L\}, \end{aligned}$$

that transform as vectors under $O(K)$ and $O(L)$ rotations, respectively, form *composite* or *supervector* order parameters that transform as vectors under the group $O(N)$, where

$$K, L < N \leq K + L.$$

According to (I) it has to be that $O_k^{(1)} = M_k$ and $\{O_l^{(2)}, M_k\} = 0$, or the other way around, so that from the two sets of matrices $\{O_k^{(1)}\}$ and $\{O_l^{(2)}\}$, one can always choose at most N matrices that mutually anticommute.

On the other hand, we name the statement in (II) organizing principle. It arranges the phases, selected by (I), along the temperature axis. Note $C_H = 0$ implies a fully and isotropically gapped state, which causes maximal gain of the condensation energy and is, therefore, favorable at the lowest temperature. On the other hand, $C_H > 0$ results in gapless states at low energies, which, hence is a configuration of higher entropy. Therefore, such states are typically more prominent at higher temperatures. As such (II) is a generalized energy-entropy argument, that goes beyond the binary distinction of whether an order is gapped or gapless, and capable of organizing more than one ordered phases with $C_H > 0$, but varying A_H , as the temperature is varied in the system. A schematic representation of the selection rules and the organizing principle is shown in Fig. 5.1.

Chemical potential plays an important role in promoting superconductivity from pure repulsive interactions by enhancing carrier density. In the above outlined algebraic framework, the chemical doping term $\hat{\mu}$ anticommutes with all pairing orders. Therefore, for a K -component superconducting order parameter $A_H \rightarrow A_H + K$ as $\hat{h} \rightarrow \hat{h} - \hat{\mu}$ at finite dop-

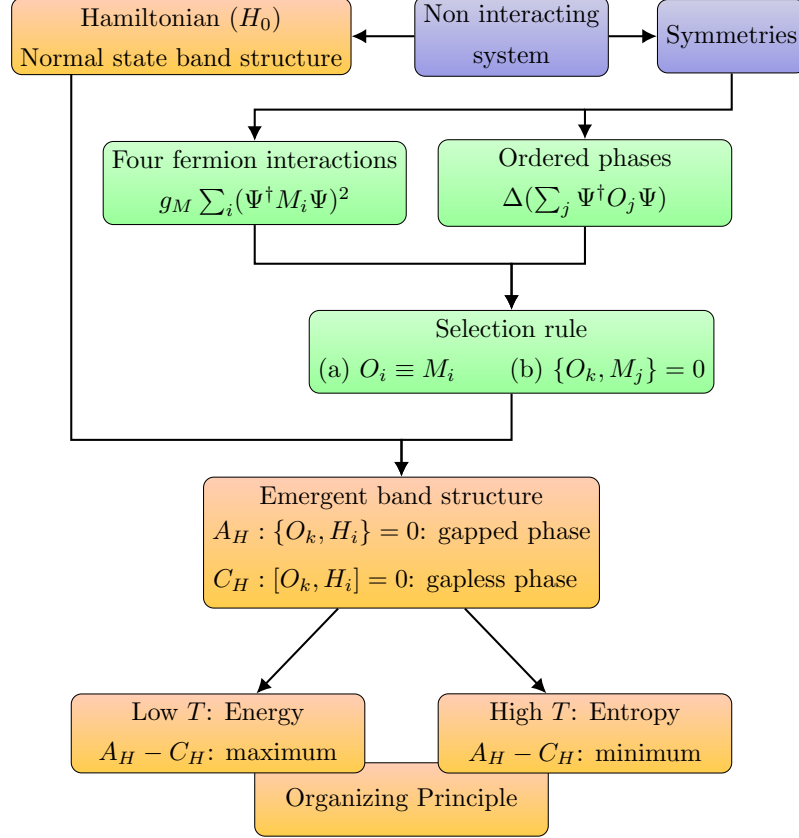


Figure 5.1: A schematic flowchart depicting the selection rules and organizing principle. Consider a noninteracting system, described by the single-particle Hamiltonian H_0 containing a set of Hermitian matrices $\{H_i\}$, a four-fermion interaction with coupling g_M and a fermionic order parameter coupled with the conjugate field Δ_O , all determined by the symmetry of the system. Here M_i and O_i are Hermitian matrices of the same dimension as H_i . Then, an ordered phase is boosted by the interaction if (a) $O_i \equiv M_i$ or (b) these two set of matrices maximally anticommute. The selected ordered phases are then arranged along the temperature axis according to the organizing principle, quantified by A_H and C_H , respectively counting the pairs of matrices from the sets $\{O_i\}$ and $\{H_i\}$ that mutually anticommute and commute. Order parameter matrices O_i that maximally anticommute (commute) with H_i yield gapped (gapless) quasiparticles inside the ordered phase and inhabit comparatively lower (higher) temperatures, following the energy-entropy argument. Finite chemical doping promotes superconductivity at the lowest temperature even from repulsive electronic interactions, as the underlying Fermi surface can only be gapped by them, also in agreement with the organizing principle. The nature of the nucleated paired state also follows the selection rule. Figure adapted from Ref. [13].

ing. By contrast, all the excitonic orders commute with $\hat{\mu}$ and thus for an L -component excitonic order parameter $A_H \rightarrow A_H - L$ as $\hat{h} \rightarrow \hat{h} - \hat{\mu}$. Therefore, at finite doping pairing states get energetically favored at the lowest temperature, while excitonic orders being more entropic are favored at higher temperature. Still, the competing excitonic and pairing orders for a given interaction channel follow the selection rule (I).

Note that (I) and (II) still leave room for *degeneracy* among the selected order parame-

ters. For example, when two bilinears gap the quasiparticle spectra and fully anticommute with the matrices in a given interaction channel, then temperature cannot distinguish between them. If, however, one of them is a pairing phase, it will be favored at low temperatures when $\mu > 0$, as it optimally gaps the underlying Fermi surface [selection rule (II)].

We now proceed to demonstrate the applicability of these rules in three different systems. We start by examining monolayer and Bernal bilayer graphene in tandem. Since the symmetries of these systems are the same, this provides a unique opportunity to shed light on the role of the normal state band structure, as any differentiation in the corresponding phase diagrams must originate from there. We then move on to apply these rules in a three-dimensional Luttinger semimetal. The Luttinger model has been used to successfully describe the electronic structure of numerous compounds, most prominently 227 pyrochlore iridates and half-Heuslers, that also display significant correlations. Besides, graphene-based layered materials have been in the center of huge interest in the past decade. These systems are therefore good candidates for anchoring our methodology and validity of the selection rules.

Chapter 6

Monolayer and bilayer graphene

In this chapter we examine the effects of electronic interactions on monolayer and Bernal bilayer honeycomb membrane of carbon atoms, and verify the applicability of the selection rules, outlined in the previous chapter. Monolayer and bilayer graphene (MLG and BLG respectively) are endowed with *identical* microscopic symmetries, described by the group D_{3d} (see Fig. 6.2). However, while MLG hosts linearly dispersing Dirac fermions as its low-energy excitations, BLG in comparison exhibits quadratically dispersing quasiparticles. This provides a unique opportunity to separate the role of the normal state band structure in the selection rules.

To briefly and schematically summarize our main findings, here we focus on generic short-range or local, but *repulsive* four-fermion interactions and construct various cuts of the phase diagram for MLG and BLG at zero and finite temperature and chemical doping by performing an unbiased leading-order renormalization group analysis in the spirit of appropriate ϵ expansions. Typically, these cuts show excitonic orders at zero chemical doping, among which charge density wave, antiferromagnet, quantum anomalous and spin Hall insulators, and various nematic and smectic liquids are the dominant ones. Often insulators (such as, antiferromagnet) are realized at the lowest temperature, while their nodal counterparts (such as, nematic and smectic orders) nucleate at a relatively higher temperature. On the other hand, as the the chemical doping is tuned away from the band touching points some pairing order sets in at the lowest temperature that maximally gaps the underlying Fermi surface, following the spirit of the Kohn-Luttinger mechanism [72, 73]. These findings are in qualitative agreement with the proposed organizing principle.

To relate our findings to a more experimentally feasible scenario, we construct the phase diagram of (un)doped MLG and BLG, when electrons therein interact with each other only through on site, nearest neighbor, and next-nearest neighbor Hubbard repulsion. Specifically for on site repulsion our results are shown in Fig. 6.1, whereas a detailed discussion follows in Sec. 6.4. At zero doping both systems support antiferromagnetic ordering. However, at finite doping while a spin-singlet *nematic* pairing develops in MLG at the lowest temperature, in doped BLG the paired state represents a translational symmetry breaking spin-singlet Kekulé superconductor. It is an example of a commensu-

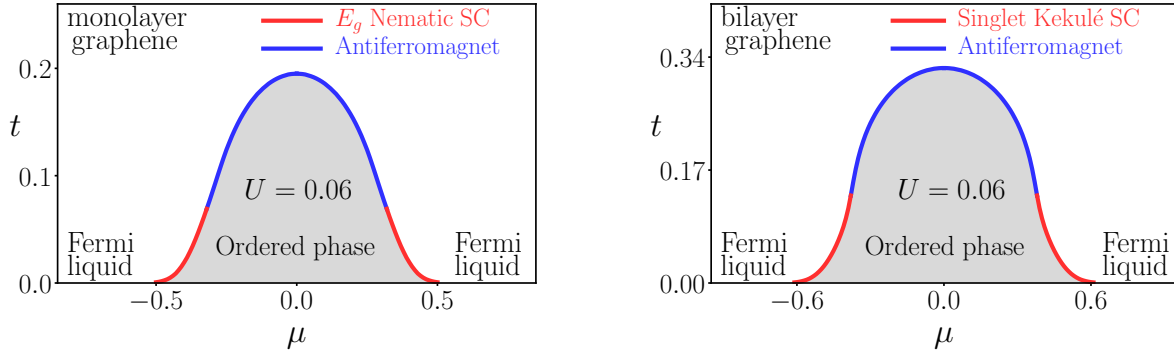


Figure 6.1: Phase diagrams of the Hubbard model, obtained from a RG analysis in (a) MLG and (b) BLG for a fixed strength of onsite Hubbard repulsion (U) as a function of temperature (t) and chemical doping (μ), respectively measured from the linear and biquadratic band touching points. All the quantities U , t and μ are dimensionless (see text for definition). The white region represents disordered chiral Fermi liquid and semimetal at finite and zero doping, respectively, and the gray region depicts an ordered state. Along the phase boundary between them, the system supports an antiferromagnet at and near, and a superconductor (SC) away from the half-filling ($\mu = 0$). Nature of the SC is mentioned in each panel. Realizations of distinct paired states in MLG and BLG solely stem from the distinct normal state band structures in these two systems. Inside the ordered state, one expects a regime of coexistence between antiferromagnet and the adjacent SC, due to their internal $O(5)$ symmetry, with pure phases on either side of it. Our RG analysis, however, cannot capture such coexistence, which nevertheless can be demonstrated from a standard mean-field analysis [142]. Here, $\mu > 0$ ($\mu < 0$) correspond to electron (hole) doped systems. Figure adapted from Ref. [13].

rate Fulde-Ferrell-Larkin-Ovchinnikov pairing [143, 144], also known as pair-density-wave. These findings are in agreement with the proposed selection rules. Our predictions can be experimentally tested on cold atomic systems, for example, where both MLG and BLG have been engineered, and both doping and the strength of the on site Hubbard repulsion can be tuned efficiently [145–148]. In addition, electronic BLG supports various ordered phases near the half filling that include both insulating and gapless (possibly nematic) states [149–154]. Therefore, increasing the carrier density by applying an external gate voltage one can, at least in principle, induce superconductivity in such systems, where our predictions can be tested directly. The present discussion provides new insight into the global phase diagram of the extended honeycomb Hubbard model in (un)doped MLG and BLG, that remained unnoticed despite the vast existing literature on this topic [11, 12, 15, 17, 19, 67, 70, 155–203].

6.1 Lattice models

In this section we introduce single-particle tight binding descriptions of electrons on the honeycomb monolayer and bilayer. Our model includes only NN hopping for MLG. But,

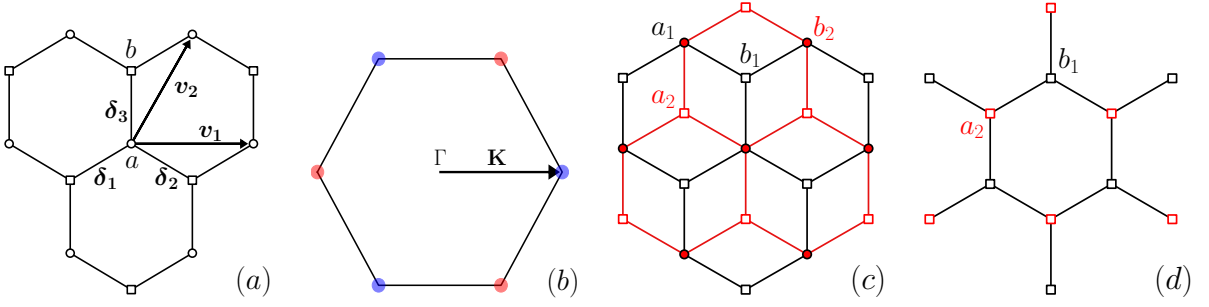


Figure 6.2: (a) Honeycomb monolayer, consisting of two interpenetrating triangular sublattices, A and B. The primitive lattice vectors \mathbf{v}_1 and \mathbf{v}_2 span the a sites (belonging to sublattice A). The b sites (belonging to sublattice B) are generated by linear combinations of $\boldsymbol{\delta}_1$, $\boldsymbol{\delta}_2$ and $\boldsymbol{\delta}_3$. (b) The BZ of MLG, a hexagonal structure rotated by 90 degrees compared to the real space lattice. Six Dirac points are located at its corners, of which two sets are inequivalent, marked with blue and red circles. The representative inequivalent valleys are chosen to be at \mathbf{K} and $-\mathbf{K}$, respectively. (c) Bernal stacked honeycomb bilayer, with the subscript denoting the layer index $i = 1, 2$ of the sites. Each a_1 and b_2 sites overlap. The eigenstates of the high energy split-off bands reside dominantly on these overlapping dimer sites. (d) After integrating out the a_1 and b_2 sites, the resulting structure is another honeycomb lattice, demonstrating the identical point group symmetry of MLG and BLG. Figure adapted from Ref. [13].

in order to capture the coupling between two layers, we incorporate interlayer hopping terms in BLG, besides the intralayer one. In what follows we restrict ourselves to carbon-based honeycomb lattices, and as such will completely neglect spin-orbit coupling, which is extremely small for carbon atoms [10].

6.1.1 Monolayer graphene

The simplest tight-binding Hamiltonian for an isolated sheet of graphene describes a bipartite lattice consisting of two interpenetrating triangular sublattices A and B with the NN hopping amplitude (t) as [8, 9]

$$H_{\text{MLG}} = t \sum_{\mathbf{A}, i} a^\dagger(\mathbf{A}) b(\mathbf{A} + \boldsymbol{\delta}_i) + \text{H.c.}, \quad (6.1)$$

where $a(\mathbf{A})$ are fermion annihilation operators on the A sublattice, generated by linear combinations of the primitive lattice vectors $\mathbf{v}_1 = \sqrt{3}a(1, 0)$ and $\mathbf{v}_2 = a/2(\sqrt{3}, 3)$, with a being the distance between neighboring atoms. On the other hand, $b(\mathbf{B})$ are fermion annihilation operators on the sites belonging to the B sublattice that are obtained as $\mathbf{B} = \mathbf{A} + \boldsymbol{\delta}_i$, with $\boldsymbol{\delta}_1 = a/2(-\sqrt{3}, -1)$, $\boldsymbol{\delta}_2 = a/2(\sqrt{3}, -1)$ and $\boldsymbol{\delta}_3 = a(0, 1)$, see Fig. 6.2(a). The reciprocal vectors are given by $\mathbf{q}_1 = 2\pi/a(1/\sqrt{3}, -1/3)$ and $\mathbf{q}_2 = 4\pi/a(0, 1/3)$. The BZ has the same hexagonal structure as the real space lattice, only rotated by 90 degrees. For convenience we shift the origin of the BZ to the middle of the hexagon (the Γ point), see Fig. 6.2(b).

The lack of the inversion symmetry of the honeycomb lattice about any given site [see Fig. 6.2(a)] results in Fermi points in the band structure of H_{MLG} instead of an extended Fermi surface, as obtained on a square lattice, for example. The spectra of H_{MLG} read

$$\epsilon_{\mathbf{k}}^{\text{MLG}} = \pm t |f(\mathbf{k})|, \quad (6.2)$$

where

$$f(\mathbf{k}) = \sum_{i=1,2,3} \exp(\mathbf{k} \cdot \boldsymbol{\delta}_i), \quad (6.3)$$

and $f(\mathbf{k})$ vanishes linearly at the six corners of the BZ [8]. Thus, $\epsilon_{\mathbf{k}}^{\text{MLG}}$ supports six Dirac points, around which the low energy dispersion is linear and isotropic [204]. However, only two of these band touching points are inequivalent, which we take to be at $\pm \mathbf{K}$, with $\mathbf{K} = \pm \frac{4\pi}{3\sqrt{3}a}(1, 0)$. The rest are connected to these two by primitive reciprocal vectors [9].

6.1.2 Bilayer graphene

One generates the Bernal stacked BLG by adding another graphene sheet on top of Fig. 6.2(a) and shifting it by e.g. $-\boldsymbol{\delta}_3$, see Fig. 6.2(c). Due to the two layers the minimal model has twice as many degrees of freedom when compared to MLG. We denote the layer index (i) with a subscript on the annihilation (a_i and b_i) and creation (a_i^\dagger and b_i^\dagger) operators, where $i = 1, 2$. The tight-binding Hamiltonian including intralayer and interlayer hopping terms is of the form [18, 19]

$$H_{\text{BLG}} = H^\parallel + H_{AB}^\perp + H_{AA}^\perp + H_{BB}^\perp, \quad (6.4)$$

where

$$\begin{aligned} H^\parallel &= t_\parallel \sum_{\mathbf{A}, i} \left[a_1^\dagger(\mathbf{A}) b_1(\mathbf{B}_i^+) + b_2^\dagger(\mathbf{A}) a_2(\mathbf{B}_i^-) \right] + \text{H.c.}, \\ H_{AB}^\perp &= t_\perp \sum_{\mathbf{A}} a_1^\dagger(\mathbf{A}) b_2(\mathbf{A}) + \text{H.c.}, \\ H_{AA}^\perp &= t_{AA} \sum_{\mathbf{A}, i} a_1^\dagger(\mathbf{A}) a_2(\mathbf{A} - \boldsymbol{\delta}_i) + \text{H.c.}, \\ H_{BA}^\perp &= t_{BA} \sum_{\mathbf{B}, i} b_1^\dagger(\mathbf{B}) a_2(\mathbf{B} + \boldsymbol{\delta}_i) + \text{H.c.} \end{aligned} \quad (6.5)$$

Here H^\parallel describes the intralayer NN hopping, where $\mathbf{B}_i^\pm = \mathbf{A} \pm \boldsymbol{\delta}_i$, while the remaining terms encompass the interlayer ones. The terms H_{AA}^\perp and H_{BA}^\perp represent remote interlayer hopping processes, which we will drop from now on. The direct hopping between the dimer sites (a_1 and b_2) is captured by H_{AB}^\perp . After setting $t_{AA} = t_{BA} = 0$, the spectra of H_{BLG}

describe four bands with the dispersions

$$\epsilon_{1,\mathbf{k}}^{\text{BLG}} = \pm \frac{t_{\parallel}^2}{2t_{\perp}} |f(\mathbf{k})|^2, \quad (6.6)$$

$$\epsilon_{2,\mathbf{k}}^{\text{BLG}} = \pm \frac{1}{\sqrt{2}} \sqrt{4t_{\parallel}^2 |f(\mathbf{k})|^2 + t_{\perp}^2 + \mathcal{O}(|f(\mathbf{k})|^4)}. \quad (6.7)$$

Since $f(\mathbf{k})$ vanishes linearly at $\pm \mathbf{K}$, $\epsilon_{1,\mathbf{k}}^{\text{BLG}}$ describes two *quadratic* band touchings, whereas the two $\epsilon_{2,\mathbf{k}}^{\text{BLG}}$ bands are gapped everywhere, also called the split-off bands. Note that H_{BA}^{\perp} produces trigonal warping that splits each quadratic band touching into four Dirac points [155]. In Sec. 6.5, we qualitatively discuss the role of trigonal warping on the phase diagrams of interacting electrons in BLG.

In this chapter we study these two systems in terms of their low-energy effective theories. As the continuum models are well established within the scientific literature [10], in presenting the respective single particle descriptions we will only quote the cornerstones of the derivations.

6.2 Low-energy effective theory

We formulate the effective continuum theories by retaining the low energy degrees of freedom of both lattice models, Eqs. (6.1) and (6.5). As the split-off bands in BLG are at higher energies, and the eigenfunctions of $\epsilon_{2,\mathbf{k}}^{\text{BLG}}$ are dominantly localized on the overlapping a_1 and b_2 sites, we can project out these bands with relative ease [10, 18, 19]. After integrating out the a_1 and b_2 sites, the resulting lattice assumes another honeycomb structure, see Fig. 6.2(d). As such, the effective BZ has the same structure as that of MLG, with the important distinction that the band touching at the six corners are now *quadratic*, in comparison to the linear band touching in MLG. Moreover, the microscopic symmetries of these two models (reflections, translation, and time reversal) are identical, about which more in a moment. Consequently, the part of the action describing local electron-electron interactions takes identical form in these two systems, see Sec. 6.2.3. This allows us to investigate the role of the normal state band structure in emergent phases within the same symmetry group.

Due to the small atomic number of carbon atoms we neglect the spin-orbit coupling in both MLG and BLG, and introduce the spin degree of freedom as a mere doubling of the Hamiltonian. Besides spin, we will also introduce a particle-hole index using the Nambu doubling, which facilitates the inclusion of both excitonic and superconducting phases within a unified framework. Note that the split-off bands now being projected out, the two effective models have the equal number of low energy degrees of freedom.

6.2.1 Non-interacting models

Let us add a spin index to the fermionic degrees of freedom and expand the fields in terms of their Fourier components as

$$r_s(\tau, \mathbf{r}) = \int \frac{d\omega}{2\pi} \int \frac{d^2\mathbf{k}}{(2\pi)^2} e^{i(\omega\tau + \mathbf{k}\cdot\mathbf{r})} r_s(\omega, \mathbf{k}), \quad (6.8)$$

where τ and ω are respectively imaginary time and frequency, $r = a$ and b for electrons on the A and B sublattices, respectively, with the spin orientation $s = \uparrow, \downarrow$. We retain the modes near the two inequivalent valleys at $\pm\mathbf{K}$, and write $r_s(\omega, \pm\mathbf{K} + \mathbf{k}) = r_s^{\pm\mathbf{K}}(\omega, \mathbf{k})$. The eight-component spinor in Fourier space is then structured according to

$$\Psi_{\omega, \mathbf{k}} = [c_{\uparrow}^{+\mathbf{K}}, c_{\uparrow}^{-\mathbf{K}}, c_{\downarrow}^{+\mathbf{K}}, c_{\downarrow}^{-\mathbf{K}}]^{\top}, \quad \text{where } c_s^v = [a_s^v, b_s^v], \quad (6.9)$$

and r_s^v are annihilation operators for fermions on the A and B sublattices with valley index $v = \pm\mathbf{K}$, and spin projection $s = \uparrow, \downarrow$. Here \top denotes transposition. Finally, we introduce the particle-hole degree of freedom as the ‘‘outermost’’ index and write a sixteen-component Nambu doubled spinors as

$$\Psi_{\omega, \mathbf{k}} \rightarrow \Psi_{\text{Nam}} = \begin{pmatrix} \Psi_{\omega, \mathbf{k}} \\ \Gamma_{210} \Psi_{-\omega, -\mathbf{k}}^* \end{pmatrix}, \quad (6.10)$$

where in the lower block we absorbed the unitary part of the time reversal operator $U = \Gamma_{210}$ [see Sec. 6.2.2], so that $\Psi_{\omega, \mathbf{k}}$ and Ψ_{Nam} transform identically under all symmetries. For the sake of brevity we suppress the subscript ‘‘Nam’’ from now on, and unless otherwise mentioned, thus $\Psi \equiv \Psi_{\text{Nam}}$ and $\Psi^\dagger \equiv \Psi_{\text{Nam}}^\dagger$.

To capture the symmetry properties of MLG and BLG, and subsequently develop the interacting models describing these two systems, we write the matrices acting on the sixteen-dimensional spinors as $\Gamma_{\mu\nu\lambda\rho} = \eta_\mu \otimes \sigma_\nu \otimes \tau_\lambda \otimes \alpha_\rho$ where $\{\alpha\}$, $\{\tau\}$, $\{\sigma\}$ and $\{\eta\}$ are four sets of Pauli matrices that operate on the sublattice or layer, valley, spin and particle-hole degrees of freedom, respectively. Here, $\mu, \nu, \lambda, \rho = 0, 1, 2, 3$, and the index 0 always corresponds to the unit matrix. In Eq. (6.10), $\Gamma_{210} = \sigma_2 \otimes \tau_1 \otimes \alpha_0$. Note that having integrated out the overlapping a_1 and b_2 sites in BLG, the sublattice and layer description is now redundant, as all the remaining a and b sites reside on layer 2 and 1, respectively. Therefore, from now on we refer to this degree of freedom simply as sublattice. Also note that by virtue of writing all sixteen-dimensional matrices in terms of Kronecker products of Pauli matrices, any two such matrices either commute or anticommute.

The non-interacting effective low-energy theory of MLG is composed of linearly dispersing chiral relativistic Dirac fermions, that persist all the way up to a non-universal ultraviolet momentum cutoff $\Lambda \sim 1/a$. In comparison, the corresponding effective theory of BLG is constituted by quadratically dispersing chiral quasiparticles (also up to a ul-

traviolet momentum cutoff Λ , determined by the energy of the split-off bands). We write the Hamiltonians for MLG and BLG respectively as

$$\hat{h}^D(\mathbf{k}) = v \left[\Gamma_{3031} p_1(\mathbf{k}) - \Gamma_{3002} p_2(\mathbf{k}) \right] - \mu \Gamma_{3000}, \quad (6.11)$$

$$\hat{h}^L(\mathbf{k}) = \frac{1}{2m} \left[\Gamma_{3001} d_1(\mathbf{k}) - \Gamma_{3032} d_2(\mathbf{k}) \right] - \mu \Gamma_{3000}, \quad (6.12)$$

where $v = ta$ is the Fermi velocity and $m = t_{\perp}/(2t_{\parallel}^2 a^2)$ is the effective mass. The momentum-dependence is described by the p -wave and d -wave cubic harmonics, that are related to the spherical harmonics Y_l^m with $l = 1$ and $l = 2$, respectively, such that

$$\begin{aligned} p_1(\mathbf{k}) &= k_x, & p_2(\mathbf{k}) &= k_y, \\ d_1(\mathbf{k}) &= k_x^2 - k_y^2, & d_2(\mathbf{k}) &= 2k_x k_y. \end{aligned} \quad (6.13)$$

We also introduced a chemical potential (μ) term, which facilitates tuning the Fermi energy to and away from the band touching points. Therefore, μ plays the analogous role as the gate voltage. Here we only consider electron like doping ($\mu > 0$). All the conclusions are equally germane for hole-doped ($\mu < 0$) systems. The chemical doping develops an extended (one-dimensional) Fermi surface from the (zero-dimensional) Fermi points, and increases the carrier density, which is conducive for the condensation of electrons into Cooper pairs. In analogy with the three-dimensional system, the quadratic fermions constituting the low-energy excitations of BLG are called Luttinger fermions.

The above models then constitutes the following non-interacting Euclidean (imaginary time) action

$$S_0^j = \int d\tau d^d \mathbf{r} \Psi^\dagger(\tau, \mathbf{r}) \left[\partial_\tau + \hat{h}^j(\mathbf{k} \rightarrow -i\nabla) \right] \Psi(\tau, \mathbf{r}), \quad (6.14)$$

with $j = D$ and L respectively for MLG and BLG. Here d is the spatial dimensionality, $\Psi^\dagger(\tau, \mathbf{r})$ and $\Psi(\tau, \mathbf{r})$ are the inverse Fourier transform of the spinors Ψ^\dagger and Ψ , and τ is the imaginary time.

6.2.2 Symmetries and action

The microscopic symmetries of the honeycomb monolayer and bilayer are identical and correspond to the D_{3d} point group. Here we cast these symmetries in terms of reflections and rotations, and show how they manifest in the low-energy theory. We augment the point group symmetries with translation invariance, discrete time reversal symmetry, as well as continuous spin $SU(2)$ and pseudospin $SU_p(2)$ rotational invariances.

The two reflection symmetries of the honeycomb lattice are sublattice (S) and valley

(T) reflections [11]. They respectively take the form

$$S = \Gamma_{0001} \oplus \begin{pmatrix} k_x \rightarrow k_x \\ k_y \rightarrow -k_y \end{pmatrix}, \quad (6.15)$$

and

$$T = \Gamma_{0010} \oplus \begin{pmatrix} k_x \rightarrow -k_x \\ k_y \rightarrow k_y \end{pmatrix}. \quad (6.16)$$

Reflection S exchanges the sublattices $A \leftrightarrow B$, but leaves the valleys invariant. Whereas under T , $\mathbf{K} \leftrightarrow -\mathbf{K}$, and hence it exchanges the Dirac points, but does not affect the sublattice degree of freedom.

Both the linear and quadratic band touching points are rotationally invariant at low energies. Let us denote the orbitals as $v_i = p_i$ or d_i for $i = 1, 2$. Then, rotations by an angle θ in orbital space take the form $R(\theta) = \exp(i\theta\Gamma_{0033}/2)$, and a rotation of the Hamiltonian corresponds to an ordinary vector rotation of the two-component vector $(v_1, v_2)^\top$

$$R(\theta)\hat{h}^j R^{-1}(\theta) \Leftrightarrow \begin{pmatrix} \cos \theta & -\sin \theta \\ \sin \theta & \cos \theta \end{pmatrix} \begin{pmatrix} v_1 \\ v_2 \end{pmatrix}. \quad (6.17)$$

For example, under rotation by $\theta = \pi/2$

$$R(\pi/2)\hat{h}^j R^{-1}(\pi/2) : \begin{pmatrix} v_1 \\ v_2 \end{pmatrix} \rightarrow \begin{pmatrix} -v_2 \\ v_1 \end{pmatrix}. \quad (6.18)$$

The corresponding rotation of momentum axes by an angle $\theta = -\pi/(2l)$ takes the form

$$\begin{pmatrix} k_x \\ k_y \end{pmatrix} \rightarrow \begin{pmatrix} \cos \theta & -\sin \theta \\ \sin \theta & \cos \theta \end{pmatrix} \begin{pmatrix} k_x \\ k_y \end{pmatrix}, \quad (6.19)$$

where the angular momentum $l = 1$ and 2 for p and d orbitals, respectively. The requisite rotation by the angle $\theta = -\pi/(2l)$ for the invariance of the Hamiltonian indicates that respectively the linear and biquadratic band touching represent momentum space vortices of vorticity l , and the wave functions of the valence and conduction bands are eigenstates of orbital angular momentum l .

Translation by a vector \mathbf{R} acts on the electron fields as

$$r_s(\omega, \mathbf{k}) \rightarrow e^{i\mathbf{k}\cdot\mathbf{R}} r_s(\omega, \mathbf{k}). \quad (6.20)$$

Therefore the matrix transforming the 16-component Nambu spinors under translation has to pick up opposite signs at the valleys at $\pm\mathbf{K}$. A translation of the spinor Ψ is then

written as

$$\Psi(\omega, \mathbf{k}) \rightarrow e^{i\mathbf{K}\cdot\mathbf{R}} \Gamma_{0030} e^{i\mathbf{k}\cdot\mathbf{R}} \Psi(\omega, \mathbf{k}), \quad (6.21)$$

with Γ_{0030} being the generator of translations. The above transformation in real space reads

$$\Psi(\tau, \mathbf{r}) \rightarrow e^{i\mathbf{K}\cdot\mathbf{R}} \Gamma_{0030} \Psi(\tau, \mathbf{r} + \mathbf{R}). \quad (6.22)$$

The reversal of time is implemented by the antiunitary operator $\mathcal{T} = UK$. Here $U = \Gamma_{0210}$ is a unitary operator and \mathcal{K} is complex conjugation. For spin-1/2 electrons, we indeed find $\mathcal{T}^2 = -1$.

The Hamiltonian operators in Eqs. (6.11) and (6.12) are manifestly invariant under $SU(2)$ spin rotations, generated by Γ_{0s00} , with $s = \{1, 2, 3\}$. Finally, the pseudospin $SU_p(2)$ transformations are generated by $\{\Gamma_{3000}, \Gamma_{1003}, \Gamma_{2003}\}$. Here Γ_{1003} and Γ_{2003} rotate between an excitonic (such as, charge density wave) and two (real and imaginary) components of a paired state (such as, s -wave pairing). While the number operator Γ_{3000} rotates the $U(1)$ superconducting phase [123]. See Tables 6.1 and 6.2. Having established the non-interacting continuum model and the operative symmetries, in the next section we build on this foundation and examine the effects of electron-electron interactions.

6.2.3 Electron-electron interactions

We incorporate *short range* or *local* electron-electron interactions by adding all symmetry-allowed momentum-independent four fermion terms to the action S_0^j . The schematic form of the interacting part of the action in the presence of such a local quartic term is

$$S_{\text{int}} = \int d\tau d^d \mathbf{r} L_{\text{int}} \equiv \int d\tau d^d \mathbf{r} g_{MN} (\Psi^\dagger M \Psi)(\Psi^\dagger N \Psi), \quad (6.23)$$

where $\Psi \equiv \Psi_{\tau, \mathbf{r}}$ and $\Psi^\dagger \equiv \Psi_{\tau, \mathbf{r}}^\dagger$, M and N are 16 dimensional (in the Nambu doubled basis) Hermitian matrices, and g_{MN} is the corresponding coupling constant. Note from Eq. (6.14) the scaling dimension of the spinors is $[\Psi_{\tau, \mathbf{r}}^\dagger] = [\Psi_{\tau, \mathbf{r}}] = d/2$, such that S_0^j is scale invariant for $j = D$ and L . Consequently, a coupling constant of local quartic terms scales as $[g_{MN}] = z - d$, where z is the dynamical scaling exponent, determining the relative scaling between energy and momentum according to $\epsilon_{\mathbf{k}} \sim |\mathbf{k}|^z$. Therefore $z = 1$ (2) in case of Dirac (Luttinger) fermions. Consequently, S_{int} remains scale invariant. As $d = 2$, sufficiently weak short range electron-electron interactions among two-dimensional Dirac fermions are *irrelevant*, and the Dirac cones remain stable up to a critical strength of interactions, where, however, the system undergoes a quantum phase transition into an ordered phase. On the other hand, in a two-dimensional system of Luttinger fermions local quartic interactions are *marginal*, and the quadratic band touching point is unstable

in the presence of infinitesimal interactions. In terms of the density of states (DoS), the Dirac system exhibits linearly vanishing DoS, namely $\rho(E) \sim |E|$, while in the case of Luttinger fermions the low-energy DoS is constant i.e., $\rho(E) \sim \text{constant}$. The scaling of the DoS determines the (ir)relevance of local interactions.

Throughout we neglect the long range tail of the Coulomb interaction. In an undoped Dirac liquid, the long range Coulomb interaction is a *marginally irrelevant* coupling (due to the vanishing DoS), irrespective of its bare strength, that otherwise causes only a logarithmic enhancement of the Fermi velocity [12, 109, 112, 205–211]. On the other hand, in undoped Luttinger liquid long range Coulomb interaction gets screened due to the finite DoS, resulting in local density-density interaction, thus only renormalizing the bare strength of the coupling g_1^s [156] [see Eq. (6.25)]. At finite temperature this approximation is further justified due to the thermal screening [94], while at finite doping conventional Thomas-Fermi screening sets in. Nevertheless, long-range Coulomb interaction can shift the phase boundaries between the ordered and disordered phases, without altering the nature of the former one, as has been shown for both two- and three-dimensional Dirac liquids [111, 113].

All the local quartic terms appearing in the interacting Lagrangian must transform as scalars under all operative symmetries introduced in Sec. 6.2.2, which severely restricts the number of couplings constants to 18. The interacting Lagrangian (L_{int}) containing all symmetry-allowed local quartic terms reads [11]

$$L_{\text{int}} = L_{\text{int}}^{\text{sing}} + L_{\text{int}}^{\text{trip}}, \quad (6.24)$$

where

$$\begin{aligned} L_{\text{int}}^{\text{sing}} &= g_1^s (\Psi^\dagger \Gamma_{3000} \Psi)^2 + g_2^s (\Psi^\dagger \Gamma_{0033} \Psi)^2 + g_3^s \left[(\Psi^\dagger \Gamma_{3001} \Psi)^2 + (\Psi^\dagger \Gamma_{3032} \Psi)^2 \right] \\ &+ g_4^s (\Psi^\dagger \Gamma_{0030} \Psi)^2 + g_5^s (\Psi^\dagger \Gamma_{3003} \Psi)^2 + g_6^s \left[(\Psi^\dagger \Gamma_{0031} \Psi)^2 + (\Psi^\dagger \Gamma_{0002} \Psi)^2 \right] \\ &+ \sum_{j=1}^2 \left\{ g_7^s (\Psi^\dagger \Gamma_{30j1} \Psi)^2 + g_8^s (\Psi^\dagger \Gamma_{00j2} \Psi)^2 + g_9^s \left[(\Psi^\dagger \Gamma_{30j0} \Psi)^2 + (\Psi^\dagger \Gamma_{30j3} \Psi)^2 \right] \right\}, \\ L_{\text{int}}^{\text{trip}} &= \sum_{s=1}^3 \left[g_1^t (\Psi^\dagger \Gamma_{0s00} \Psi)^2 + g_2^t (\Psi^\dagger \Gamma_{3s33} \Psi)^2 + g_3^t \left[(\Psi^\dagger \Gamma_{0s01} \Psi)^2 + (\Psi^\dagger \Gamma_{0s32} \Psi)^2 \right] \right. \\ &+ g_4^t (\Psi^\dagger \Gamma_{3s30} \Psi)^2 + g_5^t (\Psi^\dagger \Gamma_{0s03} \Psi)^2 + g_6^t \left[(\Psi^\dagger \Gamma_{3s31} \Psi)^2 + (\Psi^\dagger \Gamma_{3s02} \Psi)^2 \right] \\ &\left. + \sum_{j=1}^2 \left\{ g_7^t (\Psi^\dagger \Gamma_{0sj1} \Psi)^2 + g_8^t (\Psi^\dagger \Gamma_{3sj2} \Psi)^2 + g_9^t \left[(\Psi^\dagger \Gamma_{0sj0} \Psi)^2 + (\Psi^\dagger \Gamma_{0sj3} \Psi)^2 \right] \right\} \right]. \quad (6.25) \end{aligned}$$

Visibly, L_{int} separates into spin singlet ($L_{\text{int}}^{\text{sing}}$) and spin triplet ($L_{\text{int}}^{\text{trip}}$) parts, containing the matrices σ_0 and σ_s (with $s = 1, 2, 3$), acting on the spin index, respectively. The sublattice and valley degrees of freedom (accompanied by α and τ matrices, respectively) repeat for the two irreducible representations of the SU(2) spin algebra, while the particle-

hole index (η matrix) is exactly the opposite between singlet and triplet channels. Since there is only one operative SU(2) algebra in the spin sector, this suggests a redundancy in the above expression of the interacting Lagrangian. This expectation can be verified using the Fierz identity for eight-dimensional Hermitian matrices (note the particle-hole degree of freedom in this sense is an artificial doubling), see Sec. 2.2.1. After Fierz reduction there are only nine linearly independent four fermion terms, which we choose, without the loss of generality, to be the spin singlet interactions (g_i^s). For a detailed presentation of the Fierz reduction see Appendix C.3.2. Throughout, here we focus on repulsive electron-electron interactions, which in our notation corresponds to $g_\mu^j > 0$ for $\mu = 1, \dots, 9$ and $j = s, t$.

To shed light on the structure of the global phase diagram of interacting two-dimensional Dirac and Luttinger fermions, we perform Wilsonian momentum shell RG analysis at zero, as well as finite temperature (T) and chemical potential (μ), following the steps outlined in Sec. 2.2. We already established the scaling of the coupling constants to be $[g_\mu^j] = z - d$, which pins the lower critical dimension of the corresponding theories at $d = z$ and facilitates an ϵ expansion around the marginal dimensionality with $\epsilon = d - z$ [103, 120, 121]. Notice that the physical values of ϵ are 1 and 0 for two-dimensional Dirac and Luttinger fermions, respectively. However, our conclusions are insensitive to the exact value of ϵ , except the nonuniversal locations of the phase boundaries between the ordered and disordered phases.

We introduce the dimensionless temperature and chemical potential the usual way, e.g. $t = T/\epsilon_\Lambda$ and $\tilde{\mu} = \mu/\epsilon_\Lambda$, where ϵ_Λ is again the quasiparticle energy evaluated at the ultraviolet cutoff Λ . These quantities respectively for Dirac (D) and Luttinger (L) systems then read

$$\begin{aligned} t^{\text{D}} &= T/(\Lambda v), & t^{\text{L}} &= 2mT/\Lambda^2, \\ \tilde{\mu}^{\text{D}} &= \mu/(\Lambda v), & \tilde{\mu}^{\text{L}} &= 2m\mu/\Lambda^2. \end{aligned} \quad (6.26)$$

From now on we omit the tilde and denote the dimensionless chemical potential by μ . Furthermore, for brevity we suppress the D and L indices.

The scaling dimensions of these two *relevant* parameters are $[t] = [\mu] = z$, and their RG flows are described by Eqs. (2.35) and (2.36). Furthermore, we again summarize the flow equations of the coupling constants in the schematic way

$$\frac{dg_i^s}{d\ell} = -\epsilon g_i^s + \sum_{j,k} g_j^s g_k^s H_{jk}^i(t, \mu). \quad (6.27)$$

The coupling constants appearing in the RG flow equations are also dimensionless, obtained by taking $g_\mu^s \Lambda^\epsilon/(4\pi) \rightarrow g_\mu^s$. For the exact form of the functions $H_{jk}^i(t, \mu)$ see Appendix C.3.3. Eq. (6.27) implies that all orderings take place at critical couplings $g_i^s \sim \epsilon$, which is consistent with our observation of local interactions being irrelevant

SB	IREP (D_{3d})	Matrix (N)	S	T	tl	$R(\frac{\pi}{2})$	TR	SU(2)	SU _p (2)
A_{1g}^s	A_{1g}	Γ_{3000}	+	+	+	0	+	0	
A_{2g}^s	A_{2g}	Γ_{0033}	-	-	+	0	-	0	
E_g^s	E_g	$\Gamma_{3001}, \Gamma_{3032}$	+, -	+, -	+, +	1	+, +	0	
A_{1u}^s	A_{1u}	Γ_{0030}	+	-	+	0	-	0	
A_{2u}^s	A_{2u}	Γ_{3003}	-	+	+	0	+	0	I
E_u^s	E_u	$\Gamma_{0031}, \Gamma_{0002}$	+, -	-, +	+, +	1	-, -	0	III
A_{1k}^s	A_{1k}	$\Gamma_{3011}, \Gamma_{3021}$	+, +	+, -	-, -	0	+, +	0	
A_{2k}^s	A_{2k}	$\Gamma_{0012}, \Gamma_{0022}$	-, -	+, -	-, -	0	-, -	0	VI
E_k^s	E_k	$\Gamma_{3010}, \Gamma_{3023}$ $\Gamma_{3013}, \Gamma_{3020}$	+, - -, +	+, - +, -	-, - -, -	1 1	+, + +, +	0	V
A_{1g}^t	A_{1g}	Γ_{0s00}	+	+	+	0	-	1	
A_{2g}^t	A_{2g}	Γ_{3s33}	-	-	+	0	+	1	II
E_g^t	E_g	$\Gamma_{0s01}, \Gamma_{0s32}$	+, -	+, -	+, +	1	-, -	1	IV
A_{1u}^t	A_{1u}	Γ_{3s30}	+	-	+	0	+	1	
A_{2u}^t	A_{2u}	Γ_{0s03}	-	+	+	0	-	1	
E_u^t	E_u	$\Gamma_{3s31}, \Gamma_{3s02}$	+, -	-, +	+, +	1	+, +	1	
A_{1k}^t	A_{1k}	$\Gamma_{0s11}, \Gamma_{0s21}$	+, +	+, -	-, -	0	-, -	1	VII
A_{2k}^t	A_{2k}	$\Gamma_{3s12}, \Gamma_{3s22}$	-, -	+, -	-, -	0	+, +	1	
E_k^t	E_k	$\Gamma_{0s10}, \Gamma_{0s23}$ $\Gamma_{0s13}, \Gamma_{0s20}$	+, - -, +	+, - +, -	-, - -, -	1 1	-, - -, -	1	

Table 6.1: Symmetry properties of the local excitonic order parameters of the schematic form $\Delta_N(\Psi^\dagger N \Psi)$ on the honeycomb lattice, where N is a sixteen-dimensional Hermitian matrix with $s = \{1, 2, 3\}$ and $\alpha = \{1, 2\}$. The first (second) nine rows correspond to spin singlet (triplet) orders. The first three columns respectively display the symbol by which an order is referred to in Figs. 6.3-6.6, the corresponding irreducible representation of the D_{3d} group, and the order parameter matrices N . Columns 4-10 display transformation properties of the fermion bilinears under sublattice (S) and valley (T) reflections, translation (tl), orbital rotation [$R(\pi/2)$], time reversal (TR), and spin SU(2) and pseudospin SU_p(2) rotations, respectively. Here + (-) means even (odd), whereas 0 (1) means the bilinear transform as scalar (vector) under the given rotation. The order parameters marked by the same roman numeral in the SU_p(2) column are related to each other by pseudospin SU_p(2) rotations, which always relates an excitonic order to a pairing one, see Table 6.2. Blue (yellow) coloring represent mass orders in MLG (BLG), while green indicates orders that are gapped in both systems.

and marginal in MLG and BLG, respectively. Therefore, in a Dirac system all orderings set in beyond a finite strength of the interactions, while a Luttinger system is conducive for ordering even for sufficiently weak interactions. Our methodology of detecting phase transitions follows Sec. 2.2.3 [119, 142, 157, 212]. In the next section we review the possible broken symmetry phases in MLG and BLG.

SB	IREP (D_{3d})	Matrix (N)	S	T	tl	$R_{\frac{\pi}{2}}$	TR	SU(2)	SU _p (2)
A_{1g}^p	A_{1g}	$\Gamma_{\alpha 000}$	+	+	+	0	+ (-)	0	I
A_{2g}^p	A_{2g}	$\Gamma_{\alpha s 33}$	-	-	+	0	+ (-)	1	
E_g^p	E_g	$\Gamma_{\alpha 001}, \Gamma_{\alpha 032}$	+, -	+, -	+, +	1	+, + (-, -)	0	III
A_{1u}^p	A_{1u}	$\Gamma_{\alpha s 30}$	+	-	+	0	+ (-)	1	II
A_{2u}^p	A_{2u}	$\Gamma_{\alpha 003}$	-	+	+	0	+ (-)	0	
E_u^p	E_u	$\Gamma_{\alpha s 31}, \Gamma_{\alpha s 02}$	+, -	-, +	+, +	1	+, + (-, -)	1	IV
A_{1k}^p	A_{1k}	$\Gamma_{\alpha 011}, \Gamma_{\alpha 021}$	+, +	+, -	-, -	0	+, + (-, -)	0	VI
A_{2k}^p	A_{2k}	$\Gamma_{\alpha s 12}, \Gamma_{\alpha s 22}$	-, -	+, -	-, -	0	+, + (-, -)	1	VII
E_k^p	E_k	$\Gamma_{\alpha 010}, \Gamma_{\alpha 023}$	+, -	+, -	-, -	1	+, + (-, -)	0	V
		$\Gamma_{\alpha 013}, \Gamma_{\alpha 020}$	-, +	+, -	-, -	1	+, + (-, -)		

Table 6.2: Symmetry properties of the local superconducting order parameters of the schematic form $\Delta_N(\Psi^\dagger N\Psi)$ on the honeycomb lattice, where N is a sixteen-dimensional Hermitian matrix with $s = \{1, 2, 3\}$ and $\alpha = \{1, 2\}$. The notation is identical to that in Tab. 6.1. In the TR column a symbol outside (within) parentheses corresponds to $\alpha = 1$ (2). The order parameters marked by the same roman numeral in the SU_p(2) column are related to each other by pseudospin SU_p(2) rotations, which always relates an excitonic order to a pairing one, see Table 6.1.

6.2.4 Broken symmetry phases

To identify the nature of the broken symmetry phase in an unbiased fashion we introduce all symmetry-allowed local fermion bilinears to the action, which assume the schematic form $\Delta_M(\Psi^\dagger M\Psi)$, where Δ_M is the corresponding conjugate field and M is a *sixteen*-dimensional Hermitian matrix. The ordered state is characterized by the expectation value of the fermion bilinear $\langle \Psi^\dagger M\Psi \rangle \neq 0$. Note while the RG analysis of the coupling constants g_i can be performed using eight-dimensional matrices (without invoking the Nambu doubling), one has to utilize the Nambu basis in the renormalization of order parameter fields to account for the superconducting channels. The effective single-particle Hamiltonian containing all symmetry allowed local orders reads

$$H_{\text{local}} = \int d^d \mathbf{r} (h_{\text{exc}} + h_{\text{pair}}), \quad (6.28)$$

where $h_{\text{exc}} = h_{\text{exc}}^{\text{sing}} + h_{\text{exc}}^{\text{trip}}$, with

$$h_{\text{exc}}^{\text{sing}} = \Delta_1^s \Psi^\dagger \Gamma_{3000} \Psi + \Delta_2^s \Psi^\dagger \Gamma_{0033} \Psi + \Delta_3^s \left(\Psi^\dagger \Gamma_{3001} \Psi + \Psi^\dagger \Gamma_{3032} \Psi \right) + \Delta_4^s \Psi^\dagger \Gamma_{0030} \Psi$$

$$\begin{aligned}
& + \Delta_5^s \Psi^\dagger \Gamma_{3003} \Psi + \Delta_6^s \left(\Psi^\dagger \Gamma_{0031} \Psi + \Psi^\dagger \Gamma_{0002} \Psi \right) + \sum_{j=1}^2 \left[\Delta_7^s \Psi^\dagger \Gamma_{30j1} \Psi + \Delta_8^s \Psi^\dagger \Gamma_{00j2} \Psi \right. \\
& \left. + \Delta_9^s \left(\Psi^\dagger \Gamma_{30j0} \Psi + \Psi^\dagger \Gamma_{30j3} \Psi \right) \right], \tag{6.29}
\end{aligned}$$

and

$$\begin{aligned}
h_{\text{exc}}^{\text{trip}} & = \sum_{s=1}^3 \left\{ \Delta_1^t \Psi^\dagger \Gamma_{0s00} \Psi + \Delta_2^t \Psi^\dagger \Gamma_{3s33} \Psi + \Delta_3^t \left(\Psi^\dagger \Gamma_{0s01} \Psi + \Psi^\dagger \Gamma_{0s32} \Psi \right) + \Delta_4^t \Psi^\dagger \Gamma_{3s30} \Psi \right. \\
& + \Delta_5^t \Psi^\dagger \Gamma_{0s03} \Psi + \Delta_6^t \left(\Psi^\dagger \Gamma_{3s31} \Psi + \Psi^\dagger \Gamma_{3s02} \Psi \right) + \sum_{j=1}^2 \left[\Delta_7^t \Psi^\dagger \Gamma_{0sj1} \Psi + \Delta_8^t \Psi^\dagger \Gamma_{3sj2} \Psi \right. \\
& \left. \left. + \Delta_9^t \left(\Psi^\dagger \Gamma_{0sj0} \Psi + \Psi^\dagger \Gamma_{0sj3} \Psi \right) \right] \right\}, \tag{6.30}
\end{aligned}$$

whereas

$$\begin{aligned}
h_{\text{pair}} & = \sum_{\alpha=1}^2 \left\{ \Delta_{1,\alpha}^p \Psi^\dagger \Gamma_{\alpha 000} \Psi + \Delta_{3,\alpha}^p \left(\Psi^\dagger \Gamma_{\alpha 001} \Psi + \Psi^\dagger \Gamma_{\alpha 032} \Psi \right) + \Delta_{5,\alpha}^p \Psi^\dagger \Gamma_{\alpha 003} \Psi \right. \\
& + \sum_{j=1}^2 \left[\Delta_{7,\alpha}^p \Psi^\dagger \Gamma_{\alpha 0j1} \Psi + \Delta_{9,\alpha}^p \left(\Psi^\dagger \Gamma_{\alpha 0j0} \Psi + \Psi^\dagger \Gamma_{\alpha 0j3} \Psi \right) \right] + \sum_{s=1}^3 \left[\Delta_{2,\alpha}^p \Psi^\dagger \Gamma_{\alpha s33} \Psi \right. \\
& \left. + \Delta_{4,\alpha}^p \Psi^\dagger \Gamma_{\alpha s30} \Psi + \Delta_{6,\alpha}^p \left(\Psi^\dagger \Gamma_{\alpha s31} \Psi + \Psi^\dagger \Gamma_{\alpha s02} \Psi \right) + \sum_{j=1}^2 \Delta_{8,\alpha}^p \Psi^\dagger \Gamma_{\alpha sj2} \Psi \right] \right\}. \tag{6.31}
\end{aligned}$$

Here $\alpha = 1, 2$, $\Delta_{i,1}^p = \Delta_i^p \cos \phi$, $\Delta_{i,2}^p = \Delta_i^p \sin \phi$, and ϕ is the U(1) superconducting phase. According to H_{local} , 27 order parameters are organized into three groups, each containing nine entries. Namely $h_{\text{exc}}^{\text{sing}}$ and $h_{\text{exc}}^{\text{trip}}$ contain nine spin singlet and nine spin triplet excitonic bilinears, respectively, while h_{pair} accommodates five singlet and four triplet pairing orders. The nomenclature for the interaction terms and order parameters is summarized in Tables 6.3 and 6.4, while physical properties of the fermion bilinears, e.g. their irreducible point group representations, and transformations under various discrete and continuous symmetries are displayed in Tables 6.1 and 6.2.

Besides the 9 independent coupling constants g_i^s we also renormalize the 27 order parameter fields from H_{local} and arrive at their β -functions taking the schematic form

$$\bar{\beta}_{\Delta_k}^j \equiv \frac{d\Delta_k}{d\ell} - z = \sum_l F_{k,l}^j(t, \mu) g_l^s, \tag{6.32}$$

where $j = \text{D}$ and L respectively for Dirac and Luttinger fermions in MLG and BLG. Here we absorb the contribution from the scaling dimension (z) of the conjugate fields Δ into its β -function. For the exact form of $\bar{\beta}_{\Delta_k}^j$ consult Appendix C.3.3. In possession of all relevant flow equations, we construct phase diagrams in various interaction channels following the strategy outlined in Sec. 2.2.3. The phase diagrams constructed this way

spin singlet					spin triplet				
SB	Phase	CC	CF	Fig.	SB	Phase	CC	CF	Fig.
A_{1g}^s	fermionic density	g_1^s	Δ_1^s	-	A_{1g}^t	ferromagnet	g_1^t	Δ_1^t	-
A_{2g}^s	quantum anomalous Hall insulator	g_2^s	Δ_2^s	6.3(a)	A_{2g}^t	quantum spin Hall insulator	g_2^t	Δ_2^t	6.3(c)
E_g^s	nematic ₁	g_3^s	Δ_3^s	6.4(a)	E_g^t	spin-nematic ₁	g_3^t	Δ_3^t	6.4(c)
A_{1u}^s	chiral density	g_4^s	Δ_4^s	-	A_{1u}^t	chiral ferromagnet	g_4^t	Δ_4^t	-
A_{2u}^s	charge density-wave	g_5^s	Δ_5^s	6.3(b)	A_{2u}^t	antiferromagnet	g_5^t	Δ_5^t	6.3(d)
E_u^s	nematic ₂	g_6^s	Δ_6^s	6.4(b)	E_u^t	spin-nematic ₂	g_6^t	Δ_6^t	6.4(d)
A_{1k}^s	Kekulé valence bond solid	g_7^s	Δ_7^s	6.6(a)	A_{1k}^t	spin-Kekulé solid	g_7^t	Δ_7^t	6.6(c)
A_{2k}^s	Kekulé current	g_8^s	Δ_8^s	6.6(b)	A_{2k}^t	spin-Kekulé current	g_8^t	Δ_8^t	6.6(d)
E_k^s	smectic charge density-wave	g_9^s	Δ_9^s	6.5(a)	E_k^t	smectic spin density-wave	g_9^t	Δ_9^t	6.5(b)

Table 6.3: Notation, nomenclature and list of figures regarding excitonic order parameters on the honeycomb lattice. The left (right) block corresponds to spin singlet (triplet) phases, and in each block the first two columns display the symbol (SB) by which the ordered phase is referred to in Figs. 6.3-6.6, and the physical nature of the phase. Columns 3 and 4 in each block respectively show the coupling constant (CC) of quartic interaction formed as $g_N(\Psi^\dagger N \Psi)^2$, and the conjugate field (CF) of the order parameter, while the last column “Fig.” references the figure of the corresponding phase diagram.

are displayed in Figs. 6.3, 6.4, 6.5 and 6.6, and the phase transitions occurring in various interaction channels at zero and finite temperature and chemical potential are tabulated in Tables. 6.5 and 6.6.

Notice that along some phase boundaries multiple order parameter fields diverge in a degenerate fashion. However, as we cut the multi-dimensional space of couplings in a very specific way (e.g. along the axes g_i^μ), this does not necessarily indicate an enlargement of symmetry among these orders at the governing quantum critical point (as in Chapter 3, for example). Rather, this suggests that the respective order parameters simultaneously diverge with a specific phase locking of the internal degrees of freedom. For example, when the divergences of the conjugate fields for both s -wave and f -wave pairings are degenerate, the ordered state is expected to support $s + if$ or $f + is$ pairing [69], which produces a maximal gap in the quasiparticle spectra.

To facilitate further discussion on order selection in two-dimensional Dirac and Luttinger fermions, let us briefly outline some properties of the available broken symmetry phases. In this section we quote the symbol of the respective orderings, with which they are referred to in the phase diagrams [Figs. 6.3-6.6]. For the symbols and applied notation we refer the reader to Table 6.3 and 6.4, while the symmetry properties of fermion bilinears are summarized in Tables 6.1 and 6.2.

6.2.4.1 Particle-hole or excitonic orders

Due to the neglected spin-orbit coupling the excitonic order parameters (just like the interaction terms) fall into two distinct categories. Namely, for each spin singlet order, where all matrices come with the σ_0 matrix, there exists a spin triplet analogue appearing with the σ_s matrices, where $s = \{1, 2, 3\}$, operating on the spin index. We indicate this distinction by s (singlet) and t (triplet) superscripts on the corresponding conjugate fields. Since the Hamiltonians in Eqs. (6.11) and (6.12) are oblivious to spin or invariant under the rotation of the spin quantization axis, this distinction does not affect the emergent fermionic quasiparticle spectra inside the ordered state. Note, however, that any triplet ordering breaks SU(2) spin rotational symmetry and is hence accompanied by two massless Goldstone modes.

The fermionic density and spin density (respectively denoted by A_{1g}^s and A_{1g}^t) do not break any discrete lattice symmetries, while the chiral and spin-chiral chemical potential (denoted by A_{1u}^s and A_{1u}^t , respectively) break valley reflection symmetry (T). All four orders commute with both the Dirac and Luttinger Hamiltonians, resulting in a trivial renormalization of their conjugate fields at zero temperature, see Appendix C.3.1. Consequently, none of them is realized in the ordered phase at $t = 0$.

Both the Dirac and Luttinger systems altogether accommodate *six* mass orders in the particle-hole channel [19, 213]. These phases introduce an isotropic gap in the quasiparticle spectrum and are thus favorable at zero and low temperature. All of them fully anticommute with the noninteracting Hamiltonian. The quantum Hall states break both sublattice (S) and valley (T) reflection symmetries. The quantum anomalous Hall insulator (QAHI), denoted by A_{2g}^s , additionally breaks time reversal symmetry, while it is restored in its spin triplet counterpart, the quantum spin Hall insulator (QSHI), denoted by A_{2g}^t [190, 194, 214]. The charge density wave (CDW) and antiferromagnet (AFM) order parameters break sublattice reflection, but preserve valley reflection symmetry [11, 12]. They are respectively denoted by A_{2u}^s and A_{2u}^t . The QAHI, QSHI, CDW and AFM orderings represent massive phases in both Dirac and Luttinger liquids. Both models accommodate two additional masses in the family of Kekulé orders.

The Kekulé orderings break translational symmetry of the honeycomb lattice and result in the enlargement of the unit cell, while preserving the rotational invariance [17]. In MLG, the Kekulé valence bond solid (KVBS) and spin-Kekulé solid (sKS) are fully gapped phases, while the Kekulé current (KC) and spin-Kekulé current (sKC) order parameters

SB	Phase	CF
A_{1g}^p	s -wave SC	Δ_1^p
A_{2g}^p	fully gapless SC ₁	Δ_2^p
E_g^p	nematic SC ₁	Δ_3^p
A_{1u}^p	f -wave SC	Δ_4^p
A_{2u}^p	fully gapless SC ₂	Δ_5^p
E_u^p	nematic SC ₂	Δ_6^p
A_{1k}^p	singl. Kek. SC	Δ_7^p
A_{2k}^p	triplet Kekulé SC	Δ_8^p
E_k^p	smectic SC	Δ_9^p

Table 6.4: Nomenclature regarding superconducting order parameters on the honeycomb lattice. Notations are identical to those in Table 6.3.

fully commute with \hat{h}^D . Exactly the opposite is true in BLG, namely KC and sKC represent spin singlet and spin triplet masses for Luttinger fermions, respectively, while \hat{h}^L fully commutes with the KVBS and sKS order parameters [19]. The KVBS, sKS, KC and sKC phases are respectively denoted by A_{1k}^s , A_{1k}^t , A_{2k}^s and A_{2k}^t .

All rotational symmetry breaking phases are gapless, and due to the higher density of states at low energies they are more entropically favorable than their gapped counterparts. Such orderings in MLG merely shift the location of the Dirac points, while in BLG it splits each quadratic band touching into two linear Dirac cones [19]. Consequently, all the nematic and spin nematic orders cause power-law suppression of the DoS for Luttinger fermions, yielding $\rho(E) \sim |E|$ at low energies. Four nematic phases, transforming under the E_g and E_u representations of the D_{3d} point group, preserve translational invariance. Two of them are spin singlets (denoted by E_g^s and E_u^s), while two spin-nematic order parameters (denoted by E_g^t and E_u^t) additionally breaks the spin-rotational invariance. In addition to rotational invariance, translational symmetry is also broken in the two smectic phases, the smectic charge density wave and smectic spin density wave orderings, respectively denoted by E_k^s and E_k^t . The smectic phases also produce gapless, but anisotropic Dirac points in the ordered phases.

6.2.4.2 Particle-particle or superconducting orders

When we add chemical doping to these nodal systems, instead of Fermi points, they develop extended Fermi surfaces around the two independent band touching points. The chemical potential term is of the form $\mu\Gamma_{3000}$, which commutes with all excitonic orders, therefore they cannot gap such resulting metallic systems. On the other hand, all pairing orders include $\eta_\alpha = \{\eta_1, \eta_2\}$ in the particle-hole sector, and hence they can conceivably anticommute (at least partially) with $h^j(\mathbf{k})$ when μ is finite. Therefore, low temperatures

(when a gapped spectrum is favorable due to the gain of condensation energy) and finite μ are conducive for superconducting orders, as the increased carrier density is conducive for the condensation of electrons into Cooper pairs.

The Nambu basis altogether accommodates nine local or momentum-independent pairing orders, which we mark with a superscript p in Tables 6.2 and 6.4. The singlet s -wave (denoted by A_{1g}^p) and triplet f -wave (denoted by A_{1u}^p) [70] superconductors (SCs) represent fully gapped phases in MLG and BLG. The singlet and triplet Kekulé SCs break translational symmetry. The singlet Kekulé SC (denoted by A_{1k}^p) represents a mass order in the Luttinger system (BLG), but fully commutes with the Dirac Hamiltonian [19]. In the exact opposite way, the triplet Kekulé SC (denoted by A_{2k}^p) gaps a Dirac liquid, but fully commutes with \hat{h}^L [67]. Two nematic superconductors, transforming under the E_g and E_u representations of the D_{3d} group (denoted by E_g^p and E_u^p , respectively), break rotational symmetry and produce gapless quasiparticle spectra. Furthermore, the smectic pairing (denoted by E_k^p) breaks rotational and translational invariance, and also leads to gapless bands. While the nematic and smectic pairings produce point nodes in the spectra of emergent Bogoliubov-de Gennes quasiparticles, the remaining two pairings transforming under the A_{2g} and A_{2u} representations (denoted by A_{2g}^p and A_{2u}^p , respectively) produces Fermi surfaces inside the ordered phases.

6.3 Phase diagrams

In this section we scrutinize multiple cuts of the global phase diagram of interacting fermions in MLG and BLG by systematically increasing the strength of interactions in one channel at a time, both at zero and finite chemical potential. The fact that the form of contact interactions in MLG and BLG is identical and they only differ in their noninteracting Hamiltonians gives us an opportunity to further dissect the selection rules outlined in Chapter 5 and assess the imprint of normal state band structure on the global phase diagram. This is because selection rule (I) only depends on S_{int} while (II) only on S_0 . Consequently, (I) cannot distinguish between MLG and BLG, and therefore any deviation must be rooted in (II).

Each phase diagram is displayed in the (g_μ^i, t) plane, where g_μ^i is a dimensionless (bare) coupling constant with $\mu = 1, \dots, 9$ and $i = \text{singlet } (s) \text{ and triplet } (t)$, and t is dimensionless temperature. We scan for the phase boundaries by keeping temperature constant and increasing the bare interaction strength, and detect the phase boundary and the nature of symmetry breaking *between disordered and ordered phases* (see Sec. 2.2.3), marked in the phase diagrams respectively as white and gray regions. Respectively, at zero and finite doping the disordered phase represents chiral nodal Fermi liquids (with point nodes) and regular Fermi liquids (with extended Fermi surface). Phase boundaries from the disordered state into an excitonic (superconducting) order are indicated with

blue (red) lines. The RG procedure is strictly only equipped to detect the divergence of some conjugate field that directly couples with a fermion bilinear, indicating onset of the corresponding ordered state and hence a phase transition. But, it does not tell us about potential regions of coexistence of adjacent phases deep inside the ordered phase. Also note that the critical interaction strength and the transition temperature are non-universal quantities, that depend on the parameter ζ , see Eq. (2.39).

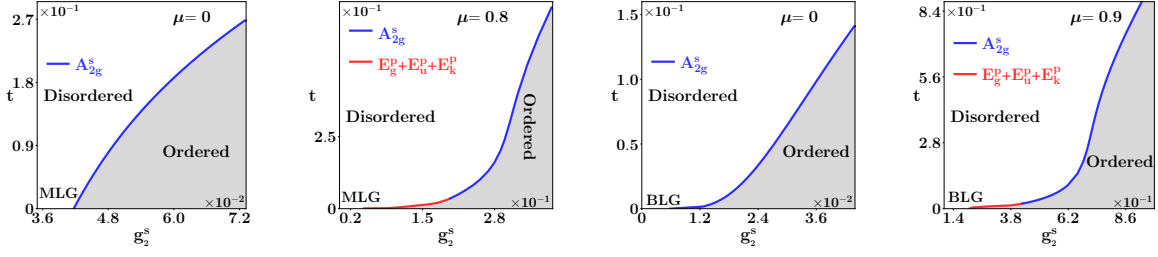
Four cuts of the phase diagram for each interaction channel (for MLG and BLG, at zero and finite chemical potential) are shown in Figs. 6.3–6.6. All phase transitions and the nature of the supervector order parameters of adjacent phases are summarized in Tables 6.5 and 6.6. Notice that we always cut the global phase diagram along one certain axis in the space of the coupling constants, which is generally not how a physical system behaves. But, unless fine tuned, among multiple running couplings there will always be one that diverges the fastest. The selection rules are then determined by the strongest diverging coupling constant. However, effective quartic interactions in a certain channel can in principle be tuned in Determinantal quantum Monte Carlo (DQMC) simulations [215], obtained by integrating out bosonic order parameter fluctuations. For brevity, when quoting a set of matrices we will use $\alpha = \{1, 2\}$ in the particle-hole or Nambu sector of the Hilbert space, indicating off-diagonal or pairing orders, and $s = \{1, 2, 3\}$ in the spin sector, indicating a spin triplet order parameter. Next we summarize the findings of the phase diagrams by tuning quartic interactions in different channels.

6.3.1 Quartic interactions: Mass channels

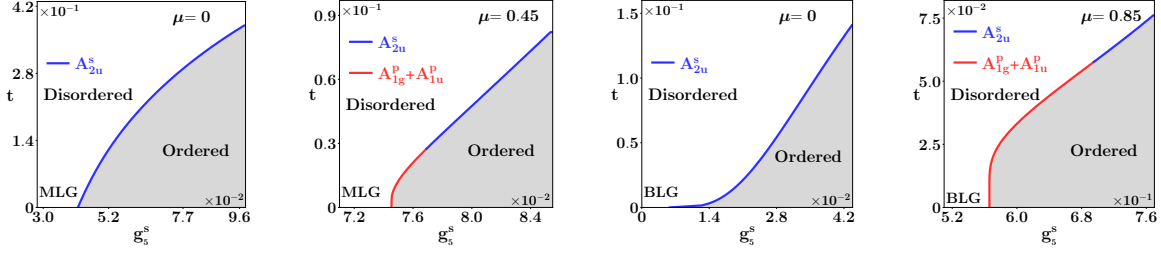
For quartic interactions in the four excitonic mass channels that are common across the two systems, selection rule (Ia) is the decisive at $\mu = 0$, namely $O_i = M_i$, where O_i (M_i) are the matrices involved in the order parameter of the broken symmetry phase (four fermion term of the given interaction channel). At $\mu > 0$ and low temperatures, we observe nucleation of “adjacent” superconducting phase(s).

1. For quartic interaction in the QAHI channel $M = \Gamma_{0033}$, which fully *commutes* with all superconducting masses. These orders are therefore not available to condense into. Instead, in both systems we observe nucleation of the E_u and E_g nematic SCs (denoted by nematic SC₁ and nematic SC₂, respectively, in Table 6.4) and the smectic SC phases. These pairing order parameters indeed fully anticommute with M [selection rule (Ib)]. The high temperature phase is the QAHI, in accordance with selection rule (Ia). The multicomponent order parameters combining QAHI and various nematic and smectic SCs in this case constitute the following supervectors

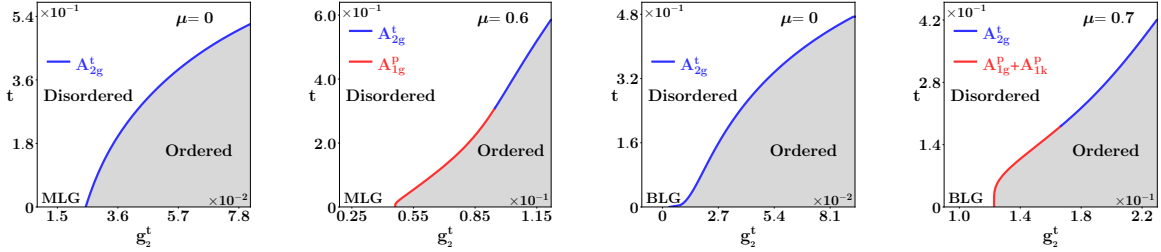
$$\mathbf{V}_1^{\text{QAHI}} = \left\{ \begin{array}{c} 2 \text{ copies of O(3) vectors} \\ \underbrace{\Gamma_{\alpha 001}, \Gamma_{\alpha 032}, \Gamma_{0033}}_{\substack{E_g^p \\ A_{2g}^s}} \end{array} \right\}, \quad \mathbf{V}_2^{\text{QAHI}} = \left\{ \begin{array}{c} 4 \text{ copies of O(4) vectors} \\ \underbrace{\Gamma_{\alpha s 31}, \Gamma_{\alpha s 02}, \Gamma_{0033}}_{\substack{E_u^p \\ A_{2g}^s}} \end{array} \right\},$$



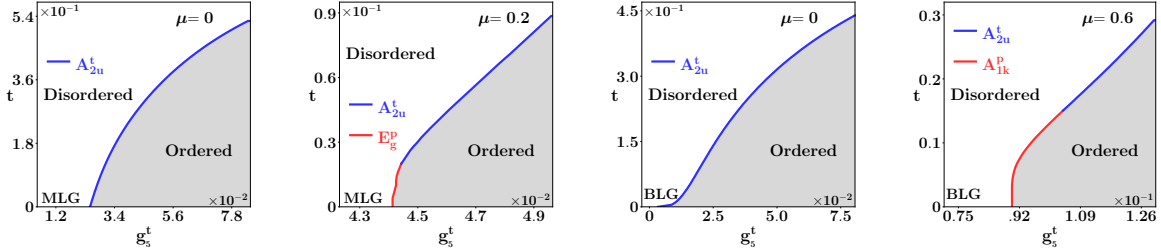
(a) Phase diagrams for the quartic interaction in the quantum anomalous Hall insulator or A_{2g} singlet channel.



(b) Phase diagrams for the quartic interactions in the charge density wave or A_{2u} singlet channel.



(c) Phase diagrams for the quartic interaction in the quantum spin Hall insulator or A_{2g} triplet channel.



(d) Phase diagrams for the quartic interaction in the antiferromagnet or A_{2u} triplet channel.

Figure 6.3: Cuts of the global phase diagram with quartic interactions in the mass channels for both MLG and BLG at zero ($\mu = 0$) and finite ($\mu > 0$) chemical doping. The horizontal [vertical] axis is bare interaction strength [dimensionless temperature, see Eq. (6.26)]. The value of the chemical doping is quoted in each panel. Multiple orders diverging in a degenerate way is indicated by a “+” sign. For the labeling of ordered phases consult Tables 6.3 and 6.4. The bilinears of adjacent phases form composite order parameters, as shown in Tables 6.5 and 6.6. See also Sec. 6.3.1. Figure adapted from Ref. [13].

$$\mathbf{V}_3^{\text{QAHI}} = \left\{ \underbrace{\Gamma_{\alpha 010}, \Gamma_{\alpha 020}, \Gamma_{\alpha 013}, \Gamma_{\alpha 023}, \Gamma_{0033}}_{E_k^p}, \underbrace{\Gamma_{0033}}_{A_{2g}^s} \right\}. \quad (6.33)$$

The corresponding cuts of the phase diagram are displayed in Fig. 6.3(a).

2. For quartic interaction in the CDW channel $M = \Gamma_{3003}$, which fully anticommutes

CC	Monolayer graphene (MLG)						Bilayer graphene (BLG)					
	$\mu = 0$			$\mu > 0$			$\mu = 0$			$\mu > 0$		
	low t	high t	symm.	low t	high t	symm.	low t	high t	symm.	low t	high t	symm.
g_2^s	A_{2g}^s	A_{2g}^s	-	E_g^p E_u^p E_k^p	A_{2g}^s	$2\otimes O(3)$ $4\otimes O(4)$ $4\otimes O(3)$	A_{2g}^s	A_{2g}^s	-	E_g^p E_u^p E_k^p	A_{2g}^s	$2\otimes O(3)$ $4\otimes O(4)$ $4\otimes O(3)$
g_3^s	E_g^s	E_g^s	-	A_{1g}^p A_{1u}^p	E_g^s	$1\otimes O(4)$ $2\otimes O(5)$	E_g^s	E_g^s	-	A_{1g}^p A_{1u}^p	E_g^s	$1\otimes O(4)$ $2\otimes O(5)$
g_5^s	A_{2u}^s	A_{2u}^s	-	A_{1g}^p A_{1u}^p	A_{2u}^s	$1\otimes O(3)$ $1\otimes O(3)$	A_{2u}^s	A_{2u}^s	-	A_{1g}^p A_{1u}^p	A_{2u}^s	$1\otimes O(3)$ $1\otimes O(3)$
g_6^s	E_u^s	E_u^s	-	E_u^s	E_u^s	-	A_{2g}^t A_{2u}^t A_{1k}^p	E_u^s	$1\otimes O(5)$ $1\otimes O(5)$ $2\otimes O(4)$	A_{1k}^p	E_u^s	$1\otimes O(4)$
g_7^s	A_{1k}^s	A_{1k}^s	-	A_{1g}^p	A_{1k}^s	$1\otimes O(4)$	A_{2u}^s A_{2u}^t A_{1g}^p	A_{1k}^s	$1\otimes O(3)$ $1\otimes O(5)$ $1\otimes O(4)$	A_{1g}^p	A_{1k}^s	$1\otimes O(4)$
g_8^s	A_{1u}^p A_{2u}^s A_{2u}^t E_g^s	E_g^s A_{2k}^s	$2\otimes O(5)$ $1\otimes O(3)$ $1\otimes O(5)$ $1\otimes O(4)$	A_{1u}^p E_g^s	E_g^s A_{2k}^s	$2\otimes O(5)$ $1\otimes O(4)$	A_{2k}^s	A_{2k}^s	-	A_{1u}^p	A_{2k}^s	$2\otimes O(5)$
g_9^s	A_{2g}^t A_{1g}^p	E_k^s	$2\otimes O(5)$ $2\otimes O(4)$	A_{1g}^p	E_k^s	$2\otimes O(4)$	A_{2g}^t A_{1g}^p	E_k^s	$2\otimes O(5)$ $2\otimes O(4)$	A_{1g}^p	E_k^s	$2\otimes O(4)$

Table 6.5: Dominant instabilities in the presence of quartic interactions in the spin singlet channels in MLG and BLG, at zero and finite chemical potential (μ). The shaded cells correspond to a second set of adjacent phases for interaction in the A_{2k} singlet (g_8^s) channel, which hosts three different phase transition between disordered and ordered phases in MLG for $\mu = 0$, see Fig. 6.6(b). The low and the high temperature phases are indicated in each scenario, suggesting adjacent phases when the two orderings are different. We then display the nature of the composite order parameters in columns “symm.”, where $k\otimes O(N)$ indicates k copies of an $O(N)$ algebra. The first column shows the coupling constant (CC) of the interaction channel. See Tables 6.3 and 6.4 for notations. See Sec. 6.3 for detailed discussion and Figs. 6.3-6.6 for various cuts of the phase diagrams.

with two superconducting masses [selection rule (Ib)], the singlet s -wave and triplet f -wave pairings, which form following the composite order parameters with CDW

$$\mathbf{V}_1^{\text{CDW}} = \left\{ \begin{array}{l} O(3) \text{ vector} \\ \overbrace{\Gamma_{\alpha 000}, \Gamma_{3003}} \\ A_{1g}^p \quad A_{2u}^s \end{array} \right\}, \quad \mathbf{V}_2^{\text{CDW}} = \left\{ \begin{array}{l} 2 \text{ copies of } O(4) \text{ vectors} \\ \overbrace{\Gamma_{\alpha s 30}, \Gamma_{3003}} \\ A_{1u}^p \quad A_{2u}^s \end{array} \right\}. \quad (6.34)$$

Indeed we observe degenerate nucleation of these two pairing phases at low temperatures

in MLG and BLG, when $\mu > 0$. The adjacent excitonic ordering is the CDW [selection rule (Ia)], which sets in at higher t where superconductivity is destroyed, see Fig. 6.3(b). The absence of order differentiation between Dirac and Luttinger systems with quartic interaction in the CDW channel is due to the fact that all dominant order parameters (one excitonic and two superconducting) fully anticommute with \hat{h}^D as well as with \hat{h}^L . At zero doping, we only find CDW ordering in both MLG and BLG [selection rule (Ia)]. In Sec. 6.4 we demonstrate the same result for NN repulsion.

3. For quartic interaction in the QSHI channel $M = \Gamma_{3s33}$, which fully anticommutes with two superconducting order parameters. One of them, the s -wave pairing, is a mass order in both systems, while the singlet Kekulé SC gaps only Luttinger fermions. Accordingly, in the Dirac system at low temperatures and finite chemical potential only s -wave SC can be observed. On the other hand, we find degenerate nucleation of s -wave and singlet Kekulé pairings in BLG. The nucleating orders and their differentiation through the underlying band structure follows from the selection rules (Ib) and (II), respectively. The high temperature phase in either case is the adjacent QSHI order, which follows from selection rule (Ia). The relevant cuts of the phase diagram are shown in Fig. 6.3(c). The supervector order parameters formed by adjacent phases read

$$\mathbf{V}_1^{\text{QSHI}} = \left\{ \begin{array}{c} \text{O(5) vector} \\ \overbrace{\Gamma_{\alpha 000}, \Gamma_{3s33}} \\ A_{1g}^p \quad A_{2g}^t \end{array} \right\}, \quad \mathbf{V}_2^{\text{QSHI}} = \left\{ \begin{array}{c} 2 \text{ copies of O(5) vectors} \\ \overbrace{\Gamma_{\alpha 011}, \Gamma_{\alpha 021}, \Gamma_{3s33}} \\ A_{1k}^p \quad A_{2g}^t \end{array} \right\}. \quad (6.35)$$

At zero doping we always find QSHI in MLG and BLG, according to selection rule (Ia).

4. For quartic interaction in the AFM channel $M = \Gamma_{0s03}$, which fully anticommutes with the E_g nematic and singlet Kekulé SCs. Latter one represents a mass order for Luttinger fermions, but fully commutes with the Dirac Hamiltonian. Therefore Kekulé SC is not a viable candidate for Dirac fermions at low temperatures. Rather, the maximally anticommuting pairing for the linearly dispersing Dirac electrons is the E_g nematic SC. The composite order parameters in these two cases read

$$\mathbf{V}_1^{\text{AFM}} = \left\{ \begin{array}{c} 2 \text{ copies of O(5) vectors} \\ \overbrace{\Gamma_{\alpha 011}, \Gamma_{\alpha 021}, \Gamma_{0s03}} \\ A_{1k}^p \quad A_{2u}^t \end{array} \right\}, \quad \mathbf{V}_2^{\text{AFM}} = \left\{ \begin{array}{c} 2 \text{ copies of O(5) vectors} \\ \overbrace{\Gamma_{\alpha 001}, \Gamma_{\alpha 032}, \Gamma_{0s03}} \\ E_g^p \quad A_{2u}^t \end{array} \right\}. \quad (6.36)$$

Therefore, at finite μ the low temperature pairing state in MLG (BLG) is singlet E_g nematic (Kekulé) SC, which follows from selection rule (Ib). The high temperature phase at finite μ in both systems is the AFM [selection rule (Ia)], see Fig. 6.3(d). At zero doping we always find AFM in both MLG and BLG. In Sec. 6.4 we again support this observation in the phase diagram of the honeycomb Hubbard model with only on site repulsion.

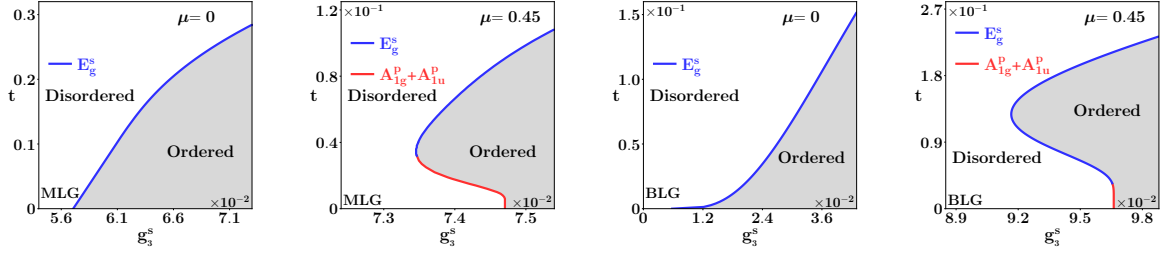
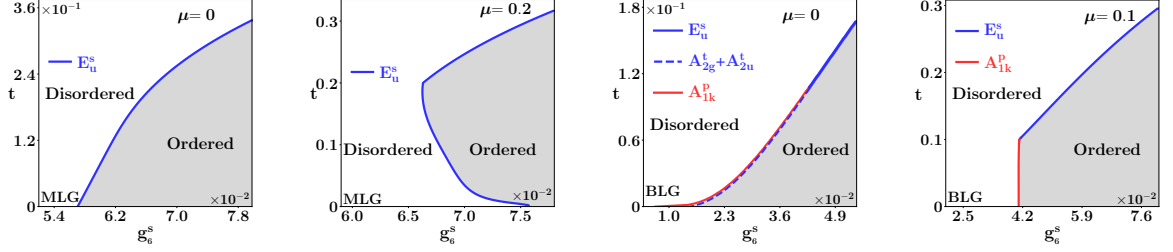
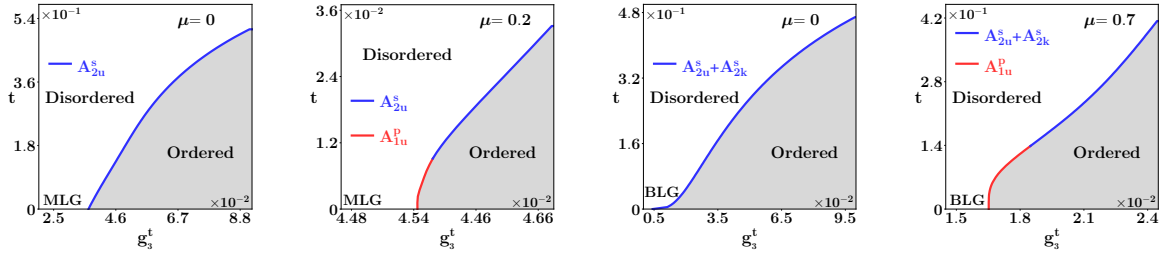
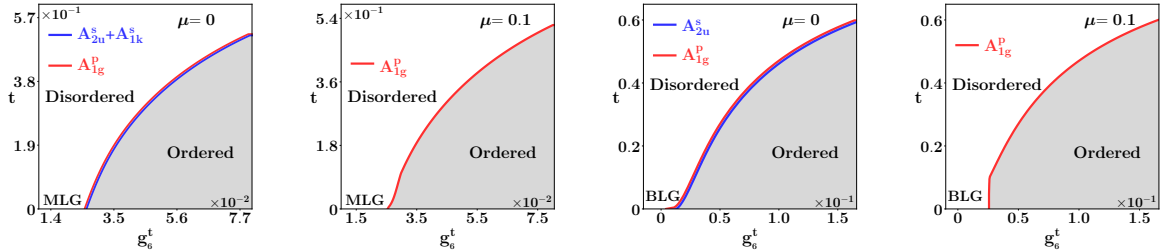
(a) Phase diagrams for the quartic interaction in the nematic₁ or E_g singlet channel.(b) Phase diagrams for the quartic interaction in the nematic₂ or E_u singlet channel.(c) Phase diagrams for the quartic interaction in the spin-nematic₁ or E_g triplet channel.(d) Phase diagrams for the quartic interaction in the spin-nematic₂ or E_u triplet channel.

Figure 6.4: Cuts of the global phase diagram with quartic interactions in the nematic and spin-nematic channels. The rest of the details are identical to those in Fig. 6.3. For the constructions of composite order parameters from adjacent phases, see Sec. 6.3.2. Figure adapted from Ref. [13].

6.3.2 Quartic interactions: Nematic channels

Nematic order parameters break rotational symmetry and they do not introduce a gap in the Luttinger or Dirac spectrum. Therefore, other *gapped* phases might be more favorable at low temperatures when we tune the quartic interactions in the nematic channels, especially if they satisfy the selection rule (Ib). Also note that in general spin fluctuations may induce charge ordering, while the opposite process is comparatively suppressed. This is because in the spin sector of the Hilbert space $\sigma_i \sigma_j$ (with $i, j = 1, 2, 3$) can conceivably

equal to σ_0 when $i = j$, but $\sigma_0\sigma_0 \neq \sigma_i$. Here two Pauli matrices are appearing from the interaction vertices, and their product results from the corresponding one-loop Feynman diagrams [see Fig. 2.1]. As a result, the spin singlet nematic interactions at zero chemical doping or high temperatures follow selection rule (Ia). In contrast, the appearing excitonic phases for interactions in their spin triplet counterparts follow selection rule (Ib). Next we systematically discuss these outcomes.

1. For quartic interaction in the E_g nematic (nematic₁) channel $M = (\Gamma_{3001}, \Gamma_{3032})$, which fully anticommutes with the s -wave and f -wave pairings, and forms the following supervector order parameters

$$\mathbf{V}_1^{E_g^s} = \left\{ \begin{array}{c} \text{O(4) vector} \\ \overbrace{\Gamma_{\alpha 000}, \Gamma_{3001}, \Gamma_{3032}} \\ \underbrace{A_{1g}^p \quad E_g^s} \end{array} \right\}, \quad \mathbf{V}_2^{E_g^s} = \left\{ \begin{array}{c} \text{2 copies of O(5) vectors} \\ \overbrace{\Gamma_{\alpha s 30}, \Gamma_{3001}, \Gamma_{3032}} \\ \underbrace{A_{1u}^p \quad E_g^s} \end{array} \right\}. \quad (6.37)$$

These two pairing phases are fully gapped in both MLG and BLG, and indeed we observe degenerate appearance of them with increased chemical doping in both systems [selection rule (Ib)]. At $\mu = 0$ or at high temperatures we find nucleation of the E_g nematic order [selection rule (Ia)] in both systems, see Fig. 6.4(a).

2. For quartic interaction in the E_u nematic (nematic₂) channel $M = (\Gamma_{0031}, \Gamma_{0002})$. These interaction matrices anticommute with the singlet Kekulé SC, which gaps the Luttinger fermions, but not the Dirac fermions. Therefore, in BLG at low temperatures we observe the singlet Kekulé SC together with the degenerate QSHI and AFM orders [selection rule (Ib)]. Adding carrier density ($\mu > 0$) favors the singlet Kekulé pairing at sufficiently low temperatures. The high temperature phase is the E_u nematic order, favored by the gain in entropy, see Fig. 6.4(b). At the same time, in MLG we find only the E_u nematic phase to be the dominant broken symmetry phase for zero and finite μ [selection rule (Ia)]. The adjacent phases then form the following composite order parameters

$$\mathbf{V}_1^{E_u^s} = \left\{ \begin{array}{c} \text{2 copies of O(4) vector} \\ \overbrace{\Gamma_{\alpha 011}, \Gamma_{\alpha 021}, \Gamma_{0031}, \Gamma_{0002}} \\ \underbrace{A_{1k}^p \quad E_u^s} \end{array} \right\}, \quad \mathbf{V}_2^{E_u^s} = \left\{ \begin{array}{c} \text{O(5) vector} \\ \overbrace{\Gamma_{3s33}, \Gamma_{0031}, \Gamma_{0002}} \\ \underbrace{A_{2g}^t \quad E_u^s} \end{array} \right\},$$

$$\mathbf{V}_3^{E_u^s} = \left\{ \begin{array}{c} \text{O(5) vector} \\ \overbrace{\Gamma_{0s03}, \Gamma_{0031}, \Gamma_{0002}} \\ \underbrace{A_{2u}^t \quad E_u^s} \end{array} \right\}. \quad (6.38)$$

3. For quartic interaction in the E_g spin-nematic (spin-nematic₁) channel the interaction matrices are $M = (\Gamma_{0s01}, \Gamma_{0s32})$. The maximally (but not fully) anticommuting pairing mass is the f -wave pairing. Among the excitonic masses, the CDW and KC orders fully anticommute with M . Note that KC is a mass order in BLG, but commutes with the Dirac Hamiltonian. Accordingly, at $\mu = 0$ or at sufficiently high temperature KC

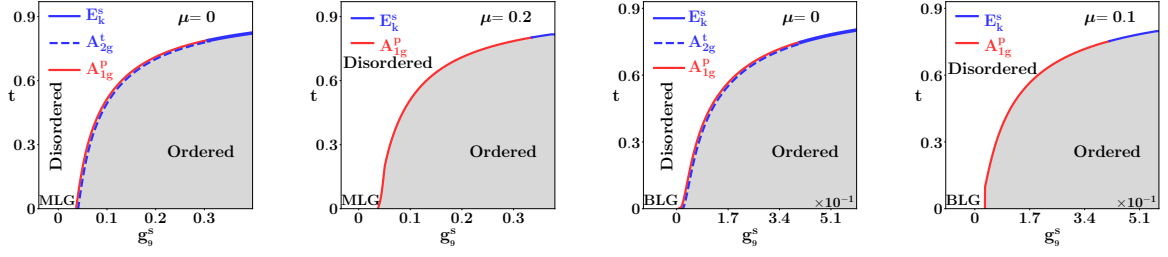
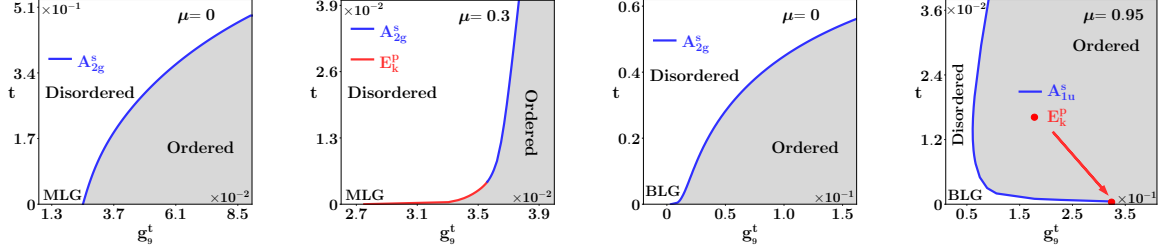
(a) Phase diagrams for the quartic interaction in the smectic charge-density-wave or E_k singlet channel.(b) Phase diagrams for the quartic interaction in the smectic spin-density-wave or E_k triplet channel.

Figure 6.5: Cuts of the global phase diagram with the quartic interactions in the smectic and spin-smectic channels. The rest of the details are identical to those in Fig. 6.3. For the constructions of composite order parameters from adjacent phases, see Sec. 6.3.3. Figure adapted from Ref. [13].

and CDW appear together in BLG, whereas in MLG we only find CDW order in this parameter regime. The f -wave pairing can be observed at $\mu > 0$ and low temperatures in both MLG and BLG, while higher t destroys the superconductivity and the system instead enters into the respective excitonic phases, see Fig. 6.4(c). Note that the E_g spin-nematic ordering is completely absent in our range of parameters, thus all appearing broken symmetry phases follow selection rule (Ib). The corresponding composite order parameters constructed from the adjacent phases read

$$\mathbf{V}_1^{E_g^t} = \left\{ \begin{array}{c} 2 \text{ copies of } O(4) \text{ vector} \\ \left\{ \overbrace{\Gamma_{\alpha s 30}, \Gamma_{3003}} \right\} \\ A_{1u}^p \quad A_{2u}^s \end{array} \right\}, \quad \mathbf{V}_2^{E_g^t} = \left\{ \begin{array}{c} 2 \text{ copies of } O(5) \text{ vectors} \\ \left\{ \overbrace{\Gamma_{\alpha s 30}, \Gamma_{0012}, \Gamma_{0022}} \right\} \\ A_{1u}^p \quad A_{2k}^s \end{array} \right\}. \quad (6.39)$$

4. For quartic interaction in the E_u spin-nematic (or spin-nematic₂) channel $M = (\Gamma_{3s31}, \Gamma_{3s02})$. These interaction matrices fully anticommute with the s -wave pairing and CDW orders, which indeed appear simultaneously on the phase diagram of MLG and BLG at zero doping, see Fig. 6.4(d). Furthermore, M also anticommutes with the KVBS order parameter, which represents a massive phase for the Dirac fermions, but commutes with the Luttinger Hamiltonian. Accordingly, KVBS accompanies CDW and s -wave pairing in MLG, but not in BLG. As all these phases represent mass orders and they fully anticommute with M , temperature does not lift the degeneracy among them. However, by adding chemical potential we select the pairing phase: s -wave SC. As only selection rule (Ib) is operative in these phase diagrams, we do not obtain any composite order parameter.

6.3.3 Quartic interactions: Smectic channels

Smectic orders break both rotational and translational symmetries, but they do not support any mass gap. Selection rule (Ia) is, therefore, not conducive for a fully gapped phase, and low temperature phases are typically inhabited by mass orders, obeying selection rule (Ib).

1. For quartic interaction in the smectic CDW channel $M = (\Gamma_{3010}, \Gamma_{3020}, \Gamma_{3013}, \Gamma_{3023})$. The low temperature region of the phase diagrams in Fig. 6.5(a) is occupied by the massive phases that fulfill selection rule (Ib): the s -wave SC and QSHI in both MLG and BLG. While at zero doping they nucleate in a degenerate fashion, finite doping favors the s -wave pairing at low temperatures. At high temperatures, we observe the smectic CDW phase at both zero and finite μ in MLG and BLG, following selection rule (Ia). The adjacent phases then form the following supervector order parameters

$$\mathbf{V}_1^{E_k^s} = \left\{ \underbrace{\Gamma_{\alpha 000}, \Gamma_{3010}, \Gamma_{3020}, \Gamma_{3013}, \Gamma_{3023}}_{E_k^s}, \underbrace{A_{1g}^p}_{2 \text{ copies of O(4) vector}} \right\}, \quad \mathbf{V}_2^{E_k^s} = \left\{ \underbrace{\Gamma_{3s33}, \Gamma_{3010}, \Gamma_{3020}, \Gamma_{3013}, \Gamma_{3023}}_{E_k^s}, \underbrace{A_{2g}^t}_{2 \text{ copies of O(5) vectors}} \right\}. \quad (6.40)$$

2. For quartic interaction in the smectic spin density wave (SDW) channel the four fermion matrices are $M = (\Gamma_{0s10}, \Gamma_{0s20}, \Gamma_{0s13}, \Gamma_{0s23})$, which fully anticommutes with the QAHI mass order. As such we observe nucleation of this phase in both systems at zero chemical potential for low, as well as high t [selection rule (Ib)]. On the other hand, there is no fully anticommuting available pairing phase, and by elevating the chemical potential we induce the only partially anticommuting smectic SC. Once superconductivity is destroyed, in MLG the system goes back into the QAHI phase. However, in BLG it is the chiral density order parameter that develops a finite expectation value at high t . This is possibly due to the high chemical potential ($\mu = 0.95$), required to induce superconductivity, which causes the system to act like a metal, as opposed to a semimetal. The relevant cuts of the global phase diagram are displayed in Fig. 6.5(b). The corresponding composite order parameters are

$$\mathbf{V}_1^{E_k^t} = \left\{ \underbrace{\Gamma_{\alpha 010}, \Gamma_{\alpha 020}, \Gamma_{\alpha 013}, \Gamma_{\alpha 023}, \Gamma_{0033}}_{E_k^p}, \underbrace{A_{2g}^s}_{4 \text{ copies of O(3) vector}} \right\}, \quad \mathbf{V}_2^{E_k^t} = \left\{ \underbrace{\Gamma_{\alpha 010}, \Gamma_{\alpha 020}, \Gamma_{\alpha 013}, \Gamma_{\alpha 023}, \Gamma_{0030}}_{E_k^p}, \underbrace{A_{1u}^s}_{4 \text{ copies of O(3) vector}} \right\}. \quad (6.41)$$

$\mathbb{C}\mathbb{C}$	Monolayer graphene (MLG)						Bilayer graphene (BLG)					
	$\mu = 0$			$\mu > 0$			$\mu = 0$			$\mu > 0$		
	low t	high t	symm.	low t	high t	symm.	low t	high t	symm.	low t	high t	symm.
g_2^t	A_{2g}^t	A_{2g}^t	-	A_{1g}^p	A_{2g}^t	$1 \otimes \text{O}(5)$	A_{2g}^t	A_{2g}^t	-	A_{1g}^p A_{1k}^p	A_{2g}^t	$1 \otimes \text{O}(5)$ $2 \otimes \text{O}(5)$
g_3^t	A_{2u}^s	A_{2u}^s	-	A_{1u}^p	A_{2u}^s	$2 \otimes \text{O}(4)$	A_{2u}^s A_{2k}^s	A_{2u}^s A_{2k}^s	-	A_{1u}^p	A_{2u}^s A_{2k}^s	$2 \otimes \text{O}(4)$ $2 \otimes \text{O}(5)$
g_5^t	A_{2u}^t	A_{2u}^t	-	E_g^p	A_{2u}^t	$2 \otimes \text{O}(5)$	A_{2u}^t	A_{2u}^t	-	A_{1k}^p	A_{2u}^t	$2 \otimes \text{O}(5)$
g_6^t	A_{2u}^s A_{1k}^s A_{1g}^p	A_{2u}^s A_{1k}^s A_{1g}^p	-	A_{1g}^p	A_{1g}^p	-	A_{2u}^s A_{1g}^p	A_{2u}^s A_{1g}^p	-	A_{1g}^p	A_{1g}^p	-
g_7^t	A_{2u}^s	A_{2u}^s	-	E_k^p	E_u^s	$4 \otimes \text{O}(3)$	A_{2u}^s	A_{2u}^s	-	E_k^p E_u^s	E_u^s A_{1k}^t	$4 \otimes \text{O}(3)$ $2 \otimes \text{O}(5)$
g_8^t	A_{2u}^s A_{1g}^p	A_{2u}^s A_{1g}^p	-	A_{1g}^p	A_{1g}^p	-	A_{2u}^s A_{1g}^p	A_{2u}^s A_{1g}^p	-	A_{1g}^p	A_{1g}^p	-
g_9^t	A_{2g}^s	A_{2g}^s	-	E_k^p	A_{2g}^s	$4 \otimes \text{O}(3)$	A_{2g}^s	A_{2g}^s	-	E_k^p	A_{1u}^s	$4 \otimes \text{O}(3)$

Table 6.6: Dominant instabilities in the presence of quartic interactions in spin triplet channels in MLG and BLG, at zero and finite chemical potential (μ). Notations are identical to those used in Tab. 6.5. See Sec. 6.3 for detailed discussion and Figs. 6.3-6.6 for various cuts of the phase diagrams.

6.3.4 Quartic interactions: Kekulé channels

Finally, we focus on the quartic interactions in the Kekulé channels. Note that all Kekulé orders (including both bond and current) at least break the translational symmetry, but preserve the rotational invariance.

1. For quartic interaction in the KVBS channel $M = (\Gamma_{3011}, \Gamma_{3021})$. The high temperature phase in both systems is KVBS itself, fulfilling selection rule (Ia). Note that for the Dirac fermions KVBS is a mass, therefore at $\mu = 0$ in MLG it persists all the way down to the lowest temperature. However, the KVBS order parameter fully commutes with \hat{h}^L and in BLG this phase is replaced by the competing massive phases, namely the CDW, AFM and s -wave SC orderings at $\mu = 0$. Since M fully anticommutes with the s -wave pairing order parameter, finite μ selects this phase in MLG as well as BLG, see Fig. 6.6(a). The corresponding supervectors are

$$\mathbf{V}_1^{\text{KVBS}} = \left\{ \begin{array}{c} \text{O}(4) \text{ vector} \\ \overbrace{\Gamma_{\alpha 000}, \Gamma_{3011}, \Gamma_{3021}} \\ A_{1g}^p \quad A_{1k}^s \end{array} \right\}, \quad \mathbf{V}_2^{\text{KVBS}} = \left\{ \begin{array}{c} \text{O}(3) \text{ vector} \\ \overbrace{\Gamma_{3003}, \Gamma_{3011}, \Gamma_{3021}} \\ A_{2u}^s \quad A_{1k}^s \end{array} \right\},$$

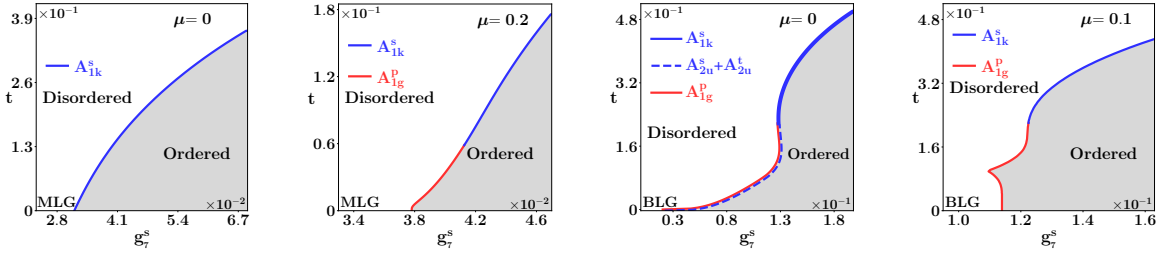
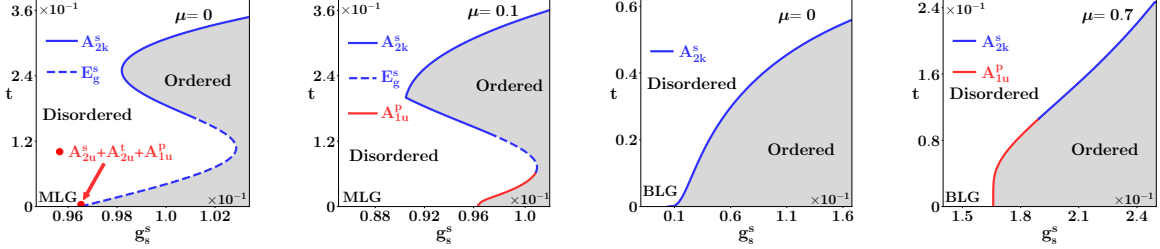
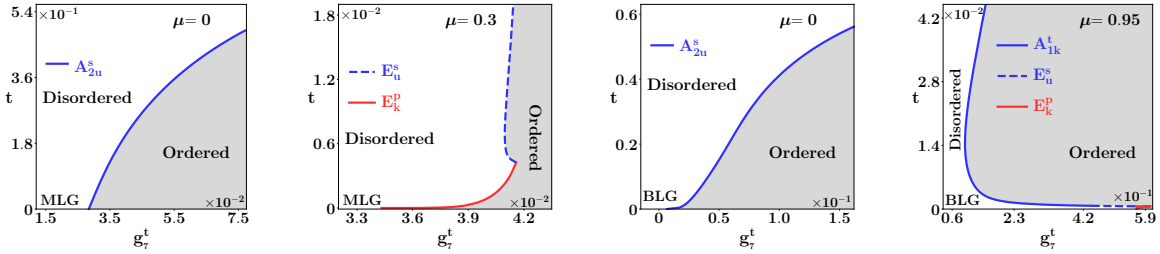
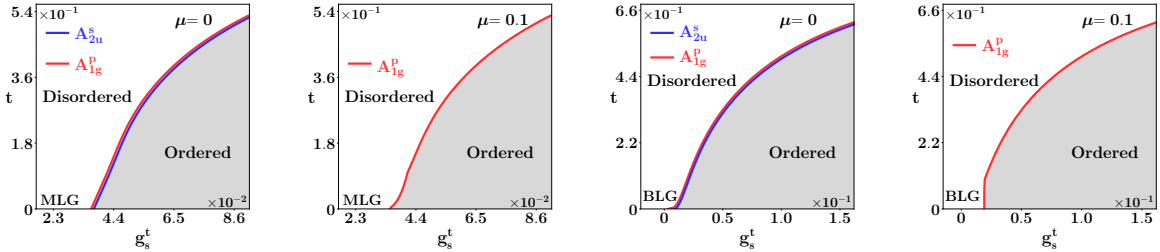
(a) Phase diagrams for the quartic interaction in the Kekulé valence bond solid or A_{1k} singlet channel.(b) Phase diagrams for the quartic interaction in the Kekulé current or A_{2k} singlet channel.(c) Phase diagrams for the quartic interaction in the spin Kekulé solid or A_{1k} triplet channel.(d) Phase diagrams for the quartic interaction in the spin Kekulé current or A_{2k} triplet channel.

Figure 6.6: Cuts of the global phase diagram with the quartic interactions in the Kekulé channels. The rest of the details are identical to those in Fig. 6.3. For the constructions of composite order parameters from adjacent phases, see Sec. 6.3.4. Figure adapted from Ref. [13].

$$\mathbf{V}_3^{\text{KVBS}} = \left\{ \begin{array}{c} \text{O}(5) \text{ vector} \\ \Gamma_{0s03}, \Gamma_{3011}, \Gamma_{3021} \\ A_{2u}^t \quad A_{1k}^s \end{array} \right\}. \quad (6.42)$$

2. The quartic interaction in the KC channel displays analogous behavior to that in the KVBS channel, but the mass nature of the phase is flipped between MLG and BLG. Here $M = (\Gamma_{0012}, \Gamma_{0022})$ and at high temperatures the dominant instability is KC in both systems [selection rule (Ia)]. In BLG the KC is a massive phase and at $\mu = 0$ it persists down to the lowest temperature. In MLG at zero chemical doping the low

temperature regime is occupied by phases that follow selection rule (Ib). At the lowest temperature and $\mu = 0$ we observe degenerate nucleation of CDW, AFM and f -wave pairing states, all representing mass orders with $C_H = 0$. Increasing the temperature the broken symmetry phase becomes the E_g nematic, for which $C_H = A_H$. See section 5 for the definitions of C_H and A_H . As the KC order parameter fully commutes with the Dirac Hamiltonian ($A_H = 0$), this ordering only occurs at high temperatures. The onset of these orderings along the temperature axis is consistent with selection rule (II). In both systems, finite chemical potential and low temperatures favor the adjacent f -wave pairing, following selection rule (Ib). The corresponding cuts of the phase diagram are displayed in Fig. 6.6(b), and the composite order parameters are

$$\begin{aligned}
\mathbf{V}_1^{\text{KC}} &= \left\{ \begin{array}{c} \text{2 copies of O(5) vector} \\ \overbrace{\Gamma_{\alpha s 30}, \Gamma_{0012}, \Gamma_{0022}} \\ \underbrace{A_{1u}^p \quad A_{2k}^s} \end{array} \right\}, & \mathbf{V}_2^{\text{KC}} &= \left\{ \begin{array}{c} \text{O(3) vector} \\ \overbrace{\Gamma_{3003}, \Gamma_{3001}, \Gamma_{3032}} \\ \underbrace{A_{2u}^s \quad E_g^s} \end{array} \right\}, \\
\mathbf{V}_3^{\text{KC}} &= \left\{ \begin{array}{c} \text{O(5) vector} \\ \overbrace{\Gamma_{0s03}, \Gamma_{3001}, \Gamma_{3032}} \\ \underbrace{A_{2u}^t \quad E_g^s} \end{array} \right\}, & \mathbf{V}_4^{\text{KC}} &= \left\{ \begin{array}{c} \text{2 copies of O(5) vector} \\ \overbrace{\Gamma_{\alpha s 30}, \Gamma_{3001}, \Gamma_{3032}} \\ \underbrace{A_{1u}^p \quad E_g^s} \end{array} \right\}, \\
\mathbf{V}_5^{\text{KC}} &= \left\{ \begin{array}{c} \text{O(4) vector} \\ \overbrace{\Gamma_{3001}, \Gamma_{3032}, \Gamma_{0012}, \Gamma_{0022}} \\ \underbrace{E_g^s \quad A_{2k}^s} \end{array} \right\}. & & (6.43)
\end{aligned}$$

3. For quartic interaction in the spin Kekulé solid (KS) channel $M = (\Gamma_{0s11}, \Gamma_{0s21})$. At zero chemical potential, following selection rule (Ib), we observe nucleation of the excitonic CDW order in both MLG and BLG. For $\mu > 0$ and low temperatures the Dirac, as well as the Luttinger fermions condense into the smectic superconductor, whereas intermediate t destroys the pairing phase and gives rise to the E_u nematic ordering, for which $C_H = A_H$. Furthermore, at even higher temperature BLG displays the spin KS phase, according to selection rule (Ia), that maximally commutes with the Luttinger Hamiltonian, $A_H = 0$. Once again, onset of these phases by increasing temperature is in accordance with selection rule (II). For the phase diagrams in this interaction channel see Fig. 6.6(c). The composite order parameters in these cases are

$$\mathbf{V}_1^{\text{sKS}} = \left\{ \begin{array}{c} \text{4 copies of O(3) vector} \\ \overbrace{\Gamma_{\alpha 010}, \Gamma_{\alpha 020}, \Gamma_{\alpha 013}, \Gamma_{\alpha 023}, \Gamma_{0031}, \Gamma_{0002}} \\ \underbrace{E_k^p \quad E_u^s} \end{array} \right\}, \quad \mathbf{V}_2^{\text{sKS}} = \left\{ \begin{array}{c} \text{2 copies of O(5) vector} \\ \overbrace{\Gamma_{0031}, \Gamma_{0002}, \Gamma_{0s11}, \Gamma_{0s21}} \\ \underbrace{E_u^s \quad A_{1k}^t} \end{array} \right\}. \quad (6.44)$$

4. For quartic interaction in the spin KC channel $M = (\Gamma_{3s12}, \Gamma_{3s22})$, which fully anti-commutes with the s -wave pairing and CDW order parameters. At $\mu = 0$ we observe

degenerate nucleation of these two phases for the entire range of temperature. Note that for both order parameters $\{O_i, M_j\} = 0$ and $C_H = 0$ (i.e., they represent fully gapped phases), and thus they are not distinguished by temperature. Only by setting $\mu > 0$ we select the s -wave SC in both MLG and BLG, see Fig. 6.6(d). In the absence of an adjacent high temperature phase we do not obtain composite order parameters in this case. Note that this is due to the fact that only selection rule (Ib) is operative in this case for both MLG and BLG.

6.4 Extended honeycomb Hubbard model

In the preceding sections we scrutinized the honeycomb monolayer and bilayer in the presence of generic short range repulsive electron-electron interactions. We demonstrated through numerous examples the validity of the selection rules and organizing principle (see Chapter. 5), by tuning the strength of interactions in one specific channel at a time at zero and finite temperature and chemical doping. However, the bare values of the interaction couplings in a physically realistic microscopic model would in principle be non-zero simultaneously in multiple interaction channels. To substantiate our findings, we here consider one of the simplest, yet realistic microscopic models for correlated electrons on the honeycomb lattice, the extended Hubbard model.

The Hamiltonian of the extended Hubbard model, describing electrons hopping on a lattice and interacting via on site, nearest neighbor (NN), and next-nearest neighbor (NNN) interactions, reads

$$H = H_0 + H_U + H_{V_1} + H_{V_2}. \quad (6.45)$$

Here H_0 describes a collection of noninteracting itinerant electrons on MLG and BLG, where it respectively produces linear and quadratic band touchings, and

$$\begin{aligned} H_U &= \frac{U}{2} \sum_{\mathbf{R}} n_{\uparrow}(\mathbf{R})n_{\downarrow}(\mathbf{R}), \\ H_{V_1} &= \frac{V_1}{2} \sum_{\langle \mathbf{A}, \mathbf{B} \rangle} \sum_{\sigma, \sigma' = \uparrow, \downarrow} n_{\sigma}(\mathbf{A})n_{\sigma'}(\mathbf{B}), \\ H_{V_2} &= \frac{V_2}{2} \sum_{\langle\langle \mathbf{R}, \mathbf{R}' \rangle\rangle} \sum_{\sigma, \sigma' = \uparrow, \downarrow} n_{\sigma}(\mathbf{R})n_{\sigma'}(\mathbf{R}'). \end{aligned} \quad (6.46)$$

Here $n_{\sigma}(\mathbf{R})$ is the number operator on the site at \mathbf{R} with spin projection $\sigma = \uparrow, \downarrow$. The sites located at \mathbf{A} (\mathbf{B}) span the A (\mathbf{B}) sublattice of the bipartite honeycomb lattice, while $\langle \dots \rangle$ and $\langle\langle \dots \rangle\rangle$ denote all pairs of NN and NNN sites respectively. Note in the case of BLG these sites reside on the emergent honeycomb lattice, resulting after integrating out the dimer sites. The terms H_U , H_{V_1} and H_{V_2} then respectively describe the on site, NN, and NNN interactions with the interaction strengths U , V_1 and V_2 .

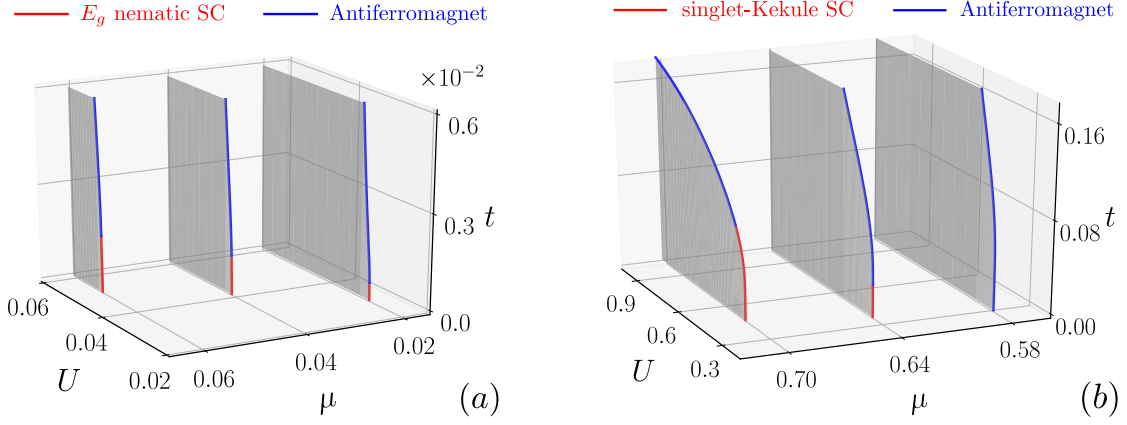


Figure 6.7: Representative cuts of the phase diagram of the extended honeycomb Hubbard model described by Eqs. (6.45) and (6.46), in the presence of only the on site repulsion ($U > 0$). Each cut is shown in the (U, t) plane, where t is dimensionless temperature and U is the strength of on site repulsive interaction, for various fixed values of dimensionless chemical potential μ [see Eq. (6.26)]. The shaded region corresponds to the ordered phase, while colored lines indicate phase boundaries of second order phase transitions from the disordered phase (white region), which at finite doping represents chiral Fermi liquids. Along such phase boundaries the blue (red) lines represent excitonic (superconducting) orders, whose nature we explicitly highlight in each panel. The effects of only $U > 0$ are displayed in panels (a) and (b) for MLG and BLG, respectively. Here U parameterizes the bare dimensionless onsite interaction strength. In both cases, the adjacent superconductor (SC) and excitonic phases form composite $O(5)$ order parameters, shown in Eq. (6.55). Figure adapted from Ref. [13].

In this section, we give a detailed walkthrough on how to translate between the Hubbard Hamiltonian, written in terms of a lattice model, and our effective low-energy description. The three distinct interaction terms (on site, NN and NNN repulsion) are addressed separately in three subsequent sections. In Bernal BLG as the split-off bands are dominantly localized on the a_1 and b_2 sites and here we consider only density-density interactions, one can integrate out fermionic density on these two sites to arrive at an effective or renormalized extended honeycomb Hubbard model defined on the low-energy sites, at the cost of renormalized strengths of the corresponding coupling constants [18]. Such trivial renormalization is, however, omitted here.

6.4.1 On site repulsion (U)

To make a connection with Eq. (6.46), we first make use of the Hamman decomposition to rewrite H_U as [12, 216]

$$H_U = \frac{U}{16} \sum_{\mathbf{A}} \left\{ [n(\mathbf{A}) + n(\mathbf{A} + \boldsymbol{\delta}_i)]^2 + [n(\mathbf{A}) - n(\mathbf{A} + \boldsymbol{\delta}_i)]^2 - [\mathbf{m}(\mathbf{A}) + \mathbf{m}(\mathbf{A} + \boldsymbol{\delta}_i)]^2 - [\mathbf{m}(\mathbf{A}) - \mathbf{m}(\mathbf{A} + \boldsymbol{\delta}_i)]^2 \right\}, \quad (6.47)$$

where $n(\mathbf{R}) = r_\sigma^\dagger(\mathbf{R})r_\sigma(\mathbf{R})$ is the number operator, $\mathbf{m} = r_\sigma^\dagger(\mathbf{R})\boldsymbol{\sigma}_{\sigma\sigma'}r_{\sigma'}(\mathbf{R})$ is the magnetization, with $r_\sigma^\dagger(\mathbf{R})$ and $r_\sigma(\mathbf{R})$ being fermionic creation and annihilation operators with spin projection $\sigma = \uparrow, \downarrow$ on the site at \mathbf{R} , and summation over repeated indices is assumed. The first (second) term in the Hamman decomposition corresponds to the total (staggered) density, while the third (fourth) term to the total (staggered) magnetization. Recalling the Fourier expansion of the fermionic fields in Eq. (6.8) and the spinor structure in Eq. (6.9), they are written as

$$n(\mathbf{A}) + n(\mathbf{B}) = \Psi^\dagger\Gamma_{3000}\Psi + \cos(2\mathbf{K} \cdot \mathbf{r})\Psi^\dagger\Gamma_{3010}\Psi + \sin(2\mathbf{K} \cdot \mathbf{r})\Psi^\dagger\Gamma_{3020}\Psi, \quad (6.48)$$

$$n(\mathbf{A}) - n(\mathbf{B}) = \Psi^\dagger\Gamma_{3003}\Psi + \cos(2\mathbf{K} \cdot \mathbf{r})\Psi^\dagger\Gamma_{3013}\Psi + \sin(2\mathbf{K} \cdot \mathbf{r})\Psi^\dagger\Gamma_{3023}\Psi, \quad (6.49)$$

$$m_s(\mathbf{A}) + m_s(\mathbf{B}) = \Psi^\dagger\Gamma_{3s00}\Psi + \cos(2\mathbf{K} \cdot \mathbf{r})\Psi^\dagger\Gamma_{3s10}\Psi + \sin(2\mathbf{K} \cdot \mathbf{r})\Psi^\dagger\Gamma_{3s20}\Psi, \quad (6.50)$$

$$m_s(\mathbf{A}) - m_s(\mathbf{B}) = \Psi^\dagger\Gamma_{3s03}\Psi + \cos(2\mathbf{K} \cdot \mathbf{r})\Psi^\dagger\Gamma_{3s13}\Psi + \sin(2\mathbf{K} \cdot \mathbf{r})\Psi^\dagger\Gamma_{3s23}\Psi, \quad (6.51)$$

where $m_s(\mathbf{R})$ is the s component of the magnetization ($s = 1, 2, 3$) on the site at \mathbf{R} .

Upon squaring the above quantities we neglect the oscillatory contributions, as any position (and thus wave-number) dependent term will be less relevant in the RG sense (as can be shown via power counting). Then the on site repulsion in the continuum theory takes the form

$$H_U = \frac{Ua^2}{16} \left\{ (\Psi^\dagger\Gamma_{3000}\Psi)^2 + (\Psi^\dagger\Gamma_{3003}\Psi)^2 + \frac{1}{2} \left[(\Psi^\dagger\Gamma_{3010}\Psi)^2 + (\Psi^\dagger\Gamma_{3020}\Psi)^2 + (\Psi^\dagger\Gamma_{3013}\Psi)^2 + (\Psi^\dagger\Gamma_{3023}\Psi)^2 \right] - (\Psi^\dagger\Gamma_{0s00}\Psi)^2 - (\Psi^\dagger\Gamma_{0s03}\Psi)^2 - \frac{1}{2} \left[(\Psi^\dagger\Gamma_{0s10}\Psi)^2 + (\Psi^\dagger\Gamma_{0s20}\Psi)^2 + (\Psi^\dagger\Gamma_{0s13}\Psi)^2 + (\Psi^\dagger\Gamma_{0s23}\Psi)^2 \right] \right\}. \quad (6.52)$$

Hence the initial condition (or bare value) of the coupling constants as a function of U is

$$\begin{aligned} g_1^s(\ell=0) = g_5^s(\ell=0) &= -\frac{Ua^2}{16}, & g_9^s(\ell=0) &= -\frac{1}{2}\frac{Ua^2}{16}, \\ g_1^t(\ell=0) = g_5^t(\ell=0) &= \frac{Ua^2}{16}, & g_9^t(\ell=0) &= \frac{1}{2}\frac{Ua^2}{16}. \end{aligned} \quad (6.53)$$

We then use the Fierz constraints to rewrite the spin triplet four fermion terms as a linear combinations of spin singlet terms, eliminating g_i^t , and subsequently rescale according to $Ua^2/16 \rightarrow U$. Doing so we arrive at

$$g_1^s(\ell=0) = -U, \quad g_5^s(\ell=0) = -U, \quad g_9^s(\ell=0) = -\frac{1}{2}U, \quad (6.54)$$

and all other linearly independent coupling constants $g_i^s(\ell=0) = 0$ for $i = 2, 3, 4, 6, 7, 8$.

To study the phase diagram of the honeycomb Hubbard model in the presence of on site repulsion we apply the same methodology as in Sec. 6.3. But instead of scanning along one certain axis in the space of coupling constants, we use Eq. (6.54) and tune U

until we detect a phase transition. The (U, t) cuts of the phase diagram for various values of μ are displayed in Figs. 6.7(a) and 6.7(b) for MLG and BLG, respectively. At $\mu = t = 0$ both the Dirac and Luttinger fermions display antiferromagnetic (A_{2u}^t) ordering, which is to be expected on a half-filled bipartite lattice in the presence of only repulsive Hubbard interactions. For finite chemical doping the induced pairing phase for linearly dispersing Dirac fermions is the E_g nematic superconductor [Fig. 6.7(a)], while for the quadratic Luttinger fermions it is the A_{1k} singlet Kekulé pairing [Fig. 6.7(b)]. Note, the adjacent excitonic and pairing phases in both systems fully anticommute with each other and form $O(5)$ supervector order parameters given by

$$\mathbf{V}_{\text{MLG}}^{\text{U}} = \left\{ \begin{array}{c} \text{2 copies of } O(5) \text{ vectors} \\ \overbrace{\Gamma_{\alpha 001}, \Gamma_{\alpha 032}, \Gamma_{0s03}} \\ E_g^p \quad A_{2u}^t \end{array} \right\}, \quad \mathbf{V}_{\text{BLG}}^{\text{U}} = \left\{ \begin{array}{c} \text{2 copies of } O(5) \text{ vectors} \\ \overbrace{\Gamma_{\alpha 011}, \Gamma_{\alpha 021}, \Gamma_{0s03}} \\ A_{1k}^p \quad A_{2u}^t \end{array} \right\}. \quad (6.55)$$

One can immediately recognize the pattern where two adjacent and fully (or partially) anticommuting phases fulfill the selection rules (Ia) and (Ib). Selection rule (Ia) in Eq. (5.2) requires that the kernel of the interaction term and the bilinear order parameter are the same. Since the quartic interactions are written in the particle-hole basis, the four-fermion term in the AFM channel is the dominant interaction with $U > 0$. Indeed the phase diagrams with finite repulsive Hubbard interactions accommodate the same ordered phases as those corresponding to the purely antiferromagnetic interaction channel [Fig. 6.3(d)]. Consequently, the resulting composite order parameters $\mathbf{V}_{\text{MLG}}^{\text{U}}$ and $\mathbf{V}_{\text{BLG}}^{\text{U}}$ are the same as $\mathbf{V}_1^{\text{AFM}}$ and $\mathbf{V}_2^{\text{AFM}}$ in Eq. (6.61), respectively. As mentioned in Sec. 6.4, the different pairing orders arising in MLG and BLG are due to the fact that the singlet Kekulé pairing is a gapped phase only in BLG, while in MLG the maximally anticommuting pairing order parameter is the E_g nematic superconductor. Such a distinction in the paired state at low temperature *solely* stems from the differences in the normal state band structures in these two systems, in agreement with selection rule (II).

6.4.2 Nearest neighbor repulsion (V_1)

Next we turn our focus to the H_{V_1} term in Eq. (6.46), which models (with $V_1 > 0$) a finite ranged Coulomb repulsion between electrons on the NN sites. We derive the initial conditions similarly to those for the on site repulsion. The Hamman decomposition in this case reads

$$H_{V_1} = \frac{V_1}{4} \sum_{\mathbf{A}} \sum_{\tau=\pm} \tau \left[n(\mathbf{A}) + \tau \sum_{i=1}^3 n(\mathbf{A} + \boldsymbol{\delta}_i) \right]^2. \quad (6.56)$$

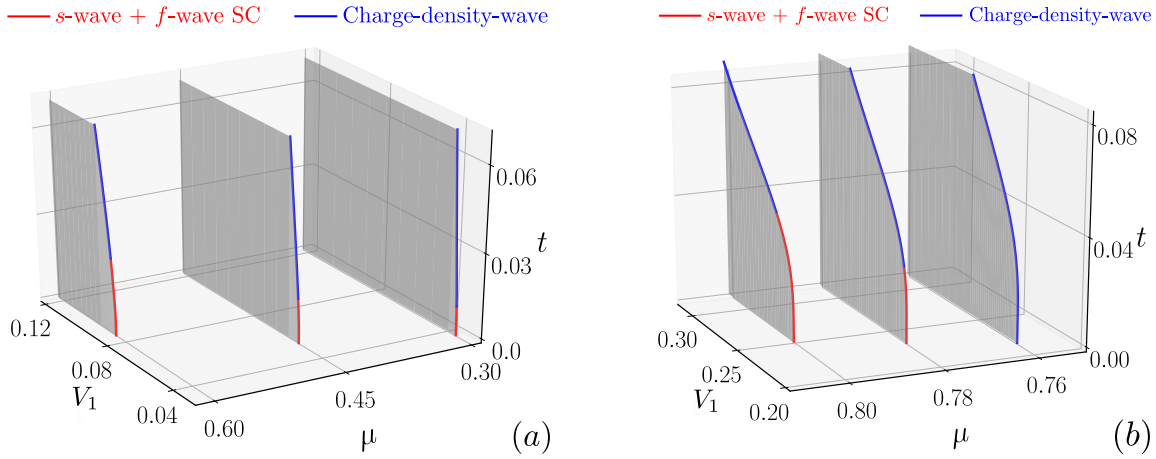


Figure 6.8: Representative cuts of the phase diagram of the extended honeycomb Hubbard model [see Eqs. (6.45) and (6.46)] in the presence of only the nearest-neighbor (NN) repulsion ($V_1 > 0$). Each cut is shown in the (V_1, t) plane, for various fixed values of chemical potential μ . The effects of $V_1 > 0$ are shown in panels (a) and (b) for MLG and BLG, respectively, where V_1 parametrizes the bare dimensionless NN interaction strength. The adjacent s -wave and f -wave superconductors (SCs) and excitonic phases respectively form $O(3)$ and $O(4)$ supervector order parameters, shown in Eq. (6.61). The rest of the details are identical to the ones in Fig. 6.7. Figure adapted from Ref. [13].

In our basis the second term takes the form

$$\sum_{i=1}^3 n(\mathbf{A} + \boldsymbol{\delta}_i) = \frac{3}{2} \Psi^\dagger \Gamma_{3000} \Psi - \frac{3}{2} \Psi^\dagger \Gamma_{3003} \Psi, \quad (6.57)$$

while the number operator on the \mathbf{A} sites can be written as

$$n(\mathbf{A}) = \frac{1}{2} \left(\Psi^\dagger \Gamma_{3000} \Psi + \Psi^\dagger \Gamma_{3003} \Psi \right) + \frac{\cos(2\mathbf{K} \cdot \mathbf{x})}{2} \left(\Psi^\dagger \Gamma_{3010} \Psi + \Psi^\dagger \Gamma_{3013} \Psi \right) + \frac{\sin(2\mathbf{K} \cdot \mathbf{x})}{2} \left(\Psi^\dagger \Gamma_{3020} \Psi + \Psi^\dagger \Gamma_{3023} \Psi \right). \quad (6.58)$$

We again neglect the oscillatory terms when taking the square of the density and the staggered density, and arrive at the expression

$$H_{V_1} = 3 \frac{V_1 a^2}{4} \left[(\Psi^\dagger \Gamma_{3000} \Psi)^2 - (\Psi^\dagger \Gamma_{3003} \Psi)^2 \right]. \quad (6.59)$$

After rescaling as $3V_1 a^2/4 \rightarrow V_1$ we obtain for the bare values of the coupling constants to be

$$g_1^s(\ell = 0) = -V_1, \quad g_5^s(\ell = 0) = V_1, \quad (6.60)$$

and $g_i^s(\ell = 0) = 0$ for $i = 2, 3, 4, 6, 7, 8, 9$.

At $\mu = t = 0$ we find the charge density wave (A_{2u}^s) ordering in both MLG [Fig. 6.8(a)] and BLG [Fig. 6.8(b)], while setting $\mu > 0$ results in a *degenerate* nucleation of singlet

s -wave and triplet f -wave pairing phases. The corresponding composite order parameters are

$$\mathbf{V}_1^{V_1} = \left\{ \begin{array}{c} \text{O(3) vector} \\ \overbrace{\Gamma_{1000}, \Gamma_{2000}, \Gamma_{3003}} \\ \underbrace{A_{1g}^p \quad A_{2u}^s} \end{array} \right\}, \quad \mathbf{V}_2^{V_1} = \left\{ \begin{array}{c} \text{2 copies of O(4) vectors} \\ \overbrace{\Gamma_{1s30}, \Gamma_{2s30}, \Gamma_{3003}} \\ \underbrace{A_{1u}^p \quad A_{2u}^s} \end{array} \right\}. \quad (6.61)$$

Following analogous logic to the on site repulsion case, we find that the quartic term in the CDW channel is the dominant interaction that fulfills the selection rule (Ia), while the adjacent pairing orders are the s -wave and f -wave superconductors, satisfying the selection rule (Ib). This can be anchored by comparing $\mathbf{V}_1^{V_1}$ and $\mathbf{V}_2^{V_1}$ with Eq. (6.34), as well as Figs. 6.8(a) and 6.8(b) with Fig. 6.3(b). Note the appearing pairing phases fully gap both systems, and therefore we do not see an order differentiation between MLG and BLG, unlike the situation for the on site repulsion. Below the transition temperature, we expect the pure superconducting state to display either $s + if$ or $f + is$ symmetry that maximally gaps the underlying Fermi surface [69].

6.4.3 Next-nearest neighbor repulsion (V_2)

Finally, we examine the effect of the H_{V_2} term in Eq. (6.46), that describes NNN repulsion. Each site on the honeycomb lattice has six NNNs, and the repulsion in this case acts between sites belonging to the same sublattice. The six vectors separating NNNs are $\pm \mathbf{v}_i$, $i = 1, 2, 3$, where \mathbf{v}_1 and \mathbf{v}_2 are the primitive lattice vectors defined in Sec. 6.1.1, and $\mathbf{v}_3 = \mathbf{v}_2 - \mathbf{v}_1$ [see Fig. 6.2]. Once again we decompose the quartic terms and write

$$H_{V_2} = \frac{V_2}{4} \sum_{\mathbf{A}, \mathbf{B}} \sum_{i=1}^3 \sum_{\tau, \lambda=\pm} \left[n(\mathbf{A}) + \tau n(\mathbf{B}) \right] \times \left[n(\mathbf{A} + \lambda \mathbf{v}_i) + \tau n(\mathbf{B} + \lambda \mathbf{v}_i) \right]. \quad (6.62)$$

The first factor of the product contains the density and staggered density, the form of which we already derived in Eqs. (6.48) and (6.49), respectively, while the two terms in the second factor can be written as

$$\sum_{i=1}^3 \sum_{\lambda=\pm} \left[n(\mathbf{A} + \lambda \mathbf{v}_i) + n(\mathbf{B} + \lambda \mathbf{v}_i) \right] \quad (6.63)$$

$$= 6\Psi^\dagger \Gamma_{3000} \Psi - 3 \cos(2\mathbf{K} \cdot \mathbf{r}) \Psi^\dagger \Gamma_{3010} \Psi - 3 \sin(2\mathbf{K} \cdot \mathbf{r}) \Psi^\dagger \Gamma_{3020} \Psi,$$

$$\sum_{i=1}^3 \sum_{\lambda=\pm} \left[n(\mathbf{A} + \lambda \mathbf{v}_i) - n(\mathbf{B} + \lambda \mathbf{v}_i) \right] \quad (6.64)$$

$$= 6\Psi^\dagger \Gamma_{3003} \Psi - 3 \cos(2\mathbf{K} \cdot \mathbf{r}) \Psi^\dagger \Gamma_{3013} \Psi - 3 \sin(2\mathbf{K} \cdot \mathbf{r}) \Psi^\dagger \Gamma_{3023} \Psi.$$

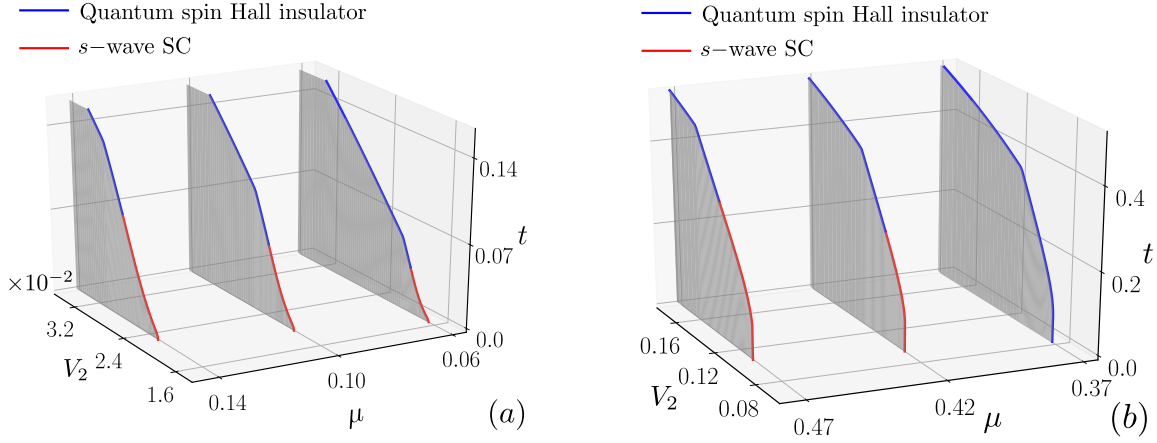


Figure 6.9: Representative cuts of the phase diagram of the extended honeycomb Hubbard model [see Eqs. (6.45) and (6.46)] in the presence of only the next nearest-neighbor (NNN) repulsion ($V_2 > 0$). Each cut is shown in the (V_2, t) plane, for various fixed values of chemical potential μ . The effects of $V_2 > 0$ are shown in panels (a) and (b) for MLG and BLG, respectively, where V_2 parametrizes the bare dimensionless NNN interaction strength. The adjacent superconductor (SC) and excitonic phases form an $O(5)$ super-vector order parameter, shown in Eq. (6.67). The rest of the details are identical to the ones in Fig. 6.7 and 6.8. Figure adapted from Ref. [13].

When performing the multiplication we again neglect any oscillatory terms, and write the continuum Hamiltonian as

$$H_{V_2} = 3\frac{V_2 a^2}{4} \left\{ 2(\Psi^\dagger \Gamma_{3000} \Psi)^2 + 2(\Psi^\dagger \Gamma_{3003} \Psi)^2 - \frac{1}{2} [(\Psi^\dagger \Gamma_{3010} \Psi)^2 + (\Psi^\dagger \Gamma_{3013} \Psi)^2 + (\Psi^\dagger \Gamma_{3020} \Psi)^2 + (\Psi^\dagger \Gamma_{3023} \Psi)^2] \right\}. \quad (6.65)$$

Rescaling $3V_2 a^2/4 \rightarrow V_2$, the initial conditions of NNN repulsion in the continuum formalism read

$$g_1^s(\ell=0) = g_5^s(\ell=0) = -2V_2, \quad g_9^s(\ell=0) = \frac{1}{2}V_2, \quad (6.66)$$

and $g_i^s(\ell=0) = 0$ for $i = 2, 3, 4, 6, 7, 8$.

At zero temperature and chemical potential we find quantum spin Hall insulator (A_{2g}^t) phase in both MLG and BLG, see Figs. 6.9(a) and 6.9(b) respectively. At finite chemical doping and sufficiently low temperatures, the adjacent pairing phase in both systems is the s -wave superconductor. These phases constitute the composite order parameter

$$\mathbf{V}^{V_2} = \left\{ \begin{array}{c} O(5) \text{ vector} \\ \overbrace{\Gamma_{\alpha 000}, \Gamma_{3s33}} \\ A_{1g}^p \quad A_{2g}^t \end{array} \right\}. \quad (6.67)$$

Note that both nucleating orders gap the Dirac, as well as the Luttinger fermions. The dominant interaction channel in the presence of NNN repulsion is the QSHI, and indeed the phase diagrams are analogous to Fig. 6.3(c), while the composite order parameter

\mathbf{V}^{V_2} is the same as $\mathbf{V}_1^{\text{QSHI}}$ in Eq. (6.35). Note, however, in contrast to the pure QSHI interaction channel, repulsive NNN interactions do not support singlet Kekulé pairing in BLG. This is likely due to the smectic charge density wave component in the corresponding initial conditions (g_9^s).

Notice, the phase diagrams of the extended Hubbard model share some common features. For example, with increasing chemical doping (1) any ordering sets in at stronger coupling, (2) the requisite strength for the repulsive interaction for the onset of any excitonic order gets pushed toward stronger coupling, and (3) range of interaction over which pairing phase is realized increases.

6.5 Summary and discussion

In this chapter we analyze a system of spinful fermions in monolayer and bilayer graphene, interacting via short range (or momentum-independent) Coulomb repulsion. We start by writing down the respective lattice models featuring tightly bound electrons and systematically deriving the low-energy continuum theories, that describe two copies of linear and biquadratic band touching, respectively. Retaining the Fourier components in the vicinity of the band touching points, we arrive at analogous descriptions for MLG and BLG, featuring the same number of degrees of freedom. Incorporating the contact interactions then involves constructing all quartic terms allowed by symmetry. As the point group describing the symmetry transformations of the lattice models is the same D_{3d} group for MLG and BLG, the interacting Lagrangian in Eq. (6.25) is *identical* in the two systems. We address the effect of short range electronic interactions in a perturbative fashion, via Wilsonian momentum-shell RG analysis and the ϵ expansion scheme up to the one-loop or leading order.

The central distinction in the continuum theories lies in the band structure, and the fact that the band touching points are linear (quadratic) in MLG (BLG). The purely linear (quadratic) dispersions result in the dynamic scaling exponent $z = 1$ (2) for Dirac (Luttinger) fermions at the non-interacting fixed point, and hence $\epsilon = d - z = 1$ (0) in the ϵ expansion. Since the coupling constants of contact interactions scale as

$$[g] = z - d = -\epsilon, \quad (6.68)$$

such interactions are irrelevant (marginal) in MLG (BLG). However, this only sets the physical value of ϵ in the RG scheme and therefore the location of the phase boundaries. More importantly, the k -linear functions (k_x and k_y) describing Dirac fermions in MLG are odd under inversion and transform under the E_u representation of the D_{3d} point group. In comparison, the d -wave harmonics ($k_x^2 - k_y^2$ and $2k_x k_y$) are even under inversion and thus transform under the E_g representation. To obtain an A_{1g} quantity, they are multiplied by matrices transforming under the same irreducible representation in the Hamiltonian.

This algebraic difference is the origin of order differentiation between MLG and BLG, as in the case for the purely on site Hubbard repulsion, which brings us to the main objective of this chapter.

In Chapter 5 we outline a set of selection rules, and argue that while rules (Ia) and (Ib) in Eq. (5.2) allow for two distinct ways for an ordered phase to be promoted via a certain contact interaction term, selection rule (II) in Eq. (5.3) is a generalized energy-entropy argument and organizes these phases along the temperature axis. The example of MLG and BLG is specifically suited to demonstrate these principles, since only (II) relies on the underlying band structure, while (I) is oblivious to it. Therefore, the ultimate ordered phases for a given interaction can in principle be different in MLG and BLG. We demonstrate the validity of the selection rules and organizing principle by increasing the strength of interactions in the individual channels and identifying the nature of symmetry breaking, see Tables 6.5 and 6.6. By adding chemical doping and forming an extended Fermi surface, we also obtain superconductivity from repulsive electronic interactions. We show that the nucleating pairing phases also obey the selection rules, and that the adjacent excitonic and pairing phases consequently constitute composite order parameters, that form an *enlarged* $O(N)$ algebra. For example, for two such competing orders with $O(N_1)$ and $O(N_2)$ symmetries, $N_1, N_2 < N \leq N_1 + N_2$.

Besides the individual interaction channels, we also consider a microscopic description of interacting electrons on the honeycomb lattice, the extended Hubbard model, containing the on site, the NN and the NNN components of the Coulomb repulsion. See Figs. 6.7–6.9 for the corresponding phase diagrams. Even though in this case we increase the strength of interactions in multiple channels at once, the dominantly diverging channel plays the role of M in the selection rules (Ia) and (Ib). Then, our findings for the extended Hubbard model are in complete agreement with the selection rules. Namely, for repulsive Hubbard U at half filling ($\mu = 0$) we find antiferromagnetic orderings in both systems, while chemical doping ($\mu > 0$) gives rise to E_g nematic pairing in MLG and A_{1k} singlet Kekulé superconductor in BLG. Either of these two pairings forms $O(5)$ composite order parameter with the antiferromagnet [see Eq. (6.55)]. In the presence of the NN repulsion ($V_1 > 0$), we find charge density wave ordering when $\mu = 0$ and simultaneous nucleation of both s -wave and f -wave pairing for $\mu > 0$ in both systems. The s -wave and f -wave pairings respectively form $O(3)$ and $O(4)$ composite order parameters with charge density wave [see Eq. (6.61)]. On the other hand, with the NNN repulsion ($V_2 > 0$), we observe a quantum spin Hall insulator phase at $\mu = 0$ and s -wave pairing for $\mu > 0$ in both systems, where these two phases maximally anticommute and form an $O(5)$ vector [see Eq. (6.67)].

This observation is in agreement with Ref. [14], where the authors carried out a non-perturbative functional RG analysis for the NN repulsive interaction. Note that only the f -wave pairing was found in this study, which, however, considered spinless fermions in MLG that does not permit s -wave pairing, due to the requisite antisymmetry property of

the electronic wave function. On the other hand, a quantum Monte Carlo study in Ref. [16] found quantum spin Hall insulator and s -wave superconductor phases, respectively at zero and finite doping. The dominant four-fermion interaction in this case is expected to be in the QSHI channel after integrating out the bosonic degrees of freedom. See Fig. 6.3(c).

In light of these qualitative agreements with non-perturbative numerical results, and considering their purely algebraic nature (based on (anti)commutation among matrices), we believe that the validity of our proposed selection rules goes beyond one-loop RG calculations. Nevertheless, in Appendix C.3.1 we show how they manifest in such a one-loop calculation at zero and finite temperature and zero chemical doping. Possible future investigations could target systems with existing experimental and/or numerical results, e.g. twisted bilayer graphene [217–220], Weyl semimetals [117, 118, 221], nodal-loop semimetals [222, 223], to name a few.

In the next chapter we revisit a system we already analyzed at zero temperature and chemical doping in Chapter 4, the three-dimensional Luttinger semimetal. Apart from the spatial dimensionality, this model is also distinct from MLG and BLG as it describes strongly spin-orbit coupled, effective spin-3/2 fermions. This gives us an opportunity to anchor our proposed selection rules and organizing principle in a significantly different system.

Chapter 7

Three dimensional Luttinger (semi)metal

In this chapter we consider the three-dimensional Luttinger semimetal, a system we studied in Chapter 4 at zero temperature and chemical doping. However, in possession of the selection rules and organizing principle, stated in Chapter 5 and verified so far in monolayer and Bernal bilayer graphene (Chapter 6), we now extend this analysis to finite temperature and chemical potential, which profoundly affect the competition among ordered phases. On one hand, the effect of finite chemical doping in nodal Fermi liquids is an enhanced carrier density via an extended Fermi surface, instead of the zero-dimensional Fermi point. This in turn promotes the condensation of electrons into Cooper pairs at low temperatures, since the corresponding superconducting order parameters can conceivably gap such a Fermi liquid (at least partially). By contrast, the effect of thermal fluctuations can promote ordered phases that are endowed with higher entropy, but are less energetically favorable. Therefore, the rich landscape of the Luttinger (semi)metal makes this system a good candidate for further anchoring the proposed selection rules and generalized energy-entropy argument.

For the details of the Luttinger model we refer the reader to Chapter 4, as well as to Appendix B.2. For example, in Sec. 4.2 we wrote down the symmetry appropriate interacting Lagrangian in terms of four independent quartic terms. We then carried out the Wilsonian RG analysis, following the spirit of ϵ expansion about the lower critical two spatial dimensions, already at finite temperature and chemical doping. While previously we took the limit $\mu \rightarrow 0$ and $t \rightarrow 0$ (in this order) in the RG flow equations (apart from the analysis of the scaling of the critical temperature, where we only took $\mu \rightarrow 0$), we here keep both of these two parameters finite. Furthermore, as in Chapter 4, we make use of the mass anisotropy parameter α , which allows us to tune the relative masses in the T_{2g} and E_g sectors of the octahedral (O_h) point group. The construction of phase diagrams follows in exactly the same way as outlined in Sec. 2.2.3.

7.1 Energy, entropy, and topology

Let us start by discussing the competition of energy and entropy [rule (II) in Chapter 5] inside ordered phases from a slightly different angle, when compared to Chapter 6. In the case of the honeycomb mono- and bilayer, we solely focused on the number of matrices in an order parameter that anticommute or commute with the Hamiltonian (A_H or C_H respectively). However, the energy-entropy competition can also be appreciated from the scaling of the DoS or the stiffness (uniform or anisotropic) of the spectral gap. This turns out to be equivalent to our previous approach, involving only matrix algebra, see Sec. 7.1.2. In what follows we highlight the reconstructed band structure inside the dominant ordered phases within a mean-field or Hartree-Fock approximation, which by construction undermines the order parameter fluctuations. The emergent band topology is computed by diagonalizing an effective single-particle Hamiltonian, composed of the noninteracting Luttinger Hamiltonian and corresponding order parameter, see Sec. 7.1.1 for details.

At zero temperature strong electronic interactions favor the phases that produce the largest spectral gap ($A_H - C_H = \text{maximal}$), as the onset of these ordered states offers maximal gain of condensation energy. In a LSM there are three candidate BSPs that yield fully gapped quasiparticle spectra: (a) an s -wave superconductor, producing a uniform and isotropic gap, and (b) two nematic orders (belonging to the T_{2g} and E_g representations), producing anisotropic gaps. As shown in Fig. 7.8, only these three phases can be found in an isotropic and interacting LSM at zero temperature.

While the s -wave pairing (nematic orders) produce a uniform (anisotropic) gap, two magnetic orders, belonging to the A_{2u} and T_{1u} representations, respectively produce eight [37] and two [43] isolated simple Weyl nodes, around which the DoS vanishes as $\varrho(E) \sim |E|^2$ for sufficiently low energies. On the other hand, each copy of the d -wave pairings accommodates two nodal loops for which the low-energy DoS scales as $\varrho(E) \sim |E|$ [see Sec. 7.1.2] [122, 136, 137, 224, 225]. Since we are interested in energy or temperature scales much smaller than the ultraviolet cutoff or bandwidth ($|E| \ll 1$), the structure of the spectral gap (isotropic or anisotropic) and power-law scaling of DoS carry sufficient information to organize the ordered phases according to their contribution to condensation energy and entropy, summarized in Fig. 7.5. In brief, existence of more gapless points (resulting in higher DoS near $E = 0$) yields larger entropy, while a more uniform gap leads to higher gain in condensation energy. This conclusion is consistent with the organizing principle [rule (II) in Chapter 5], as the low-energy DoS increases with increasing (decreasing) C_H (A_H), see Fig. 7.5. We can verify these expectations e.g., in various cuts of the phase diagram in Fig. 7.8, at finite temperature but at zero chemical potential. Note, since the DoS in a LSM scales as $\varrho(E) \sim \sqrt{E}$ (maximal entropy), it can always be found at sufficiently high (weak) enough temperature (interactions).

A similar conclusion can also be arrived at when the chemical potential is placed away from the biquadratic band touching point. At finite chemical doping all particle-

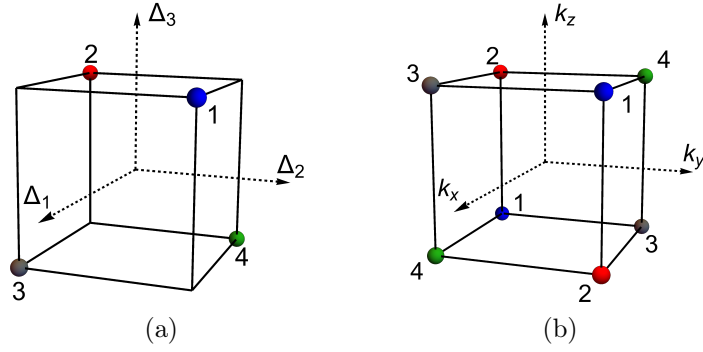


Figure 7.1: (a) Four phase lockings (blue, red, green and black dots) of the three component T_{2g} nematic order, see Eq. (7.1), that yield gapless phase (topological Dirac semimetal) inside the ordered state. Corresponding locations of two Dirac points in momentum space are shown in panel (b). For any other generic phase locking, the ordered phase is a time-reversal symmetry preserving insulator. Dirac points are located along the body-diagonals (C_{3v} axes in a cubic system). Figure adapted from Ref. [119].

hole (two nematic and two magnetic) orders produce a Fermi surface (according to the Luttinger theorem [226]) and hence a finite DoS. By contrast, any superconducting order at finite doping maximally gaps the Fermi surface. Therefore, at finite chemical doping superconducting orders are energetically superior to the excitonic orders, and they can be realized at sufficiently low temperature even in the presence of repulsive electronic interactions. Concomitantly, the particle-hole orders are pushed to the higher temperature and interaction regime, see Fig. 7.9.

Even though we gain valuable insights into the organization of various BSPs in the global phase diagram of strongly interacting spin-3/2 fermions from the competition between energy and entropy inside the ordered phases (guided by emergent topology of reconstructed band structure), the phase diagrams shown in Figs. 7.8 and 7.9 are obtained from an unbiased RG analysis, which systematically accounts for quantum fluctuations beyond the saddle point or mean-field approximation. To proceed, in the next section we discuss the reconstructed band structure in various ordered phases.

7.1.1 Reconstructed band structure and emergent topology

We now consider the reconstructed band structure inside different BSPs which provides valuable information regarding the emergent topology inside ordered phases. The onset of any ordering discussed in Sec. 4.2.1 destabilizes the biquadratic touching and gives rise to either gapped or gapless quasiparticles (see below). Furthermore, this exercise will allow us to appreciate the energy-entropy competition among different orderings [see Sec. 7.1.2], which ultimately plays a decisive role in the organization of various phases in the global phase diagram of interacting Luttinger fermions.

1. T_{2g} nematicity: The three component order-parameter for the T_{2g} nematic phase

gives birth to gapless quasiparticles for the following *four* configurations

$$\Delta_1 = \frac{|\Delta_1|}{\sqrt{3}} \left\{ \underbrace{(+, +, +)}_1, \underbrace{(-, -, +)}_2, \underbrace{(+, -, -)}_3, \underbrace{(-, +, -)}_4 \right\}. \quad (7.1)$$

These four phase lockings are respectively shown as blue, red, green and black points in Fig. 7.1(a). The gapless phase corresponds to a *topological* Dirac semimetal (since nematicity preserves the Kramers degeneracy of valence and conduction bands), similar to the ones recently found in Cd₃As₂ [75] and Na₃Bi [32]. The DoS in a Dirac semimetal vanishes as $\varrho(E) \sim |E|^2$. The Dirac points are located along the body diagonals (the C_{3v} axes) of a cubic system and respectively placed at

$$\mathbf{k} = \pm \left\{ \underbrace{(1, 1, 1)}_1, \underbrace{(1, 1, -1)}_2, \underbrace{(1, -1, 1)}_3, \underbrace{(1, -1, -1)}_4 \right\} k_0, \quad (7.2)$$

where $k_0 = [2m_1\Delta_1/3]^{1/2}$, as shown in Fig. 7.1(b). For any other phase locking within the T_{2g} sector the system becomes an *insulator*. The spectral gap in the insulating phase is *anisotropic* and it is energetically superior over the gapless Dirac semimetal phase, at least at low temperatures.

2. E_g nematicity: The two component E_g nematic order is most conveniently described in terms of the following parametrization

$$\Delta_2 = \frac{|\Delta_2|}{\sqrt{2}} \left(\sin \phi_{E_g}, \cos \phi_{E_g} \right), \quad (7.3)$$

where ϕ_{E_g} is the internal angle in the order-parameter space. Only for

$$\phi_{E_g} = \left\{ \underbrace{0}_1, \underbrace{2\pi/3}_2, \underbrace{4\pi/3}_3 \right\} \quad (7.4)$$

the quasi-particle spectra are gapless, as shown in Fig. 7.2(a), and the ordered phase represents a topological Dirac semimetal. Specifically, for $\phi_{E_g} = 0, 2\pi/3, 4\pi/3$, the Dirac points are respectively located on the k_z , k_x and k_y axes (the C_{4v} axes), see Fig. 7.2(b), and the separation of two Dirac points is given by $2k_0$, where $k_0 = [2m_2\Delta_2/\sqrt{2}]^{1/2}$. For any other phase locking within the E_g sector, the system becomes an insulator. Recently, it was shown that the gapless phases in both T_{2g} and E_g nematic phases correspond to higher-order Dirac semimetals supporting one-dimensional hinge modes, whereas the insulating phases accommodate a *mixed* topology, see Ref. [227] and Chapter 8 for a detailed discussion.

3. A_{2u} magnet: In the presence of an octupolar A_{2u} ordering, the two-fold degeneracy of the valence and conduction band gets lifted and a pair of Kramers non-degenerate

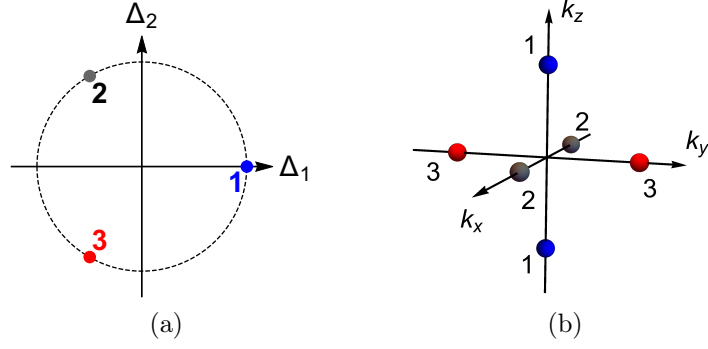


Figure 7.2: (a) Three possible phase lockings (shown by blue, black and red dots) of two-component E_g nematic order, see Eq. (7.4), that give rise to topological Dirac semimetals inside the ordered phase. The corresponding Dirac points inside the E_g nematic phase are located on the k_z , k_x and k_y axes (C_{4v} axes in a cubic system), as shown in panel (b), in contrast to the situation inside the T_{2g} nematic phase, see Fig. 7.1(b). For any other phase locking the system is an insulator. Figure adapted from Ref. [119].

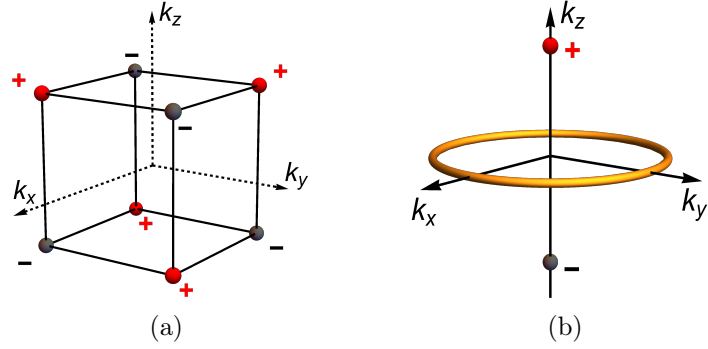


Figure 7.3: (a) Location of eight Weyl nodes in the presence of A_{2u} octupolar order, which in a pyrochlore lattice corresponds to the all-in all-out magnetic order. Here, red and gray dots respectively correspond to the source (+) and sink (-) of Abelian Berry curvature, with monopole charge ± 1 . (b) Nodal structure in the presence of a uniaxial T_{1u} order (when its moment points along \hat{z}), supporting two Weyl nodes separated along \hat{k}_z (red and gray dots) and a nodal loop (dark yellow ring) in the $k_x - k_y$ plane. When the moment of the uniaxial T_{1u} order points along \hat{x} and \hat{y} direction, the Weyl nodes are respectively separated along the k_x and k_y axes, and the nodal-loops are found in the $k_y - k_z$ and $k_x - k_z$ plane. By contrast, inside a *triplet* T_{1u} phase, only two Weyl nodes are found along one of the body diagonals. Figure adapted from Ref. [119].

bands touch each other at the following *eight* points in the Brillouin zone [see Fig. 7.3(a)]

$$\mathbf{k} = (\pm 1, \pm 1, \pm 1) k_0, \quad (7.5)$$

where $k_0 = \sqrt{2m_1\Delta_3/3}$. They represent simple Weyl points, which act as source (4 of them) and sink (4 of them) of Abelian Berry curvature of unit strength. However, due to an octupolar arrangement of the Weyl nodes, the net Berry curvature through any high-symmetry plane is precisely *zero* and this phase does not support any anomalous Hall effect. The DoS at low energies then scales as $\varrho(E) \sim |E|^2$ [37, 43, 134].

4. T_{1u} magnet: For each component of T_{1u} magnetic order (represented by the matrix operator $\Gamma_{45}\Gamma_j$ with $j = 1, 2, 3$) the ordered phase supports *two* Weyl nodes along one of the C_{4v} axes and a *nodal-loop* in the corresponding basal plane. For example, when $\langle \Psi^\dagger \Gamma_{45} \Gamma_3 \Psi \rangle \equiv \Delta_4^3 \neq 0$ the left and right chiral Weyl nodes are located at $(0, 0, \pm k_0)$, where $k_0 = \sqrt{2m_2\Delta_4}$, and a nodal-loop is found in the $k_x - k_y$ plane, as shown in Fig. 7.3(b). Similarly, for $j = 1$ and 2 the Weyl nodes are separated along the k_x and k_y axes, and the nodal-loops are respectively found in the $k_y - k_z$ and $k_x - k_z$ planes. Due to the presence of two Weyl nodes, each configuration of two-in two-out magnetic order supports a finite anomalous Hall effect in the plane perpendicular to the separation of the Weyl nodes. However, any *triplet* magnetic order, represented by $\mathbf{\Delta}_4 = |\Delta_4|(\pm 1, \pm 1, \pm 1)/\sqrt{3}$, gets rid of the nodal loop and supports only *two* Weyl nodes along one of the body-diagonals (C_{3v} axes). Hence, triplet T_{1u} magnetic orders are energetically favored over their uniaxial counterparts [43].¹

5. A_{1g} or *s*-wave pairing: Notice that the matrix operator representing an *s*-wave pairing fully anti-commutes with the Luttinger Hamiltonian (for any value of α) and thus corresponds to a genuine *mass* for Luttinger fermions. The quasiparticle spectra inside the paired state is fully gapped, but the phase is topologically *trivial*.

6. T_{2g} pairing: Three *d*-wave pairings, proportional to Γ_1 , Γ_2 and Γ_3 matrices, belong to the T_{2g} representation and respectively possess the symmetry of d_{yz} , d_{xz} and d_{xy} pairings. Each component supports two nodal loops in the ordered phase, as shown in the first three rows of Table 7.1 [122, 136]. Two nodal loops for the Γ_3 or d_{xy} pairing are shown in Fig. 7.4(a). The two nodal loops for Γ_1 or d_{yz} and Γ_2 or d_{xz} pairings can respectively be obtained by rotating the ones shown for d_{xy} pairing by an angle $\frac{\pi}{2}$, with respect to the k_y and k_x axes.

7. E_g pairing: E_g pairings proportional to Γ_4 and Γ_5 matrices respectively possess the symmetry of $d_{x^2-y^2}$ and $d_{3z^2-r^2}$ pairings and each of them supports two nodal loops, as shown in the last two rows of Table 7.1 [122, 136]. Note that two nodal loops for the $d_{x^2-y^2}$ pairing can be realized by rotating the ones for the d_{xy} pairing by an angle $\frac{\pi}{4}$ about the k_z axis. However, two nodal loops for the $d_{3z^2-r^2}$ pairing, shown in Fig. 7.4(b), cannot be rotated into the ones for the $d_{x^2-y^2}$ pairing. Therefore, despite the fact that the $d_{3z^2-r^2}$ and $d_{x^2-y^2}$ pairings belong to the same E_g representation, they are not energetically degenerate [122, 228]. Since the radius of the nodal loops for the $d_{3z^2-r^2}$ pairing is the *smallest*, this paired state is the energetically most favorable among five *d*-wave pairings.²

¹The low energy DoS in the presence of a nodal loop and two point nodes (due to a uniaxial T_{1u} order) is dominated by the former and scales as $\varrho(E) \sim |E|$, while in a triplet T_{1u} state the DoS scales as $\varrho(E) \sim |E|^2$ (due to the point nodes). Hence, formation of the triplet ordering causes power-law suppression of the DoS and increases the condensation energy gain.

²Even though $d + id$ type, such as $d_{x^2-y^2} + id_{3z^2-r^2}$, pairing can eliminate nodal loops from the quasiparticle spectra in favor of point nodes around which $\varrho(E) \sim |E|^2$ in a single band Fermi liquid [228], the strong inter-band coupling causes inflation of such nodes in doped LSM and yields Fermi surface of BdG quasiparticles, leading to a constant DoS at lowest energy, followed by $\varrho(E) \sim |E|^2$ a higher energies [229]. Presently, it is not clear between (a) individual *d*-wave pairings and (b) $d + id$ type pairings, which one is energetically more advantageous. However, based on the power-law scaling of DoS, we expect individual *d*-wave pairings to be energetically favored over $d + id$ type pairings at least when

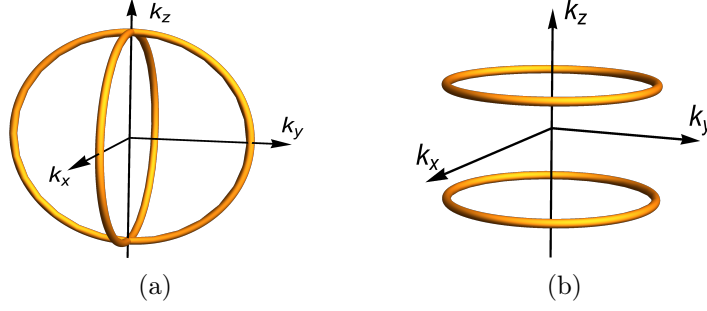


Figure 7.4: Structure of two nodal loops in the presence of an underlying (a) d_{xy} and (b) $d_{3z^2-r^2}$ pairings. These two pairings are respectively represented by Γ_3 and Γ_5 matrices for the Luttinger fermions. Note that the nodal loops for $d_{yz}(\Gamma_1)$, $d_{xz}(\Gamma_2)$, $d_{x^2-y^2}(\Gamma_4)$ pairings can be obtained by rotating the ones shown here for d_{xy} pairing about suitable momentum axes (see text). However, the two nodal loops for the $d_{3z^2-r^2}$ pairing are disjoint from the remaining ones (note these two nodal loops do not cross each other), see Sec. 7.1.1 and Table 7.1. Figure adapted from Ref. [119].

Pairing matrix	IREP (O_h).	Equations for nodal loops	Symmetry
Γ_1	T_{2g}	$k_x^2 + k_y^2 = 2m\Delta$, $k_x^2 + k_z^2 = 2m\Delta$	d_{yz}
Γ_2	T_{2g}	$k_x^2 + k_y^2 = 2m\Delta$, $k_z^2 + k_y^2 = 2m\Delta$	d_{xz}
Γ_3	T_{2g}	$k_y^2 + k_z^2 = 2m\Delta$, $k_x^2 + k_z^2 = 2m\Delta$	d_{xy}
Γ_4	E_g	$k_z^2 + k_\perp^2 = 2m\Delta$, $k_x = \pm k_y$	$d_{x^2-y^2}$
Γ_5	E_g	$k_\perp^2 = 4m\Delta/3$, $k_z = \pm k_\perp/\sqrt{2}$	$d_{3z^2-r^2}$

Table 7.1: The structure of two nodal loops in the presence of five individual d -wave pairings, belonging to the T_{2g} and E_g representations, where $k_\perp^2 = k_x^2 + k_y^2$. We display the symmetry of each d -wave pairing in the proximity to the Fermi surface (realized on the conduction or valence band) in the last column. Note that two nodal loops for d_{xy} , d_{xz} , d_{yz} and $d_{x^2-y^2}$ pairings can be rotated into each other, while those in the presence of $d_{3z^2-r^2}$ pairing are disconnected from the remaining ones, see Fig. 7.4. For the sake of simplicity we here assume $m_1 = m_2 = m$, for which the nodal loops are *circular* in shape. For $m_1 \neq m_2$, the nodal loops become *elliptic*. Here, Δ is the amplitude of d -wave pairings.

7.1.2 Energy and Entropy Inside Ordered Phases

From the computation of the reconstructed band structure we can gain insight into the condensation energy (Δ_F) and entropy (Δ_S) inside the ordered phases. While the *stiffness* of the spectral gap measures the gain of condensation energy, the scaling of the DoS at low-energies (due to gapless quasiparticles) measures the entropy. Recall

the inter-band coupling is strong, which is the case when pairing results from pure Hubbardlike repulsive interactions. This conclusion is in accordance with the organizing principle discussed in Sec. IIB1 and the energy-entropy argument, summarized in Fig. 7.5. The $|E|$ -linear DoS for individual d -wave pairings (stemming from the underlying nodal loops) results in a T -linear scaling of the penetration depth, as observed in YPtBi [58].

that the s -wave pairing yields fully gapped spectra (isotropic), while the nematic orders produce either an anisotropic gap or gapless quasiparticles. Hence, the former ordering is associated with higher (lower) gain in condensation energy (entropy). On the other hand, the DoS vanishes as $\rho(E) \sim |E|$ and $|E|^2$ respectively in the presence of a nodal-loop and Dirac or Weyl points. We found that the A_{2u} magnetic order gives birth to eight Weyl nodes, while only two Weyl nodes can be found inside the *triplet* T_{1u} magnetic order. By contrast, all five d -wave pairings are accompanied by two nodal loops (see Table 7.1). Therefore, we can organize these ordered phases according to their contribution to (a) condensation energy and (b) entropy gain, as shown in Fig. 7.5. The LSM, on the other hand, accommodates the largest amount of gapless fermionic excitations near zero energy, where the DoS vanishes as $\rho(E) \sim \sqrt{E}$. Hence, the LSM is endowed with largest entropy.³

This logic is consistent with the organizing principle, or selection rule (II) from Chapter 5, which can be verified by counting the number of matrix pairs A_H (C_H) in an order parameter that anticommute (commute) with the Luttinger Hamiltonian. Clearly, when $\mu = 0$

$$A_H + C_H = 5. \quad (7.6)$$

Then, for the s -wave pairing, two nematic orders, two magnetic orders and five d -wave pairings $A_H = 5, 4, 2, 1$, while $C_H = 0, 1, 3, 4$, respectively. Then for any ordered phase

$$\Delta_F \sim A_H, \quad \Delta_S \sim C_H. \quad (7.7)$$

Therefore, the analysis of the low-energy DoS in establishing a hierarchy of ordered phases with respect to their energy (entropy) gain is equivalent to counting the pairs of matrices A_H and C_H , as we saw in Chapter 6. Our analysis at finite temperature (in the regime where the dimensionless temperature $t = 2mT/\Lambda^2 \ll 1$) captures such energy-entropy competition, which we discuss in Secs. 7.2.1 and 7.2.2.

The hierarchy of the energy and entropy gains inside the ordered phases changes when the chemical potential is placed away from the band touching point (i.e., $\mu \neq 0$). Since any pairing operator *anticommutes* with the number operator ($\hat{N} = \eta_3 \Gamma_0$), superconducting orders maximally gap (either fully by the s -wave pairing or partially by the individual d -wave pairings) the Fermi surface. By contrast, any excitonic order always gives birth to a Fermi surface, according to the Luttinger theorem [226]. Hence, at finite doping all superconductors are energetically superior over the particle-hole orders, while excitonic orders are accompanied by larger entropy (due to presence of a Fermi surface). The energy-entropy competition at finite μ is also captured by the RG analysis, discussed in

³Such an organization of ordered phases according to their contributions to the gain of condensation energy and entropy is purely based on the power-law dependence of low-energy DoS or the stiffness (isotropic or anisotropic) of the spectral gap. This procedure, however, cannot distinguish two phases with similar scaling of the DoS, such as between A_{2u} and triplet T_{1u} magnetic orders (producing Weyl nodes), or the stiffness of the spectral gap, such as between T_{2g} and E_g nematic orders (producing anisotropic gaps). A more microscopic analysis is needed to resolve these situations.

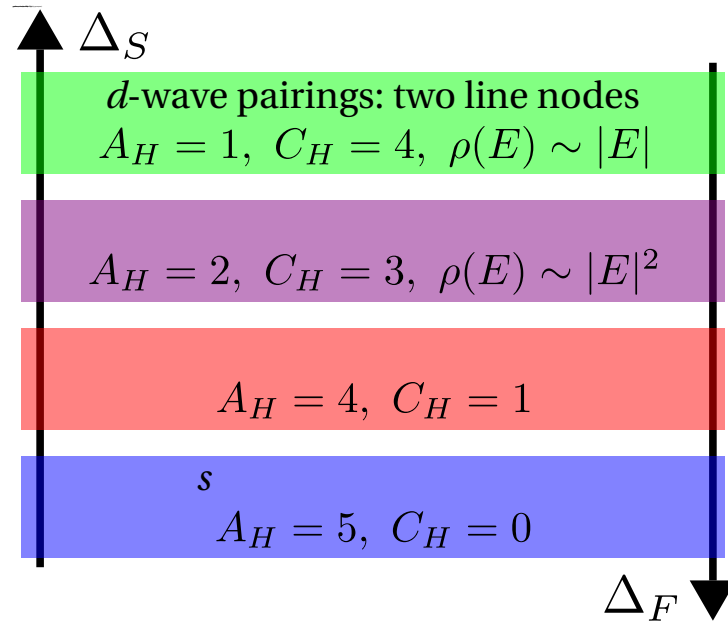


Figure 7.5: Hierarchy of various dominant orders in an interacting Luttinger semimetal according to the gain of the condensation energy (Δ_F) and entropy (Δ_S) inside the ordered phases. The condensation energy (entropy) gain increases in the direction of the $\Delta_F(\Delta_S)$ arrow. If an order-parameter matrix (M) anticommutes (commutes) with $A_H(C_H)$ number of matrices appearing in the Luttinger model [see Eq. (4.2)], then $\Delta_F \sim A_H$ and $\Delta_S \sim C_H$ (qualitatively), see Sec. 7.1.2 for detailed discussion. At finite chemical doping superconducting orders are always energetically superior over the excitonic ones. In the global phase diagram, phases with higher gain in condensation energy (entropy) appear at low (high) temperature, see for example Figs. 7.8 and 7.9. We also display the scaling of density of states [$\rho(E)$] at low-energies in the presence of both point and line nodes. Notice that with increasing A_H (C_H) the stiffness of the spectral gap (amount of gapless quasiparticles), determining the scaling of the DoS at low-energy, increases. Figure adapted from Ref. [119].

Sec. 7.2.3, leading to the phase diagrams shown in Figs. 7.9 and 7.10. In the presence of the chemical potential term in Eq. (4.2), $A_H \rightarrow A_H + 1$ for pairing orders and $A_H \rightarrow A_H - 1$ for excitons, while $A_H + C_H = 6$ for each order parameter matrix [for the definition of A_H and C_H see Eq. (5.1)].

7.2 Electron-electron interactions

Next we proceed to examine the dominant instabilities in various interaction channels in the Luttinger model at finite temperature and chemical doping. Note, in Sec 4.2 we already discussed the intricacies of the RG analysis in the Luttinger system. However, at that point we took the limit $\mu \rightarrow 0, t \rightarrow 0$, and focused on the quantum critical properties of the system, where only energetic considerations come into play. Here we address the competition of various BSPs and the role of thermal fluctuations and an extended Fermi surface therein.

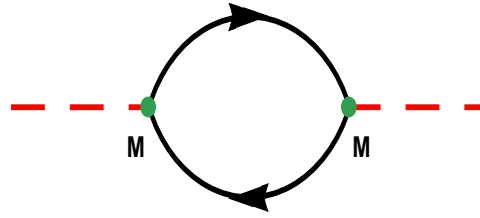


Figure 7.6: The Feynman diagram contributing to the leading order bare susceptibility (χ_M), given in Eq. (7.8), for zero external momentum and frequency. The *red* dashed (*black* solid) lines represent the order parameter (fermionic) fields. The two vertices (*green* dots) are accompanied by the appropriate eight-dimensional Hermitian order-parameter matrix M , appearing in the corresponding fermion bilinear $\Psi_{\text{Nam}}^\dagger M \Psi_{\text{Nam}}$. Figure adapted from Ref. [119].

First, however, we revisit the anisotropy parameter α in a mean-field framework. Note, by tuning α we can eliminate either the T_{2g} or the E_g sector from the Luttinger Hamiltonian in a continuous fashion. As the pertinent Clifford algebra only allows for 5 four-dimensional, mutually anticommuting Hermitian matrices [already exhausted by the Luttinger Hamiltonian, see Eq. (4.2)], this lets us affect the landscape of possible mass orders in a meaningful way. For example, by decreasing the weight significantly in the E_g sector (by sending $\alpha \rightarrow 0$), we make the E_g nematic order “almost mass”, while the same can be achieved for the T_{2g} nematic order when sending $\alpha \rightarrow \pi/2$. This ultimately effects the hierarchy of ordered phases in terms of their condensation energy and entropy gain.

7.2.1 Mean-field susceptibility

To gain insights into the propensity toward the formation of various orderings, we first compute the bare mean-field susceptibility (χ_M) of all possible symmetry allowed fermionic bilinears $\Psi_{\text{Nam}}^\dagger M \Psi_{\text{Nam}}$, where M is an eight dimensional Hermitian matrix (see Sec. 4.2.1). For simplicity we set $\mu = 0$. For zero external momentum and frequency this quantity is given by

$$\chi_M = -\frac{1}{2} \int \frac{d^3\mathbf{k}}{(2\pi)^3} \sum_{i\omega_n} \text{Tr} [M G_{\mathbf{k}}(i\omega_n) M G_{\mathbf{k}}(i\omega_n)]. \quad (7.8)$$

The relevant Feynman diagram is shown in Fig. 7.6 and the “-” sign arises from the fermion bubble. Here $G_{\mathbf{k}}(i\omega_n)$ is the fermionic Green’s function in the Nambu doubled basis. The factor of $1/2$ takes care of the artificial Nambu doubling. Results are displayed in Fig. 7.7. Next we discuss the scaling of χ_M in different channels for a few specific values of the mass anisotropy parameter.

7.2.1.1 Isotropic Luttinger Semimetal ($\alpha = \frac{\pi}{4}$)

For $\alpha = \frac{\pi}{4}$, the effective masses for the T_{2g} and E_g orbitals are equal (i.e. $m_1 = m_2$) and the system enjoys an enlarged spherical symmetry. Since each one of the five Γ -matrices

(representing two nematic orders) anti-commutes with four matrices and commutes with one matrix appearing in the Luttinger Hamiltonian, two nematic orders belonging to the T_{2g} (red curve) and E_g (orange curve) representations possess *equal* susceptibility. On the other hand, all ten commutators (representing various magnetic orders) anti-commute with three and commute with two matrices appearing in this model. Hence, magnetic orders in the A_{2u} (purple curve) and T_{1u} (magenta curve) channels also possess equal susceptibility. Two copies of the d -wave pairing, transforming under the T_{2g} (dark green curve) and E_g (dark yellow curve) representations, have degenerate susceptibilities, as all five d -wave pairing matrices commute with four matrices and anti-commute with only one matrix appearing in the Luttinger model. As the s -wave pairing fully anti-commutes with the Luttinger Hamiltonian, it always possesses the largest susceptibility (blue curve) for any α .

Susceptibilities for different BSPs (characterized by the bilinear order parameter $\Psi_{\text{Nam}}^\dagger M \Psi_{\text{Nam}} \sim A_H$, the number of matrices in $\hat{h}_{\text{L}}^{\text{Nam}}(\mathbf{k})$ anti-commuting with M). This simple correspondence is operative irrespective of the choice of α . Note that in an isotropic system $A_H = 5, 4, 3$ and 1 for the s -wave pairing, nematicity, magnetic orders and d -wave pairings, respectively, hence

$$\chi_M \left(\alpha = \frac{\pi}{4} \right) : s\text{-wave} > \text{nematic} > \text{magnetic} > d\text{-wave}.$$

Computation of the bare susceptibility suggests a strong propensity toward the formation of s -wave pairing and two nematic orders in the world of interacting spin-3/2 fermions with isotropic dispersion. The magnetic orders and d -wave pairings are expected to be suppressed near $\alpha = \frac{\pi}{4}$, at least at zero temperature [see Figs 4.2 and 7.8]. We also note that the gain in free-energy [see Sec. 7.1.2] and the mean-field susceptibility follow the same hierarchy $\Delta_F, \chi_M \sim A_H$.

7.2.1.2 Anisotropic Luttinger Semimetal near $\alpha = \frac{\pi}{2}$

When the effective mass in the T_{2g} orbital becomes sufficiently large, the Luttinger model simplifies to

$$\lim_{\alpha \rightarrow \frac{\pi}{2}} \hat{h}_{\text{L}}^{\text{Nam}}(\mathbf{k}) = -\eta_3 \frac{k^2}{2m_2} \sum_{j=4}^5 \Gamma_j \hat{d}_j(\hat{\mathbf{k}}). \quad (7.9)$$

This Hamiltonian possesses an emergent $\text{SU}(2) \otimes \text{U}(1)$ chiral symmetry, where $\{\Gamma_{45} \Gamma_j\}$ with $j = 1, 2, 3$ are the three generators of an $\text{SU}(2)$ rotation, whereas a $\text{U}(1)$ rotation is generated by $\hat{N} = \eta_3 \Gamma_0$, the number operator. In this limit the Hamiltonian is similar to the one for spinless fermions in Bernal-stacked bilayer graphene, which altogether supports

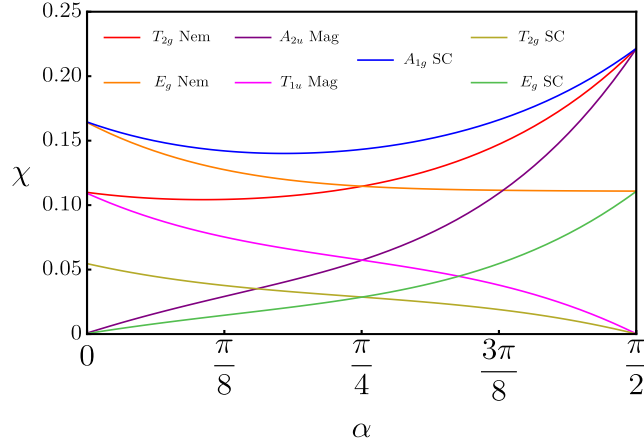


Figure 7.7: Bare mean-field susceptibility [see Eq. (7.8)] for zero external momentum and frequency [see Fig. 7.6 for the relevant Feynman diagram] for various orderings at zero temperature and chemical doping, as a function of α [parametrizing the anisotropy between the mass parameters in the T_{2g} and E_g orbitals]. Here, χ is measured in units of $m\Lambda$. For $\alpha = \frac{\pi}{4}$ two nematic orders and two d -wave pairings (belonging to the T_{2g} and E_g representations) possess equal susceptibilities, and so do two magnetic orders (transforming under the A_{2u} and T_{1u} representations). The A_{1g} s -wave pairing always possesses the largest susceptibility (for any α) as it represents a *mass* for spin-3/2 fermions. Susceptibilities for the s -wave pairing, T_{2g} nematic and A_{2u} magnetic orders display exact degeneracy as $\alpha \rightarrow \frac{\pi}{2}$, when all of them become *mass* [see Sec. 7.2.1.2]. On the other hand, as $\alpha \rightarrow 0$ the s -wave pairing and E_g nematicity become *mass* and their bare susceptibilities are degenerate and largest [see Sec. 7.2.1.3]. For detailed discussion consult Sec. 7.2.1. Figure adapted from Ref. [119].

six masses, given by

$$\mathbf{M}_{\frac{\pi}{2}} = \left\{ \begin{array}{c} \text{SO(5) vector} \\ \underbrace{\eta_3 (\Gamma_1, \Gamma_2, \Gamma_3)}_{T_{2g} \text{ nematic}}, \underbrace{(\eta_1, \eta_2) \Gamma_0}_{s\text{-wave}}, \underbrace{\eta_0 \Gamma_{45}}_{A_{2u} \text{ magnet}} \end{array} \right\}. \quad (7.10)$$

Note that three components of the T_{2g} nematicity break the continuous $SU(2)$ chiral symmetry, while the s -wave pairing breaks the global $U(1)$ symmetry. On the other hand, the A_{2u} magnet transforms as a scalar under the chiral rotation and breaks only time-reversal-symmetry. These three mass orders possess the largest and equal susceptibilities as $\alpha \rightarrow \frac{\pi}{2}$, see Fig. 7.7. Therefore, repulsive interactions favor two excitonic masses for zero [see Figs. 4.2(a), (c), and (d)], and s -wave pairing [see Fig. 7.10(a)] for finite chemical doping.

Also note that each member of the following vector

$$\mathbf{M}'_{\frac{\pi}{2}} = \left\{ \begin{array}{c} \text{multiplet of SO(3) vectors} \\ \underbrace{\eta_3 (\Gamma_4, \Gamma_5)}_{E_g \text{ nematic}}, \underbrace{(\eta_1, \eta_2) (\Gamma_4, \Gamma_5)}_{E_g \text{ d-wave}} \end{array} \right\}. \quad (7.11)$$

anti-commutes and commutes with one matrix appearing in $\lim_{\alpha \rightarrow \frac{\pi}{2}} \hat{h}_L^{\text{Nam}}(\mathbf{k})$. Hence, E_g nematicity and d -wave pairing have identical susceptibilities as $\alpha \rightarrow \frac{\pi}{2}$, but $\chi_{\mathbf{M}'_{\frac{\pi}{2}}} < \chi_{\mathbf{M}_{\frac{\pi}{2}}}$. As a result such an anisotropic system can accommodate an E_g d -wave pairing at finite chemical doping, see Fig. 7.10(c). However, T_{1u} magnet and T_{2g} d -wave superconductor have exactly *zero* susceptibility as they *fully commute* with $\lim_{\alpha \rightarrow \frac{\pi}{2}} \hat{h}_L^{\text{Nam}}(\mathbf{k})$. Hence, onset of these two orders is unlikely when $\alpha \approx \frac{\pi}{2}$.

7.2.1.3 Anisotropic Luttinger Semimetal near $\alpha = 0$

Finally, we compare the susceptibility for various orders when the mass of the E_g orbital becomes sufficiently large. The Luttinger Hamiltonian then takes the form ⁴

$$\lim_{\alpha \rightarrow 0} \hat{h}_L^{\text{Nam}}(\mathbf{k}) = -\eta_3 \frac{k^2}{2m_1} \sum_{j=1}^3 \Gamma_j \hat{d}_j(\hat{\mathbf{k}}), \quad (7.12)$$

which possesses an emergent $U(1) \otimes U(1)$ chiral symmetry, generated by $\eta_0 \Gamma_{45}$ and $\eta_3 \Gamma_0$. The mass orders in this limiting scenario constitute the following vector

$$\mathbf{M}_0 = \left\{ \begin{array}{c} \text{SO(4) vector} \\ \underbrace{\eta_3 (\Gamma_4, \Gamma_5)}_{E_g \text{ nematic}}, \underbrace{(\eta_1, \eta_2) \Gamma_0}_{s\text{-wave}} \end{array} \right\}. \quad (7.13)$$

and consequently the E_g nematicity and s -wave pairing acquire an identical and the largest susceptibility as $\alpha \rightarrow 0$, see Fig. 7.7. Hence, a competition between these two ordered phases can be anticipated near $\alpha = 0$ [see Figs. 7.10(b) and 4.2(b)]. Any order parameter from the following vector anti-commutes with two matrices and commutes with one matrix appearing in Eq. (7.12)

$$\mathbf{M}'_0 = \left\{ \begin{array}{c} \text{multiplet of SO(3) vectors} \\ \underbrace{\eta_3 (\Gamma_1, \Gamma_2, \Gamma_3)}_{T_{2g} \text{ nematic}}, \underbrace{\eta_0 \Gamma_{45} (\Gamma_1, \Gamma_2, \Gamma_3)}_{T_{1u} \text{ magnet}} \end{array} \right\}, \quad (7.14)$$

and they also possess degenerate susceptibilities, but $\chi_{\mathbf{M}'_0} < \chi_{\mathbf{M}_0}$. As a result, a competition between T_{1u} magnet and T_{2g} nematicity can also be observed around $\alpha = 0$, see Fig. 4.2(d). On the other hand, the T_{2g} d -wave pairing matrices anti-commute with one matrix and commute with two matrices appearing in Eq. (7.12) and its susceptibility is smaller than the orders appearing in \mathbf{M}_0 and \mathbf{M}'_0 . Nonetheless, when assisted by finite chemical doping, the T_{2g} d -wave pairing can be realized even for repulsive magnetic interaction in the T_{1u} channel, as shown in Fig. 7.10(d). Finally, we note that A_{2u} magnet

⁴This Hamiltonian is quite similar to the one for three-dimensional massless Dirac fermions, with the crucial difference that for the Dirac Hamiltonian $\hat{d}_j(\hat{k}) \sim k_j$, while for the Luttinger Hamiltonian $\hat{d}_j(\hat{k}) \sim |\epsilon_{jlm}| \hat{k}_l \hat{k}_m$, where $j, l, m = 1, 2, 3$.

and E_g d -wave pairing fully commute with $\lim_{\alpha \rightarrow 0} \hat{h}(\mathbf{k})$ and possess *zero* susceptibility. Hence, onset of these two orders around $\alpha = 0$ is extremely unlikely.

Note that various matrices appearing in $\mathbf{M}_{\frac{\pi}{2}}$, $\mathbf{M}'_{\frac{\pi}{2}}$, \mathbf{M}_0 , \mathbf{M}'_0 can form composite order-parameters and the enlarged symmetries among distinct orderings are displayed in Eqs. (7.10), (7.11), (7.13), (7.14). Such enlargement of order-parameter vectors plays an important role in determining the confluence of competing orders, see selection rule (I) in Chapter 5.

7.2.2 Renormalization group analysis

After gaining insight into the propensity toward various orderings in the Luttinger system, next we seek to investigate the onset of different BSPs and the competition among them within the framework of an unbiased RG analysis. This will allow us to go beyond the mean-field analysis, presented in the last section, and systematically incorporate quantum fluctuations. For this, we already set the stage in Secs. 4.2.2 and 4.2.3, where we unraveled the fixed point structure of the Luttinger semimetal for various values of α . Besides, in Secs. 4.2.4 and 4.2.5 we extracted the critical exponents of the second order phase transitions, leading from LSM into various BSPs, under the tuning of the bare interaction strength. What remains now is to address the role of temperature and chemical potential in the competition of ordered phases, an analysis analogous to that in Secs 6.3 and 6.4. We start with reconstructing the phase diagrams at finite temperature but zero chemical doping for the isotropic model. Finally, we examine the case where $T, \mu > 0$ for different values of α .

7.2.2.1 Phase diagrams at finite temperature

Besides the scaling of the transition temperature, we also investigate the phase diagram of an interacting LSM at finite temperature, allowing us to demonstrate the competition between condensation energy gain and entropy. For concreteness we focus on the isotropic system ($\alpha = \frac{\pi}{4}$), where this competition is most pronounced. As argued in Sec. 7.1.2, the onset of s -wave pairing leads to the maximal gain in condensation energy, while the two nematic orders produce higher entropy in comparison to the former. Two specific cuts of the global phase diagram, Figs. 7.8(a) and 7.8(b), show that while s -wave pairing is realized at low temperature, nematicities set in at higher temperature as we increase the strength of nematic interactions (g_1 and g_2) in the system.

By contrast, when we tune the magnetic interactions (namely g_3 and g_4), an isotropic LSM becomes unstable in favor of two nematic orders at $t = 0$. Such an outcome can be substantiated from the simple picture of condensation energy gain, as A_{2u} and T_{1u} magnetic orders accommodate Weyl nodes (yielding more entropy), while nematicities produce anisotropic spectral gap (leading to higher gain of condensation energy), see Sec. 7.1.2. As we tune the strength of the A_{2u} (T_{1u}) magnetic interaction, E_g (T_{2g}) nematic

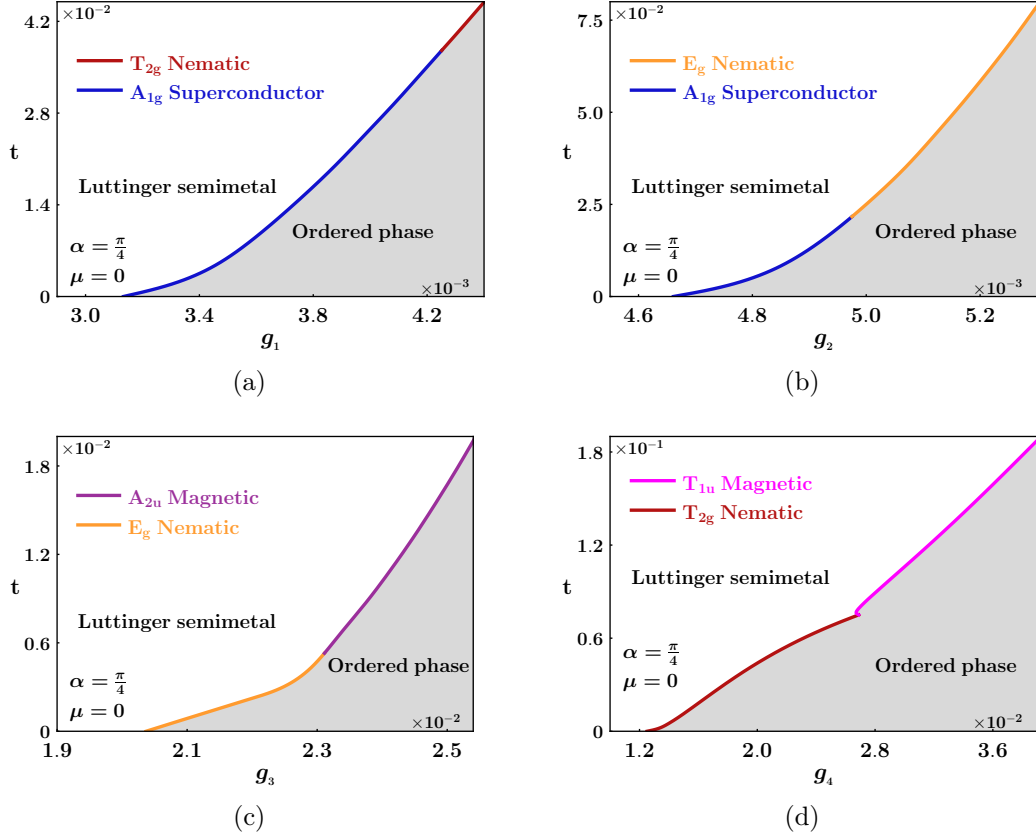


Figure 7.8: Various cuts of the finite temperature (t) phase diagram of an interacting isotropic Luttinger semimetal. The interaction couplings (g_i) are measured in units of ϵ . However, the nature of the order states in all cuts of the phase diagram is independent of the value of $\epsilon > 0$. Panels (a) and (b) respectively depict onset of T_{2g} and E_g nematic orders at higher temperatures as we tune interactions in these two channels. Recall while the s -wave superconductor yields fully gapped spectra, both nematic phases produce anisotropic gaps [see Sec. 7.1.1]. Hence, the energy-entropy competition [see Sec. 7.1.2] favors s -wave pairing (nematic phases) at low (high) temperature. When we tune the strength of (c) A_{2u} and (d) T_{1u} magnetic interactions, E_g and T_{2g} nematic orders set in at low temperature, respectively, and corresponding magnetic orders nucleate only at higher temperature, since both magnetic orders produce gapless Weyl fermions (less gain of condensation energy, but higher entropy). The white regions represent Luttinger semimetal without any ordering. The gray shaded region to the ordered phase, and its boundaries with Luttinger semimetal, occupied by various ordered phases are shown in different colors. Figure adapted from Ref. [119].

order sets in at lower and A_{2u} (T_{1u}) magnet at higher temperature, see Figs. 7.8(c) and 7.8(d).

The LSM is endowed with the largest entropy in the global phase diagram of interacting spin-3/2 fermions, since $\varrho(E) \sim \sqrt{E}$, in comparison to any BSP. Consequently, the requisite strength of interactions for any ordering increases with increasing temperature, irrespective of the nature of the BSP. Therefore, our RG analysis for an interacting LSM at finite temperature corroborates the energy-entropy competition picture [selection rule (II) in Chapter 5] and substantiates the following outcome: *ordered phases providing*

larger condensation energy gain are found at lower temperature, while at higher temperature, phases with larger entropy are favored. This observation is also consistent with the notion of reconstructed band structure and emergent topology, discussed in Sec. 7.1.1. Therefore, the phase diagram of an interacting LSM at finite temperature is guided by topological structure (gapped or nodal) of the competing BSPs.

We close this section by answering the following question: Why do we find two magnetic orders in an isotropic LSM at finite temperature, since this system supports only one QCP, see Table 4.1, where all the magnetic orders bear negative scaling dimension (see Table 4.2)? Note that any QCP can only be accessed at $t = 0$, whereas finite- t introduces an infrared cutoff ℓ_*^t [see Eqs. (2.38) and (2.39)] for the RG flow of the quartic couplings, and thus prohibits a direct access to any QCP. Hence, at finite- t , when magnetic interactions are sufficiently strong, the system can bypass the basin of attraction of $\text{QCP}_{\frac{1}{4}}$ and nucleate magnetic phases at moderately high temperature.

7.2.3 RG analysis in Luttinger metal ($\mu \neq 0$)

Finally we proceed to the RG analysis when the chemical potential (μ) is placed away from the biquadratic band touching point. The chemical potential introduces yet another infrared cutoff ℓ_*^μ [see Eqs. (2.38) and (2.39)], suggesting that the RG flow equations of the three quartic coupling constants should be stopped when the renormalized chemical potential $\mu(\ell)$ reaches the scale of the band-width $E_\Lambda = \Lambda^2/(2m)$. At finite temperature and chemical doping, two infrared scales compete and the *smaller* one ℓ_* (say), determines the ultimate infrared cutoff for the RG flow of g_j . The construction of phase diagrams is as outlined in Sec. 2.2.3 and applied e.g. in Sec. 6.3. The resulting phase diagrams for various choices of chemical potential, temperature, coupling constants and the mass anisotropy parameter (α) are shown in Figs. 7.9–7.11.

We note that in an isotropic system and for strong enough nematic interactions an s -wave pairing can be realized even for zero chemical doping [see Figs. 7.8(a) and 7.8(b)]. With increasing doping the s -wave pairing occupies larger portion of the phase diagram, while two nematic phases get pushed toward stronger coupling, see Fig. 7.9(a) and 7.9(b). However, the d -wave pairings do not set in for zero chemical doping. Nonetheless, when the magnetic interactions in the A_{2u} and T_{1u} channels are strong, the presence of a Fermi surface is conducive to the nucleation of d -wave pairings, belonging to the E_g and T_{2g} representations, respectively, see Figs. 7.9(c) and 7.9(d).

Now we focus on the anisotropic system. We chose the mass anisotropy parameter α such that at zero chemical doping the repulsive electronic interactions accommodate either nematic or magnetic orders, see Fig. 4.2. Specifically for $\alpha = 1.5$ (close to $\frac{\pi}{2}$) the system enters into the T_{2g} nematic [see Fig. 7.10(a)] or A_{2u} magnetic [see Fig. 7.10(c)] phase, while for $\alpha = 0.1$ (close to 0) we find E_g nematic [see Fig. 7.10(b)] or T_{1u} magnetic [see Figs. 7.10(d) and 7.11] order. For such specific choices of α , the QPTs into T_{2g} ne-

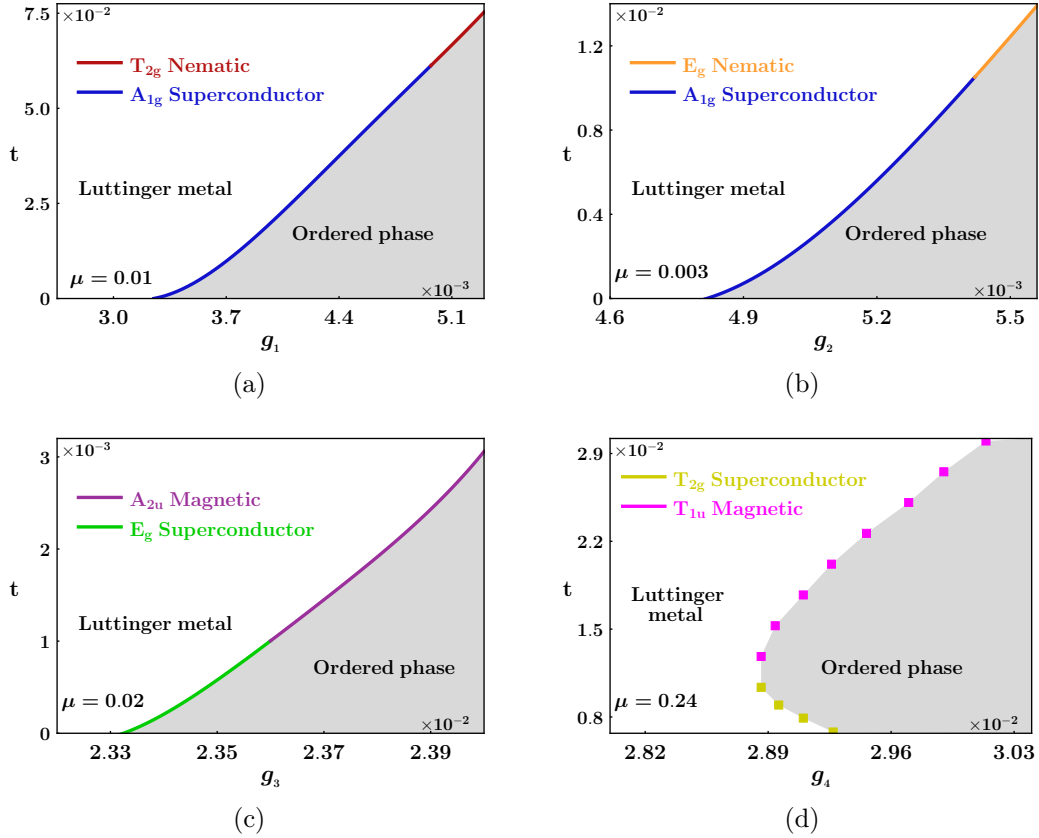


Figure 7.9: Realization of various pairing orders with finite chemical potential ($\mu > 0$). Top row: realization of s -wave pairing at low temperatures for quartic interactions in the (a) T_{2g} and (b) E_g nematic channels. The high-temperature phase in both cases is the corresponding nematic ordering. Bottom row: Onset of d -wave pairing belonging to the (c) E_g representation from magnetic interaction in the A_{2u} channel, and (d) T_{2g} representation from repulsive magnetic interaction in the T_{1u} channel. Magnetic interactions are therefore conducive for the nucleation of d -wave pairings in a correlated Luttinger metal. The high temperature phase in both cases is the corresponding magnetic order. Here coupling constants are measured in units of ϵ and the gray shaded regions represent ordered states. Note that the shape of the phase boundaries in (d) suggests that the LSM-ordered phase transition at low temperatures and finite chemical doping is possibly first-order in nature. Even though the RG methodology is tailored to capture continuous transitions, the possibility of a *first-order* transition is extremely sparse. The boundaries between Luttinger metal and various ordered phases are shown in different colors. Figure adapted from Ref. [119].

matic, E_g nematic, A_{2u} magnetic and T_{1u} magnetic orders are respectively controlled by QCP_0^1 , $\text{QCP}_{\frac{\pi}{2}}^1$, $\text{QCP}_{\frac{\pi}{2}}^2$ and QCP_0^2 [see Sec. 4.2.3 and Table 4.1]. At QPT_0^1 and $\text{QPT}_{\frac{\pi}{2}}^1$ the s -wave pairing possesses the largest scaling dimension among all possible local pairings [see Table 4.2]. Hence, in the presence of finite chemical doping, repulsive interactions in the nematic channels become conducive to s -wave pairing, as shown in Figs. 7.10(a) and 7.10(b). On the other hand, at $\text{QPT}_{\frac{\pi}{2}}^2$ (QCP_0^2), the d -wave pairing belonging to the E_g (T_{2g}) representation possesses the largest scaling dimension. Therefore, repulsive interactions in the A_{2u} (g_3) and T_{1u} (g_4) magnetic channels become conducive to the nu-

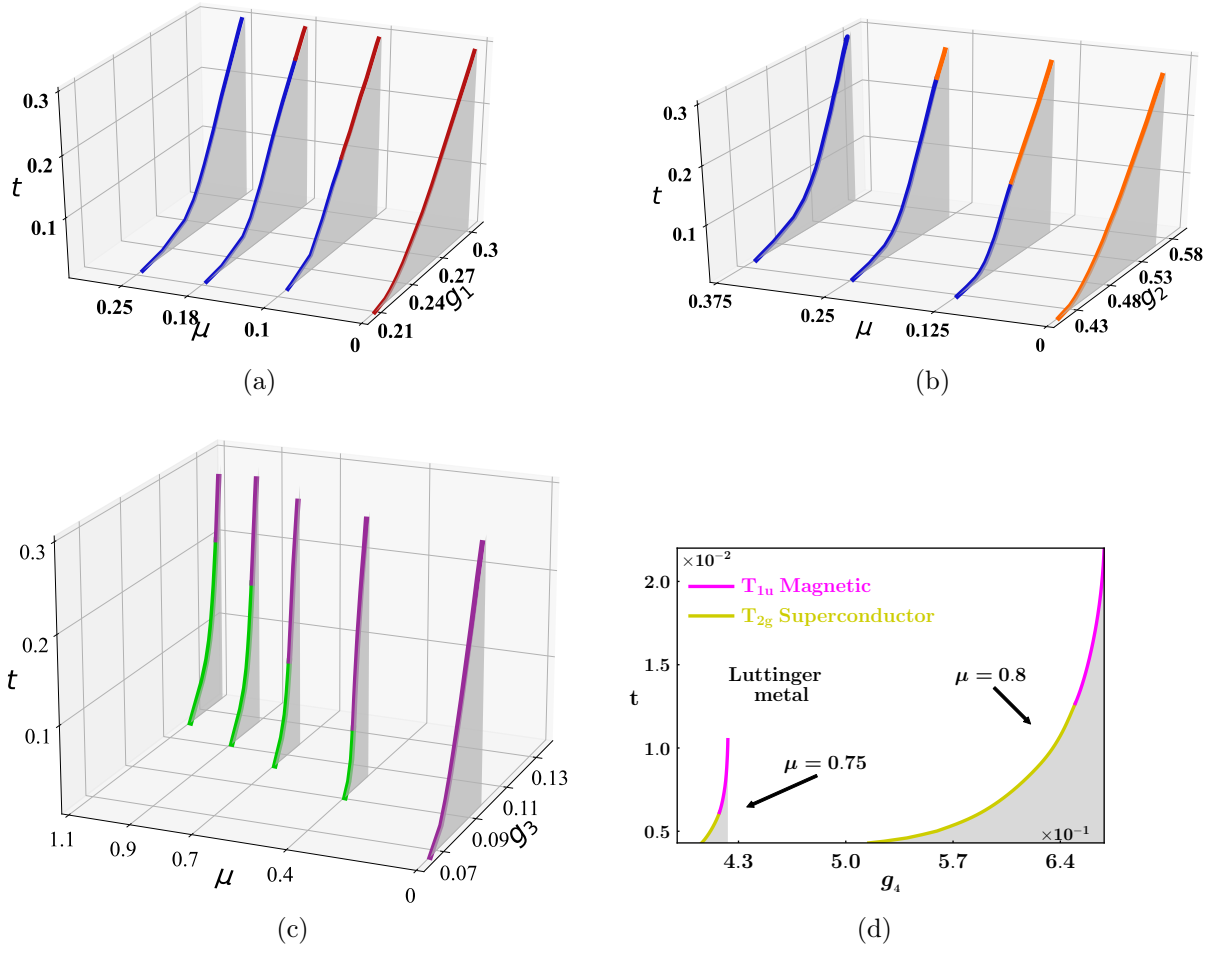


Figure 7.10: Specific cuts of the phase diagram of an interacting, anisotropic Luttinger metal ($\alpha \neq \frac{\pi}{4}$), showing the appearance of various superconducting phases at finite chemical doping ($|\mu| > 0$) from repulsive electron-electron interactions, but only excitonic orders for $\mu = 0$. (a) and (b): appearance of a conventional s -wave pairing (blue lines) from strong repulsive interaction in the T_{2g} and E_g nematic channels for $\alpha = 1.5$ and $\alpha = 0.1$, respectively [see also Figs. 4.2(a) and 4.2(b)]. The phase boundaries with the Luttinger (semi)metal are respectively denoted by red and orange lines. (c) and (d): nucleation of topological d -wave pairings, belonging to the E_g and T_{2g} representations (green and yellow lines respectively), from strong repulsive magnetic interactions in the A_{2u} and T_{1u} channels for $\alpha = 1.5$ and $\alpha = 0.1$ [see also Figs. 4.2(c) and (d)]. The phase boundaries of A_{2u} and T_{1u} magnetic phases with Luttinger (semi)metal are shown in purple and magenta. Due to a large separation of the interaction strength g_4 required for any ordering at $\mu = 0$ and $|\mu| > 0$, we display the $\mu = 0$ cut of the phase diagram from (d) in Fig. 7.11. The region at weaker interaction and higher temperature is occupied by correlated Luttinger metal (white regions), without any long-range ordering. In panels (a) and (b) $100 g_i \rightarrow g_i$ and in (c) $10 g_i \rightarrow g_i$. Throughout the coupling constants are measured in units of ϵ and the ordered states are displayed as the gray shaded regions. Figure adapted from Ref. [119].

cleation of E_g [for $\alpha = 1.5$] and T_{2g} [for $\alpha = 0.1$] d -wave pairings, respectively, as shown in Figs. 7.10(c) and 7.10(d). We therefore conclude that *nematic and magnetic interactions among spin-3/2 Luttinger fermions are respectively conducive to the s -wave and d -wave pairings*. Otherwise, at finite chemical doping the excitonic orderings set in only for

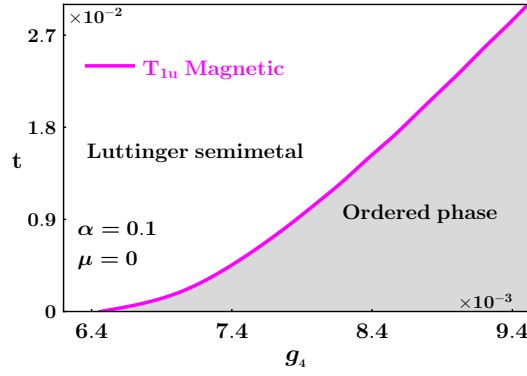


Figure 7.11: The phase diagram of an interacting Luttinger semimetal for $\alpha = 0.1$ and $\mu = 0$, obtained by tuning the strength of the magnetic interaction in the T_{1u} channel (g_4), measured in units of ϵ . The shaded (white) region represents the ordered phase (Luttinger semimetal). Figure adapted from Ref. [119].

stronger couplings. Such a generic feature is also consistent with the energy-entropy competition picture as the superconducting phases maximally gap the Fermi surface (yielding optimal gain of condensation energy), while excitonic orders are accompanied by a Fermi surface with constant DoS (producing more entropy).

7.2.4 Selection rules: Examples

To close our discussion on the competing phases in the Luttinger system, and further verify our proposed selection rules as it pertains to adjacent phases, let us point out some prototypical examples.

1. The T_{2g} nematic order (an $O(3)$ order-parameter) and s -wave pairing (an $O(2)$ order-parameter) constitute an $O(5)$ vector [see Eq. (7.10)], and these two ordered phases reside next to each other, see Figs. 4.2(a), 7.8(a), 7.9(a), and 7.10(a), when we tune the strength of g_1 .
2. The E_{2g} nematicity (an $O(2)$ order-parameter) and s -wave pairing constitute an $O(4)$ composite order parameter see Eq. (7.13). Figures 4.2(b), 7.8(b), 7.9(b), and 7.10(b) display a confluence of these two ordered phases, as one tunes the interaction g_2 .
3. The E_g nematicity and A_{2u} magnet (described by an $O(1)$ or Z_2 order-parameter) form an $O(3)$ vector [see Fig. 7.12(a)], and these two ordered phases often (in particular, when g_3 is tuned) reside next to each other, see Figs. 4.2(c) and 7.8(c).
4. One can construct multiple copies of $O(3)$ composite order parameters by combining the components of T_{2g} nematic and T_{1u} (an $O(3)$ order-parameter) magnetic orders [see Fig. 7.12(b) and (c)], and these two phases can be realized by tuning the quartic interaction g_4 , see Figs 4.2(d) and 7.8(d).

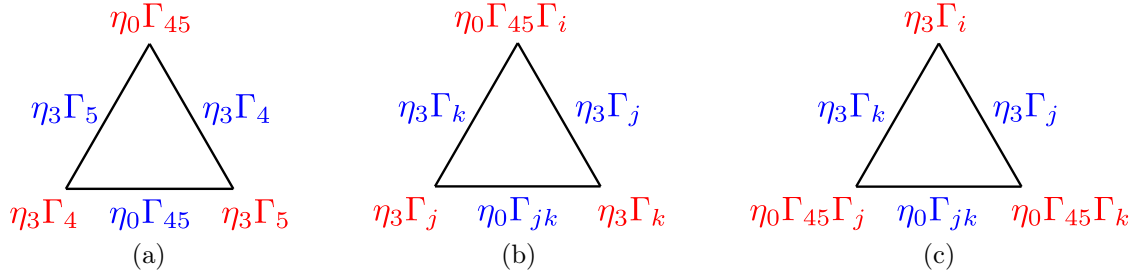


Figure 7.12: Schematic representations of SU(2) symmetry among (a) E_g nematic and A_{2u} magnetic orders, and (b)-(c) components of T_{2g} nematic and T_{1u} magnetic orders (with $i \neq j \neq k = 1, 2, 3$). Three vertices of each triangle are occupied by the order parameter matrices (in red), represented in the Nambu doubled basis [Ψ_{Nam} , see Eq. (4.13)]. Three arms of each triangle represent SU(2) rotations. The generators of SU(2) rotations (also in Nambu doubled basis) are shown in blue. Figure adapted from Ref. [119].

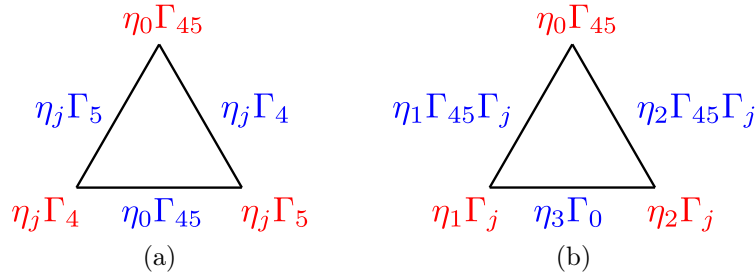


Figure 7.13: Schematic representation of SU(2) symmetry between the A_{2u} magnetic order and d -wave pairing belonging to the E_g representation. Notations are the same as in Fig. 7.12. In panel (a) $j = 1, 2$, whereas in panel (b) $j = 4, 5$. Figure adapted from Ref. [119].

5. A_{2u} magnetic order and E_g d -wave pairing (an O(2) order-parameter) can be combined to form O(3) vectors [see Fig. 7.13]. When the chemical potential is finite and we tune the strength of g_3 , the system accommodates a paired (magnetic) state at low (high) temperature, see Figs. 7.9(c) and 7.10(c).
6. Finally, note that multiple copies of an O(3) vector can be formed by combining the components of T_{1u} magnetic order and T_{2g} d -wave pairing (an O(2) order-parameter), see Fig. 7.14. These two phases reside next to each other at finite chemical doping when we tune the quartic coupling g_4 , see Figs. 7.9(d) and 7.10(d).

From the matrix representations of all quartic interactions [see Eq. (4.15)] and order parameters [see Eqs. (4.17) and (4.19)] the readers can convince themselves that the above examples are in agreement with our proposed selection rule from Chapter 5. It is admitted that we arrive at the conclusion from a leading order RG analysis. However, the selection rules themselves solely rely on the internal symmetry among competing orders. We therefore believe that our proposed selection rule is ultimately non-perturbative in nature, which can be tested at least in numerical experiments, for example.

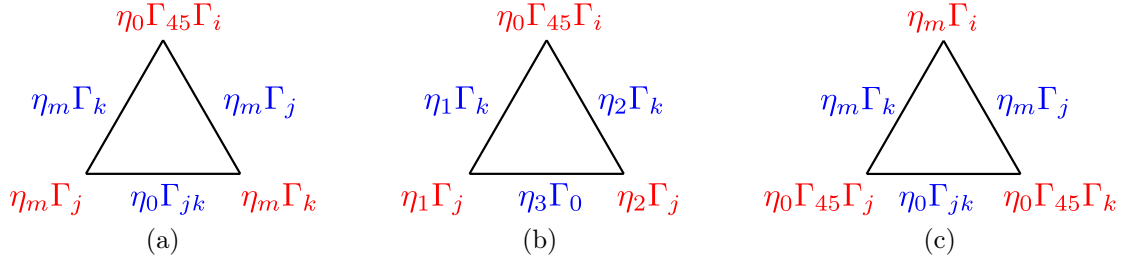


Figure 7.14: Schematic representation of SU(2) symmetry between the components of the T_{1u} magnetic order and T_{2g} d -wave pairing, with $i \neq j \neq k = 1, 2, 3$ [for (a), (b), (c)] and $m = 1, 2$ in (a) and (c). Notations are the same as in Fig. 7.12. Figure adapted from Ref. [119].

7.3 Summary and Discussions

Here we revisit the interacting Luttinger (semi)metal, previously introduced in Chapter 4, and examine it from the point of view of the selection rules and organizing principle, pronounced in Chapter 5. We already established the dominant instabilities in this system at zero temperature and chemical potential. We saw that in an isotropic system an s -wave pairing and two nematic orders are the prominent candidates for a broken symmetry phase. We also observed the absence of magnetic orders or d -wave pairing, at least when $t = 0$, which we explained with these orders being energetically inferior, due to the gapless spectra inside the ordered phase. Now we allow for finite temperature and chemical potential, and scrutinize various cuts of the global phase diagram. With increasing temperature, one finds a smooth crossover from nematic to magnetic phases, as shown in Fig. 7.8. This is an example of the organizing principle, or selection rule (II) from Chapter 5.

We introduce (chemical) doping as a non-thermal tuning parameter to map out the global phase diagram of an interacting Luttinger metal, see Sec. 7.2.3. Since paired states maximally gap the Fermi surface, their appearance at the lowest temperature is quite natural, at least when $|\mu| > 0$. By contrast, excitonic phases (insulators or semimetals) become metallike (possessing a finite density of states) at finite chemical doping, according to the Luttinger theorem [226]. Therefore, particle-hole orders are accompanied by higher entropy due to the presence of a Fermi surface (with a constant density of states). To demonstrate the energy-entropy competition in a metallic system, we choose the mass anisotropy parameter α such that at $\mu = 0$ the system only supports excitonic orders. Upon raising (lowering) the chemical potential to the conduction (valence) band, we observe that a superconducting order develops at low temperature and the excitonic order gets pushed toward higher temperature and stronger interactions, see Figs. 7.9 and 7.10. Therefore, the overall structure of the global phase diagram is compatible with the energy-entropy competition, dictated by the emergent band topology of competing broken

symmetry phases.

As an immediate outcome of the selection rules (Chapter 5) we realize that while repulsive interactions (short-range) in the nematic channels are conducive to s -wave pairing [see Figs. 7.8(a) and (b), 7.9(a) and (b), 7.10(a) and (b)], magnetic interactions favor nucleation of d -wave pairings [see Figs. 7.9(c) and (d), 7.10(c) and (d)] among effective spin-3/2 Luttinger fermions.

A few specific cuts of the global phase diagram corroborate with the ones extracted experimentally in $\text{Ln}_2\text{Ir}_2\text{O}_7$ [230] and half-Heusler compounds [57]. For example, a finite temperature phase transition from A_{2u} or all-in all-out magnetic order to a Luttinger semimetal has been observed in the majority of 227 pyrochlore iridates (except for $\text{Ln}=\text{Pr}$) [230], and Fig. 7.8(c) qualitatively captures this phenomena (for strong enough g_3). By contrast, $\text{Pr}_2\text{Ir}_2\text{O}_7$ supports a large anomalous Hall effect below 1.5K [41,42,231]. Note that a triplet T_{1u} or 3-in 1-out magnetic order supports anomalous Hall effect due to the presence of only two Weyl nodes in the ordered state (see Sec. 7.1.1 and Ref. [43]) and the phase diagram from Fig. 7.8(d) shows the appearance of T_{1u} magnetic order at finite temperature for strong enough interaction (g_4). It is worth recalling that ARPES measurements strongly suggest that isotropic Luttinger semimetal describes the normal states of both $\text{Nd}_2\text{Ir}_2\text{O}_7$ and $\text{Pr}_2\text{Ir}_2\text{O}_7$ [50,51]. On the other hand, half-Heusler compounds LnPdBi display a confluence of magnetic order and superconductivity [57], and the phase diagrams shown in Figs. 7.9(c) and (d), and 7.10(c) and (d) capture such competition (at least qualitative). This connection can be further substantiated from a recent penetration depth ($\Delta\lambda$) measurement in YPtBi [58], suggesting $\Delta\lambda \sim T/T_c$ (roughly) at low enough temperature, where $T_c = 0.78\text{K}$ is the superconducting transition temperature. Such a T-linear dependence of the penetration depth can result from gapless BdG fermions yielding $\varrho(E) \sim |E|$. Any d -wave pairing, producing two nodal loops (see Table 7.1), is therefore a natural candidate for the paired state in half-Heuslers (see also Refs. [122,136,137,224]). It is admitted that more microscopic analysis is needed to gain further insights into the global phase diagram of strongly interacting spin-3/2 fermions in various materials, which we leave for future investigation.

Part III

Higher-order topology in nodal semimetals

In the previous chapters we examined the effects of electronic interactions in nodal semimetals. The presence of Fermi points that replace the extended Fermi surface of a conventional Fermi liquid already has nontrivial consequences in terms of interaction induced spontaneous symmetry breaking, for example the absence of Kohn-Luttinger mechanism [72, 73] or the presence of interband scattering. In the following chapters, we leave the realm of interaction physics and examine nodal semimetals from the point of view of their topological properties. These two main themes of this thesis are, however, not entirely disjoint. For example, as we see shortly, the band Hamiltonian we write down in Chapter 8 can be seen as a description of the broken symmetry phase due to nematic ordering in a Luttinger semimetal (see Chapters 4 and 7), which ultimately endows nontrivial band topology.

For the basic knowledge on topological semimetals, the topological invariants, the bulk-boundary correspondence, surface states, etc. we refer the reader to the existing literature [21, 22, 77, 78, 232, 233]. However, to facilitate the upcoming discussion we now briefly review the notion of higher-order topological phases, which will be germane shortly. Traditionally, the bulk-boundary correspondence in a d -dimensional topological system refers to the boundary modes residing on a $(d-1)$ -dimensional surface, also characterized by the codimension $d_c = d - (d-1) = 1$ [21, 22, 77, 78, 233] (see also Eq. 1.1). These are nowadays called first-order topological phases. This notion has since been generalized to encompass boundary modes with $d_c > 1$, e.g., pointlike corner (with $d_c = d$) and one-dimensional hinge (with $d_c = d-1$) modes, which led to the construction of insulating (electric and thermal) and nodal higher-order topological phases [79–83, 85, 227, 234–248]. Namely, an n th order topological phase hosts boundary modes of codimension $d_c = n$. In what follows we examine such systems from two different aspects.

In Chapter 8 we demonstrate a possible construction of higher-order topological phases starting from the parent Luttinger semimetal (described in lengths in Chapters 4 and 7), and applying uniaxial strain. Strain explicitly breaks discrete rotational symmetry by favoring a direction (the direction of compressive or tensile strain), hence resulting in nematic phases. In Sec. 7.1.1 we outlined the reconstructed band structure inside nematic phases of a three-dimensional Luttinger semimetal. The cubic point group allows for two distinct types of deformation of the relevant d orbitals, splitting the previously five-fold degenerate $l = 2$ states into the T_{2g} and E_g sectors (three- and two-fold degenerate respectively). In general, both nematic sectors are *gapped*. However, for certain specific phase lockings the system exhibits a pair of *topological Dirac nodes*, see Figs. 7.1 and 7.2. We argue that these phases can be engineered by applying tensile or compressive strain along certain high-symmetry directions, the C_{3v} and C_{4v} axes for T_{2g} and E_g strain, respectively. We also show that the resulting phase diagram hosts various topological phases, including topological insulator of mixed topology and Dirac semimetal, as well as higher-order topological Dirac semimetal.

In Chapter 9 we address the question of stability of three-dimensional second-order

Dirac semimetal in the presence of random charge impurities. The phase diagrams of first-order topological Weyl and Dirac semimetals have been studied extensively, and these systems are generally believed to withstand weak enough disorder [24, 89, 90, 106, 249–267]. However, at some critical disorder strength they undergo a quantum phase transition into a diffusive metal phase. This phase transition falls outside the realm of the Anderson metal-insulator transition, which happens at even stronger disorder for first-order Weyl and Dirac semimetals. In this context, we have to mention the existence of debated, exponentially small rare-region effects [268–270], that might suggest an avoided quantum criticality in these systems. In spite of these first-order phases being stable against weak enough disorder, nothing a priori guarantees similar stability of their higher-order counterparts. Nevertheless, since any real-world material inherently contains impurities, an important step towards the realization of gapless higher-order topological phases (strain engineered or otherwise) is to study these systems in the presence of disorder. Note that, in contrast, insulating higher-order topological phases are expected to possess immunity against at least sufficiently weak disorder due to the presence of a finite band gap.

Chapter 8

Strain-engineered higher-order topological phases in a Luttinger semimetal

Let us start by first making a connection between our study of topology and broken symmetry phases. Though somewhat tangential, we already encountered such an example. Namely, in Sec. 7.1.1 we demonstrated that the organizing principle, ordering the available broken symmetry phases based on their condensation energy and entropy gains (see Chapter 5), can be appreciated from the point of view of the scaling of low-energy DoS, a direct consequence of the emergent band topology inside the ordered phase. In this section, however, we primarily focus on the surface states, appearing on the boundaries as a result of the bulk band topology.

In the preceding chapters we assumed general local electronic interactions, and unraveled the structure of a multidimensional flow of coupling constants under the RG transformation, to capture the dominant ordering via spontaneous symmetry breaking. Here we introduce an explicit breaking of rotational symmetry via the application of external strain, and assume this to represent the largest energy scale in the problem. Furthermore, we propose the Luttinger semimetal (LSM), consisting of spin-3/2 fermions with a biquadratic touching of Kramers degenerate valence and conduction bands [132, 133] (see Chapters 4 and 7), as a platform to strain engineer higher-order topological (HOT) phases.

Strain-engineering is of intense interest, being instrumental for the identification of nematic phases in correlated materials, such as cuprates, pnictides and heavy-fermion compounds [271, 272]. It also gives rise to exotic phenomena, such as axial magnetic fields in two- and three-dimensional Dirac and Weyl materials, producing topologically protected *zeroth* Landau levels [273, 274], or a quantum phase transition between a topological Dirac semimetal (TDSM) and trivial band insulator [123, 146, 275, 276], to name a few.

We here show that strain in a three dimensional LSM can induce a variety of higher-

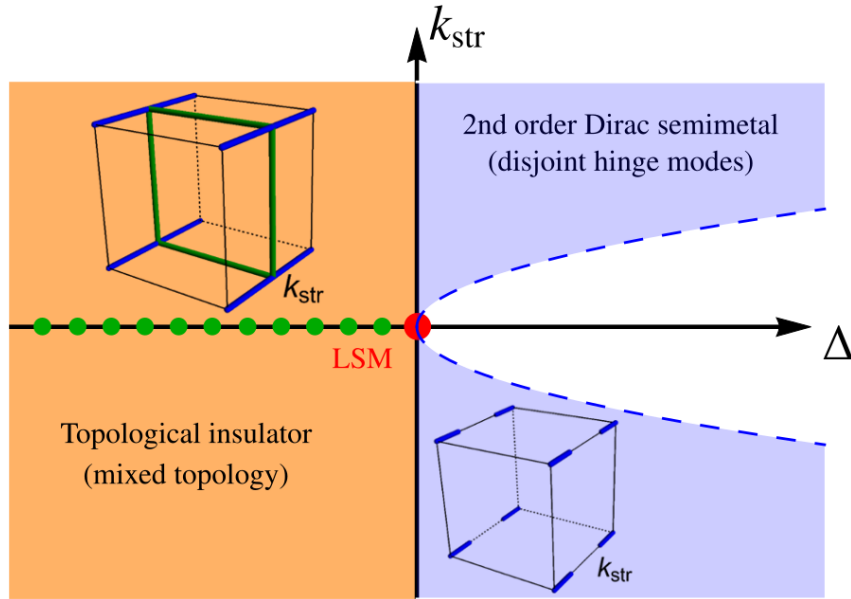


Figure 8.1: Schematic phase diagram of a LSM (red dot), in the presence of an external strain of magnitude $|\Delta|$. Here $\text{sgn}(\Delta) = + (-)$ corresponds to tensile (compressive) strain, which gives rise to a second order Dirac semimetal (topological insulator). The momentum in the direction of the external strain is k_{str} , and in the semimetal phase two Dirac points are separated along this axis, located at $\pm k_{\text{str}}^*$, where $k_{\text{str}}^* \sim \sqrt{|\Delta|}$. Both phases produce four hinge states of codimension $d_c = 2$, along k_{str} , see blue lines in the cubes (inset). In the insulating (Dirac semimetal) phase the hinge modes exist for any k_{str} ($|k_{\text{str}}| > k_{\text{str}}^*$). The insulator also supports edge modes (red lines) with $d_c = 1$ on the $k_{\text{str}} = 0$ plane (green dots), occupying two planes orthogonal to k_{str} . Hence, the topological insulator accommodates a mixed topology. The white region ($|k_{\text{str}}| < k_{\text{str}}^*$) is devoid of any boundary mode. In practice, k_{str} is a high symmetry ([100] or [111]) direction. Figure adapted from Ref. [227].

order topological (HOT) phases [79], both gapless and insulating. When stress is applied to a LSM along certain high-symmetry directions, such as the C_{4v} (x, y and z coordinate axes) or C_{3v} (four body diagonal or [111]) directions, the resulting strain induces either a TDSM or a topological insulator, when the sign of the strain is positive or negative (which we refer to as tensile or compressive, respectively). Both support four copies of one-dimensional hinge modes ($d_c = 2$) in the direction of the applied strain. In addition, the insulator supports edge modes that reside on two-dimensional surfaces ($d_c = 1$) perpendicular to the applied strain, thus exhibiting *mixed* topology. The resulting phase diagram is schematically shown in Fig. 8.1. Our results may be of experimental relevance to HgTe [45], gray-Sn [47,48], 227 pyrochlore iridates [50,51,134] and half-Heuslers [53–55]. Experimentally, tunable compressive or tensile strain can be applied using piezoelectric-based uniaxial stress apparatus [277] (by gluing the sample between the jaws of the uniaxial pressure device [278]), or on thin films by growing them on a substrate with slightly different lattice constant [279]. Although high-quality 227 pyrochlore iridate crystals tend to be small, methods to apply uniaxial stress to miniaturized samples are under active development.

8.1 Toy model

To set the stage, we first consider a model describing three-dimensional HOT phases (both insulator and semimetal), constituted by spin-1/2 fermions. The corresponding Hamiltonian can be decomposed as $\hat{h}_{\text{HOT}}(\mathbf{k}) = \hat{h}_0^{\mathbf{k}} + \hat{h}_1^{\mathbf{k}}$, where [83, 227, 239, 246]

$$\begin{aligned}\hat{h}_0^{\mathbf{k}} &= t \sum_{j=1}^2 S_j \gamma_j + \left[t_z C_z - m_z + t_0 \sum_{j=1}^2 (C_j - 1) \right] \gamma_3, \\ \hat{h}_1^{\mathbf{k}} &= \Delta_1 (C_y - C_x) \gamma_4 + \Delta_2 S_x S_y \gamma_5,\end{aligned}\tag{8.1}$$

$C_j \equiv \cos(k_j a)$, $S_j \equiv \sin(k_j a)$, k_j s are components of momenta, and a is the lattice spacing, set to unity. Four-component γ matrices satisfy the anticommuting Clifford algebra $\{\gamma_j, \gamma_k\} = 2\delta_{jk}$, for $j, k = 1, \dots, 5$. Even though the following discussion does not depend on the representation of γ matrices, for the sake of concreteness we choose

$$\gamma_1 = \sigma_3 \otimes \tau_1, \quad \gamma_2 = \sigma_0 \otimes \tau_2, \quad \gamma_3 = \sigma_0 \otimes \tau_3, \quad \gamma_4 = \sigma_1 \otimes \tau_1, \quad \gamma_5 = \sigma_2 \otimes \tau_1.\tag{8.2}$$

Two sets of Pauli matrices $\boldsymbol{\sigma}$ and $\boldsymbol{\tau}$ respectively operate on spin and sublattice indices.

Expanding $\hat{h}_{\text{HOT}}(\mathbf{k})$ around the $\Gamma = (0, 0, 0)$ point yields the effective low-energy model for HOT phases

$$\hat{h}_{\text{HOT}}^{\Gamma}(\mathbf{k}) = v \sum_{j=1}^2 k_j \gamma_j + \left[-\frac{t_z}{2} k_z^2 + \bar{\Delta} + t_0 \frac{k_{\perp}^2}{2} \right] \gamma_3 + \frac{1}{2} \Delta_1 (k_x^2 - k_y^2) \gamma_4 + \Delta_2 k_x k_y \gamma_5,\tag{8.3}$$

where $\bar{\Delta} = m_z - t_0$, $k_{\perp} = (k_x^2 + k_y^2)^{1/2}$ and $v = t$ bears the dimension of Fermi velocity. For $\Delta_1 = 0 = \Delta_2$, the system respectively describes a TDSM and a three-dimensional quantum spin Hall insulator (3D-QSHI) for $\bar{\Delta} > 0$ and $\bar{\Delta} < 0$. In the former phase, the Dirac points are located at $\mathbf{k} = (0, 0, \pm k_z^*)$, where $k_z^* = \sqrt{2\bar{\Delta}/t_z}$. The transition between these two phases takes place at $\bar{\Delta} = 0$, where the low-energy density of states scales as $|E|^{3/2}$ [24]. Both TDSM and 3D-QSHI can be constructed by stacking two-dimensional quantum spin Hall insulators (2D-QSHIs) in momentum space along the k_z direction (maintaining the translational symmetry), and the corresponding band inversion takes place at $k_{\perp}^* = [(t_z k_z^2 - 2\bar{\Delta})/t_0]^{1/2}$. Hence, for $t_0, t_z > 0$, the band inversion occurs for any k_z when $\bar{\Delta} < 0$. By contrast, when $\bar{\Delta} > 0$ it takes place only for $k_z > k_z^*$ and $k_z < -k_z^*$, while the two-dimensional insulators occupying the region $|k_z| \leq k_z^*$ are topologically trivial.

Both TDSM and 3D-QSHI support two copies of Fermi arc surface states, the loci of the zero-energy modes, associated with the one-dimensional counter-propagating edge states for opposite spin projections of the underlying 2D-QSHIs. Therefore, in the 3D-QSHI phase the Fermi arc exists for any k_z , while two disjoint pieces of arc are found for $k_z > k_z^*$ and $k_z < -k_z^*$ in the TDSM phase. In real space, such Fermi arcs occupy two-

dimensional surfaces in the xz and yz planes, and hence are characterized by codimension $d_c = 1$. Thus, both the TDSM and 3D-QSHI represent first order topological phases.

Turning on $\hat{h}_1^{\mathbf{k}}$ generates a mass for the one-dimensional edge states of the underlying 2D-QSHIs, as $\{\hat{h}_0^{\mathbf{k}}, \hat{h}_1^{\mathbf{k}}\} = 0$. Furthermore, this term hybridizes the edge modes for opposite spin projections. As $\hat{h}_1^{\mathbf{k}}$ changes sign under a discrete four-fold rotation, it assumes the profile of a domain wall. For $\Delta_2 = 0$, four states at precisely zero energy appear at the corner of such a system (according to a generalized Jackiw-Rebbi index theorem [280]) where $\hat{h}_1^{\mathbf{k}}$ changes sign, for $|k_z| > k_z^*$ when $\bar{\Delta} > 0$ or any k_z when $\bar{\Delta} < 0$. The collection of such corner localized zero-energy modes ultimately constitutes four copies of one-dimensional *hinge* states, extended along the z direction, implying a second order topological phase. Even when Δ_2 is finite, the hinge modes persist at half-filling, but now away from zero energy due to the loss of the spectral symmetry with open boundaries. Next we proceed to demonstrate these outcomes by diagonalizing Eq. (8.1) on a cubic lattice.

8.2 Lattice models

In this section we demonstrate appearance of the two-dimensional ribbon-like and one-dimensional hinge-like surface states for the Hamiltonian in Eq. (8.1) (describing a three-dimensional topological Dirac semimetal or insulator), which we diagonalize on a cubic lattice. The global phase diagram of the above model displays a confluence of topological (gapless as well as gapped) and trivial phases, which has been discussed in details in Ref. [24]. Instead of delving into such discussion again, we here focus on a few specific and relevant cases. For example, a first-order topological Dirac semimetal is realized for $t = t_z = t_0 = 1$, $m = 0$, and $\Delta_1 = \Delta_2 = 0$, and the Dirac points are then located at $(0, 0, \pm\pi/2)$. This phase supports doubly degenerate Fermi arc surface states [see Fig. 8.2(a)] that occupy the two-dimensional xz and yz surfaces, see Fig. 8.2(d). On the other hand, a topological quantum spin Hall insulator is found for $t = t_0 = 1$, $t_z = 0.5$, $m_z = -0.7$, and $\Delta_1 = \Delta_2 = 0$, for example. This phase also supports two-dimensional Fermi arc surface states, as shown in Figs. 8.3(a) and 8.3(d). The Fermi arcs are characterized by codimension $d_c = 1$, and these two topological phases are first order. Finally, we note that since $\hat{h}_0^{\mathbf{k}}$ contains only three mutually anticommuting matrices, it can always be cast into a block diagonal form and each such block is two-dimensional. Hence, $\hat{h}_0^{\mathbf{k}}$ is described by effective spin-1/2 fermions.

Second order topological phases can now be constructed by systematically reducing the dimensionality of Fermi arc surface states. If the crystal is cleaved such that the corners are at $(x, y) = (\pm L/2, \pm L/2)$ (for any z), this can be achieved by setting $\Delta_1 > 0$ in Eq. (8.1). Since $\{\hat{h}_0^{\mathbf{k}}, \hat{h}_1^{\mathbf{k}}\} = 0$, the above perturbation acts as a mass for the two dimensional Fermi arc surface states. However, it changes sign under four-fold or C_4 rotation, and hence the Fermi arcs get only partially gapped in their presence, yielding one-dimensional hinge modes with $d_c = 2$. The system then describes second order topological phases. The

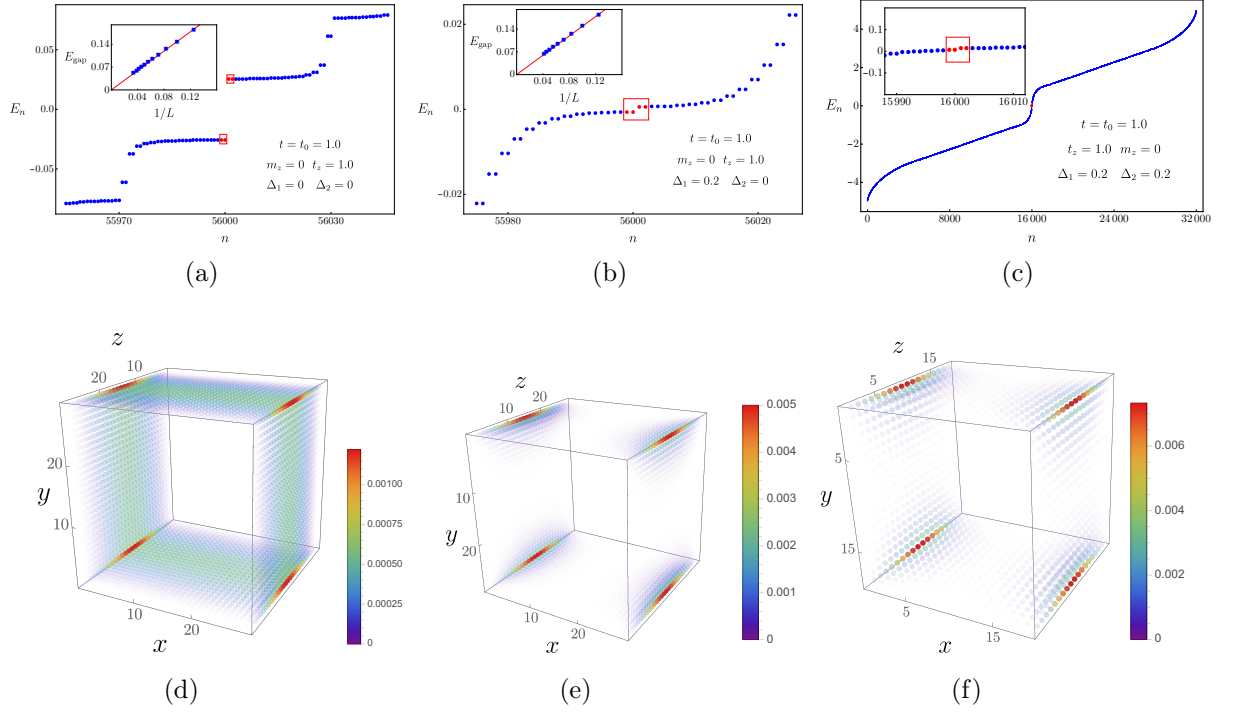


Figure 8.2: Energy spectra of first [second] order Dirac semimetals are shown in (a) [(b) and (c)]. Here, n is the index of energy eigenvalue E_n . Various parameters, appearing in Eq. (8.1), for the numerical simulation are shown in each panel. We diagonalize the tight binding model on a cubic lattice of linear dimension L in all directions, where $L = 30$ for (a) and (b), and $L = 20$ for (c). The finite spectral gaps (E_{gap}) near zero energy in panels (a) and (b) are solely due to finite system effects, which vanish as $L \rightarrow \infty$ (see insets). A similar gap also exists among four states (marked in red) in panel (c), which also vanishes as $L \rightarrow \infty$ (not shown here explicitly). Hence, the system always describes a Dirac semimetal in the thermodynamic limit ($L \rightarrow \infty$). (d) Local density of states (LDoS) associated with the Fermi arc surface states [see red dots in (a)], occupying the two dimensional xz and yz surfaces (thus characterized by codimension $d_c = 1$). LDoS associated with four hinge modes of $d_c = 2$ appearing in panels (b) and (c) are respectively shown in (e) and (f). For finite Δ_2 the energy spectra lose spectral symmetry about zero energy, but we continue to find four hinge modes at half-filling. Figure adapted from Ref. [227].

underlying mechanism of such systematic dimensional reduction of the topological surface states is discussed in the Chapter 8. Numerical demonstration of the hinge modes for a second order Dirac semimetal and topological insulator are respectively shown in Figs. 8.2 and 8.3. Note, when the crystal is cleaved in an orientation rotated by 45 degrees about the z axis, the Δ_1 and Δ_2 terms in Eq. (8.1) switch roles. In the next section we proceed to demonstrate the emergence of HOT phases for spin-3/2 Luttinger fermions in the presence of external strain.

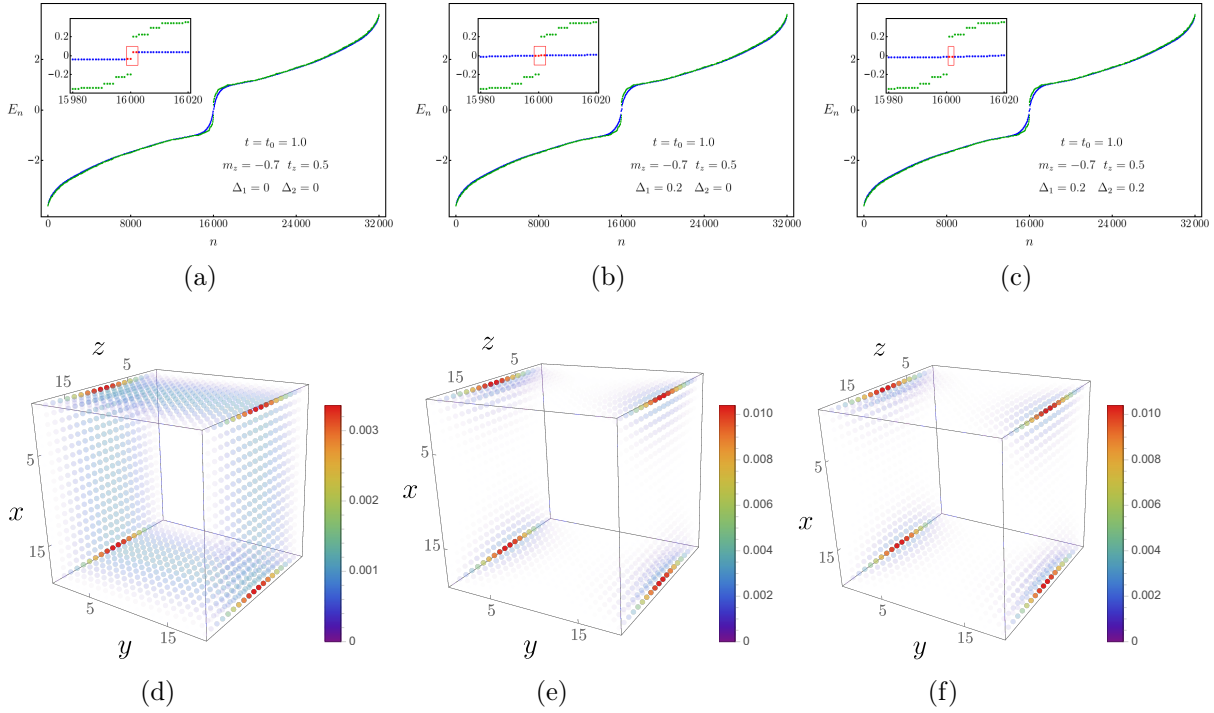


Figure 8.3: Energy spectra of first [second] order topological insulators are shown in (a) [(b) and (c)] with periodic (green) and open (blue) boundaries. Here, n is the index of energy eigenvalue E_n . Various parameters appearing in Eq. (8.1), for the numerical simulation are shown in each panel. We diagonalize the tight binding model on a cubic lattice of linear dimension $L = 20$ in all directions. (d) Local density of states (LDoS) associated with the Fermi arc surface states [see red dots in (a)], occupying the two dimensional xz and yz surfaces (thus characterized by codimension $d_c = 1$). LDoS associated with four hinge modes of $d_c = 2$, appearing in panels (b) and (c) [see the red dots] are shown in (e) and (f) respectively. For finite Δ_2 the energy spectra lose spectral symmetry about zero energy, but we continue to find four hinge modes at half-filling. Figure adapted from Ref. [227].

8.3 Luttinger model

Let us recall the Luttinger Hamiltonian from Eq. (4.2), describing a biquadratic touching of Kramers degenerate valence and conduction bands of spin-3/2 fermions

$$\hat{h}_L(\mathbf{k}) = - \left[\frac{1}{2m_1} \sum_{j=1}^3 d_j(\mathbf{k}) \Gamma_j + \frac{1}{2m_2} \sum_{j=4}^5 d_j(\mathbf{k}) \Gamma_j \right], \quad (8.4)$$

where Γ s are four-dimensional mutually anticommuting Hermitian matrices, satisfying the anticommuting Clifford algebra $\{\Gamma_j, \Gamma_k\} = 2\delta_{jk}$, for $j, k = 1, \dots, 5$. The form of the d -wave harmonics plays an important role in promoting higher-order topology. They are

given by

$$\begin{aligned} d_1(\mathbf{k}) &= \sqrt{3}k_y k_z, & d_2(\mathbf{k}) &= \sqrt{3}k_x k_z, & d_3(\mathbf{k}) &= \sqrt{3}k_y k_x, \\ d_4(\mathbf{k}) &= \frac{\sqrt{3}}{2}(k_x^2 - k_y^2), & d_5(\mathbf{k}) &= \frac{1}{2}(2k_z^2 - k_x^2 - k_y^2). \end{aligned} \quad (8.5)$$

Note $d_4(\mathbf{k})$ and $d_3(\mathbf{k})$ are analogous to the Δ_1 and Δ_2 terms in Eq. (8.3) respectively. Momenta \mathbf{k} are measured from the band touching point, located at $\mathbf{k} = 0$. Without the loss of generality we set $m_1 = m_2 = m$ [which corresponds to setting $\alpha = \pi/4$ in Eq. (4.6)], even though in a cubic environment $m_1 \neq m_2$, and assume $m > 0$. This leads to the familiar biquadratic band touching, described by the spectra $\pm|\mathbf{k}|^2/(2m)$ for the conduction and valence bands respectively, both of which are two-fold degenerate. If we organize the corresponding four-component spinor basis according to $\Psi_{\mathbf{k}}^\top = (c_{\mathbf{k},\frac{3}{2}}, c_{\mathbf{k},\frac{1}{2}}, c_{\mathbf{k},-\frac{1}{2}}, c_{\mathbf{k},-\frac{3}{2}})$, where $c_{\mathbf{k},m_s}$ is the fermion annihilation operator with momentum \mathbf{k} and spin projection m_s , then the Γ matrices belong to the following representation

$$\Gamma_1 = \kappa_3 \otimes \sigma_2, \quad \Gamma_2 = \kappa_3 \otimes \sigma_1, \quad \Gamma_3 = \kappa_2 \otimes \sigma_0, \quad \Gamma_4 = \kappa_1 \otimes \sigma_0, \quad \Gamma_5 = \kappa_3 \otimes \sigma_3. \quad (8.6)$$

The Pauli matrices $\{\kappa_\mu\}$ and $\{\sigma_\mu\}$ for $\mu = 0, \dots, 3$ respectively operate on the sign and magnitude of m_s . While such band touching is protected by cubic symmetry, the Kramers degeneracy of the bands is ensured by time-reversal (\mathcal{T}) and parity (\mathcal{P}) or inversion symmetries. Specifically, under the reversal of time $\mathbf{k} \rightarrow -\mathbf{k}$ and $\Psi_{\mathbf{k}} \rightarrow \Gamma_1 \Gamma_3 \Psi_{-\mathbf{k}}$, and $\mathcal{T} = \Gamma_1 \Gamma_3 \mathcal{K}$, where \mathcal{K} is the complex conjugation, yielding $\mathcal{T}^2 = -1$, but under the spatial inversion $\mathbf{k} \rightarrow -\mathbf{k}$ and $\Psi_{\mathbf{k}} \rightarrow \Psi_{-\mathbf{k}}$.

External strain modulates this unconventional band touching. While respecting the \mathcal{P} and \mathcal{T} symmetries (thus maintaining the Kramers degeneracy of the bands), it reduces the cubic symmetry of the system, and depending on its nature (compressive or tensile) destabilizes the biquadratic band touching in favor of an insulating or a gapless phase. In practice, strain is applied along high symmetry directions, such as C_{4v} and C_{3v} axes, and according to the octahedral (O_h) point group is classified as E_g and T_{2g} strains, respectively [43]. We begin the following discussion with the former case, and systematically unveil the topological properties of such time-reversal invariant strain-engineered phases.

8.4 E_g strain

In Sec. 7.1.1 we outlined some properties of the reconstructed band structure in (among others) the nematic phases in a LSM. Since our goal is to elicit these phases by applying strain, our previous analysis is directly applicable. Recall the parametrization of the (two-component) E_g nematic order parameter from Eq. (7.3). Analogously, the coupling of a generic strain, transforming under the E_g representation, with spin-3/2 Luttinger

fermions is captured by the Hamiltonian

$$\hat{h}_{E_g} = \Delta (\sin \phi \Gamma_4 + \cos \phi \Gamma_5), \quad (8.7)$$

where $|\Delta|$ is its amplitude and ϕ is the internal phase [119, 122]. An external strain applied along the z direction is parametrized by $\phi = 0$ (tensile) or π (compressive). On the other hand, the tensile and compressive strain along the x (y) direction respectively correspond to $\phi = 2\pi/3$ ($4\pi/3$) and $5\pi/3$ ($\pi/3$). If we associate tensile strain with a gapless phase (featuring Dirac points), $\phi = 0, 2\pi/3$, and $5\pi/3$ are consistent with the same phase lockings of ϕ_{E_g} , resulting in Dirac points along the z , x , and y directions respectively, see Fig. 7.2. If we denote the Hamiltonian operator associated with strain applied along the j direction as $\hat{h}_{E_g}^j$, then

$$\begin{aligned} \hat{h}_{E_g}^z &= |\Delta| \Gamma_5 \operatorname{sgn}(\Delta), & \hat{h}_{E_g}^x &= \frac{|\Delta|}{2} [\sqrt{3}\Gamma_4 - \Gamma_5] \operatorname{sgn}(\Delta), \\ \hat{h}_{E_g}^y &= -\frac{|\Delta|}{2} [\sqrt{3}\Gamma_4 + \Gamma_5] \operatorname{sgn}(\Delta). \end{aligned} \quad (8.8)$$

In this notation, the tensile and compressive strain respectively correspond to $\operatorname{sgn}(\Delta) = +$ and $-$.

We first focus on strain applied along the z direction,

$$\begin{aligned} \hat{h}_{E_g}^{z,t} &= v_z [k_x \Gamma_2 + k_y \Gamma_1] + \left[-\frac{k_z^2}{2m} + |\Delta| \operatorname{sgn}(\Delta) + \frac{k_{\perp}^2}{4m} \right] \Gamma_5 \\ &\quad - \frac{1}{2m} \left[\frac{\sqrt{3}}{2} (k_x^2 - k_y^2) \Gamma_4 + \sqrt{3} k_x k_y \Gamma_3 \right], \end{aligned} \quad (8.9)$$

which can be identified with $\hat{h}_{\text{HOT}}(\mathbf{k})$ (Eq. 8.3), with the following correspondence

$$v = v_z, \quad t_z = 2t_0 = \frac{1}{m}, \quad \bar{\Delta} = \Delta, \quad \Delta_1 = \Delta_2 = -\frac{\sqrt{3}}{2m}, \quad (8.10)$$

where $v_z = \sqrt{3}k_z/(2m)$, and

$$\gamma_1 = \Gamma_2, \quad \gamma_2 = \Gamma_1, \quad \gamma_3 = \Gamma_5, \quad \gamma_4 = \Gamma_4, \quad \gamma_5 = \Gamma_5. \quad (8.11)$$

The only (and important) difference is that v_z vanishes for $k_z = 0$. Otherwise, for any finite k_z , the emergent topology of strained spin-3/2 Luttinger fermions directly follows the previous discussion. For example, tensile strain along the z -direction produces a TDSM with Dirac points located at $(0, 0, \pm k_z^0)$, where $k_z^0 = \sqrt{2m|\Delta|}$, with compressive strain yielding a topological insulator [43, 119, 281, 282]. We next focus on the $k_z = 0$ plane to fully characterize the emergent topology and the resulting boundary modes of these two phases.

In the $k_z = 0$ plane, $\hat{h}_{E_g}^{z,t}$ from Eq. (8.9) can be cast (after suitable unitary rotation,

see Appendix D.4) in a block-diagonal form $H_+ \oplus H_-$, where for $\sigma = \pm$

$$H_\sigma = \left[|\Delta| \operatorname{sgn}(\Delta) + \frac{k_\perp^2}{4m} \right] \tau_3 - \frac{1}{2m} [d_4(\mathbf{k})\sigma\tau_1 + d_3(\mathbf{k})\tau_2], \quad (8.12)$$

since it involves only three mutually anticommuting four-dimensional Hermitian matrices. For $\operatorname{sgn}(\Delta) = +$, the $k_z = 0$ plane hosts a trivial insulator (devoid of band inversion), supporting no boundary modes. Therefore, the TDSM phase hosts one-dimensional hinge modes with $d_c = 2$ only for $|k_z| > k_z^0$, extended along the z direction, and is thus of second-order in nature.

By contrast, when $\operatorname{sgn}(\Delta) < 0$, the $k_z = 0$ plane is occupied by a 2D-QSHI, composed of two superimposed copies of anomalous Hall insulators of Chern numbers $C = \pm 2$ for opposite spin projections ($\sigma = \pm$), accommodating two copies of counter-propagating edge modes for opposite spin projections that reside in the xz and yz planes. For any finite k_z , on the other hand, the insulating phase supports only corner localized modes, ultimately constituting four hinge states along the z direction. Hence, the resulting three-dimensional topological insulator hosts both one-dimensional hinge modes (with $d_c = 2$) and two-dimensional edge modes ($d_c = 1$), and thus supports *mixed* topological boundary modes.

We now show that irrespective of the direction of the applied strain, the effective single-particle Hamiltonian always takes the form of $\hat{h}_{E_g}^{z,t}$, see Eq. (8.9), after suitable relabeling of the momentum axes and redefinitions of the mutually anticommuting Γ matrices. Hence, the above discussion is sufficient to capture the emergent topology of strain-engineered phases in Luttinger systems. To explicitly demonstrate this in our present framework, we continue with the E_g strain, and construct the equivalent of the Hamiltonian in Eq. (8.9) for strain along the (symmetry equivalent) x direction. Introducing new sets of momenta $q_x = k_z, q_y = k_y, q_z = k_x$ such that q_z is aligned along the x direction, and four-component Hermitian matrices

$$\bar{\Gamma}_1 = \Gamma_3, \quad \bar{\Gamma}_2 = \Gamma_2, \quad \bar{\Gamma}_3 = \Gamma_1, \quad \bar{\Gamma}_4 = (\Gamma_4 + \sqrt{3}\Gamma_5)/2, \quad \bar{\Gamma}_5 = (\sqrt{3}\Gamma_4 - \Gamma_5)/2, \quad (8.13)$$

such that they also satisfy the anticommuting Clifford algebra $\{\bar{\Gamma}_j, \bar{\Gamma}_k\} = 2\delta_{jk}$, for $j, k = 1, \dots, 5$, yields

$$\hat{h}_L(\mathbf{k}) + \hat{h}_{E_g}^x \rightarrow -\frac{1}{2m} \sum_{j=1}^5 d_j(\mathbf{q})\bar{\Gamma}_j + |\Delta| \bar{\Gamma}_5 \operatorname{sgn}(\Delta), \quad (8.14)$$

similar to $\hat{h}_{E_g}^{z,t}$, see Eq. (8.9). Therefore, the resulting TDSM phase (for $\operatorname{sgn}(\Delta) = +$) supports only four hinge modes along the x direction, while the insulator (for $\operatorname{sgn}(\Delta) = -$) in addition accommodates edge mode residing on the xy and xz planes. Following similar steps, the readers can convince themselves that the hinge modes in both TDSM and insulating phases are aligned in the direction of external strain, when it is applied along

the y direction, while the two-dimensional edge mode in the later phase live on the xy and yz planes (see Appendix D.4). Next we proceed to discuss the effects of external strains, applied along the C_{3v} or body diagonal or [111] directions, named T_{2g} strain.

8.5 T_{2g} strain

Analogously, to the E_g case, we can parametrize an external strain applied along a body diagonal or C_{3v} axis just like the corresponding T_{2g} nematic order parameter, see Eq. (7.1) and Fig. 7.1. The effective single-particle Hamiltonian capturing such a strain in a system of spin-3/2 Luttinger fermions reads

$$\hat{h}_{T_{2g}} = \frac{|\Delta|}{\sqrt{3}} \left[\text{sgn}(\Delta_1) \Gamma_1 + \text{sgn}(\Delta_2) \Gamma_2 + \text{sgn}(\Delta_3) \Gamma_3 \right], \quad (8.15)$$

where $|\Delta| = \sqrt{\Delta_1^2 + \Delta_2^2 + \Delta_3^2}$, with $\Delta_{1,2,3}$ the components of the strain along one of the [111] direction in the x, y, z axes, respectively. In this notation, tensile and compressive strain respectively correspond to $\text{sgn}(\Delta) = \pm$, where $\text{sgn}(\Delta) = \prod_{j=1}^3 \text{sgn}(\Delta_j)$. To demonstrate the effects of a T_{2g} strain, we align it along one of the specific body diagonal, the [1, 1, 1], direction, for which either (a) $\text{sgn}(\Delta_j) = +$ (tensile) or (b) $\text{sgn}(\Delta_j) = -$ (compressive), for $j = 1, 2, 3$. This yields (a) a pair of Dirac points along the [111] body diagonal at $\mathbf{k} = \pm k_{[111]}^0 (1, 1, 1)$, where $k_{[111]}^0 = \sqrt{2m|\Delta|/3}$, or (b) an insulator.

To address the emergent topology of these two phases, we introduce a new set of momenta with $q_z \parallel [1, 1, 1]$

$$q_x = \frac{k_x - k_y}{\sqrt{2}}, \quad q_y = \frac{k_x + k_y - 2k_z}{\sqrt{6}}, \quad q_z = \frac{k_x + k_y + k_z}{\sqrt{3}},$$

and define a new set of $\bar{\Gamma}$ matrices satisfyig the Clifford algebra $\{\bar{\Gamma}_j, \bar{\Gamma}_k\} = 2\delta_{jk}$, for $j, k = 1 \cdots 5$,

$$\begin{aligned} \bar{\Gamma}_1 &= - \left[\frac{1}{3\sqrt{2}} (\Gamma_1 + \Gamma_2 - 2\Gamma_3) + \sqrt{\frac{2}{3}} \Gamma_5 \right], & \bar{\Gamma}_2 &= - \frac{\Gamma_1 - \Gamma_2 - 2\Gamma_4}{\sqrt{6}}, \\ \bar{\Gamma}_3 &= \frac{\Gamma_1 - \Gamma_2 + \Gamma_4}{\sqrt{3}}, & \bar{\Gamma}_4 &= \frac{\Gamma_1 + \Gamma_2 - 2\Gamma_3 - \sqrt{3}\Gamma_5}{3}, & \bar{\Gamma}_5 &= \frac{\Gamma_1 + \Gamma_2 + \Gamma_3}{\sqrt{3}}. \end{aligned}$$

The resulting effective single particle Hamiltonian in the presence of an external strain reads

$$\hat{h}_L(\mathbf{k}) + \frac{|\Delta|}{\sqrt{3}} \text{sgn}(\Delta) \sum_{j=1}^3 \Gamma_j \rightarrow \hat{h}_L(\mathbf{q}) + |\Delta| \bar{\Gamma}_5 \text{sgn}(\Delta), \quad (8.16)$$

similar to $\hat{h}_{E_g}^{z,t}$, see Eq. (8.9). Hence, the resulting TDSM phase (for $\text{sgn}(\Delta) = +$) hosts four copies of hinge modes along the [111] direction. Besides such hinge modes, on the other hand, the strain engineered insulator (for $\text{sgn}(\Delta) = -$) supports edge modes localized on two-dimensional surfaces perpendicular to the [111] direction. One arrives at similar

conclusions when the external strain is applied along any other three body diagonal, namely $[1-1-1]$, $[-11-1]$ and $[-1-11]$, directions, see Appendix D.4.

8.6 Summary and discussion

We find that the LSM can harbor HOT phases when it is subjected to external strains, applied along certain high symmetry directions. Some well known members of this family are HgTe [45], gray-Sn [47, 48], 227 pyrochlore iridates [50, 51, 134] and half-Heusler compounds [53–55]. In particular, we show that tensile strain gives rise to higher-order (namely, second) topological Dirac semimetals, hosting only one-dimensional localized hinge modes. On the other hand, compressive strain engineered topological insulating phases, besides the hinge modes also give rise to edge modes, residing on the two-dimensional surfaces perpendicular to the direction of the applied strain. By contrast, four hinge modes are always found in the direction of the applied strain. These boundary modes can, at least in principle, be detected from ARPES and STM measurements, for example. While application of strain along one of the C_{4v} axes, such as the z direction, is promising in gray-Sn, for example, our findings in the presence of an external strain along the body diagonal or $[111]$ directions can be relevant for 227 pyrochlore iridates (due to the natural growth of crystals in this direction) [279]. Note that the Ir d electrons in the pyrochlore lattice are surrounded by an octahedron of O atoms, which is the dual polyhedron of a cube. Therefore, deformations of this crystal structure have the same splitting effect of the $l = 2$ energy levels into T_{2g} and E_g orbitals.

A natural question that arises when one considers possible experimental realization of such hinge modes, is whether the HOT phase proposed in this chapter proves stable in the presence of disorder. This matter is clearly of high importance, as any real material sample is inevitably littered with various impurities. In the next chapter we address this question and examine the effects of random potential disorder or charge impurities, which is the dominant source of elastic scattering in any real material, on a HOTDSM phase.

Chapter 9

Disordered higher-order Dirac semimetal

In the previous chapter we proposed an experimentally feasible route to engineer a higher order topological Dirac semimetal (HOTDSM) by applying uniaxial strain on a collection of quadratically dispersing effective spin-3/2 fermions, constituting a three-dimensional Luttinger semimetal. A question regarding the stability of HOT semimetals in the presence of interactions and/or disorder arises naturally. Due to a finite gap in the quasiparticle spectra, while the HOT insulators are expected to be robust against sufficiently weak interactions and disorder, their influence on gapless HOT phases demand more careful analyses.

Here we focus on a three-dimensional HOTDSM introduced in Chapter 8, supporting one-dimensional hinge modes in systems with open boundaries, and scrutinize its stability when littered with pointlike quenched random charge impurities. From complementary real space numerical analyses in periodic systems and field-theoretic momentum space renormalization group calculation, we conclude that HOTDSM is a stable phase of matter in the presence of sufficiently weak disorder. However, the system undergoes a continuous quantum phase transition (QPT) into a trivial diffusive metal at finite disorder, where the density of states (DoS) at zero energy is finite, while it vanishes in the HOTDSM. We arrive at these conclusions from the scaling of the average DoS, computed using the kernel polynomial method (KPM) [283] in periodic systems. The phase diagrams obtained from these two complementary methods are shown in Figs. 9.1(a) and 9.1(b), respectively, which are in qualitative agreement. As a direct consequence of the bulk boundary correspondence, the associated topological hinge modes in open boundary systems gradually fade away with increasing randomness and completely melt into a trivial metallic bulk for sufficiently strong disorder, as shown in Fig. 9.2. Therefore, sharp hinge localized topological modes in principle can be observed at least in weakly disordered HOTDSMs, via angle-resolved photoemission spectroscopy (ARPES) and scanning tunneling microscope (STM).

Moreover, numerically extracted values for the dynamical scaling exponent (DSE)

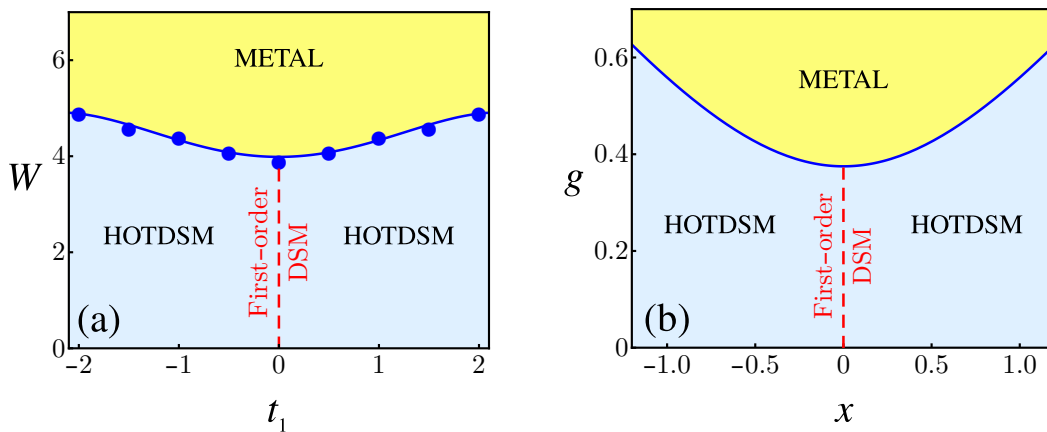


Figure 9.1: Phase diagrams of a dirty HOTSMS extracted from (a) the scaling of DoS at zero energy (numerically) in a lattice model [obtained from Eq. (8.1) by taking $\Delta_1 = \Delta_2 = t_1$], and (b) a leading-order RG analysis of the continuum model [Eq. (9.6)], which are in qualitative agreement. A first-order DSM is realized along the red dashed lines (a) $t_1 = 0$ or (b) $x = 0$, where $x = b\Lambda/v$, with $\Lambda(v)$ as the ultraviolet cutoff (Fermi velocity), and $v \sim ta$, $b \sim t_1 a^2$, $\Lambda \sim a^{-1}$ (a is the lattice spacing). When disorder W or g (dimensionless disorder coupling in the continuum theory) is weak, HOT and first-order DSMs are stable. But, at stronger disorder they undergo a QPT into a metallic phase, where DoS at zero energy is finite. The blue dots in (a) are numerically obtained transition points between DSM and metal, across which we find single-parameter scaling of DoS [Fig. 9.3]. Figure adapted from Ref. [284].

and correlation length exponent (CLE) across a broad range of parameters (that also includes first-order DSMs) appear to be the same within the numerical accuracy [see Table 9.1], and yield satisfactory single-parameter data collapses across the (HOT)DSM-metal continuous QPT [see Fig. 9.3]. To this end we note that while a HOTSMS breaks time-reversal (\mathcal{T}) and lattice four-fold (C_4) rotational symmetries, a first-order DSM preserves them. Therefore, this observation in turn strongly promotes the notion of an emergent *superuniversality* near a diffusive quantum critical point (QCP) in the entire family of dirty DSMs, irrespective of their symmetries and the topological order. We also substantiate these findings from a leading-order momentum space RG analysis, see Sec. 9.3.

9.1 Lattice model and symmetries

Our starting point is the tight-binding model for a three-dimensional HOTSMS, obtained by stacking layers of 2D-QSHI along the k_z axis in momentum space, exactly as shown in Chapter 8. The Hamiltonian is the sum $\hat{h}_{\text{HOT}}(\mathbf{k}) = \hat{h}_0^{\mathbf{k}} + \hat{h}_1^{\mathbf{k}}$, where $\hat{h}_0^{\mathbf{k}}$ and $\hat{h}_1^{\mathbf{k}}$ are defined in Eq. (8.1). For the rest of this analysis we set $m_z = 0$ and $t = t_0 = t_z = 1$ as well as $\Delta_1 = \Delta_2 = t_1$. Then, $t_1 = 0$ again describes the first-order DSM, with the Dirac points at $\mathbf{k} = (0, 0, \pm\frac{\pi}{2}) \equiv \pm\mathbf{K}$, yielding $\rho(E) \sim |E|^2$ scaling of DoS at low energies.

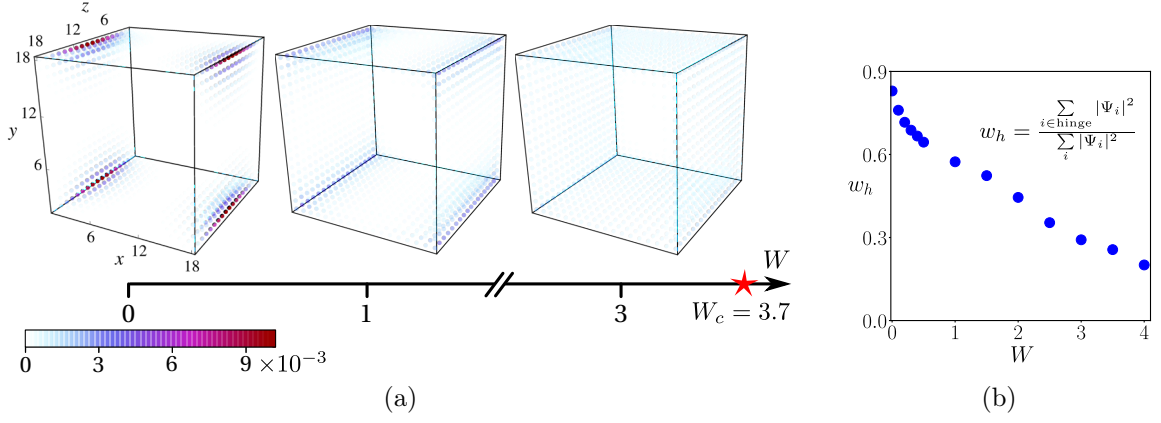


Figure 9.2: (a) Melting of topological hinge states of a HOTDSM with increasing disorder (W) in an open boundary cubic system with linear dimension $L = 18$ in each direction, obtained by averaging the local DoS over 300 independent disorder realizations. To recover the particle-hole symmetry (on average), we switch off the Γ_5 term in the lattice model [see Eq. (8.1)], which is not responsible for the hinge states when the crystal is cleaved such that its four corners are at $(\pm \frac{L}{2}, \pm \frac{L}{2})$ for any z . The critical disorder $W_c = 3.7 \pm 0.1$ is obtained from the scaling of average DoS in a periodic system of $L = 200$. The dissolution of the hinges into the bulk sets in for $W < W_c$ due to the finite size effects. (b) Scaling of the hinge localization (w_h) of the topological hinge modes with increasing disorder (W), confirming its gradual melting. Figure adapted from Ref. [284].

This system then supports ribbon like edge modes localized on the xz and yz planes [see Fig. 8.2(d)], and two copies of Fermi arcs connecting the Dirac points on the $k_x k_z$ or $k_y k_z$ plane. A first-order DSM preserves the time-reversal symmetry (TRS): $\mathcal{T} = \sigma_2 \otimes \tau_0 \mathcal{K}$, where \mathcal{K} is the complex conjugation, the parity (\mathcal{P}) symmetry, under which $\mathbf{r} \rightarrow -\mathbf{r}$ and $\mathcal{P} = \sigma_0 \otimes \tau_3$, as well as the C_4 rotational symmetry, which sends $k_x \rightarrow k_y$, $k_y \rightarrow -k_x$ and is generated by $\mathcal{R} = \sigma_3 \otimes \tau_3$.

To achieve the 1D hinge modes, as before, we turn on the Wilson mass term $\hat{h}_1^{\mathbf{k}}$ by setting $t_1 > 0$, which results in zero-dimensional corner modes in the underlying layers of 2D-QSHI. The collection of these states then forms the four hinges in the 3D system, see Figs. 8.2(e) and 8.2(f). Note that the momentum-dependent mass breaks TRS, as well as C_4 rotational symmetry. Besides, the HOTDSM breaks the parity (\mathcal{P}) symmetry. We then define a pseudo time-reversal symmetry $\mathcal{T}' = \mathcal{P}\mathcal{T}$, such that $(\mathcal{T}')^2 = -1$. The HOTDSM preserves such pseudo time-reversal symmetry, which in turn assures the Kramers degeneracy of the valence and conduction bands [245]. Furthermore, the composite $C_4\mathcal{T}$ and $C_4\mathcal{P}$ symmetries are also preserved by the HOTDSM. Note, however, that the first- and second-order DSM are endowed with distinct symmetries.

As $\hat{h}_1^{\mathbf{k}}$ vanishes *quadratically* with momentum around the Dirac points, it only reduces the DoS at sufficiently low energies without altering its overall $\rho(E) \sim |E|^2$ scaling [Fig. 9.4(a)]. The subdominant influence of the Wilson mass on the DoS suggests that the HOTDSM is possibly stable for sufficiently weak disorder, and enters into a metallic phase via a QPT at finite disorder, *qualitatively* similar to the situation in first-order

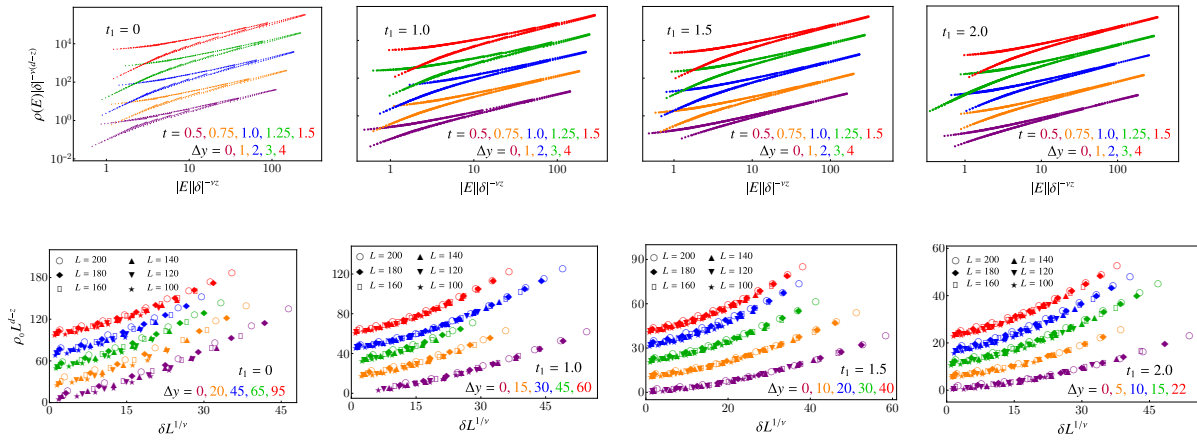


Figure 9.3: Top: Data collapses for $\rho(E)$ in a system of $L = 200$. For clarity, we shift the data sets for different values of t according to $\log_{10}[\rho(E)|\delta|^{-\nu(d-z)}] + \Delta y$ (quoted in each panel). All data sets collapse on three branches. The semimetallic (lower) and metallic (upper-left) branches meet inside the quantum critical regime (upper-right). For the scaling of the DoS in these three regimes see Eqs. (9.3), (9.4) and (9.5) respectively. Bottom: Finite size data collapses for $\rho(0)(\equiv \rho_0)$ inside the metallic phase. We vertically shift the data sets for different values of t according to $\rho_0 L^{d-z} + \Delta y$. Figure adapted from Ref. [284].

Dirac and Weyl semimetals [24, 89, 90, 106, 249–267], up to exponentially small, but debated rare region effect [268–270]. Next we anchor these anticipations by implementing the tight-binding model from Eq. (8.1) on a cubic lattice with periodic boundary in each direction and numerically computing the DoS using the KPM, and investigate the critical properties of the HOTDSM-metal QPT. We consider pointlike charge impurities, which is the dominant source of elastic scattering in any real material, distributed uniformly and independently within the range $[-W/2, W/2]$ at each site of the cubic lattice. Numerically obtained critical exponents are summarized in Table 9.1, which we use to perform a finite energy (size) data collapse, shown in Fig. 9.3 top (bottom).

9.2 Numerical analysis of density of states

To formulate the scaling theory for DoS, we concentrate around the dirty QCP at $W = W_c$, and parametrize the reduced distance from it by $\delta = (W - W_c)/W_c$. The number of states $N(E, L)$ in a d -dimensional system of linear size L below some energy E is in general a function of two dimensionless parameters, L/ξ and E/E_0 . Here ξ is the correlation length, which diverges at the QCP as $\xi \sim \delta^{-\nu}$, and $E_0 \sim \xi^{-z}$ is the corresponding energy scale with ν and z being the CLE and DSE respectively. Since the number of states is proportional to L^d , the functional form of $N(E, L)$ ought to be [257, 260, 262]

$$N(E, L) = (L/\xi)^d F(E\xi^z, L/\xi), \quad (9.1)$$

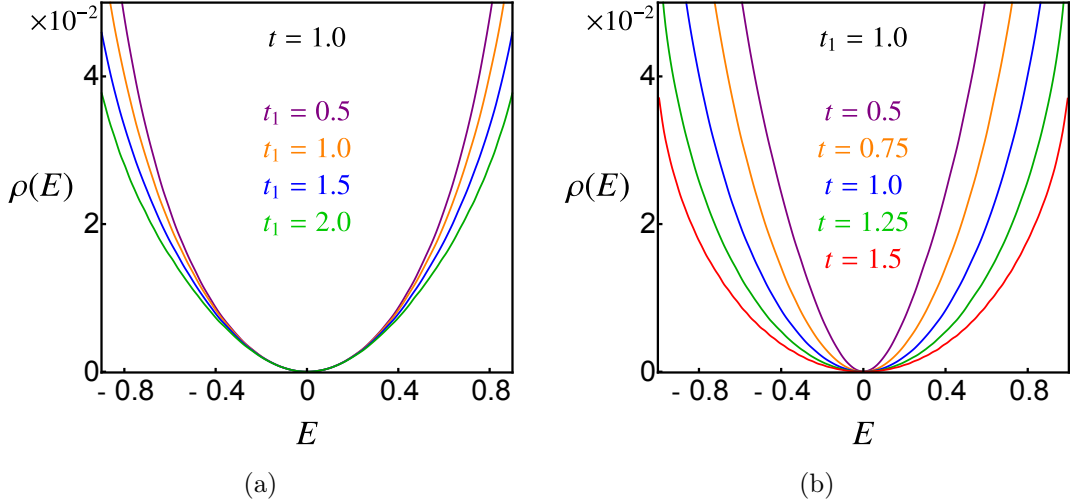


Figure 9.4: Scaling of DoS with (a) the C_4 symmetry breaking Wilson mass (t_1), yielding a HOTDSM, for fixed t or Fermi velocity and (b) t for fixed t_1 in the clean system of $L = 200$ for $W = 0.05$. With increasing t_1 or t the DoS decreases, without altering the $\rho(E) \sim |E|^2$ scaling, leading to the enhancement of critical disorder strength (W_c) for metallicity [Fig. 9.1 and Table 9.1]. Figure adapted from Ref. [284].

where $F(x, y)$ is an unknown, but universal function of its arguments. The DoS is then given by

$$\rho(E) = \frac{1}{L^d} \frac{dN(E, L)}{dE} = \delta^{(d-z)\nu} G(|E|\delta^{-z\nu}, L^{1/\nu}\delta). \quad (9.2)$$

To investigate the scaling behavior of the universal function G , we consider the scaling of $\rho(E)$ at low energies inside the HOTDSM and metallic phases, as well as inside the quantum critical regime around the QCP at $W = W_c$. For now we assume L to be sufficiently large, such that the L -dependence of G can be neglected.

For linearly dispersing HOT Dirac fermions the DoS at low energies scales as $\rho(E) \sim |E|^{d-1}$ (see Fig. 9.4) when $\delta < 0$ or $W < W_c$, thus

$$\rho(E) \sim \delta^{(d-z)\nu} (|E||\delta|^{-z\nu})^{d-1} = |E|^{d-1} |\delta|^{-(z-1)d\nu}. \quad (9.3)$$

By contrast, inside the metallic phase the DoS at zero energy is finite, leading to

$$\rho(E \approx 0) \sim \delta^{(d-z)\nu} (|E|\delta^{-z\nu})^0 = \delta^{(d-z)\nu}, \quad (9.4)$$

for $\delta > 0$ or $W > W_c$. Lastly, at the critical point ($\delta = 0$) the correlation length ξ diverges, and therefore the ξ independence of G implies

$$\rho(E) \sim \delta^{(d-z)\nu} (|E|\delta^{-z\nu})^{(d-z)/z} = |E|^{(d-z)/z}. \quad (9.5)$$

Since the DoS at zero energy vanishes for $W \leq W_c$ and becomes finite in a metal, one can treat $\rho(0)$ as a bonafide order-parameter in dirty HOTDSM to pin down the HOTDSM-metal QPT.

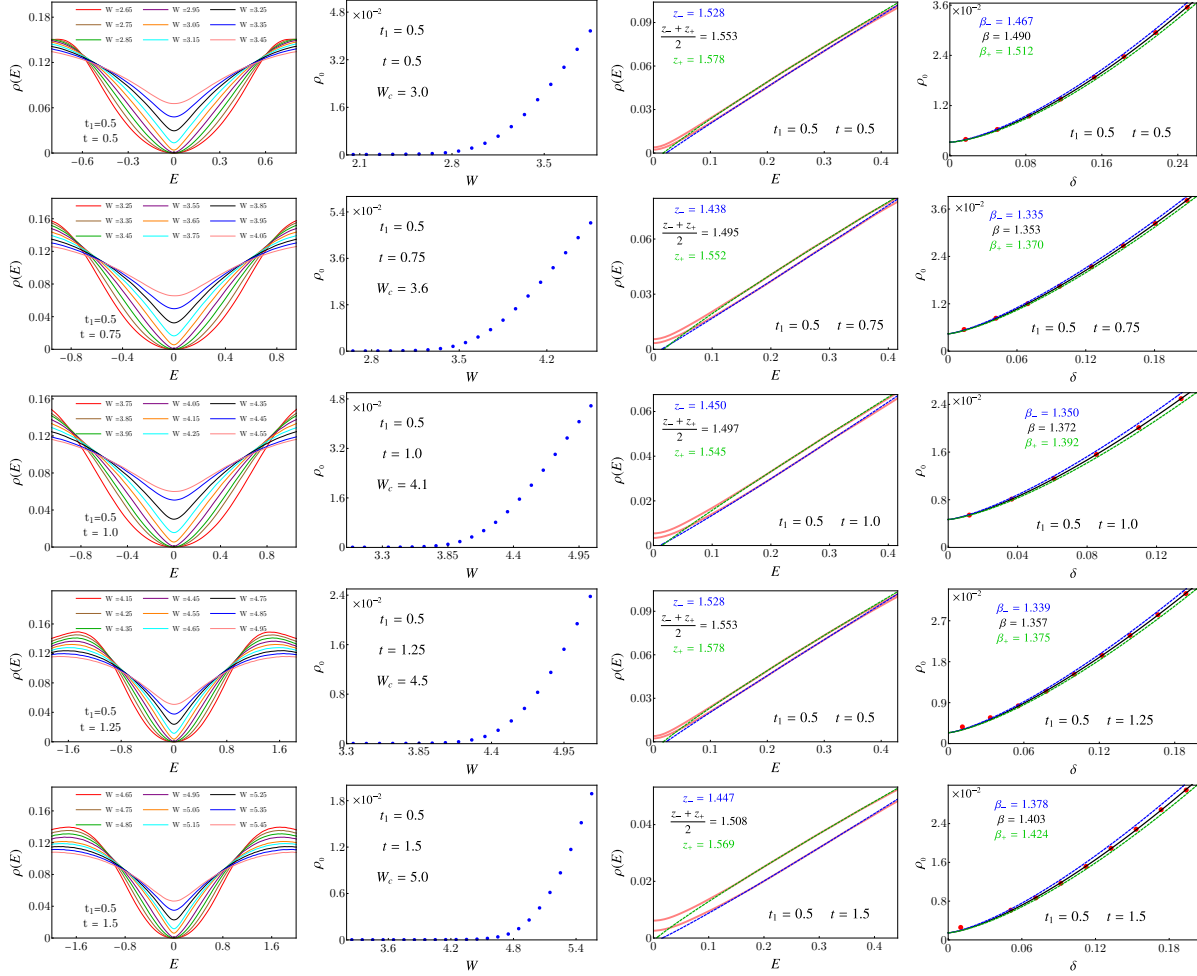


Figure 9.5: Scaling analysis of DOS in a HOTDSM (for fixed $t_1 = 0.5$). For fixed t_1 , as t (or Fermi velocity) increases, W_c increases. From Fig. 9.4 we note that for any fixed t (or Fermi velocity) as t_1 (determining the strength of the C_4 symmetry breaking Wilson mass, yielding the HOTDSM) increases, the DoS decreases at low energies, without altering $\rho(E) \sim |E|^2$. Concomitantly, for fixed t the critical disorder W_c for metallicity increases with increasing t_1 . Figure adapted from Ref. [284].

We now proceed to extract the critical exponents, namely z and ν , across the (HOT)DSM-metal QPT by analyzing the scaling of DoS, computed using the KPM, in the following way. We reconstruct the average DoS in a cubic system for various choices of t and t_1 . First, we identify the critical disorder strength W_c , where $\rho(0)$ deviates from zero. Subsequently, we compute (a) the DSE z from the scaling of $\rho(E)$ around $W = W_c$ [see Eq. (9.5)], and (b) the order-parameter exponent $\beta \equiv (d - z)\nu$ from the scaling of $\rho(0)$ inside the metallic phase [see Eq. (9.4)]. Finally, from the known values of z and β , we compute the CLE ν . Below we outline the aforementioned steps of the numerical analysis in details.

DoS. We reconstruct the DOS from the lattice model [see Eq. (8.1)] on a cubic lattice of linear dimension $L = 200$ and with periodic boundaries in each direction, see first column

of Fig. 9.5¹. For each (t_1, t) point in parameter space, where $t_1 \in \{0, 0.5, 1.0, 1.5, 2.0\}$ and $t \in \{0.5, 0.75, 1.0, 1.25, 1.5\}$, we sample the disorder axis with a resolution $\Delta W = 0.1$. For convenience, we choose the disorder values such that $W = n\Delta W + 0.05$, where $n \in \mathbb{Z}$ (integers).

Critical disorder. The first step in the analysis is to extract the critical disorder strength W_c , where the order parameter $\rho_0 \equiv \rho(0)$ deviates from zero, see second column of Fig. 9.5¹. In practice we find the closest value that satisfies $W_c = n\Delta W$, $n \in \mathbb{Z}$. The shift between sampling W and determining W_c ensures (without the loss of objectivity) that no data set is exactly at $\delta = (W - W_c)/W_c = 0$, which would lead to divergences in the finite energy data collapse.

Dynamic critical exponent. The dynamical critical exponent z is obtained by directly fitting the low-energy DoS with the function $\rho(E) \sim E^{d/z-1}$ with $d = 3$. Again, in practice we fit the two adjacent data sets for $W = W_c \pm 0.05$, then take the average of the obtained values z_- and z_+ , which also serve as fitting error bars in the computation of z , see third column of Fig. 9.5¹.

Correlation length exponent. As the next step we extract the order parameter critical exponent β , by fitting the function $\rho_0(\delta) \sim \delta^\beta$ in the metallic phase for $0 < \delta \ll 1$, where $\delta = (W - W_c)/W_c$ is the reduced distance from the critical point and $\beta = (d - z)\nu$. Finite size effects lead to $\rho_0(W) > 0$ already for $W = W_c$, resulting in $\rho_0(\delta)$ not going to exactly zero for $\delta = 0$, hence we introduce a non-zero intercept that is subject to fitting, but bounded from above by the first $\rho(\delta)$ data point, see fourth column of Fig. 9.5¹. Also, we compute β_\pm for which the resulting curves envelope all data points that were used for fitting. The correlation length exponent and its error bars are then computed using the scaling relation $\nu_{(\pm)} = \beta/(d - z_{(\pm)})$, where the final error is taken to be $\Delta\nu = \max(\nu_-, \nu_+)$.

Across a wide range of hopping parameters (t and t_1)¹ we find that $z \approx 1.5$ and $\nu \approx 1.0$ in a periodic system with linear dimension $L = 200$ in each direction, which are fairly close (within the numerical accuracy) to the ones found for first-order Dirac and Weyl semimetals. The results of the numerical analysis are summarized in Table 9.1. Furthermore, with the numerically extracted values of the critical exponents, we obtain convincing data collapses by comparing $\rho(E)|E|^{-\nu(d-z)}$ vs $E\delta^{-\nu z}$ in a periodic system with $L = 200$, see Fig. 9.3 (top row). All data points collapse onto three curves, corresponding to the DSM (lower ones), a metal (upper left ones) and the quantum critical regime (upper right ones). Finally, from the same set of exponents (computed in a $L = 200$ periodic cubic system) we obtain excellent finite size data collapses by comparing $\rho(0)L^{d-z}$ with $L^{1/\nu}\delta$ inside the metallic phase for $100 \leq L \leq 200$ [Fig. 9.3 (bottom row)]. Therefore, within a sufficiently wide range of system size $100 \leq L \leq 200$ the critical exponents (ν and z) do not change within our numerical accuracy. All together our extensive numerical analyses strongly suggest an emergent superuniversality across the DSM-metal QPT irrespective of their symmetries and the topological order (first or second), which now we substantiate

¹Due to its large volume we do not show the rest of the data sets in this work. However, they are available from the author upon request.

t_1	t	W_c	ΔW_c	β	$\Delta\beta$	z	Δz	ν	$\Delta\nu$
0.0	0.50	2.8	0.1	1.47	0.03	1.50	0.059	0.98	0.05
	0.75	3.4	0.1	1.48	0.02	1.52	0.053	1.00	0.05
	1.00	3.9	0.1	1.47	0.02	1.49	0.05	0.98	0.04
	1.25	4.4	0.1	1.43	0.02	1.50	0.044	0.95	0.04
	1.50	4.8	0.1	1.41	0.03	1.50	0.027	0.94	0.03
0.5	0.50	3.0	0.1	1.49	0.02	1.55	0.025	1.03	0.03
	0.75	3.6	0.1	1.35	0.02	1.50	0.057	0.90	0.05
	1.00	4.1	0.1	1.37	0.02	1.50	0.048	0.91	0.04
	1.25	4.5	0.1	1.36	0.02	1.51	0.048	0.91	0.04
	1.50	5.0	0.1	1.40	0.02	1.51	0.061	0.94	0.05
1.0	0.50	3.3	0.1	1.63	0.03	1.50	0.008	1.08	0.02
	0.75	3.9	0.1	1.48	0.02	1.51	0.046	0.99	0.04
	1.00	4.4	0.1	1.58	0.02	1.45	0.026	1.02	0.03
	1.25	4.7	0.1	1.53	0.03	1.48	0.022	1.00	0.03
	1.50	5.2	0.1	1.55	0.04	1.48	0.008	1.02	0.03
1.5	0.50	3.6	0.1	1.63	0.03	1.51	0.004	1.09	0.02
	0.75	4.1	0.1	1.62	0.03	1.50	0.002	1.08	0.02
	1.00	4.6	0.1	1.51	0.02	1.50	0.025	1.01	0.03
	1.25	5.1	0.1	1.46	0.02	1.51	0.021	0.98	0.03
	1.50	5.5	0.1	1.55	0.04	1.50	0.017	1.03	0.04
2.0	0.50	3.9	0.1	1.66	0.04	1.50	0.021	1.11	0.04
	0.75	4.4	0.1	1.58	0.02	1.51	0.013	1.06	0.03
	1.00	4.9	0.1	1.47	0.03	1.51	0.016	0.99	0.03
	1.25	5.4	0.1	1.42	0.02	1.50	0.014	0.95	0.02
	1.50	5.8	0.1	1.48	0.04	1.50	0.035	0.99	0.05
Average				1.496	0.026	1.500	0.030	0.997	0.036

Table 9.1: Summary of the scaling analysis for $\rho(E)$ in a cubic system of linear dimension $L = 200$ in each direction. Here $t_1 = 0$ (finite) corresponds to first- (second-)order DSM. While the critical disorder (W_c) for metallicity (a nonuniversal quantity) depends on the hopping parameters, t and t_1 [Eq. (8.1)], the critical exponents z and ν are centered around 1.5 and 1.0, respectively. This observation suggests that the universality class of the DSM-metal QPT does not depend on the symmetry or topological order (first or second), thereby yielding a superuniversality in the entire family of disordered DSM, in qualitative agreement with the findings from the momentum space RG analysis. Here ΔX is the fitting error of X , for $X = z, \beta, \nu$.

from a leading-order momentum space RG analysis.

9.3 Renormalization group analysis

To perform the momentum space RG analysis in a dirty HOTDSM, we consider the

following low-energy model

$$\hat{h}_{\pm}(\mathbf{p}) = v_{\perp} \sum_{j=1}^2 \gamma_j p_j \pm v_3 p_3 \gamma_3 + b \sum_{j=4}^5 d_j(\mathbf{p}) \gamma_j, \quad (9.6)$$

obtained by expanding $\hat{h}_{\text{HOT}}(\mathbf{k})$ in Eq. (8.1) around one of the Dirac points at $\pm \mathbf{K}$ with $\mathbf{p} = -\mathbf{K} + \mathbf{k}$. Here $v_{\perp} = ta$, $v_3 = t_2 a$, $b = t_1 a^2/2$, and $(d_4, d_5)(\mathbf{p}) = (p_1^2 - p_2^2, 2p_1 p_2)$. We retain the relevant higher-order momentum terms (proportional to b), such that $\hat{h}_{\pm}(\mathbf{p})$ is symmetry identical to the lattice models $\hat{h}_{\text{HOT}}(\mathbf{k})$, and represents the correct low-energy model for HOTDSM. The purpose of the following momentum space RG analysis is to provide a supportive argument in favor of the numerically observed superuniversality, resulting in (almost) identical values of the critical exponents ν and z near the diffusive QCP in the entire family of DSMs that includes both first-order (for $b = 0$) and higher-order (for $|b| > 0$) DSMs.

Even though in the bare theory $v_3 = v_{\perp} \equiv v$ (for $t = t_z$ in the lattice model), in general their RG flows are different when $|b| > 0$, as it breaks the rotational symmetry between $\mathbf{p}_{\perp} = (p_1, p_2)$ and p_3 . To incorporate the effects of disorder we consider the following imaginary time (τ) Euclidian action in d dimensions [24, 254]

$$S = \int d\tau \int d^d x \Psi^{\dagger} \left[\partial_{\tau} + \sum_{\alpha=\pm} \hat{h}_{\alpha}(\mathbf{p} \rightarrow -i\nabla) - \Phi \right] \Psi + \frac{1}{2\Delta} \int d^d x \Phi |\nabla|^m \Phi, \quad (9.7)$$

where Φ is the disorder field that minimally couples to the four-component fermionic fields (Ψ) like a gauge field. The two-point correlator for the disorder fields in the real and momentum space are respectively

$$\langle \Phi(\mathbf{x}) \Phi(\mathbf{y}) \rangle = \frac{\Delta}{|\mathbf{x} - \mathbf{y}|^{d-m}}, \quad \langle \Phi(\mathbf{q}) \Phi(\mathbf{0}) \rangle = \frac{\Delta}{|\mathbf{q}|^m}. \quad (9.8)$$

As $m \rightarrow 0$, we recover Gaussian white noise distribution. To motivate the form of this correlation function, note that $m \rightarrow 0$ yields a constant value in momentum space, which corresponds to a Dirac delta function in real space, or uncorrelated disorder. The pertinent representation of the Dirac delta function follows from the Riesz potential [285], and reads

$$\delta^d(\mathbf{x} - \mathbf{y}) = \lim_{\alpha \rightarrow 0} \frac{\Gamma\left(\frac{d-\alpha}{2}\right)}{2^{\alpha} \pi^{d/2} \Gamma(\alpha/2)} \frac{1}{|\mathbf{x} - \mathbf{y}|^{(d-\alpha)}}, \quad (9.9)$$

where $\delta^d(\mathbf{x})$ is the d -dimensional Dirac delta function. Comparing with Eq. 9.8 yields $\langle \Phi(\mathbf{x}) \Phi(\mathbf{y}) \rangle \sim \delta^d(\mathbf{x} - \mathbf{y})$ when $m \rightarrow 0$ [254].

The scaling dimensions of momentum and frequency are $[q] = 1$ and $[\omega] = z$, respectively. The scale invariance of S implies $[\Psi] = d/2$, $[v] = z - 1$, $[b] = z - 2$, and $[\Phi] = z + \eta_{\Phi}$, where η_{Φ} is the anomalous dimension of the disorder field, yielding $[\Delta] = 2(z + \eta_{\Phi}) - (d - m)$. At the clean HOTDSM fixed point $z = 1$ due to linearly dispersing excitations at sufficiently low energies, and $\eta_{\Phi} = 0$ due to the gauge invariance

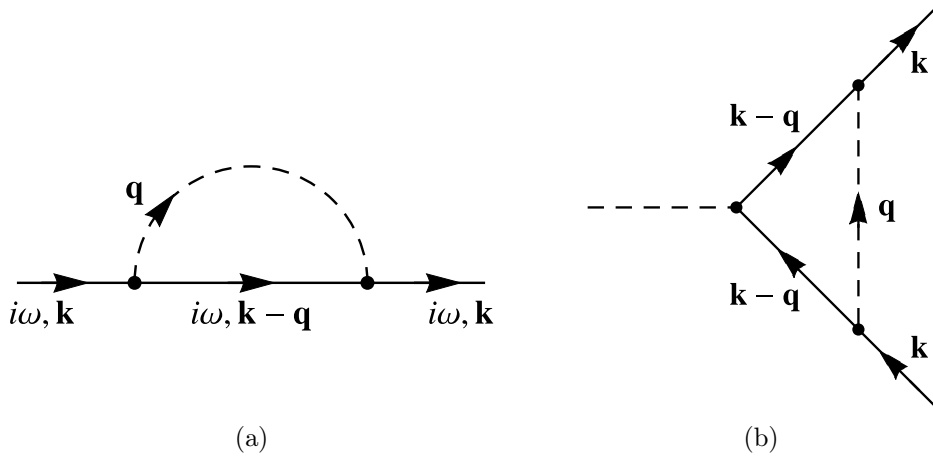


Figure 9.6: (a) fermionic self energy and (b) vertex correction diagrams, contributing to the leading-order RG analysis. Solid (dashed) lines represent fermion (disorder) fields. Figure adapted from Ref. [284].

of S . Therefore $[\Delta] = m - 1$ in $d = 3$, showing that (a) for Gaussian white noise distribution ($m = 0$) disorder is an irrelevant perturbation at the HOTDSM fixed point (since $[\Delta] = -1$), and (b) the QPT to a metal at strong disorder can be addressed by performing a controlled RG analysis in terms of a *small* parameter $\epsilon = 1 - m$, about $\epsilon = 0$ for which disorder is *marginal*, although ultimately we set $\epsilon = 1$.

To derive the RG flow equations, we integrate out a thin momentum shell within momentum $\Lambda e^{-\ell} < |\mathbf{k}| < \Lambda$, where $\ell (> 0)$ is the logarithm of the RG scale and Λ is the ultraviolet momentum cutoff. The relevant Feynman diagrams are shown in Fig. 9.6. After accounting for the quantum corrections up to the leading-order, the RG flow equations read (see Appendix E.5.1 for details)

$$\begin{aligned}
 \frac{dv_3}{d\ell} &= gv_3 [2f_1(x) - f_3(x)] \equiv (z - 1)v_3, \\
 \frac{dg}{d\ell} &= g[-\epsilon + 2(z - 1)], \quad \frac{dx}{d\ell} = -x + \mathcal{O}(xg), \\
 \frac{d}{d\ell} \left(\frac{v_\perp}{v_3} \right) &= g \left(\frac{v_\perp}{v_3} \right) [f_3(x) - f_\perp(x)],
 \end{aligned} \tag{9.10}$$

where $g = \Delta\Lambda^\epsilon/(2\pi^2v^2)$ is the dimensionless disorder coupling, $x = b\Lambda/v$ is also dimensionless, and

$$\begin{aligned}
 f_1(x) &= \frac{1}{2} \int_0^\pi d\theta \frac{\sin \theta}{1 + x^2 \sin^4 \theta}, & f_3(x) &= \int_0^\pi d\theta \frac{\sin \theta \cos^2 \theta}{(1 + x^2 \sin^4 \theta)^2}, \\
 f_\perp(x) &= \frac{1}{2} \int_0^\pi d\theta \frac{\sin^3 \theta (1 + 2x^2 \sin^2 \theta)}{(1 + x^2 \sin^4 \theta)^2},
 \end{aligned} \tag{9.11}$$

with $S_\theta \equiv \sin \theta$, $C_\theta \equiv \cos \theta$. Since we are interested in the leading-order RG analysis, (1) quantum corrections are computed by setting $v_\perp = v_3 = v$, and (2) only the engineering dimension of x has been taken into account. The flow equation of v_3 is fixed by its scaling

dimension, yielding dynamic scaling exponent

$$z = 1 + g [2f_1(x) - f_3(x)]. \quad (9.12)$$

The flow equation for g then supports two fixed points: (1) an infrared stable one at $g = 0$, describing a clean HOTDSM, and (2) an infrared unstable QCP at

$$g = g_* = \epsilon / [2(2f_1(x) - f_3(x))]. \quad (9.13)$$

The latter one controls the QPT into a metal at finite disorder, where $z = 1 + \epsilon/2 = 3/2$ for Gaussian white noise distribution ($\epsilon = 1$) for any x . The CLE at the dirty QCP reads

$$\nu^{-1} = \left. \frac{d(dg/d\ell)}{dg} \right|_{g=g_*} = \epsilon. \quad (9.14)$$

Note that (g_*, x) determines the phase boundary between the DSMs and a metal [solid blue line in Fig. 9.1(b)], which is symmetric about $x = 0$, as all the functions in Eq. (9.11) are symmetric under $x \rightarrow -x$. One also obtains *identical* DSE z from the flow equation of v_\perp (see Appendix E.5.1).

Finally we note that the four-fold symmetry breaking Wilson mass (x) is always an *irrelevant* parameter. Thus in the deep infrared regime ($\ell \rightarrow \infty$) $x \rightarrow 0$, where $f_\perp(0) = f_3(0) = 2/3$, and the velocity anisotropy becomes *marginal*. Consequently, the ratio v_\perp/v_3 ultimately flows to its bare value, set by the hopping parameters t and t_z . Therefore, the Wilson mass (x) despite breaking the TRS and C_4 symmetry only changes the location of the dirty QCP (g_*) without altering the universality class of the semimetal-metal QPT (determined by ν and z , see Table 9.1), giving rise to a *superuniversality* in the entire family of dirty DSMs, that includes its first- and second-order cousins. Although not guaranteed a priori, the irrelevance of x does not change even after we account for its entire one-loop quantum correction (see Appendix E.5.1), which is in agreement with the exact numerical findings that the universality class the HOTDSM-metal QPT remains unchanged for $t_1 \gg t$ (Table 9.1).

9.4 Summary and Discussion

Here we investigate the stability of a HOTDSM in the presence of quenched charge impurities, and identify a semimetal-metal QPT at finite disorder. While the topological hinge modes gradually melt across this quantum phase transition in open boundary systems (Fig. 9.2), similar to the Fermi arcs in dirty Weyl semimetals [286], we come to the conclusion that the symmetry and topological order (first or second) does not affect its universality class (Table 9.1), thus yielding a *superuniversality* in the entire family of dirty DSMs. Since real materials are inherently dirty, the stability of HOTDSM is critical for its experimental realization and observation of the hinge modes (via scanning tunneling

microscopy, for example) in sufficiently clean systems. We also note that HOTDSM in general is more stable than its first-order counterpart due to the suppression of DoS by the Wilson mass (Fig. 9.1). In the future, it will be worthwhile to investigate the nature of the critical wavefunctions in dirty HOTDSM, and search for measurable signatures of the discrete C_4 symmetry breaking.

Conclusions

Our main objective in the scope of this thesis was to shed light on the pattern of symmetry breaking in nodal Fermi liquids, arising due to electronic interactions, and propose a few simple directives that give us the correct intuition about the dominant instabilities therein. We did this following a systematic analysis of some paradigmatic systems, featuring linear and quadratic band touchings in two and three dimensions. For each model we wrote down the appropriate interacting Lagrangian, containing all symmetry-allowed local four fermion terms, and carried out a renormalization group (RG) analysis, controlled by a suitable ϵ expansion about the appropriate lower critical spatial dimension.

In Part I we began with the study of emergent symmetries in various gapless fermionic systems. In contrast to exact symmetries, emergent symmetries do not realize on all energy scales and may or may not be imposed in the Lagrangian at the bare or microscopic level. In the context of this thesis they emerge at the infrared unstable fixed points or quantum critical points of interaction couplings, accessed via the renormalization group transformation. At the corresponding fixed point, order parameters that are connected by the emergent symmetry form composite order parameters and acquire identical RG corrections to the scaling dimension. In Chapter 3 we studied a collection of three-dimensional chiral Dirac fermions, that in the noninteracting limit enjoy a global $U(1) \otimes SU(2)$ chiral symmetry. Without imposing such chiral symmetry in the interacting theory, we observe the partial or full restoration of it at various infrared unstable fixed points. Next, in Chapter 4 we turned our attention to a three-dimensional Luttinger semimetal, where full rotational symmetry manifests between the E_g and T_{2g} nematic phases of the corresponding O_h point group, for example, so long as we do not explicitly introduce cubic deformations.

Besides emergent symmetries, the notion of composite order parameters also arose with respect to adjacent competing phases, that reside next to each other in a phase diagram, when tuning some control parameter such as the strength of interactions, temperature, or chemical doping. In this context, we pronounced the selection rules and organizing principle in Chapter 5. The selection rules tell us which local order parameters are promoted given a dominant four fermion Hubbardlike interaction. To gain a more symmetry-based formulation, one can restate this result in terms of order parameters of adjacent phases forming composite order parameters, that transform under a symmetry group that is larger than those of its constituents. However, the same symmetry en-

largement in this case should not necessarily be attributed to the emergent symmetry of the underlying quantum critical point. The phases preselected by the selection rules are ordered along the temperature axis by the organizing principle, based on a generalized energy-entropy argument. These rules manifest directly in a leading order renormalization group calculation, as shown in Appendix C.3.1. However, ultimately they only rely on the exact symmetries of the system, which are independent of perturbation theory. While a rigorous proof of the selection rules and organizing principle is lacking at the moment, in this work we anchored their validity in several paradigmatic systems by comparing with nonperturbative numerical works and experiments, which we mention here once again in what follows.

To exemplify the selection rule and organizing principle, in Chapter 6 we studied interacting electrons in monolayer and bilayer graphene in a parallel manner. Since these two systems are endowed with identical microscopic symmetries, from the point of view of the selection rules they are only distinguished by their noninteracting band structure. This gave us a unique opportunity to pin down the role of the normal state band structure in determining the nature of the ordered phase. Besides examining each interaction channel individually, we utilized the extended Hubbard model, containing on site, nearest neighbor, and next-nearest neighbor interactions, to supply the renormalization group analysis with microscopically motivated initial conditions. For zero chemical doping, both monolayer and bilayer graphene support antiferromagnetic, charge-density-wave, and quantum spin Hall insulator ordering for repulsive on site, nearest neighbor and next-nearest neighbor interactions, respectively. For finite doping, we observed the onset of s -wave pairing in both systems for repulsive nearest neighbor and next-nearest neighbor interactions (accompanied by f -wave pairing for the first one). On the other hand, due to the distinct band structure we observed the onset of E_g nematic pairing for Dirac and singlet-Kekulé pairing for Luttinger fermions in the presence of on site repulsion in monolayer and bilayer graphene, respectively. These phase diagrams are qualitatively consistent with non-perturbative numerical results. Namely, a functional renormalization group analysis in Ref. [14] found charge-density-wave and f -wave pairing for zero and finite doping respectively, in the presence of nearest neighbor repulsion. Note that this study considered spinless fermions, which do not permit s -wave pairing due to the requisite antisymmetric electronic wave function. On the other hand, a quantum Monte Carlo study in Ref. [16] found quantum spin Hall insulator and s -wave superconductor phases, respectively at zero and finite doping.

In Chapter 7 we examined the effects of electronic interactions in a strong spin-orbit coupled Luttinger semimetal, constituted by effective spin- $\frac{3}{2}$ fermions and displaying bi-quadratic band touching. Such model describes the normal state of several materials, among which 227 pyrochlore iridates and half-Heusler compounds are known to exhibit signatures of strong electronic correlations. Comparably strong spin-orbit coupling and interactions result in interesting physical phenomena, including topological Mott insulator

and Weyl semimetal, making the Luttinger semimetal a worthwhile system of interest. We applied our methodology of renormalization group analysis and ϵ expansion, as well as the proposed selection rules and organizing principle in this system. We confirmed that Hubbardlike four fermion interactions can destabilize the quadratic band touching toward magnetic phases, as observed in the pyrochlore iridates [39,41,42]. Besides, we successfully captured the competition between magnetic orders and d -wave superconductivity when tuning the chemical doping away from the band touching point in the presence of magnetic interactions. This observation is consistent with the phase diagram of half-Heusler compounds [57, 58].

In the last two chapters of this thesis we deviated from interaction physics and explored the emergent or engineered topology in nodal semimetals, as well as their stability in the presence of disorder. In Chapter 8 we showed that eliciting nematic ordering in a Luttinger semimetal by the application of uniaxial strain results in either a three-dimensional topological insulator or Dirac semimetal. Tunable compressive and tensile strain can be achieved experimentally by using a piezoelectric apparatus and gluing the sample between the jaws of the pressure device. Alternatively, a thin film sample can be grown on a substrate with slightly mismatched lattice constant. We argued that both of these emergent phases host surface states residing on one-dimensional edges, which are therefore higher-order topological in nature. In Chapter 9 we then demonstrated the stability of the second-order Dirac semimetal phase in the presence of random potential disorder and established that the critical exponents of the Dirac semimetal-diffusive metal phase transition are independent of the order (first or second) of the underlying topological system. Since the first and second order phases possess distinct symmetries, and the corresponding surface states have different dimensionality, we called this phenomenon an emergent superuniversality.

Topology is traditionally considered in the single particle description, where interactions are often neglected. However, in contrast to topological insulators, semimetals do not have the protection of a finite spectral gap against perturbations such as electronic interactions. A possible future direction of the work presented here is an attempt at bringing these concepts closer together in nodal systems. The topological invariants, though usually expressed using the band description, can be defined, for example, via the fermionic Green's function [287]. Interactions can leave their imprint on the Green's function via self energy corrections, opening the way for examining their effect on the topological invariants. Another possible future outgrowth, following a similar spirit, is studying the emergence of superconductivity from repulsive interactions in doped three-dimensional topological systems. Interaction effects have been studied in Weyl and multi-Weyl semimetals [4,5,49,118,288–293], as well as nodal-loop semimetals [222,223,294–296]. Presently, proximity effect and applied pressure represent a major avenue toward the realization of superconductivity in noncentrosymmetric type II Weyl semimetals [297–300]. At the same time, there is intense search for pairing phases in nodal-loop semimetals,

that seem to exhibit exotic phenomena, such as topological or anisotropic superconductivity [301–305]. This field is, however, still at its infancy. Moreover, our analysis of emergent symmetries at infrared unstable quantum critical points can be directly extended to monolayer graphene. In such a system an emergent $SO(5)$ symmetry at two distinct quantum critical points connects the (i) antiferromagnet and Kekulé valence bond solid and (ii) quantum spin Hall insulator and s -wave pairing orders [306]. In any case, correlated multiband systems with nontrivial topology is a frontier of condensed matter physics with many interesting possibilities, which can be systematically explored following the methodology outlined in this thesis.

Appendices

The following appendices contain supplementary material to Chapters 3–9.

A.1 Three-dimensional chiral Dirac semimetal

This appendix includes complementary calculations for three-dimensional Dirac fermions described in Chapter 3, interacting via local four-fermion terms. In the subsequent sections we present the symmetry classification of local four-fermion terms, as well as the Fierz reduction of quartic terms for isotropic and anisotropic Dirac semimetal.

A.1.1 Symmetry classification of four-fermion interaction

Classifying the available local or density-density four-fermion terms is of crucial importance when constructing an interacting action that transforms as a scalar under all operative symmetries. The momentum-independent four-fermion interactions for three-dimensional Dirac fermions are captured by the quartic terms of the form

$$(\Psi^\dagger \Gamma_{\mu\nu} \Psi)(\Psi^\dagger \Gamma_{\rho\lambda} \Psi), \quad (15)$$

where $\Gamma_{\mu\nu} = \tau_\mu \otimes \sigma_\nu$ with $\mu, \nu, \rho, \lambda = 0, \dots, 3$. By imposing discrete parity (\mathcal{P}), time-reversal (\mathcal{T}), and charge conjugation (\mathcal{C}) symmetries, we reduce 136 possible interaction terms to the ones where both $\Psi^\dagger \Gamma_{\mu\nu} \Psi$ and $\Psi^\dagger \Gamma_{\rho\lambda} \Psi$ are either even or odd under \mathcal{P} , \mathcal{T} and \mathcal{C} separately, such that each quartic term is invariant under all three individual discrete symmetries. The classification of sixteen fermion bilinears under these three discrete symmetries is displayed in Table 2. As there are no two identical rows in this table, there exists no interaction term that mixes any two different rows. Hence, the remaining four-fermion terms that are invariant under \mathcal{P} , \mathcal{T} and \mathcal{C} are

$$(\Psi^\dagger \Gamma_{\mu\nu} \Psi)^2 \quad (16 \text{ of them}), \quad (16)$$

$$(\Psi^\dagger \Gamma_{\mu j} \Psi)(\Psi^\dagger \Gamma_{\mu k} \Psi) \quad (12 \text{ of them}), \quad (17)$$

where $j \neq k = 1, 2, 3$.

The number of quartic terms is further reduced when we invoke the spatial rotational symmetry. First of all, all terms from Eq. (17) get eliminated, as they do not transform as scalars nor as vectors under the $O(3)$ spatial rotations. Furthermore, rotational symmetry organizes the terms in Eq. (16) into four scalars ($O(3)$ vectors) for $\Gamma_{\mu 0}$ ($\Gamma_{\mu j}$), with $j = 1, 2, 3$. Therefore, the eight symmetry allowed four-fermion terms are of the form

$$(\Psi^\dagger \Gamma_{\mu 0} \Psi)^2 \text{ and } \sum_{j=1}^3 (\Psi^\dagger \Gamma_{\mu j} \Psi)^2. \quad (18)$$

In Eq. (3.8) the matrices $\Gamma_{\mu 0}$ and $\Gamma_{\mu j}$ appear with couplings g_μ^s , g_μ^t respectively. We note that each component of $\Gamma_{\mu 0}$ ($\Gamma_{\mu j}$) for $\mu = 0, \dots, 3$ transforms as scalar (three-

bilinear	\mathcal{P}	\mathcal{T}	\mathcal{C}	O(3)
$\Psi^\dagger \Gamma_{00} \Psi$	+	+	-	0
$\Psi^\dagger \Gamma_{10} \Psi$	-	+	+	0
$\Psi^\dagger \Gamma_{20} \Psi$	-	-	+	0
$\Psi^\dagger \Gamma_{30} \Psi$	+	+	+	0
$\Psi^\dagger \Gamma_{0j} \Psi$	+	-	+	1
$\Psi^\dagger \Gamma_{1j} \Psi$	-	-	-	1
$\Psi^\dagger \Gamma_{2j} \Psi$	-	+	-	1
$\Psi^\dagger \Gamma_{3j} \Psi$	+	-	-	1

Table 2: Classification of 16 fermion bilinears under the discrete parity (\mathcal{P}), time reversal (\mathcal{T}) and charge conjugation (\mathcal{C}) symmetries. Here + (-) sign corresponds to even (odd) transformation of the bilinear under a specific symmetry, and $j = 1, 2, 3$. The fifth column shows whether a fermion bilinear transform as a scalar (0) or a three-component vector (1) under the spatial O(3) rotations, generated by $\{\Gamma_{01}, \Gamma_{02}, \Gamma_{03}\}$.

component vector) under the spatial O(3) rotations, generated by $\{\Gamma_{01}, \Gamma_{02}, \Gamma_{03}\}$. As the O(3) group is *isomorphic* to SU(2), we can immediately conclude that the total number of linearly independent quartic terms in an isotropic Dirac semimetal is *four*, the dimensionality of the vectors $\Gamma_{\mu 0}$ and $\Gamma_{\mu j}$. Furthermore, we can choose four O(3) scalar quartic terms $(\Psi^\dagger \Gamma_{\mu 0} \Psi)^2$ as the linearly independent four-fermion interactions. Next we explicitly demonstrate these outcomes using the Fierz identity.

A.1.2 Fierz reduction of four-fermion interaction

We perform the Fierz reduction, presented in a general manner in Sec. 2.2.1, in the context of three-dimensional Dirac fermions. Setting $D = 4$ and $x = y$ in Eq. (2.21) we obtain

$$(\Psi^\dagger \Gamma_{\mu\nu} \Psi)(\Psi^\dagger \Gamma_{\rho\lambda} \Psi) = -\frac{1}{16} \sum_{\alpha, \beta, \gamma, \delta} (\text{Tr} \Gamma_{\mu\nu} \Gamma_{\alpha\beta} \Gamma_{\rho\lambda} \Gamma_{\gamma\delta}) \times (\Psi^\dagger \Gamma_{\alpha\beta} \Psi)(\Psi^\dagger \Gamma_{\gamma\delta} \Psi), \quad (19)$$

where $\alpha, \beta, \gamma, \delta = 0, \dots, 3$. In the following two subsections we reconstruct the Fierz matrix F from Eq. (2.22) for the isotropic and anisotropic DSM. Since these two systems are bestowed with different symmetries, the explicit forms of the corresponding Fierz matrices and the numbers of independent quartic terms are distinct, and are thus discussed separately.

A.1.2.1 Isotropic Dirac semimetal

For the isotropic Dirac semimetal there are eight symmetry allowed quartic terms, see Eq. (3.8), which can be organized into X according to

$$X^\top = \left[(\Psi^\dagger \Gamma_{00} \Psi)^2, (\Psi^\dagger \Gamma_{10} \Psi)^2, (\Psi^\dagger \Gamma_{20} \Psi)^2, (\Psi^\dagger \Gamma_{30} \Psi)^2, \right. \\ \left. \sum_{j=1}^3 (\Psi^\dagger \Gamma_{0j} \Psi)^2, \sum_{j=1}^3 (\Psi^\dagger \Gamma_{1j} \Psi)^2, \sum_{j=1}^3 (\Psi^\dagger \Gamma_{2j} \Psi)^2, \sum_{j=1}^3 (\Psi^\dagger \Gamma_{3j} \Psi)^2 \right]. \quad (20)$$

The corresponding eight-dimensional Fierz matrix reads as

$$F_{\text{iso}} = \begin{pmatrix} 5 & 1 & 1 & 1 & 1 & 1 & 1 & 1 \\ 1 & 5 & -1 & -1 & 1 & 1 & -1 & -1 \\ 1 & -1 & 5 & -1 & 1 & -1 & 1 & -1 \\ 1 & -1 & -1 & 5 & 1 & -1 & -1 & 1 \\ 3 & 3 & 3 & 3 & 3 & -1 & -1 & -1 \\ 3 & 3 & -3 & -3 & -1 & 3 & 1 & 1 \\ 3 & -3 & 3 & -3 & -1 & 1 & 3 & 1 \\ 3 & -3 & -3 & 3 & -1 & 1 & 1 & 3 \end{pmatrix}, \quad (21)$$

with $R(F_{\text{iso}}) = 4$. Therefore, the number of independent coupling constants is $D(F_{\text{iso}}) - R(F_{\text{iso}}) = 4$, where D and R stand for dimension and rank respectively. Without any loss of generality, we choose the four single-component quartic terms containing $\Gamma_{\mu 0}$, each of which transforms as a scalar under spatial $O(3)$ rotations, as the independent ones, see Eq. (3.9). The remaining four quartic terms containing $\Gamma_{\mu j}$, which for any given μ transform as a three-component vector under spatial $O(3)$ rotations, can be expressed as

$$\sum_{j=1}^3 (\Psi^\dagger \Gamma_{0j} \Psi)^2 = -2(\Psi^\dagger \Gamma_{00} \Psi)^2 - (\Psi^\dagger \Gamma_{10} \Psi)^2 - (\Psi^\dagger \Gamma_{20} \Psi)^2 - (\Psi^\dagger \Gamma_{30} \Psi)^2, \\ \sum_{j=1}^3 (\Psi^\dagger \Gamma_{1j} \Psi)^2 = -(\Psi^\dagger \Gamma_{00} \Psi)^2 - 2(\Psi^\dagger \Gamma_{10} \Psi)^2 + (\Psi^\dagger \Gamma_{20} \Psi)^2 + (\Psi^\dagger \Gamma_{30} \Psi)^2, \\ \sum_{j=1}^3 (\Psi^\dagger \Gamma_{2j} \Psi)^2 = -(\Psi^\dagger \Gamma_{00} \Psi)^2 + (\Psi^\dagger \Gamma_{10} \Psi)^2 - 2(\Psi^\dagger \Gamma_{20} \Psi)^2 + (\Psi^\dagger \Gamma_{30} \Psi)^2, \\ \sum_{j=1}^3 (\Psi^\dagger \Gamma_{3j} \Psi)^2 = -(\Psi^\dagger \Gamma_{00} \Psi)^2 + (\Psi^\dagger \Gamma_{10} \Psi)^2 + (\Psi^\dagger \Gamma_{20} \Psi)^2 - 2(\Psi^\dagger \Gamma_{30} \Psi)^2. \quad (22)$$

Therefore, whenever we generate any one of these quartic terms through the quantum loop corrections, it is expressed in terms of the four quartic terms appearing in Eq. (3.9). Furthermore, the fact that an interacting isotropic chiral Dirac semimetal can be described by only four linearly independent quartic terms is consistent with the existence of four independent superconducting orders, tabulated in Table 3.2 (last four rows).

A.1.2.2 Anisotropic Dirac semimetals

When we introduce an anisotropy between the in-plane (v_x and v_y , with $v_x = v_y = v_\perp$) and the perpendicular or out of the plane (v_z) components of the Fermi velocity, which is germane in a tetragonal system, each three-component quartic term splits into two, with the corresponding coupling constants splitting as $g_\mu^t \rightarrow (g_\mu^\perp, g_\mu^z)$ for $\mu = 0, \dots, 3$, yielding the interacting Lagrangian

$$L_{\text{int}}^{\text{ani}} = \sum_{\mu=0}^3 g_\mu^s (\Psi^\dagger \Gamma_{\mu 0} \Psi)^2 + \sum_{\mu=0}^3 \left[g_\mu^\perp \sum_{j=1}^2 (\Psi^\dagger \Gamma_{\mu j} \Psi)^2 + g_\mu^z (\Psi^\dagger \Gamma_{\mu 3} \Psi)^2 \right]. \quad (23)$$

Hence the array (X) containing all the quartic terms reads

$$X^\top = \left[(\Psi^\dagger \Gamma_{00} \Psi)^2, (\Psi^\dagger \Gamma_{10} \Psi)^2, (\Psi^\dagger \Gamma_{20} \Psi)^2, (\Psi^\dagger \Gamma_{30} \Psi)^2, \sum_{j=1}^2 (\Psi^\dagger \Gamma_{0j} \Psi)^2, (\Psi^\dagger \Gamma_{03} \Psi)^2, \right. \\ \left. \sum_{j=1}^2 (\Psi^\dagger \Gamma_{1j} \Psi)^2, (\Psi^\dagger \Gamma_{13} \Psi)^2, \sum_{j=1}^2 (\Psi^\dagger \Gamma_{2j} \Psi)^2, (\Psi^\dagger \Gamma_{23} \Psi)^2, \sum_{j=1}^2 (\Psi^\dagger \Gamma_{3j} \Psi)^2, (\Psi^\dagger \Gamma_{33} \Psi)^2 \right]. \quad (24)$$

The twelve-dimensional Fierz matrix then reads

$$F_{\text{ani}} = \begin{pmatrix} 5 & 1 & 1 & 1 & 1 & 1 & 1 & 1 & 1 & 1 & 1 & 1 \\ 1 & 5 & -1 & -1 & 1 & 1 & 1 & 1 & -1 & -1 & -1 & -1 \\ 1 & -1 & 5 & -1 & 1 & 1 & -1 & -1 & 1 & 1 & -1 & -1 \\ 1 & -1 & -1 & 5 & 1 & 1 & -1 & -1 & -1 & -1 & 1 & 1 \\ 2 & 2 & 2 & 2 & 4 & -2 & 0 & -2 & 0 & -2 & 0 & -2 \\ 1 & 1 & 1 & 1 & -1 & 5 & -1 & 1 & -1 & 1 & -1 & 1 \\ 2 & 2 & -2 & -2 & 0 & -2 & 4 & -2 & 0 & 2 & 0 & 2 \\ 1 & 1 & -1 & -1 & -1 & 1 & -1 & 5 & 1 & -1 & 1 & -1 \\ 2 & -2 & 2 & -2 & 0 & -2 & 0 & 2 & 4 & -2 & 0 & 2 \\ 1 & -1 & 1 & -1 & -1 & 1 & 1 & -1 & -1 & 5 & 1 & -1 \\ 2 & -2 & -2 & 2 & 0 & -2 & 0 & 2 & 0 & 2 & 4 & -2 \\ 1 & -1 & -1 & 1 & -1 & 1 & 1 & -1 & 1 & -1 & -1 & 5 \end{pmatrix}, \quad (25)$$

and now $\text{R}(F_{\text{ani}}) = 7$. Therefore, we have five linearly independent quartic terms. The additional coupling constant (besides g_μ^s with $\mu = 0, \dots, 3$) can be chosen to be g_1^z , for example, see Sec. 3.2.6. The remaining seven quartic terms are then given by

$$\sum_{j=1}^2 (\Psi^\dagger \Gamma_{0j} \Psi)^2 = - (\Psi^\dagger \Gamma_{00} \Psi)^2 - (\Psi^\dagger \Gamma_{20} \Psi)^2 - (\Psi^\dagger \Gamma_{30} \Psi)^2 + (\Psi^\dagger \Gamma_{13} \Psi)^2, \\ (\Psi^\dagger \Gamma_{03} \Psi)^2 = - (\Psi^\dagger \Gamma_{00} \Psi)^2 - (\Psi^\dagger \Gamma_{10} \Psi)^2 - (\Psi^\dagger \Gamma_{13} \Psi)^2, \\ \sum_{j=1}^2 (\Psi^\dagger \Gamma_{1j} \Psi)^2 = - (\Psi^\dagger \Gamma_{00} \Psi)^2 - 2(\Psi^\dagger \Gamma_{10} \Psi)^2 + (\Psi^\dagger \Gamma_{20} \Psi)^2 + (\Psi^\dagger \Gamma_{30} \Psi)^2 - (\Psi^\dagger \Gamma_{13} \Psi)^2,$$

$$\begin{aligned}
 \sum_{j=1}^2 (\Psi^\dagger \Gamma_{2j} \Psi)^2 &= -(\Psi^\dagger \Gamma_{00} \Psi)^2 - (\Psi^\dagger \Gamma_{20} \Psi)^2 + (\Psi^\dagger \Gamma_{30} \Psi)^2 - (\Psi^\dagger \Gamma_{13} \Psi)^2, \\
 (\Psi^\dagger \Gamma_{23} \Psi)^2 &= (\Psi^\dagger \Gamma_{10} \Psi)^2 - (\Psi^\dagger \Gamma_{20} \Psi)^2 + (\Psi^\dagger \Gamma_{13} \Psi)^2, \\
 \sum_{j=1}^2 (\Psi^\dagger \Gamma_{3j} \Psi)^2 &= -(\Psi^\dagger \Gamma_{00} \Psi)^2 + (\Psi^\dagger \Gamma_{20} \Psi)^2 - (\Psi^\dagger \Gamma_{30} \Psi)^2 - (\Psi^\dagger \Gamma_{13} \Psi)^2, \\
 (\Psi^\dagger \Gamma_{33} \Psi)^2 &= (\Psi^\dagger \Gamma_{10} \Psi)^2 - (\Psi^\dagger \Gamma_{30} \Psi)^2 + (\Psi^\dagger \Gamma_{13} \Psi)^2.
 \end{aligned} \tag{26}$$

The fact that an interacting anisotropic (tetragonal) Dirac semimetal is described by five linearly independent quartic terms can be justified from the fact that a Dirac system with reduced in-plane rotational symmetry supports five independent local pairings, as the three-component vector pairing Δ_2^p (see Table 3.2) splits into the in-plane (with $j = 1, 2$) and out of plane (with $j = 3$) components. Similarly, one can show that in orthorhombic system ($v_x \neq v_y \neq v_z$), an interacting Dirac semimetal is described by six linearly independent local four-fermion interactions.

B.2 Three-dimensional Luttinger (semi)metal

This appendix contains supplementary information for the three-dimensional Luttinger (semi)metal, described in Chapters 4 and 7. First we present computation of thermodynamic and transport properties. Then, we provide additional details of the Luttinger model, as well as show the Fierz reduction of quartic interactions explicitly. Details of the RG flow equations and the fixed point analysis follow.

B.2.1 Specific heat and compressibility

Here we present the scaling of specific heat (C_V) and compressibility (κ) in a three-dimensional noninteracting Luttinger system, when the chemical potential (μ) is placed away from the band touching point. We begin with the expression for the free-energy density in this system, given by (after setting $k_B = 1$)

$$f = -gT \sum_{\tau=\pm} \int \frac{d^3\mathbf{k}}{(2\pi)^3} \ln \left[2 \cosh \left(\frac{E_{\mathbf{k}}^\tau}{2T} \right) \right], \tag{27}$$

where g is the degeneracy of the valence and conduction band, hence $g = 2$, and the quasiparticle spectra is given by

$$E_{\mathbf{k}}^\tau = \frac{k^2}{2m} + \tau\mu. \tag{28}$$

The chemical potential and momentum (\mathbf{k}) are measured from the band touching point.

One can rewrite the above expression for the free energy density as

$$f = -\frac{g}{2} \sum_{\tau=\pm} \int \frac{d^3\mathbf{k}}{(2\pi)^3} E_{\mathbf{k}}^{\tau} - gT \sum_{\tau=\pm} \int \frac{d^3\mathbf{k}}{(2\pi)^3} \ln \left[1 + \exp \left(-\frac{E_{\mathbf{k}}^{\tau}}{T} \right) \right]. \quad (29)$$

The first term is independent of temperature and not important for the thermodynamic properties of the system. So we focus only on the second term. After proper rescaling of variables the free-energy density becomes

$$f = -DT^{5/2} \frac{(2m)^{3/2}}{4\pi^2} \sum_{\tau=\pm} \int_0^{\infty} dy \sqrt{y} \ln [1 + e^{-y-\tau\tilde{\mu}}], \quad (30)$$

leading to

$$f = T^{5/2} \frac{(2m)^{3/2}}{4\pi^{3/2}} \left[\text{Li}_{\frac{5}{2}}(-e^{\mu/T}) + \text{Li}_{\frac{5}{2}}(-e^{-\mu/T}) \right], \quad (31)$$

where $\tilde{\mu} = \mu/T$, and $\text{Li}_s(z)$ represents the polylogarithm function of order s and argument z . For $\tilde{\mu} \ll 1$ the free-energy density reads as

$$f = -gT^{5/2} \frac{(2m)^{3/2}}{8\pi^{3/2}} \left[a + b \frac{\mu^2}{T^2} + c \frac{\mu^4}{T^4} + \dots \right], \quad (32)$$

where

$$\begin{aligned} a &= \frac{1}{2} (4 - \sqrt{2}) \zeta \left(\frac{5}{2} \right) \approx 1.7344, & b &= (1 - \sqrt{2}) \zeta \left(\frac{1}{2} \right) \approx 0.6049, \\ c &= \frac{1}{12} (1 - 4\sqrt{2}) \zeta \left(-\frac{3}{2} \right) \approx 0.00989. \end{aligned} \quad (33)$$

From the above expression of the free-energy density we arrive the expression for specific heat and compressibility respectively as

$$C_V = -T \frac{\partial^2 f}{\partial T^2} \approx T^{3/2} \frac{(2m)^{3/2}}{32\pi^{3/2}} \left[15a - b \frac{\mu^2}{T^2} \right], \quad (34)$$

$$\kappa = -\frac{\partial^2 f}{\partial \mu^2} \approx \sqrt{T} \frac{(2m)^{3/2}}{2\pi^{3/2}} \left[b + 6c \frac{\mu^2}{T^2} \right]. \quad (35)$$

From these two expressions we finally arrive at the following universal ratio

$$\frac{C_V/T}{\kappa} = \frac{15(4 - \sqrt{2})}{16(1 - \sqrt{2})} \times \frac{\zeta(5/2)}{\zeta(1/2)} \approx 5.37611. \quad (36)$$

This number is a characteristic of a $z = 2$ noninteracting scale invariant fixed point in $d = 3$.

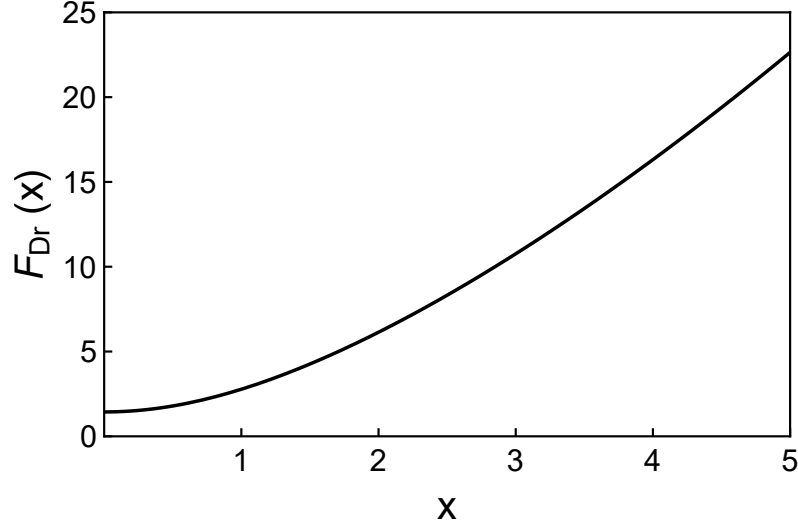


Figure 7: Scaling of the universal function $F_{\text{Dr}}(x)$ with its argument x , appearing in the expression for the Drude conductivity of Luttinger fermions, see Eq. (42). Figure adapted from Ref. [119].

B.2.2 Dynamic conductivity

This section is devoted to disclosing some key steps of the computation of the dynamic conductivity in a Luttinger system. We focus on an isotropic system (for the sake of simplicity) and explicitly compute the z -component of the conductivity (σ_{zz}). Due to the cubic symmetry $\sigma_{zz} = \sigma_{xx} = \sigma_{yy} \equiv \sigma$ (say). To this end we use the Kubo formula and compute the polarization bubble as a function of external (Matsubara) frequency

$$\Pi_{zz}(i\omega_n) = -\frac{e^2}{\beta} \sum_m \int_{\mathbf{k}} \mathbf{Tr} \left[\hat{j}_z G_0(ip_m, \mathbf{k}) \hat{j}_z \times G_0(ip_m + i\omega_n, \mathbf{k}) \right], \quad (37)$$

where e is the electronic charge, β is the inverse temperature and the current operator along the z direction is given by

$$\left. \frac{\partial H_L(k_z - A\hat{z})}{\partial A} \right|_{A=0} = \hat{j}_z = -\frac{1}{2m} \left[\sqrt{3} k_y \Gamma_1 + \sqrt{3} k_x \Gamma_2 + 2 k_z \Gamma_5 \right]. \quad (38)$$

In the spectral representation the noninteracting Greens function reads as

$$G_0(i\omega_n, \mathbf{k}) = \int_{-\infty}^{\infty} \frac{d\epsilon}{2\pi} \frac{\mathcal{A}(\epsilon, \mathbf{k})}{i\omega_n - \epsilon}, \quad (39)$$

where

$$\mathcal{A}(\epsilon, \mathbf{k}) = \pi \sum_{\tau=\pm} \left(1 + \tau \sum_{j=1}^5 \Gamma_j \hat{d}_j \right) \delta \left(\omega + \mu - \tau \frac{k^2}{2m} \right) \quad (40)$$

Components of $\hat{\mathbf{d}}$ are shown in Eq. (45). After performing the analytic continuation to real frequency $i\omega \rightarrow \omega + i\eta$, we find the dynamic conductivity using the Kubo formula

$$\sigma_{zz}(\omega) = \frac{\Im \Pi_{zz}(i\omega \rightarrow \omega + i\eta)}{\omega}. \quad (41)$$

From the above expression we obtain both Drude and inter-band components of the dynamic conductivity. They respectively read

$$\sigma_{\text{Dr}}(\omega, T) = e^2 \delta\left(\frac{\omega}{T}\right) \sqrt{m T} F_{\text{Dr}}\left(\frac{\mu}{T}\right), \quad (42)$$

$$\sigma_{\text{IB}}(\omega, T) = e^2 \sqrt{m \omega} \sum_{\tau=\pm} \tanh\left(\frac{\omega + 2\tau\mu}{4T}\right). \quad (43)$$

The universal function $F_{\text{Dr}}(x)$ appearing in the expression of the Drude component is given by

$$F_{\text{Dr}}(x) = \frac{32}{3} \int_0^\infty du u^{3/2} \sum_{\tau=\pm} \text{sech}^2\left(u + \tau \frac{\mu}{2T}\right). \quad (44)$$

The scaling of this function is shown in Fig. 7. Note, inter-band component of the optical conductivity $\sigma_{\text{IB}}(\omega, T)$ vanishes as $\sqrt{\omega}$ as $\omega \rightarrow 0$, and the LSM can be identified as a *power-law insulator*.

B.2.3 Details of Luttinger model

Next we present some essential details of the Luttinger model, introduced in Sec. 4.1. The components of a five-dimensional unit vector $\hat{\mathbf{d}}(\hat{\mathbf{k}})$, appearing in the Luttinger Hamiltonian [see Eq. (4.2)], are given by

$$\begin{aligned} \hat{d}_1 &= \frac{i[Y_2^1 + Y_2^{-1}]}{\sqrt{2}} = \frac{\sqrt{3}}{2} \sin 2\theta \sin \phi = \sqrt{3} \hat{k}_y \hat{k}_z, \\ \hat{d}_2 &= \frac{[Y_2^{-1} + Y_2^1]}{\sqrt{2}} = \frac{\sqrt{3}}{2} \sin 2\theta \cos \phi = \sqrt{3} \hat{k}_x \hat{k}_z, \\ \hat{d}_3 &= \frac{i[Y_2^{-2} + Y_2^{-2}]}{\sqrt{2}} = \frac{\sqrt{3}}{2} \sin^2 \theta \sin 2\phi = \sqrt{3} \hat{k}_y \hat{k}_x, \\ \hat{d}_4 &= \frac{[Y_2^{-2} + Y_2^2]}{\sqrt{2}} = \frac{\sqrt{3}}{2} \sin^2 \theta \cos 2\phi = \frac{\sqrt{3}}{2} [\hat{k}_x^2 - \hat{k}_y^2], \\ \hat{d}_5 &= Y_2^0 = \frac{1}{2} (3 \cos^2 \theta - 1) = \frac{1}{2} [2\hat{k}_z^2 - \hat{k}_x^2 - \hat{k}_y^2], \end{aligned} \quad (45)$$

where $Y_l^m \equiv Y_l^m(\theta, \phi)$, $\hat{d}_j \equiv \hat{d}_j(\hat{\mathbf{k}})$, and θ and ϕ are the polar and azimuthal angles in the momentum space, respectively. Five mutually anti-commuting Γ matrices are

$$\begin{aligned} \Gamma_1 &= \frac{1}{\sqrt{3}} \{J_y, J_z\}, & \Gamma_2 &= \frac{1}{\sqrt{3}} \{J_x, J_z\}, & \Gamma_3 &= \frac{1}{\sqrt{3}} \{J_x, J_y\}, \\ \Gamma_4 &= \frac{1}{\sqrt{3}} [J_x^2 - J_y^2], & \Gamma_5 &= \frac{1}{3} [2J_z^2 - J_x^2 - J_y^2], \end{aligned} \quad (46)$$

where $\{A, B\} \equiv AB + BA$, and \mathbf{J} are three spin-3/2 matrices [see also Eq. (4.4)]. The above five Γ matrices are the components of the rank-two symmetric traceless tensor operator [122]

$$T_{\mu\nu} = \frac{1}{\sqrt{3}} \left[\{J_\mu, J_\nu\} - \frac{2}{3} \delta_{\mu\nu} \mathbf{J}^2 \right], \quad (47)$$

which transforms in the $S = 2$ representation of $SU(2)$ under spin rotations. In the basis specified in Sec. 4, the spin-3/2 matrices are defined as

$$\begin{aligned} J_x &= \frac{1}{2} \begin{pmatrix} 0 & \sqrt{3} & 0 & 0 \\ \sqrt{3} & 0 & 2 & 0 \\ 0 & 2 & 0 & \sqrt{3} \\ 0 & 0 & \sqrt{3} & 0 \end{pmatrix}, & J_y &= \frac{i}{2} \begin{pmatrix} 0 & -\sqrt{3} & 0 & 0 \\ \sqrt{3} & 0 & -2 & 0 \\ 0 & 2 & 0 & -\sqrt{3} \\ 0 & 0 & \sqrt{3} & 0 \end{pmatrix}, \\ J_z &= \frac{1}{2} \begin{pmatrix} 3 & 0 & 0 & 0 \\ 0 & 1 & 0 & 0 \\ 0 & 0 & -1 & 0 \\ 0 & 0 & 0 & -3 \end{pmatrix}. \end{aligned} \quad (48)$$

Both $\hat{\mathbf{d}}$ and $\mathbf{\Gamma}$ transform as vectors under the cubic point group (O_h), and their scalar product yields the Luttinger Hamiltonian, an A_{1g} quantity. On the other hand, ten commutators $\Gamma_{jk} = [\Gamma_j, \Gamma_k]/(2i)$ with $j > k$ can be expressed in terms of the products of *odd* number of spin-3/2 matrices as follows

$$\begin{aligned} \Gamma_{45} &= -\frac{2}{\sqrt{3}} [J_x J_y J_z + J_z J_y J_x], & \Gamma_{12} &= \frac{1}{3} [7J_z - 4J_z^3], & \Gamma_{13} &= -\frac{1}{3} [7J_y - 4J_y^3], \\ \Gamma_{23} &= \frac{1}{3} [7J_x - 4J_x^3], & \Gamma_{34} &= -\frac{1}{6} [13J_z - 4J_z^3], & \Gamma_{35} &= \frac{1}{\sqrt{3}} \{J_z, J_x^2 - J_y^2\}, \\ \Gamma_{14} &= \frac{1}{12} [13J_x - 4J_x^3] + \frac{1}{2} \{J_x, J_y^2 - J_z^2\}, & \Gamma_{24} &= \frac{1}{12} [13J_y - 4J_y^3] - \frac{1}{2} \{J_y, J_z^2 - J_x^2\}, \\ \Gamma_{15} &= \frac{1}{4\sqrt{3}} [13J_x - 4J_x^3] - \frac{1}{2\sqrt{3}} \{J_x, J_y^2 - J_z^2\}, \\ \Gamma_{25} &= -\frac{1}{4\sqrt{3}} [13J_y - 4J_y^3] - \frac{1}{2\sqrt{3}} \{J_y, J_z^2 - J_x^2\}. \end{aligned} \quad (49)$$

The four-dimensional identity matrix can be written as $\Gamma_0 = \frac{4}{15} (J_x^2 + J_y^2 + J_z^2)$.

B.2.4 Fierz Identity

In this section we present the Fierz reduction of the number of quartic terms for the interacting Luttinger system. To perform this exercise for generic local density-density interactions we introduce a *six* component vector

$$X^\top = \left[(\Psi^\dagger \Gamma_0 \Psi)^2, \sum_{j=1}^3 (\Psi^\dagger \Gamma_j \Psi)^2, \sum_{j=4}^5 (\Psi^\dagger \Gamma_j \Psi)^2, (\Psi^\dagger \Gamma_{45} \Psi)^2 \right], \quad (50)$$

$$\left. \sum_{j=1}^3 (\Psi^\dagger \Gamma_j \Gamma_{45} \Psi)^2, \sum_{j=1}^3 \sum_{k=4}^5 (\Psi^\dagger \Gamma_{jk} \Psi)^2 \right],$$

constituted by the quartic terms appearing in H_{int} , see Eq. (4.11). We recall Eq. (2.21) and set $D = 4$ and $x = y$. Then the Fierz matrix [Eq. (2.22)] reads

$$F = \begin{pmatrix} 5 & 1 & 1 & 1 & 1 & 1 \\ 3 & 3 & -3 & 3 & -1 & 1 \\ 2 & -2 & 4 & -2 & 2 & 0 \\ 1 & 1 & -1 & 5 & 1 & -1 \\ 3 & -1 & 3 & 3 & 3 & -1 \\ 6 & 2 & 0 & -6 & -2 & 4 \end{pmatrix}. \quad (51)$$

The rank of F is 3. Hence, the number of linearly independent quartic terms is $D(F) - R(F) = 6 - 3 = 3$, where D and R are respectively the dimensionality and the rank. We chose four-fermion interactions proportional to λ_0 , λ_1 and λ_3 as *three* linearly independent quartic terms. The remaining three quartic terms can then be expressed in terms of linear combinations of the above three according to

$$\begin{aligned} (\Psi^\dagger \Gamma_{45} \Psi)^2 &= -\frac{1}{2} (\Psi^\dagger \Psi)^2 - \frac{1}{2} \sum_{j=1}^3 (\Psi^\dagger \Gamma_j \Psi)^2 + \frac{1}{2} \sum_{j=4}^5 (\Psi^\dagger \Gamma_j \Psi)^2, \\ \sum_{j=1}^3 (\Psi^\dagger \Gamma_j \Gamma_{45} \Psi)^2 &= -\frac{3}{2} (\Psi^\dagger \Psi)^2 + \frac{1}{2} \sum_{j=1}^3 (\Psi^\dagger \Gamma_j \Psi)^2 - \frac{3}{2} \sum_{j=4}^5 (\Psi^\dagger \Gamma_j \Psi)^2, \\ \sum_{j=1}^3 \sum_{k=4}^5 (\Psi^\dagger \Gamma_{jk} \Psi)^2 &= -3 (\Psi^\dagger \Psi)^2 - \sum_{j=1}^3 (\Psi^\dagger \Gamma_j \Psi)^2. \end{aligned} \quad (52)$$

Therefore, during the RG analysis whenever we generate any one of the above three quartic terms we can immediately express them in terms of the ones proportional to λ_0 , λ_1 and λ_2 . Therefore, the interacting model [see Eq. (4.12)] remains closed under coarse graining to any order in the perturbation theory.

B.2.5 Details of RG flow equations

The RG flow equations, displayed in Eq. (4.21), are expressed in terms of the functions $H_{km}^j(\alpha, t, \mu)$, where $j, k, m = 0, 1, 2$. For brevity we here drop the explicit dependence of these functions on α, t and μ . The functions appearing in the β function of g_0 are given by

$$\begin{aligned} H_{00}^0 &= \frac{5}{4} \left[-f_0 - \tilde{f}_0 - 4f_g - 6f_t \right], & H_{11}^0 &= \frac{5}{4} \left[-6\tilde{f}_0 - 6f_g + 6\tilde{f}_g - 3f_t + 3\tilde{f}_t \right], \\ H_{22}^0 &= \frac{5}{4} \left[f_0 - 3\tilde{f}_0 - 3f_t + 3\tilde{f}_t \right], & H_{01}^0 &= \frac{5}{4} \left[6f_0 + 6f_g + 6\tilde{f}_g + 18f_t + 12\tilde{f}_t \right], \end{aligned}$$

$$H_{02}^0 = \frac{5}{2} \left[2f_0 + 5f_g + 3f_t + 3\tilde{f}_g + 3\tilde{f}_t \right], \quad H_{12}^0 = \frac{15}{2} \left[-f_0 - \tilde{f}_0 - f_g + \tilde{f}_g - 2f_t + 2\tilde{f}_t \right]. \quad (53)$$

The six functions appearing in the RG flow equation for g_1 are given by

$$\begin{aligned} H_{00}^1 &= \frac{5}{4}(f_t + \tilde{f}_t), & H_{11}^1 &= \frac{5}{4}(-5f_0 + \tilde{f}_0 + 10f_g + 2\tilde{f}_g + 10f_t + 10\tilde{f}_t), \\ H_{22}^1 &= \frac{5}{4}(-f_0 - \tilde{f}_0 + 3f_t + \tilde{f}_t), & H_{01}^1 &= \frac{5}{2}(2f_0 - \tilde{f}_0 - 3f_g + \tilde{f}_g - \tilde{f}_t), \\ H_{02}^1 &= -\frac{5}{2}(f_g - \tilde{f}_g + f_t - \tilde{f}_t), & H_{12}^1 &= -\frac{5}{2}(3f_0 + \tilde{f}_0 - 7f_g - \tilde{f}_g - 2\tilde{f}_t). \end{aligned} \quad (54)$$

Finally, the flow equation for g_2 is expressed in terms of the following six functions

$$\begin{aligned} H_{00}^2 &= \frac{5}{4}(f_g + \tilde{f}_g), & H_{11}^2 &= \frac{5}{4}(-3f_0 - 3\tilde{f}_0 + 3f_g + 3\tilde{f}_g + 3f_t - 3\tilde{f}_t), \\ H_{22}^2 &= \frac{5}{4}(-3f_0 + \tilde{f}_0 + 4f_g + 4\tilde{f}_g + 9f_t + 3\tilde{f}_t), & H_{01}^2 &= \frac{5}{4}(-6f_t + 6\tilde{f}_t), \\ H_{02}^2 &= \frac{5}{2}(2f_0 - \tilde{f}_0 + f_g - \tilde{f}_g - 3f_t), & H_{12}^2 &= \frac{15}{2}(-f_0 - f_g + \tilde{f}_g + 4f_t + \tilde{f}_t). \end{aligned} \quad (55)$$

Note that in the above expression $f_j \equiv f_j(\alpha, t, \mu)$ and $\tilde{f}_j \equiv \tilde{f}_j(\alpha, t, \mu)$ s for $j = 0, t, g$, and

$$\begin{aligned} f_0(\alpha, t, \mu) &= -\frac{1}{2} \int d\Omega \frac{1}{2t} \sum_{\tau=\pm 1} \left[\operatorname{sech}^2 \left(\frac{f + \tau\mu}{2t} \right) + \frac{2t}{f} \tanh \left(\frac{f + \tau\mu}{2t} \right) \right], \\ f_t(\alpha, t, \mu) &= -\frac{1}{2} \int d\Omega \frac{\cos^2 \alpha}{2t} \sum_{\tau=\pm 1} \left[\frac{1}{f^2} \operatorname{sech}^2 \left(\frac{f + \tau\mu}{2t} \right) - \frac{2t}{f^3} \tanh \left(\frac{f + \tau\mu}{2t} \right) \right] \sum_{j=1}^3 \frac{\hat{d}_j^2}{3}, \\ f_g(\alpha, t, \mu) &= -\frac{1}{2} \int d\Omega \frac{\sin^2 \alpha}{2t} \sum_{\tau=\pm 1} \left[\frac{1}{f^2} \operatorname{sech}^2 \left(\frac{f + \tau\mu}{2t} \right) - \frac{2t}{f^3} \tanh \left(\frac{f + \tau\mu}{2t} \right) \right] \sum_{j=4}^5 \frac{\hat{d}_j^2}{2}, \\ \tilde{f}_0(\alpha, t, \mu) &= -\frac{1}{2} \int d\Omega \frac{1}{\mu \left(1 - \left(\frac{\mu}{f} \right)^2 \right)} \sum_{\tau=\pm 1} \tanh \left(\frac{f + \tau\mu}{2t} \right) \left[\tau + \frac{\mu}{f} - 2\tau \left(\frac{\mu}{f} \right)^2 \right], \\ \tilde{f}_t(\alpha, t, \mu) &= \frac{1}{2} \int d\Omega \frac{\cos^2 \alpha}{f^2 \mu \left(1 - \left(\frac{\mu}{f} \right)^2 \right)} \sum_{\tau=\pm 1} \tanh \left(\frac{f + \tau\mu}{2t} \right) \left[-\tau + \frac{\mu}{f} \right] \sum_{j=1}^3 \frac{\hat{d}_j^2}{3}, \\ \tilde{f}_g(\alpha, t, \mu) &= \frac{1}{2} \int d\Omega \frac{\sin^2 \alpha}{f^2 \mu \left(1 - \left(\frac{\mu}{f} \right)^2 \right)} \sum_{\tau=\pm 1} \tanh \left(\frac{f + \tau\mu}{2t} \right) \left[-\tau + \frac{\mu}{f} \right] \sum_{j=4}^5 \frac{\hat{d}_j^2}{2}, \end{aligned} \quad (56)$$

where $d\Omega = \sin \theta d\theta d\phi$, $f \equiv f(\alpha, \theta, \phi)$ and

$$f(\alpha, \theta, \phi) = \sqrt{\cos^2 \alpha (\hat{d}_1^2 + \hat{d}_2^2 + \hat{d}_3^2) + \sin^2 \alpha (\hat{d}_4^2 + \hat{d}_5^2)}. \quad (57)$$

The definition of $\hat{\mathbf{d}}$ is already provided in Eq. (45).

In terms of f_j s and \tilde{f}_j s we can express the leading order RG flow equations for all

FPs	$(g_0^*, g_1^*, g_2^*) \times 10^3$	EVs of SM
Gaussian	(0, 0, 0)	$(-1, -1, -1)\epsilon$
QCP $_{\frac{1}{4}}^1$	$(2.24, 2.03, 2.03)\epsilon$	$(\mathbf{1}, -0.870, -0.704)\epsilon$
QCP $_{\frac{1}{2}}^1$	$(1.49, 1.47, 1.26)\epsilon$	$(-1.075, \mathbf{1}, -0.654)\epsilon$
QCP $_{\frac{2}{2}}^2$	$(-2.93, -2.84, 3.76)\epsilon$	$(-1.169, \mathbf{1}, -0.933)\epsilon$
BCP $_{\frac{\pi}{2}}$	$(-1.58, -1.33, 5.54)\epsilon$	$(1.271, \mathbf{1}, -0.527)\epsilon$
QCP $_0^1$	$(1.95, 1.71, 1.94)\epsilon$	$(\mathbf{1}, -0.889, -0.642)\epsilon$
QCP $_0^2$	$(-5.98, 4.80, -5.87)\epsilon$	$(-1.131, \mathbf{1}, -0.134)\epsilon$
BCP $_0$	$(-5.60, 4.97, -5.48)\epsilon$	$(-1.075, \mathbf{1}, 0.132)\epsilon$

Table 3: Three eigenvalues (EVs) of the stability matrix (SM) $M(g_0, g_1, g_2)$, defined in Eq. (59) at various fixed points (FPs) located at (g_0^*, g_1^*, g_2^*) , see Table 4.1. We highlighted the +1 eigenvalue in bold font. The trivial Gaussian fixed point is found for any arbitrary value of α .

source terms [see Eq. (4.23)] as

$$\begin{aligned}
\frac{d \ln \Delta_0}{dl} - 2 &= -\frac{5}{4}(f_0 + 2f_g + 3f_t)(3g_0 - 3g_1 - 2g_2), \\
\frac{d \ln \Delta_1}{dl} - 2 &= \frac{5}{4}(f_0 - 2f_g - f_t)(g_0 - 5g_1 - 2g_2), \\
\frac{d \ln \Delta_2}{dl} - 2 &= \frac{5}{4}(f_0 - 3f_t)(g_0 - 3g_1 - 4g_2), \\
\frac{d \ln \Delta_3}{dl} - 2 &= \frac{5}{4}(f_0 - 2f_g + 3f_t)(g_0 + 3g_1 - 2g_2), \\
\frac{d \ln \Delta_4}{dl} - 2 &= \frac{5}{4}(f_0 + 2f_g - f_t)(g_0 - g_1 + 2g_2), \\
\frac{d \ln \Delta_5}{dl} - 2 &= \frac{5}{4}(f_0 + f_t)(g_0 + g_1), \\
\frac{d \ln \Delta_{A_{1g}}^P}{dl} - 2 &= -\frac{5}{4}(\tilde{f}_0 - 2\tilde{f}_g - 3\tilde{f}_t)(g_0 + 3g_1 + 2g_2), \\
\frac{d \ln \Delta_{T_{2g}}^P}{dl} - 2 &= -\frac{5}{4}(\tilde{f}_0 + 2\tilde{f}_g + \tilde{f}_t)(g_0 - g_1 - 2g_2), \\
\frac{d \ln \Delta_{E_g}^P}{dl} - 2 &= -\frac{5}{4}(\tilde{f}_0 + 3\tilde{f}_t)(g_0 - 3g_1).
\end{aligned} \tag{58}$$

These flow equations are schematically shown in Eq. (4.24).

B.2.6 Stability matrix analysis

To gain insight into the local structure of the RG flow trajectories in the close proximity to any fixed point, we perform the *stability* analysis around them, as outlined in Sec. 2.2.2.1. In the context of the 3D Luttinger semimetal, Eq. (2.27) takes the explicit

form

$$M(g_0, g_1, g_2) = \begin{bmatrix} \frac{d\beta_{g_0}}{dg_0} & \frac{d\beta_{g_1}}{dg_0} & \frac{d\beta_{g_2}}{dg_0} \\ \frac{d\beta_{g_0}}{dg_1} & \frac{d\beta_{g_1}}{dg_1} & \frac{d\beta_{g_2}}{dg_1} \\ \frac{d\beta_{g_0}}{dg_2} & \frac{d\beta_{g_1}}{dg_2} & \frac{d\beta_{g_2}}{dg_2} \end{bmatrix}. \quad (59)$$

We classify the fixed points, located at (g_0^*, g_1^*, g_2^*) , according to the number of positive and negative eigenvalues of $M(g_0^*, g_1^*, g_2^*)$.

1. There exists only one fixed point at $(g_0^*, g_1^*, g_2^*) = (0, 0, 0)$ with three negative eigenvalues $(-1, -1, -1)\epsilon$ of the stability matrix. This fixed point, referred as *Gaussian* in Table 3, is stable from all directions and represents the noninteracting stable LSM for sufficiently weak but generic short-range interactions.

2. Fixed points possessing one positive and two negative eigenvalues for the stability matrix are the QCPs. Such fixed points control continuous QPTs from LSM to BSPs. Since such QPTs can be triggered by tuning only one parameter (the interaction strength along the relevant direction, determined by the eigenvector associated with the positive eigenvalue of the stability matrix), they are continuous in nature. Concomitantly, a single parameter scaling emerges in the vicinity of all QCPs. The positive eigenvalue of the stability matrix also determines the inverse of the correlation length exponent (ν) at the QCPs [see also Sec. 4.2.4].

3. Fixed points with two positive and one negative eigenvalues for the stability matrix are the BCPs. Typically BCPs are found when there exists more than one QCP in the multi-dimensional coupling constant space. For example, only around $\alpha = \frac{\pi}{2}$ and 0, when the coupled RG flow equations support two QCPs, there exists one BCP (respectively denoted by $\text{BCP}_{\frac{\pi}{2}}$ and BCP_0). Existence of such a BCP is necessary to ensure the continuity of the RG flow trajectories. A BCP also separates the basin of attractions of two QCPs.

A summary of the eigenvalues for the stability matrix is presented in Table 3. We did not find any fixed point with three positive eigenvalues of the corresponding stability matrix.

C.3 Two-dimensional Dirac and Luttinger liquids

In what follows we present auxiliary calculations concerning the renormalization group analysis of interacting electrons in monolayer and Bernal bilayer graphene. First, we review the diagrammatic contributions to order parameter fields. Then, we present the Fierz reduction of quartic interaction terms. Finally, we show the explicit form of the RG flow equations.

C.3.1 Diagrammatic contributions to order parameter fields

In this section, we review the possible one-loop contributions to the anomalous dimension of various order parameter or conjugate fields that couple to some fermion bilinear as $\Delta_O(\Psi^\dagger O\Psi)$, in an interacting theory containing local four fermion interactions of the schematic form $g_M(\Psi^\dagger M\Psi)^2$. The purpose of this exercise is to demonstrate the manifestation of the selection rules and organizing principle, introduced in Chapter 5 [see Eqs. (5.2) and (5.3)], in a one-loop perturbative calculation. We here consider one-component order parameter and quartic interaction terms. In general, we can apply the following to multi-component interactions and order parameters by adding the contributions from individual pairs. In order to demonstrate the organizing principle, in this appendix we incorporate finite temperature. However, we set chemical potential to zero. Note that the effect of chemical doping is an increased propensity toward superconducting orders.

In the above outlined scenario there are two sources of one-loop correction to an order parameter field, the bubble and vertex diagrams [see Fig. 2.2(b) and (c) respectively], denoted by $B(t)$ and $V(t)$, respectively, where t is the dimensionless temperature [see Eq. (6.26)]. The contribution from the bubble diagram reads

$$\begin{aligned} B(t) &= -2T \text{Tr} \sum_{n=-\infty}^{\infty} \int \frac{d^d \mathbf{k}}{(2\pi)^d} [MG(i\omega_n, \mathbf{k})OG(i\omega_n, \mathbf{k})] \\ &= 2T \text{Tr} \sum_{n=-\infty}^{\infty} \int \frac{d^d \mathbf{k}}{(2\pi)^d} \frac{\omega_n^2 + g(\mathbf{k})}{(\omega_n^2 + \epsilon_{\mathbf{k}}^2)^2} MO, \end{aligned} \quad (60)$$

where

$$g(\mathbf{k}) = \begin{cases} +\epsilon_{\mathbf{k}}^2, & \text{if } \{O, H\} = 0, \\ -\epsilon_{\mathbf{k}}^2, & \text{if } [O, H] = 0, \\ 0, & \text{if } A_H = C_H, \end{cases} \quad (61)$$

where A_H (C_H) is the number of anticommuting (commuting) matrix pairs between the order parameter and the Hamiltonian (H), $\omega_n = (2n+1)\pi T$ are the fermionic Matsubara frequencies, $G(i\omega_n, \mathbf{k}) = [i\omega_n - H]^{-1}$ is the fermionic Greens function and $\epsilon_{\mathbf{k}}$ is the positive eigenvalue of H (see Appendix C.3.3). Due to the trace (Tr), $B(t)$ is nonzero only if $O = M$ [selection rule (Ia), or Eq. (5.2a)].

Performing the Matsubara sum and integrating over the momentum shell $\Lambda e^{-\ell} < |\mathbf{k}| < \Lambda$, we obtain

$$B(t) = \text{dim}(M) \frac{\Lambda^d}{2\pi\epsilon_\Lambda} \begin{cases} f_E(t), & \text{if } \{O, H\} = 0, \\ f_S(t), & \text{if } [O, H] = 0, \\ [f_E(t) + f_S(t)]/2, & \text{if } A_H = C_H, \end{cases} \quad (62)$$

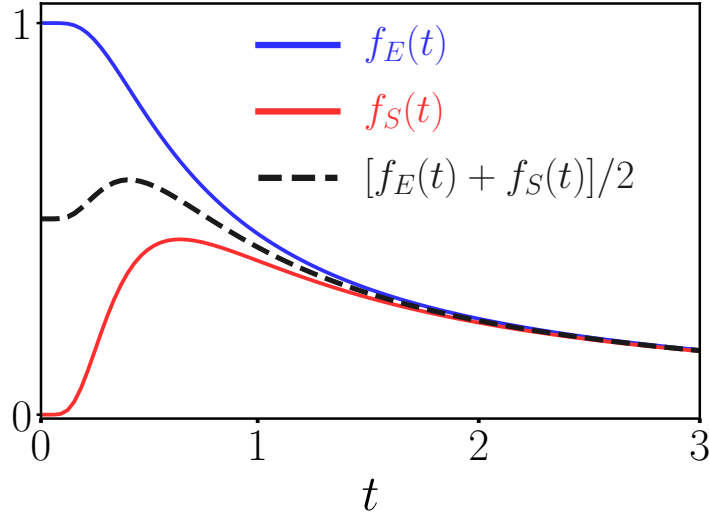


Figure 8: Functions of dimensionless temperature t from Eq. (63), resulting from the loop integrals at zero chemical doping. At low temperatures $f_E(t)$ dominates, while $f_S(t)$ is small. Consequently, order parameters that fully commute with the Hamiltonian only get renormalized through their engineering dimensions at zero temperature. Partially anti-commuting order parameters acquire a one-loop correction proportional to the arithmetic mean $[f_E(t) + f_S(t)]/2$. Figure adapted from Ref. [13].

		$[O, H] = 0$	$\{O, H\} = 0$	$A_H = C_H = 1$
$O = M$		0	$\dim(M) - 1$	$\frac{1}{2}[\dim(M) - 1]$
$O \neq M$	$\{O, M\} = 0$	0	1	1/2
	$[O, M] = 0$	0	-1	-1/2

Table 4: Anomalous dimension to the one-loop order (see Fig. 2.2) in units of $2\pi\Lambda^d/\epsilon_\Lambda$ acquired by the order parameter $\Delta_O(\Psi^\dagger O\Psi)$ in the presence of a four fermion interaction term $g_M(\Psi^\dagger M\Psi)^2$. Here $\dim(M)$ is the dimension of the Hermitian matrix M and the normal state band structure is described by the single-particle Hamiltonian H .

where $\dim(M)$ is the dimension of M , and

$$f_E(t) = \tanh\left(\frac{1}{2t}\right), \quad f_S(t) = \frac{1}{2t} \operatorname{sech}^2\left(\frac{1}{2t}\right). \quad (63)$$

The functions $f_E(t)$ and $f_S(t)$, as well as their arithmetic average are shown in Fig. 8. Note that $f_E(0) = 1$ and $f_S(0) = 0$, and thus the energetically favorable fully gapped phases dominate at low temperatures. On the other hand, at higher temperatures $f_E(t)$ decreases and $f_S(t)$ increases, hence giving way to phases with higher entropy gain, a manifestation of the organizing principle [rule (II) or Eq. (5.3)]. In this context recall that while $\{O, H\} = 0$ leads to fully and isotropically gapped spectra in the ordered phase, $[O, H] = 0$ yields gapless quasiparticles therein. A partially anticommuting ($A_H = C_H$) order parameter acquires a contribution that is the average of the former two cases.

The vertex correction yields the following contribution

$$\begin{aligned} V(t) &= 2T \sum_{n=-\infty}^{\infty} \int \frac{d^d \mathbf{k}}{(2\pi)^d} [MG(i\omega_n, \mathbf{k})OG(i\omega_n, \mathbf{k})M] \\ &= -2 \sum_{n=-\infty}^{\infty} \int \frac{d^d \mathbf{k}}{(2\pi)^d} \frac{\omega_n^2 + g(\mathbf{k})}{(\omega_n^2 + \epsilon_{\mathbf{k}}^2)^2} M O M, \end{aligned} \quad (64)$$

where $g(\mathbf{k})$ is defined in Eq. (61). After performing the Matsubara sum and the shell integral this contribution reads

$$V(t) = \pm \frac{\Lambda^d}{2\pi\epsilon_{\Lambda}} \begin{cases} f_E(t), & \text{if } \{O, H\} = 0, \\ f_S(t), & \text{if } [O, H] = 0, \\ [f_E(t) + f_S(t)]/2, & \text{if } A_H = C_H, \end{cases} \quad (65)$$

where the positive (negative) sign follows if O and M mutually anticommute (commute). The above results at *zero temperature* can be summarized as follows.

(a) An order parameter O that fully commutes with the Hamiltonian acquires identically zero anomalous dimension, irrespective of the interaction channel.

(b) An order parameter that fully anticommutes with the Hamiltonian acquires *positive* anomalous dimension if it fulfills $O = M$ or $\{O, M\} = 0$ [selection rules (Ia) and (Ib), or Eqs. (5.2a) and (5.2b) respectively], and *negative* anomalous dimension if it fulfills $[O, M] = 0$ but $O \neq M$.

(c) An order parameter that partially anticommutes with the Hamiltonian (here $A_H = C_H = 1$) acquires anomalous dimension that is the *average* of cases (a) and (b).

These findings are also summarized in Table 4. Note since $\epsilon_{\mathbf{k}} \sim |\mathbf{k}|^z$ the quantity $\Lambda^d/\epsilon_{\Lambda} \sim \Lambda^{d-z} = \Lambda^{\epsilon}$. Indeed at the lower critical dimension where $\epsilon = 0$ the cutoff dependence drops out from $B(t)$ and $V(t)$.

C.3.2 Fierz reduction of local interaction terms

Here we present the Fierz reduction, outlined in Sec. 2.2.1, in the context of spinful fermions in monolayer and bilayer graphene. There are altogether eighteen momentum-independent quartic terms, that describe all the local quartic interactions. We report the existence of nine linearly independent four fermion terms, which we choose, without the loss of generality, to be the spin singlet interactions. Since we write all quartic terms in the particle-hole basis, we here refrain from using the Nambu basis, and Ψ and Ψ^\dagger are eight-component spinors structured according to Eq. (6.9).

We start by organizing the interaction terms into an eighteen-component array as

$\mathbf{X} = [\mathbf{X}^s, \mathbf{X}^t]^\top$, where

$$\begin{aligned} \mathbf{X}^s = & \left\{ (\Psi^\dagger \Gamma_{000} \Psi)^2, (\Psi^\dagger \Gamma_{033} \Psi)^2, (\Psi^\dagger \Gamma_{001} \Psi)^2 + (\Psi^\dagger \Gamma_{032} \Psi)^2, (\Psi^\dagger \Gamma_{030} \Psi)^2, (\Psi^\dagger \Gamma_{003} \Psi)^2, \right. \\ & \left. (\Psi^\dagger \Gamma_{031} \Psi)^2 + (\Psi^\dagger \Gamma_{002} \Psi)^2, \sum_{j=1}^2 (\Psi^\dagger \Gamma_{0j1} \Psi)^2, \sum_{j=1}^2 (\Psi^\dagger \Gamma_{0j2} \Psi)^2, \sum_{j=1}^2 \sum_{k=0,3} (\Psi^\dagger \Gamma_{0jk} \Psi)^2 \right\}^\top, \quad (66) \\ \mathbf{X}^t = & \left\{ \sum_{s=1}^3 (\Psi^\dagger \Gamma_{s00} \Psi)^2, \sum_{s=1}^3 (\Psi^\dagger \Gamma_{s33} \Psi)^2, \sum_{s=1}^3 [(\Psi^\dagger \Gamma_{s01} \Psi)^2 + (\Psi^\dagger \Gamma_{0s32} \Psi)^2], \right. \\ & \sum_{s=1}^3 (\Psi^\dagger \Gamma_{s30} \Psi)^2, \sum_{s=1}^3 (\Psi^\dagger \Gamma_{s03} \Psi)^2, \sum_{s=1}^3 (\Psi^\dagger \Gamma_{s31} \Psi)^2 + (\Psi^\dagger \Gamma_{s02} \Psi)^2, \sum_{s=1}^3 \sum_{j=1}^2 (\Psi^\dagger \Gamma_{sj1} \Psi)^2, \\ & \left. \sum_{s=1}^3 \sum_{j=1}^2 (\Psi^\dagger \Gamma_{sj2} \Psi)^2, \sum_{s=1}^3 \sum_{j=1}^2 \sum_{k=0,3} (\Psi^\dagger \Gamma_{sjk} \Psi)^2 \right\}^\top, \quad (67) \end{aligned}$$

and \mathbf{X}^s and \mathbf{X}^t contain the spin singlet and triplet quartic terms, respectively.

We now set $D = 8$ and $x = y$ in Eq. (2.21) and calculate the eighteen-dimensional Fierz matrix F as defined in Eq. (2.22) to obtain

$$F = \begin{pmatrix} -9 & -1 & -1 & -1 & -1 & -1 & -1 & -1 & -1 & -1 & -1 & -1 & -1 & -1 & -1 & -1 & -1 & -1 \\ -1 & -9 & 1 & -1 & -1 & 1 & -1 & -1 & 1 & -1 & -1 & 1 & -1 & -1 & 1 & -1 & -1 & 1 \\ -2 & 2 & -8 & -2 & 2 & 0 & -2 & 2 & 0 & -2 & 2 & 0 & -2 & 2 & 0 & -2 & 2 & 0 \\ -1 & -1 & -1 & -9 & -1 & -1 & 1 & 1 & 1 & -1 & -1 & -1 & -1 & -1 & 1 & 1 & 1 & 1 \\ -1 & -1 & 1 & -1 & -9 & 1 & 1 & 1 & -1 & -1 & -1 & 1 & -1 & -1 & 1 & 1 & 1 & -1 \\ -2 & 2 & 0 & -2 & 2 & -8 & 2 & -2 & 0 & -2 & 2 & 0 & -2 & 2 & 0 & 2 & -2 & 0 \\ -2 & -2 & -2 & 2 & 2 & 2 & -8 & 0 & 0 & -2 & -2 & -2 & 2 & 2 & 2 & 0 & 0 & 0 \\ -2 & -2 & 2 & 2 & 2 & -2 & 0 & -8 & 0 & -2 & -2 & 2 & 2 & 2 & -2 & 0 & 0 & 0 \\ -4 & 4 & 0 & 4 & -4 & 0 & 0 & 0 & -8 & -4 & 4 & 0 & 4 & -4 & 0 & 0 & 0 & 0 \\ -3 & -3 & -3 & -3 & -3 & -3 & -3 & -3 & -3 & -7 & 1 & 1 & 1 & 1 & 1 & 1 & 1 & 1 \\ -3 & -3 & 3 & -3 & -3 & 3 & -3 & -3 & 3 & 1 & -7 & -1 & 1 & 1 & -1 & 1 & 1 & -1 \\ -6 & 6 & 0 & -6 & 6 & 0 & -6 & 6 & 0 & 2 & -2 & -8 & 2 & -2 & 0 & 2 & -2 & 0 \\ -3 & -3 & -3 & -3 & -3 & -3 & 3 & 3 & 3 & 1 & 1 & 1 & -7 & 1 & 1 & -1 & -1 & -1 \\ -3 & -3 & 3 & -3 & -3 & 3 & 3 & 3 & -3 & 1 & 1 & -1 & 1 & -7 & -1 & -1 & -1 & 1 \\ -6 & 6 & 0 & -6 & 6 & 0 & 6 & -6 & 0 & 2 & -2 & 0 & 2 & -2 & -8 & -2 & 2 & 0 \\ -6 & -6 & -6 & 6 & 6 & 6 & 0 & 0 & 0 & 2 & 2 & 2 & -2 & -2 & -2 & -8 & 0 & 0 \\ -6 & -6 & 6 & 6 & 6 & -6 & 0 & 0 & 0 & 2 & 2 & -2 & -2 & -2 & 2 & 0 & -8 & 0 \\ -12 & 12 & 0 & 12 & -12 & 0 & 0 & 0 & 0 & 4 & -4 & 0 & -4 & 4 & 0 & 0 & 0 & -8 \end{pmatrix}. \quad (68)$$

The number of independent quartic terms is given by $D(F) - R(F) = 18 - 9 = 9$, where D and R indicate the dimensionality and the rank respectively. We can extract the relevant equations by reordering the columns of F and performing row reduction. Choosing the spin singlet interactions as the independent ones we obtain nine equations

for the triplet interactions which we can write compactly in matrix form as

$$\mathbf{X}^t = \frac{1}{2} \begin{pmatrix} 3 & 1 & 1 & 1 & 1 & 1 & 1 & 1 & 1 \\ 1 & 3 & -1 & 1 & 1 & -1 & 1 & 1 & -1 \\ 2 & -2 & 2 & 2 & -2 & 0 & 2 & -2 & 0 \\ 1 & 1 & 1 & 3 & 1 & 1 & -1 & -1 & -1 \\ 1 & 1 & -1 & 1 & 3 & -1 & -1 & -1 & 1 \\ 2 & -2 & 0 & 2 & -2 & 2 & -2 & 2 & 0 \\ 2 & 2 & 2 & -2 & -2 & -2 & 2 & 0 & 0 \\ 2 & 2 & -2 & -2 & -2 & 2 & 0 & 2 & 0 \\ 4 & -4 & 0 & -4 & 4 & 0 & 0 & 0 & 2 \end{pmatrix} \mathbf{X}^s. \quad (69)$$

However, when nine linearly independent couplings are chosen in the spin singlet channels, we do not generate any quartic term in the spin triplet channel via coarse grain. Nevertheless, the above linear relations allow us to set the initial condition for any quartic interaction in the spin triplet channel in the RG equations, even though they are expressed in terms of the quartic interactions in the spin singlet channel (for example in case of the Hubbard model), and that way construct various cuts of the phase diagrams shown in Figs. 6.3-6.6.

C.3.3 Renormalization group (RG) flow equations

Here we provide further details to the RG analysis at finite temperature and chemical doping. Finite temperature causes the previously continuous Matsubara frequency to take on discrete values, $\omega \rightarrow \omega_n = (2n + 1)\pi T$, with $n \in \mathbb{Z}$ (integers) for fermions, where T is the dimensionfull temperature. Using the compact notations $\Omega_{\pm} = i\omega \pm \mu$, the four distinct loop integrals read

$$\begin{aligned} I_{\omega} &= T \sum_{\omega_n} \int \frac{d\mathbf{k}}{(2\pi)^d} \frac{\Omega_+^2}{(\Omega_+^2 - \epsilon_{\mathbf{k}}^2)^2} = -\frac{1}{4\pi} \frac{\Lambda^d}{\epsilon_{\Lambda}} f_{\omega}(t, \mu) l, \\ \tilde{I}_{\omega} &= T \sum_{\omega_n} \int \frac{d\mathbf{k}}{(2\pi)^d} \frac{\Omega_+ \Omega_-}{(\Omega_+^2 - \epsilon_{\mathbf{k}}^2)(\Omega_-^2 - \epsilon_{\mathbf{k}}^2)} = -\frac{1}{4\pi} \frac{\Lambda^d}{\epsilon_{\Lambda}} \tilde{f}_{\omega}(t, \mu) l, \\ I_k &= T \sum_{\omega_n} \int \frac{d\mathbf{k}}{(2\pi)^d} \frac{v_i^2(\mathbf{k})}{(\Omega_+^2 - \epsilon_{\mathbf{k}}^2)^2} = \frac{1}{4\pi} \frac{\Lambda^d}{\epsilon_{\Lambda}} f_k(t, \mu) l, \\ \tilde{I}_k &= T \sum_{\omega_n} \int \frac{d\mathbf{k}}{(2\pi)^d} \frac{v_i^2(\mathbf{k})}{(\Omega_+^2 - \epsilon_{\mathbf{k}}^2)(\Omega_-^2 - \epsilon_{\mathbf{k}}^2)} = \frac{1}{4\pi} \frac{\Lambda^d}{\epsilon_{\Lambda}} \tilde{f}_k(t, \mu) l, \end{aligned} \quad (70)$$

where $\epsilon_{\mathbf{k}}^2 = v_1^2(\mathbf{k}) + v_2^2(\mathbf{k})$, with $v_i(\mathbf{k}) = p_i(\mathbf{k})$ and $d_i(\mathbf{k})$ for Dirac and Luttinger fermions, respectively. For the definitions of these cubic harmonics see Sec. 6.2.1. Here $\epsilon_{\Lambda} = \epsilon_{|\mathbf{k}|=\Lambda}$ is the given quasiparticle spectrum evaluated at the ultraviolet momentum cutoff Λ . The functions of dimensionless temperature and chemical potential [see Eq. (6.26)] are of the

form

$$\begin{aligned}
f_\omega(t, \mu) &= \sum_{\tau=\pm} \left[\frac{\operatorname{sech}^2\left(\frac{1+\tau\mu}{2t}\right)}{4t} + \frac{\tanh\left(\frac{1+\tau\mu}{2t}\right)}{2} \right], \\
\tilde{f}_\omega(t, \mu) &= \sum_{\tau=\pm} \frac{\tau \tanh\left(\frac{1+\tau\mu}{2t}\right)(1 + \tau\mu - 2\mu^2)}{2\mu(1 - \mu^2)}, \\
f_k(t, \mu) &= \frac{1}{2} \sum_{\tau=\pm} \left[-\frac{\operatorname{sech}^2\left(\frac{1+\tau\mu}{2t}\right)}{4t} + \frac{\tanh\left(\frac{1+\tau\mu}{2t}\right)}{2} \right], \\
\tilde{f}_k(t, \mu) &= \frac{1}{2} \sum_{\tau=\pm} \frac{-\tau \tanh\left(\frac{1+\tau\mu}{2t}\right)(1 - \tau\mu)}{2\mu(1 - \mu^2)}. \tag{71}
\end{aligned}$$

Note, in the limit of zero chemical doping (but at finite temperature) they become

$$\frac{1}{2} \left[f_\omega(t, \mu \rightarrow 0) \pm 2f_k(t, \mu \rightarrow 0) \right] = \begin{cases} + : f_E(t), \\ - : f_S(t), \end{cases} \tag{72}$$

where $f_E(t)$ and $f_S(t)$ are defined in Eq. (63) and are shown in Fig. 8. On the other hand, in the limit of both zero temperature and zero chemical doping the functions take on the values

$$\begin{aligned}
f_\omega(t \rightarrow 0, \mu \rightarrow 0) &= 1, & \tilde{f}_\omega(t \rightarrow 0, \mu \rightarrow 0) &= 1, \\
f_k(t \rightarrow 0, \mu \rightarrow 0) &= \frac{1}{2}, & \tilde{f}_k(t \rightarrow 0, \mu \rightarrow 0) &= \frac{1}{2}. \tag{73}
\end{aligned}$$

In the rest of this appendix we display the flow equations of various coupling constants and order parameter conjugate fields, appearing in the theory of two-dimensional Dirac and Luttinger semimetals. Let us recall the schematic form of them from Eqs. (6.27) and (6.32),

$$\frac{dg_i^s}{d\ell} = -\epsilon g_i^s + \sum_{j,k} g_j^s g_k^s H_{jk}^i(t, \mu), \tag{74}$$

$$\bar{\beta}_{\Delta_k}^j \equiv \frac{d\Delta_k}{d\ell} - z = \sum_l F_{k,l}^j(t, \mu) g_l^s. \tag{75}$$

To differentiate between the two systems, we use the notation $H_{jk}^i(t, \mu) = M_{jk}^i(t, \mu)$ and $B_{jk}^i(t, \mu)$ for MLG and BLG respectively. These functions are obtained by computing the Feynman diagrams (c)-(f) in Fig. 2.1. All the terms that are not explicitly shown are zero. In case of the conjugate fields we write out the full β functions, $\bar{\beta}_{\Delta_k}^D$ ($\bar{\beta}_{\Delta_k}^L$) for MLG (BLG), which are obtained by computing the Feynman diagrams from Fig. 2.2. For brevity, we suppress the t and μ dependence of the functions from Eq. (71).

C.3.3.1 Monolayer graphene

The functions appearing in the RG flow equation for g_1^s in MLG are

$$\begin{aligned}
M_{11}^1 &= -24f_k - 10f_\omega - 2\tilde{f}_\omega, & M_{22}^1 &= 2f_\omega - 2\tilde{f}_\omega, & M_{33}^1 &= 4f_\omega - 4\tilde{f}_\omega, & M_{44}^1 &= 2f_\omega - 2\tilde{f}_\omega, \\
M_{55}^1 &= 2f_\omega - 2\tilde{f}_\omega, & M_{66}^1 &= 4f_\omega - 4\tilde{f}_\omega, & M_{77}^1 &= 4f_\omega - 4\tilde{f}_\omega, & M_{88}^1 &= 4f_\omega - 4\tilde{f}_\omega, \\
M_{99}^1 &= 8f_\omega - 8\tilde{f}_\omega, & M_{12}^1 &= 8f_k + 4f_\omega, & M_{13}^1 &= 16f_k + 8f_\omega, & M_{14}^1 &= 8f_k + 4f_\omega, \\
M_{15}^1 &= 8f_k + 4f_\omega, & M_{16}^1 &= 24f_k + 8f_\omega - 8\tilde{f}_k, & M_{17}^1 &= 16f_k + 8f_\omega, & M_{18}^1 &= 16f_k + 8f_\omega, \\
M_{19}^1 &= 32f_k + 16f_\omega, & M_{26}^1 &= 8f_k + 8\tilde{f}_k, & M_{34}^1 &= 8f_k - 8\tilde{f}_k, & M_{35}^1 &= 8f_k + 8\tilde{f}_k, \\
M_{79}^1 &= 16f_k + 16\tilde{f}_k, & M_{89}^1 &= 16f_k - 16\tilde{f}_k.
\end{aligned} \tag{76}$$

The functions appearing in the RG flow equation for g_2^s in MLG are

$$\begin{aligned}
M_{22}^2 &= 24f_k - 12f_\omega, & M_{33}^2 &= 4f_\omega + 4\tilde{f}_\omega, & M_{66}^2 &= 4f_\omega + 4\tilde{f}_\omega, & M_{99}^2 &= 8f_\omega + 8\tilde{f}_\omega, \\
M_{12}^2 &= -8f_k + 8f_\omega - 4\tilde{f}_\omega, & M_{16}^2 &= 8f_k + 8\tilde{f}_k, & M_{23}^2 &= 16f_k - 8f_\omega, & M_{24}^2 &= -8f_k + 4f_\omega, \\
M_{25}^2 &= -8f_k + 4f_\omega, & M_{26}^2 &= 24f_k - 8f_\omega - 8\tilde{f}_k, & M_{27}^2 &= -16f_k + 8f_\omega, \\
M_{28}^2 &= -16f_k + 8f_\omega, & M_{29}^2 &= 32f_k - 16f_\omega, & M_{34}^2 &= 8f_k + 8\tilde{f}_k, & M_{35}^2 &= 8f_k - 8\tilde{f}_k, \\
M_{45}^2 &= 4f_\omega - 4\tilde{f}_\omega, & M_{78}^2 &= 8f_\omega - 8\tilde{f}_\omega, & M_{79}^2 &= 16f_k - 16\tilde{f}_k, & M_{89}^2 &= 16f_k + 16\tilde{f}_k.
\end{aligned} \tag{77}$$

The functions appearing in the RG flow equation for g_3^s in MLG are

$$\begin{aligned}
M_{33}^3 &= -16f_\omega, & M_{77}^3 &= 4f_k + 4\tilde{f}_k, & M_{88}^3 &= 4f_k + 4\tilde{f}_k, & M_{99}^3 &= 16f_k + 16\tilde{f}_k, \\
M_{13}^3 &= 8f_\omega - 4\tilde{f}_\omega, & M_{14}^3 &= 4f_k - 4\tilde{f}_k, & M_{15}^3 &= 4f_k + 4\tilde{f}_k, & M_{23}^3 &= 4\tilde{f}_\omega, & M_{24}^3 &= 4f_k + 4\tilde{f}_k, \\
M_{25}^3 &= 4f_k - 4\tilde{f}_k, & M_{34}^3 &= 4f_\omega, & M_{35}^3 &= -4f_\omega, & M_{36}^3 &= 16f_k - 16\tilde{f}_k, & M_{37}^3 &= 8f_\omega, \\
M_{38}^3 &= -8f_\omega, & M_{46}^3 &= 4f_\omega - 4\tilde{f}_\omega, & M_{56}^3 &= 4f_\omega + 4\tilde{f}_\omega, & M_{78}^3 &= 8f_k - 8\tilde{f}_k, \\
M_{79}^3 &= 8f_\omega - 8\tilde{f}_\omega, & M_{89}^3 &= 8f_\omega + 8\tilde{f}_\omega.
\end{aligned} \tag{78}$$

The functions appearing in the RG flow equation for g_4^s in MLG are

$$\begin{aligned}
M_{44}^4 &= -24f_k - 12f_\omega, & M_{77}^4 &= 4f_\omega + 4\tilde{f}_\omega, & M_{88}^4 &= 4f_\omega + 4\tilde{f}_\omega, & M_{99}^4 &= 8f_\omega + 8\tilde{f}_\omega, \\
M_{13}^4 &= 8f_k - 8\tilde{f}_k, & M_{14}^4 &= 8f_k + 8f_\omega - 4\tilde{f}_\omega, & M_{23}^4 &= 8f_k + 8\tilde{f}_k, & M_{24}^4 &= 8f_k + 4f_\omega, \\
M_{25}^4 &= 4f_\omega - 4\tilde{f}_\omega, & M_{34}^4 &= 16f_k + 8f_\omega, & M_{36}^4 &= 8f_\omega - 8\tilde{f}_\omega, & M_{45}^4 &= 8f_k + 4f_\omega, \\
M_{46}^4 &= 24f_k + 8f_\omega - 8\tilde{f}_k, & M_{47}^4 &= -16f_k - 8f_\omega, & M_{48}^4 &= -16f_k - 8f_\omega, \\
M_{49}^4 &= -32f_k - 16f_\omega, & M_{56}^4 &= 8f_k + 8\tilde{f}_k, & M_{79}^4 &= 16f_k - 16\tilde{f}_k, & M_{89}^4 &= 16f_k + 16\tilde{f}_k.
\end{aligned} \tag{79}$$

The functions appearing in the RG flow equation for g_5^s in MLG are

$$\begin{aligned}
M_{55}^5 &= 24f_k - 12f_\omega, & M_{99}^5 &= 8f_\omega - 8\tilde{f}_\omega, & M_{13}^5 &= 8f_k + 8\tilde{f}_k, & M_{15}^5 &= -8f_k + 8f_\omega - 4\tilde{f}_\omega, \\
M_{23}^5 &= 8f_k - 8\tilde{f}_k, & M_{24}^5 &= 4f_\omega - 4\tilde{f}_\omega, & M_{25}^5 &= -8f_k + 4f_\omega, & M_{35}^5 &= 16f_k - 8f_\omega,
\end{aligned}$$

$$\begin{aligned}
M_{36}^5 &= 8f_\omega + 8\tilde{f}_\omega, & M_{45}^5 &= -8f_k + 4f_\omega, & M_{46}^5 &= 8f_k + 8\tilde{f}_k, & M_{56}^5 &= 24f_k - 8f_\omega - 8\tilde{f}_k, \\
M_{57}^5 &= 16f_k - 8f_\omega, & M_{58}^5 &= 16f_k - 8f_\omega, & M_{59}^5 &= -32f_k + 16f_\omega, & M_{78}^5 &= 8f_\omega + 8\tilde{f}_\omega, \\
M_{79}^5 &= 16f_k + 16\tilde{f}_k, & M_{89}^5 &= 16f_k - 16\tilde{f}_k.
\end{aligned} \tag{80}$$

The functions appearing in the RG flow equation for g_6^s in MLG are

$$\begin{aligned}
M_{11}^6 &= 2f_k - 2\tilde{f}_k, & M_{22}^6 &= 2f_k - 2\tilde{f}_k, & M_{33}^6 &= 8f_k - 8\tilde{f}_k, & M_{44}^6 &= 2f_k - 2\tilde{f}_k, \\
M_{55}^6 &= 2f_k - 2\tilde{f}_k, & M_{66}^6 &= 8f_k - 16f_\omega - 8\tilde{f}_k, & M_{77}^6 &= 4f_k - 4\tilde{f}_k, & M_{88}^6 &= 4f_k - 4\tilde{f}_k, \\
M_{99}^6 &= 16f_k - 16\tilde{f}_k, & M_{12}^6 &= 4f_k + 4\tilde{f}_k, & M_{16}^6 &= 8f_\omega - 4\tilde{f}_\omega, & M_{26}^6 &= 4\tilde{f}_\omega, \\
M_{34}^6 &= 4f_\omega - 4\tilde{f}_\omega, & M_{35}^6 &= 4f_\omega + 4\tilde{f}_\omega, & M_{45}^6 &= 4f_k + 4\tilde{f}_k, & M_{46}^6 &= 4f_\omega, & M_{56}^6 &= -4f_\omega, \\
M_{67}^6 &= -8f_\omega, & M_{68}^6 &= 8f_\omega, & M_{78}^6 &= 8f_k + 8\tilde{f}_k, & M_{79}^6 &= 8f_\omega + 8\tilde{f}_\omega, & M_{89}^6 &= 8f_\omega - 8\tilde{f}_\omega.
\end{aligned} \tag{81}$$

The functions appearing in the RG flow equation for g_7^s in MLG are

$$\begin{aligned}
M_{77}^7 &= 32f_k - 16f_\omega, & M_{17}^7 &= -8f_k + 8f_\omega - 4\tilde{f}_\omega, & M_{19}^7 &= 8f_k + 8\tilde{f}_k, & M_{27}^7 &= -8f_k + 4f_\omega, \\
M_{28}^7 &= 4f_\omega - 4\tilde{f}_\omega, & M_{29}^7 &= 8f_k - 8\tilde{f}_k, & M_{37}^7 &= -8f_k + 8f_\omega + 8\tilde{f}_k, & M_{38}^7 &= 8f_k - 8\tilde{f}_k, \\
M_{39}^7 &= 8f_\omega - 8\tilde{f}_\omega, & M_{47}^7 &= 8f_k + 4\tilde{f}_\omega, & M_{49}^7 &= 8f_k - 8\tilde{f}_k, & M_{57}^7 &= 8f_k - 4f_\omega, \\
M_{58}^7 &= 4f_\omega + 4\tilde{f}_\omega, & M_{59}^7 &= 8f_k + 8\tilde{f}_k, & M_{67}^7 &= 24f_k - 8f_\omega - 8\tilde{f}_k, & M_{68}^7 &= 8f_k + 8\tilde{f}_k, \\
M_{69}^7 &= 8f_\omega + 8\tilde{f}_\omega.
\end{aligned} \tag{82}$$

The functions appearing in the RG flow equation for g_8^s in MLG are

$$\begin{aligned}
M_{88}^8 &= -32f_k - 16f_\omega, & M_{18}^8 &= 8f_k + 8f_\omega - 4\tilde{f}_\omega, & M_{19}^8 &= 8f_k - 8\tilde{f}_k, & M_{27}^8 &= 4f_\omega - 4\tilde{f}_\omega, \\
M_{28}^8 &= 8f_k + 4f_\omega, & M_{29}^8 &= 8f_k + 8\tilde{f}_k, & M_{37}^8 &= 8f_k - 8\tilde{f}_k, & M_{38}^8 &= -8f_k - 8f_\omega + 8\tilde{f}_k, \\
M_{39}^8 &= 8f_\omega + 8\tilde{f}_\omega, & M_{48}^8 &= -8f_k + 4\tilde{f}_\omega, & M_{49}^8 &= 8f_k + 8\tilde{f}_k, & M_{57}^8 &= 4f_\omega + 4\tilde{f}_\omega, \\
M_{58}^8 &= -8f_k - 4f_\omega, & M_{59}^8 &= 8f_k - 8\tilde{f}_k, & M_{67}^8 &= 8f_k + 8\tilde{f}_k, & M_{68}^8 &= 24f_k + 8f_\omega - 8\tilde{f}_k, \\
M_{69}^8 &= 8f_\omega - 8\tilde{f}_\omega.
\end{aligned} \tag{83}$$

The functions appearing in the RG flow equation for g_9^s in MLG are

$$\begin{aligned}
M_{99}^9 &= -16f_\omega, & M_{17}^9 &= 4f_k + 4\tilde{f}_k, & M_{18}^9 &= 4f_k - 4\tilde{f}_k, & M_{19}^9 &= 8f_\omega - 4\tilde{f}_\omega, \\
M_{27}^9 &= 4f_k - 4\tilde{f}_k, & M_{28}^9 &= 4f_k + 4\tilde{f}_k, & M_{29}^9 &= 4\tilde{f}_\omega, & M_{37}^9 &= 4f_\omega - 4\tilde{f}_\omega, \\
M_{38}^9 &= 4f_\omega + 4\tilde{f}_\omega, & M_{39}^9 &= 16f_k + 16\tilde{f}_k, & M_{47}^9 &= 4f_k - 4\tilde{f}_k, & M_{48}^9 &= 4f_k + 4\tilde{f}_k, \\
M_{49}^9 &= 4\tilde{f}_\omega, & M_{57}^9 &= 4f_k + 4\tilde{f}_k, & M_{58}^9 &= 4f_k - 4\tilde{f}_k, & M_{59}^9 &= 8f_\omega - 4\tilde{f}_\omega, \\
M_{67}^9 &= 4f_\omega + 4\tilde{f}_\omega, & M_{68}^9 &= 4f_\omega - 4\tilde{f}_\omega, & M_{69}^9 &= 16f_k - 16\tilde{f}_k.
\end{aligned} \tag{84}$$

The RG flow equations for the conjugate fields associated with all the spin singlet

excitonic orders in MLG are

$$\begin{aligned}
\bar{\beta}_{\Delta_1^s}^D &= -2(7g_1^s - g_2^s - 2g_3^s - g_4^s - g_5^s - 2g_6^s - 2g_7^s - 2g_8^s - 4g_9^s)(2f_k + f_\omega), \\
\bar{\beta}_{\Delta_2^s}^D &= -2(g_1^s - 7g_2^s - 2g_3^s + g_4^s + g_5^s - 2g_6^s + 2g_7^s + 2g_8^s - 4g_9^s)(2f_k - f_\omega), \\
\bar{\beta}_{\Delta_3^s}^D &= 2(g_1^s - g_2^s - 8g_3^s + g_4^s - g_5^s + 2g_7^s - 2g_8^s)f_\omega, \\
\bar{\beta}_{\Delta_4^s}^D &= 2(g_1^s + g_2^s + 2g_3^s - 7g_4^s + g_5^s + 2g_6^s - 2g_7^s - 2g_8^s - 4g_9^s)(2f_k + f_\omega), \\
\bar{\beta}_{\Delta_5^s}^D &= -2(g_1^s + g_2^s - 2g_3^s + g_4^s - 7g_5^s - 2g_6^s - 2g_7^s - 2g_8^s + 4g_9^s)(2f_k - f_\omega), \\
\bar{\beta}_{\Delta_6^s}^D &= 2(g_1^s - g_2^s + g_4^s - g_5^s - 8g_6^s - 2g_7^s + 2g_8^s)f_\omega, \\
\bar{\beta}_{\Delta_7^s}^D &= -2(g_1^s + g_2^s + 2g_3^s - g_4^s - g_5^s - 2g_6^s - 8g_7^s)(2f_k - f_\omega), \\
\bar{\beta}_{\Delta_8^s}^D &= 2(g_1^s + g_2^s - 2g_3^s - g_4^s - g_5^s + 2g_6^s - 8g_8^s)(2f_k + f_\omega), \\
\bar{\beta}_{\Delta_9^s}^D &= 2(g_1^s - g_2^s - g_4^s + g_5^s - 8g_9^s)f_\omega.
\end{aligned} \tag{85}$$

The RG flow equations for the conjugate fields associated with all the spin triplet excitonic orders in MLG are

$$\begin{aligned}
\bar{\beta}_{\Delta_1^t}^D &= 2(g_1^s + g_2^s + 2g_3^s + g_4^s + g_5^s + 2g_6^s + 2g_7^s + 2g_8^s + 4g_9^s)(2f_k + f_\omega), \\
\bar{\beta}_{\Delta_2^t}^D &= -2(g_1^s + g_2^s - 2g_3^s + g_4^s + g_5^s - 2g_6^s + 2g_7^s + 2g_8^s - 4g_9^s)(2f_k - f_\omega), \\
\bar{\beta}_{\Delta_3^t}^D &= 2(g_1^s - g_2^s + g_4^s - g_5^s + 2g_7^s - 2g_8^s)f_\omega, \\
\bar{\beta}_{\Delta_4^t}^D &= 2(g_1^s + g_2^s + 2g_3^s + g_4^s + g_5^s + 2g_6^s - 2g_7^s - 2g_8^s - 4g_9^s)(2f_k + f_\omega), \\
\bar{\beta}_{\Delta_5^t}^D &= -2(g_1^s + g_2^s - 2g_3^s + g_4^s + g_5^s - 2g_6^s - 2g_7^s - 2g_8^s + 4g_9^s)(2f_k - f_\omega), \\
\bar{\beta}_{\Delta_6^t}^D &= 2(g_1^s - g_2^s + g_4^s - g_5^s - 2g_7^s + 2g_8^s)f_\omega, \\
\bar{\beta}_{\Delta_7^t}^D &= -2(g_1^s + g_2^s + 2g_3^s - g_4^s - g_5^s - 2g_6^s)(2f_k - f_\omega), \\
\bar{\beta}_{\Delta_8^t}^D &= 2(g_1^s + g_2^s - 2g_3^s - g_4^s - g_5^s + 2g_6^s)(2f_k + f_\omega), \\
\bar{\beta}_{\Delta_9^t}^D &= 2(g_1^s - g_2^s - g_4^s + g_5^s)f_\omega.
\end{aligned} \tag{86}$$

The RG flow equations for the conjugate fields associated with all the local pairing orders in MLG are

$$\begin{aligned}
\bar{\beta}_{\Delta_1^p}^D &= 2(g_1^s - g_2^s + 2g_3^s - g_4^s + g_5^s - 2g_6^s + 2g_7^s - 2g_8^s + 4g_9^s)(2\tilde{f}_k - \tilde{f}_\omega), \\
\bar{\beta}_{\Delta_2^p}^D &= -2(g_1^s - g_2^s - 2g_3^s - g_4^s + g_5^s + 2g_6^s + 2g_7^s - 2g_8^s - 4g_9^s)(2\tilde{f}_k + \tilde{f}_\omega), \\
\bar{\beta}_{\Delta_3^p}^D &= -2(g_1^s + g_2^s - g_4^s - g_5^s + 2g_7^s + 2g_8^s)\tilde{f}_\omega, \\
\bar{\beta}_{\Delta_4^p}^D &= 2(g_1^s - g_2^s + 2g_3^s - g_4^s + g_5^s - 2g_6^s - 2g_7^s + 2g_8^s - 4g_9^s)(2\tilde{f}_k - \tilde{f}_\omega), \\
\bar{\beta}_{\Delta_5^p}^D &= -2(g_1^s - g_2^s - 2g_3^s - g_4^s + g_5^s + 2g_6^s - 2g_7^s + 2g_8^s + 4g_9^s)(2\tilde{f}_k + \tilde{f}_\omega), \\
\bar{\beta}_{\Delta_6^p}^D &= 2(-g_1^s - g_2^s + g_4^s + g_5^s + 2(g_7^s + g_8^s))\tilde{f}_\omega, \\
\bar{\beta}_{\Delta_7^p}^D &= -2(g_1^s - g_2^s + 2g_3^s + g_4^s - g_5^s + 2g_6^s)(2\tilde{f}_k + \tilde{f}_\omega), \\
\bar{\beta}_{\Delta_8^p}^D &= 2(g_1^s - g_2^s - 2g_3^s + g_4^s - g_5^s - 2g_6^s)(2\tilde{f}_k - \tilde{f}_\omega),
\end{aligned}$$

$$\bar{\beta}_{\Delta_p^D}^D = -2(g_1^s + g_2^s + g_4^s + g_5^s)\tilde{f}_\omega. \quad (87)$$

C.3.3.2 Bilayer graphene

The functions appearing in the RG flow equation for g_1^s in BLG are

$$\begin{aligned} B_{11}^1 &= -24f_k - 10f_\omega - 2\tilde{f}_\omega, & B_{22}^1 &= 2f_\omega - 2\tilde{f}_\omega, & B_{33}^1 &= 4f_\omega - 4\tilde{f}_\omega, & B_{44}^1 &= 2f_\omega - 2\tilde{f}_\omega, \\ B_{55}^1 &= 2f_\omega - 2\tilde{f}_\omega, & B_{66}^1 &= 4f_\omega - 4\tilde{f}_\omega, & B_{77}^1 &= 4f_\omega - 4\tilde{f}_\omega, & B_{88}^1 &= 4f_\omega - 4\tilde{f}_\omega, \\ B_{99}^1 &= 8f_\omega - 8\tilde{f}_\omega, & B_{12}^1 &= 8f_k + 4f_\omega, & B_{13}^1 &= 24f_k + 8f_\omega + 8\tilde{f}_k, & B_{14}^1 &= 8f_k + 4f_\omega, \\ B_{15}^1 &= 8f_k + 4f_\omega, & B_{16}^1 &= 16f_k + 8f_\omega, & B_{17}^1 &= 16f_k + 8f_\omega, & B_{19}^1 &= 32f_k + 16f_\omega, \\ B_{23}^1 &= 8f_k - 8\tilde{f}_k, & B_{46}^1 &= 8f_k + 8\tilde{f}_k, & B_{56}^1 &= 8f_k - 8\tilde{f}_k, & B_{79}^1 &= 16f_k + 16\tilde{f}_k, \\ B_{89}^1 &= 16f_k - 16\tilde{f}_k. \end{aligned} \quad (88)$$

The functions appearing in the RG flow equation for g_2^s in BLG are

$$\begin{aligned} B_{22}^2 &= 24f_k - 12f_\omega, & B_{33}^2 &= 4f_\omega + 4\tilde{f}_\omega, & B_{66}^2 &= 4f_\omega + 4\tilde{f}_\omega, & B_{99}^2 &= 8f_\omega + 8\tilde{f}_\omega, \\ B_{12}^2 &= -8f_k + 8f_\omega - 4\tilde{f}_\omega, & B_{13}^2 &= 8f_k - 8\tilde{f}_k, & B_{23}^2 &= 24f_k - 8f_\omega + 8\tilde{f}_k, \\ B_{24}^2 &= -8f_k + 4f_\omega, & B_{25}^2 &= -8f_k + 4f_\omega, & B_{26}^2 &= 16f_k - 8f_\omega, & B_{27}^2 &= -16f_k + 8f_\omega, \\ B_{28}^2 &= -16f_k + 8f_\omega, & B_{29}^2 &= 32f_k - 16f_\omega, & B_{45}^2 &= 4f_\omega - 4\tilde{f}_\omega, & B_{46}^2 &= 8f_k - 8\tilde{f}_k, \\ B_{56}^2 &= 8f_k + 8\tilde{f}_k, & B_{78}^2 &= 8f_\omega - 8\tilde{f}_\omega, & B_{79}^2 &= 16f_k - 16\tilde{f}_k, & B_{89}^2 &= 16f_k + 16\tilde{f}_k. \end{aligned} \quad (89)$$

The functions appearing in the RG flow equation for g_3^s in BLG are

$$\begin{aligned} B_{11}^3 &= 2f_k + 2\tilde{f}_k, & B_{22}^3 &= 2f_k + 2\tilde{f}_k, & B_{33}^3 &= 8f_k - 16f_\omega + 8\tilde{f}_k, & B_{44}^3 &= 2f_k + 2\tilde{f}_k, \\ B_{55}^3 &= 2f_k + 2\tilde{f}_k, & B_{66}^3 &= 8f_k + 8\tilde{f}_k, & B_{77}^3 &= 4f_k + 4\tilde{f}_k, & B_{88}^3 &= 4f_k + 4\tilde{f}_k, \\ B_{99}^3 &= 16f_k + 16\tilde{f}_k, & B_{12}^3 &= 4f_k - 4\tilde{f}_k, & B_{13}^3 &= 8f_\omega - 4\tilde{f}_\omega, & B_{23}^3 &= 4\tilde{f}_\omega, & B_{34}^3 &= 4f_\omega, \\ B_{35}^3 &= -4f_\omega, & B_{37}^3 &= 8f_\omega, & B_{38}^3 &= -8f_\omega, & B_{45}^3 &= 4f_k - 4\tilde{f}_k, & B_{46}^3 &= 4f_\omega - 4\tilde{f}_\omega, \\ B_{56}^3 &= 4f_\omega + 4\tilde{f}_\omega, & B_{78}^3 &= 8f_k - 8\tilde{f}_k, & B_{79}^3 &= 8f_\omega - 8\tilde{f}_\omega, & B_{89}^3 &= 8f_\omega + 8\tilde{f}_\omega. \end{aligned} \quad (90)$$

The functions appearing in the RG flow equation for g_4^s in BLG are

$$\begin{aligned} B_{44}^4 &= -24f_k - 12f_\omega, & B_{77}^4 &= 4f_\omega + 4\tilde{f}_\omega, & B_{88}^4 &= 4f_\omega + 4\tilde{f}_\omega, & B_{99}^4 &= 8f_\omega + 8\tilde{f}_\omega, \\ B_{14}^4 &= 8f_k + 8f_\omega - 4\tilde{f}_\omega, & B_{16}^4 &= 8f_k + 8\tilde{f}_k, & B_{24}^4 &= 8f_k + 4f_\omega, & B_{25}^4 &= 4f_\omega - 4\tilde{f}_\omega, \\ B_{26}^4 &= 8f_k - 8\tilde{f}_k, & B_{34}^4 &= 24f_k + 8f_\omega + 8\tilde{f}_k, & B_{35}^4 &= 8f_k - 8\tilde{f}_k, & B_{36}^4 &= 8f_\omega - 8\tilde{f}_\omega, \\ B_{45}^4 &= 8f_k + 4f_\omega, & B_{46}^4 &= 16f_k + 8f_\omega, & B_{47}^4 &= -16f_k - 8f_\omega, & B_{48}^4 &= -16f_k - 8f_\omega, \\ B_{49}^4 &= -32f_k - 16f_\omega, & B_{79}^4 &= 16f_k - 16\tilde{f}_k, & B_{89}^4 &= 16f_k + 16\tilde{f}_k. \end{aligned} \quad (91)$$

The functions appearing in the RG flow equation for g_5^s in BLG are

$$B_{55}^5 = 24f_k - 12f_\omega, \quad B_{99}^5 = 8f_\omega - 8\tilde{f}_\omega, \quad B_{15}^5 = -8f_k + 8f_\omega - 4\tilde{f}_\omega, \quad B_{16}^5 = 8f_k - 8\tilde{f}_k,$$

$$\begin{aligned}
B_{24}^5 &= 4f_\omega - 4\tilde{f}_\omega, & B_{25}^5 &= -8f_k + 4f_\omega, & B_{26}^5 &= 8f_k + 8\tilde{f}_k, & B_{34}^5 &= 8f_k - 8\tilde{f}_k, \\
B_{35}^5 &= 24f_k - 8f_\omega + 8\tilde{f}_k, & B_{36}^5 &= 8f_\omega + 8\tilde{f}_\omega, & B_{45}^5 &= -8f_k + 4f_\omega, & B_{56}^5 &= 16f_k - 8f_\omega, \\
B_{57}^5 &= 16f_k - 8f_\omega, & B_{58}^5 &= 16f_k - 8f_\omega, & B_{59}^5 &= -32f_k + 16f_\omega, & B_{78}^5 &= 8f_\omega + 8\tilde{f}_\omega, \\
B_{79}^5 &= 16f_k + 16\tilde{f}_k, & B_{89}^5 &= 16f_k - 16\tilde{f}_k.
\end{aligned} \tag{92}$$

The functions appearing in the RG flow equation for g_6^s in BLG are

$$\begin{aligned}
B_{66}^6 &= -16f_\omega, & B_{77}^6 &= 4f_k - 4\tilde{f}_k, & B_{88}^6 &= 4f_k - 4\tilde{f}_k, & B_{99}^6 &= 16f_k - 16\tilde{f}_k, & B_{14}^6 &= 4f_k + 4\tilde{f}_k, \\
B_{15}^6 &= 4f_k - 4\tilde{f}_k, & B_{16}^6 &= 8f_\omega - 4\tilde{f}_\omega, & B_{24}^6 &= 4f_k - 4\tilde{f}_k, & B_{25}^6 &= 4f_k + 4\tilde{f}_k, & B_{26}^6 &= 4\tilde{f}_\omega, \\
B_{34}^6 &= 4f_\omega - 4\tilde{f}_\omega, & B_{35}^6 &= 4f_\omega + 4\tilde{f}_\omega, & B_{36}^6 &= 16f_k + 16\tilde{f}_k, & B_{46}^6 &= 4f_\omega, & B_{56}^6 &= -4f_\omega, \\
B_{67}^6 &= -8f_\omega, & B_{68}^6 &= 8f_\omega, & B_{78}^6 &= 8f_k + 8\tilde{f}_k, & B_{79}^6 &= 8f_\omega + 8\tilde{f}_\omega, & B_{89}^6 &= 8f_\omega - 8\tilde{f}_\omega.
\end{aligned} \tag{93}$$

The functions appearing in the RG flow equation for g_7^s in BLG are

$$\begin{aligned}
B_{77}^7 &= -32f_k - 16f_\omega, & B_{17}^7 &= 8f_k + 8f_\omega - 4\tilde{f}_\omega, & B_{19}^7 &= 8f_k + 8\tilde{f}_k, & B_{27}^7 &= 8f_k + 4f_\omega, \\
B_{28}^7 &= 4f_\omega - 4\tilde{f}_\omega, & B_{29}^7 &= 8f_k - 8\tilde{f}_k, & B_{37}^7 &= 24f_k + 8f_\omega + 8\tilde{f}_k, & B_{38}^7 &= 8f_k - 8\tilde{f}_k, \\
B_{39}^7 &= 8f_\omega - 8\tilde{f}_\omega, & B_{47}^7 &= -8f_k + 4\tilde{f}_\omega, & B_{49}^7 &= 8f_k - 8\tilde{f}_k, & B_{57}^7 &= -8f_k - 4f_\omega, \\
B_{58}^7 &= 4f_\omega + 4\tilde{f}_\omega, & B_{59}^7 &= 8f_k + 8\tilde{f}_k, & B_{67}^7 &= -8f_k - 8f_\omega - 8\tilde{f}_k, & B_{68}^7 &= 8f_k + 8\tilde{f}_k, \\
B_{69}^7 &= 8f_\omega + 8\tilde{f}_\omega.
\end{aligned} \tag{94}$$

The functions appearing in the RG flow equation for g_8^s in BLG are

$$\begin{aligned}
B_{88}^8 &= 32f_k - 16f_\omega, & B_{18}^8 &= -8f_k + 8f_\omega - 4\tilde{f}_\omega, & B_{19}^8 &= 8f_k - 8\tilde{f}_k, & B_{27}^8 &= 4f_\omega - 4\tilde{f}_\omega, \\
B_{28}^8 &= -8f_k + 4f_\omega, & B_{29}^8 &= 8f_k + 8\tilde{f}_k, & B_{37}^8 &= 8f_k - 8\tilde{f}_k, & B_{38}^8 &= 24f_k - 8f_\omega + 8\tilde{f}_k, \\
B_{39}^8 &= 8f_\omega + 8\tilde{f}_\omega, & B_{48}^8 &= 8f_k + 4\tilde{f}_\omega, & B_{49}^8 &= 8f_k + 8\tilde{f}_k, & B_{57}^8 &= 4f_\omega + 4\tilde{f}_\omega, \\
B_{58}^8 &= 8f_k - 4f_\omega, & B_{59}^8 &= 8f_k - 8\tilde{f}_k, & B_{67}^8 &= 8f_k + 8\tilde{f}_k, & B_{68}^8 &= -8f_k + 8f_\omega - 8\tilde{f}_k, \\
B_{69}^8 &= 8f_\omega - 8\tilde{f}_\omega.
\end{aligned} \tag{95}$$

The functions appearing in the RG flow equation for g_9^s in BLG are

$$\begin{aligned}
B_{99}^9 &= -16f_\omega, & B_{17}^9 &= 4f_k + 4\tilde{f}_k, & B_{18}^9 &= 4f_k - 4\tilde{f}_k, & B_{19}^9 &= 8f_\omega - 4\tilde{f}_\omega, & B_{27}^9 &= 4f_k - 4\tilde{f}_k, \\
B_{28}^9 &= 4f_k + 4\tilde{f}_k, & B_{29}^9 &= 4\tilde{f}_\omega, & B_{37}^9 &= 4f_\omega - 4\tilde{f}_\omega, & B_{38}^9 &= 4f_\omega + 4\tilde{f}_\omega, & B_{39}^9 &= 16f_k + 16\tilde{f}_k, \\
B_{47}^9 &= 4f_k - 4\tilde{f}_k, & B_{48}^9 &= 4f_k + 4\tilde{f}_k, & B_{49}^9 &= 4\tilde{f}_\omega, & B_{57}^9 &= 4f_k + 4\tilde{f}_k, & B_{58}^9 &= 4f_k - 4\tilde{f}_k, \\
B_{59}^9 &= 8f_\omega - 4\tilde{f}_\omega, & B_{67}^9 &= 4f_\omega + 4\tilde{f}_\omega, & B_{68}^9 &= 4f_\omega - 4\tilde{f}_\omega, & B_{69}^9 &= 16f_k - 16\tilde{f}_k.
\end{aligned} \tag{96}$$

The RG flow equations for the conjugate fields associated with all the spin singlet excitonic orders in BLG are

$$\bar{\beta}_{\Delta_1^s}^L = -2(2f_k + f_\omega)(7g_1^s - g_2^s - 2g_3^s - g_4^s - g_5^s - 2g_6^s - 2g_7^s - 2g_8^s - 4g_9^s),$$

$$\begin{aligned}
\bar{\beta}_{\Delta_2^L}^L &= -2(2f_k - f_\omega)(g_1^s - 7g_2^s - 2g_3^s + g_4^s + g_5^s - 2g_6^s + 2g_7^s + 2g_8^s - 4g_9^s), \\
\bar{\beta}_{\Delta_3^L}^L &= 2f_\omega(g_1^s - g_2^s - 8g_3^s + g_4^s - g_5^s + 2g_7^s - 2g_8^s), \\
\bar{\beta}_{\Delta_4^L}^L &= 2(2f_k + f_\omega)(g_1^s + g_2^s + 2g_3^s - 7g_4^s + g_5^s + 2g_6^s - 2g_7^s - 2g_8^s - 4g_9^s), \\
\bar{\beta}_{\Delta_5^L}^L &= -2(2f_k - f_\omega)(g_1^s + g_2^s - 2g_3^s + g_4^s - 7g_5^s - 2g_6^s - 2g_7^s - 2g_8^s + 4g_9^s), \\
\bar{\beta}_{\Delta_6^L}^L &= 2f_\omega(g_1^s - g_2^s + g_4^s - g_5^s - 8g_6^s - 2g_7^s + 2g_8^s), \\
\bar{\beta}_{\Delta_7^L}^L &= 2(2f_k + f_\omega)(g_1^s + g_2^s + 2g_3^s - g_4^s - g_5^s - 2g_6^s - 8g_7^s), \\
\bar{\beta}_{\Delta_8^L}^L &= -2(2f_k - f_\omega)(g_1^s + g_2^s - 2g_3^s - g_4^s - g_5^s + 2g_6^s - 8g_8^s), \\
\bar{\beta}_{\Delta_9^L}^L &= 2f_\omega(g_1^s - g_2^s - g_4^s + g_5^s - 8g_9^s).
\end{aligned} \tag{97}$$

The RG flow equations for the conjugate fields associated with all the spin triplet excitonic orders in BLG are

$$\begin{aligned}
\bar{\beta}_{\Delta_1^L}^L &= 2(2f_k + f_\omega)(g_1^s + g_2^s + 2g_3^s + g_4^s + g_5^s + 2g_6^s + 2g_7^s + 2g_8^s + 4g_9^s), \\
\bar{\beta}_{\Delta_2^L}^L &= -2(2f_k - f_\omega)(g_1^s + g_2^s - 2g_3^s + g_4^s + g_5^s - 2g_6^s + 2g_7^s + 2g_8^s - 4g_9^s), \\
\bar{\beta}_{\Delta_3^L}^L &= 2f_\omega(g_1^s - g_2^s + g_4^s - g_5^s + 2g_7^s - 2g_8^s), \\
\bar{\beta}_{\Delta_4^L}^L &= 2(2f_k + f_\omega)(g_1^s + g_2^s + 2g_3^s + g_4^s + g_5^s + 2g_6^s - 2g_7^s - 2g_8^s - 4g_9^s), \\
\bar{\beta}_{\Delta_5^L}^L &= -2(2f_k - f_\omega)(g_1^s + g_2^s - 2g_3^s + g_4^s + g_5^s - 2g_6^s - 2g_7^s - 2g_8^s + 4g_9^s), \\
\bar{\beta}_{\Delta_6^L}^L &= 2f_\omega(g_1^s - g_2^s + g_4^s - g_5^s - 2g_7^s + 2g_8^s), \\
\bar{\beta}_{\Delta_7^L}^L &= 2(2f_k + f_\omega)(g_1^s + g_2^s + 2g_3^s - g_4^s - g_5^s - 2g_6^s), \\
\bar{\beta}_{\Delta_8^L}^L &= -2(2f_k - f_\omega)(g_1^s + g_2^s - 2g_3^s - g_4^s - g_5^s + 2g_6^s), \\
\bar{\beta}_{\Delta_9^L}^L &= 2f_\omega(g_1^s - g_2^s - g_4^s + g_5^s).
\end{aligned} \tag{98}$$

The RG flow equations for the conjugate fields associated with all the local pairing orders in BLG are

$$\begin{aligned}
\bar{\beta}_{\Delta_1^L}^L &= 2(2\tilde{f}_k - \tilde{f}_\omega)(g_1^s - g_2^s + 2g_3^s - g_4^s + g_5^s - 2g_6^s + 2g_7^s - 2g_8^s + 4g_9^s), \\
\bar{\beta}_{\Delta_2^L}^L &= -2(2\tilde{f}_k + \tilde{f}_\omega)(g_1^s - g_2^s - 2g_3^s - g_4^s + g_5^s + 2g_6^s + 2g_7^s - 2g_8^s - 4g_9^s), \\
\bar{\beta}_{\Delta_3^L}^L &= -2\tilde{f}_\omega(g_1^s + g_2^s - g_4^s - g_5^s + 2g_7^s + 2g_8^s), \\
\bar{\beta}_{\Delta_4^L}^L &= 2(2\tilde{f}_k - \tilde{f}_\omega)(g_1^s - g_2^s + 2g_3^s - g_4^s + g_5^s - 2g_6^s - 2g_7^s + 2g_8^s - 4g_9^s), \\
\bar{\beta}_{\Delta_5^L}^L &= -2(2\tilde{f}_k + \tilde{f}_\omega)(g_1^s - g_2^s - 2g_3^s - g_4^s + g_5^s + 2g_6^s - 2g_7^s + 2g_8^s + 4g_9^s), \\
\bar{\beta}_{\Delta_6^L}^L &= 2\tilde{f}_\omega(-g_1^s - g_2^s + g_4^s + g_5^s + 2g_7^s + 2g_8^s), \\
\bar{\beta}_{\Delta_7^L}^L &= 2(2\tilde{f}_k - \tilde{f}_\omega)(g_1^s - g_2^s + 2g_3^s + g_4^s - g_5^s + 2g_6^s), \\
\bar{\beta}_{\Delta_8^L}^L &= -2(2\tilde{f}_k + \tilde{f}_\omega)(g_1^s - g_2^s - 2g_3^s + g_4^s - g_5^s - 2g_6^s), \\
\bar{\beta}_{\Delta_9^L}^L &= -2\tilde{f}_\omega(g_1^s + g_2^s + g_4^s + g_5^s).
\end{aligned} \tag{99}$$

D.4 Strain-engineered higher order topology

In this appendix we provide auxiliary material to strain-engineered higher order topological Dirac semimetal and insulator, described in Chapter 8. We demonstrate the effects of strain applied along the y axis or a $\langle 111 \rangle$ direction, and show that it takes the same form as strain applied along the z -direction, after suitable redefinition of the momentum axes. Subsequently, we present the block-diagonalization of the Luttinger Hamiltonian in the $k_z = 0$ plane.

D.4.1 Effects of external strain along y axis and $\langle 111 \rangle$ directions

In Sec. 8.4, we address the effects of E_g strain applied along the z and x axes. Here, we present some key details of analogous analysis, when the strain is applied along the y axis, for which we introduce a new set of momentum $q_x = k_x$, $q_y = k_z$, $q_z = k_y$, such that $q_z \parallel [010]$. Accordingly, we introduce a new set of mutually anticommuting $\bar{\Gamma}$ matrices, satisfying the anticommuting Clifford algebra $\{\bar{\Gamma}_j, \bar{\Gamma}_k\} = 2\delta_{jk}$ for $j, k = 1, \dots, 5$

$$\bar{\Gamma}_1 = \Gamma_1, \bar{\Gamma}_2 = \Gamma_3, \bar{\Gamma}_3 = \Gamma_2, \bar{\Gamma}_4 = \frac{1}{2}(\Gamma_4 - \sqrt{3}\Gamma_5), \bar{\Gamma}_5 = -\frac{1}{2}(\sqrt{3}\Gamma_4 + \Gamma_5).$$

Under these transformations, the effective single particle Hamiltonian reads [see Eqs. (8.4) and (8.8)]

$$\begin{aligned} \hat{h}_L(\mathbf{k}) + \hat{h}_{E_g}^y &= -\frac{1}{2m} \sum_{j=1}^5 d_j(\mathbf{k})\Gamma_j - \frac{|\Delta|}{2} \left[\sqrt{3}\Gamma_4 + \Gamma_5 \right] \text{sgn}(\Delta) \\ &\equiv -\frac{1}{2m} \sum_{j=1}^5 d_j(\mathbf{q})\bar{\Gamma}_j + |\Delta| \text{sgn}(\Delta)\bar{\Gamma}_5, \end{aligned} \quad (100)$$

which takes the form of Eq. (8.9) (obtained when strain is applied along the $[001]$ direction).

In Sec. 8.5 we also addressed the effects of external strain applied along one of the specific $\langle 111 \rangle$ or C_{3v} or body diagonal directions (the T_{2g} strain), namely the $[111]$ direction. We here display the key steps of the analogous analysis, when the strain is applied along the other three body diagonals. First, we consider the strain applied along the $[1\bar{1}\bar{1}]$ direction. Then $\text{sgn}(\Delta_1) = +(-)$, $\text{sgn}(\Delta_2) = -(+)$ and $\text{sgn}(\Delta_3) = -(+)$ for tensile (compressive) strain, yielding $\text{sgn}(\Delta) = +(-)$ [see Eq. (8.15)]. We now introduce the following set of momenta

$$q_x = \frac{k_x + k_y}{\sqrt{2}}, \quad q_y = \frac{k_x - k_y + 2k_z}{\sqrt{6}}, \quad q_z = \frac{k_x - k_y - k_z}{\sqrt{3}},$$

such that $q_z \parallel [\bar{1}\bar{1}\bar{1}]$, and a set of five mutually anticommuting $\bar{\Gamma}$ matrices

$$\begin{aligned}\bar{\Gamma}_1 &= -\left[\frac{1}{3\sqrt{2}}(\Gamma_1 - \Gamma_2 + 2\Gamma_3) + \sqrt{\frac{2}{3}}\Gamma_5\right], & \bar{\Gamma}_2 &= -\frac{\Gamma_1 + \Gamma_2 - 2\Gamma_4}{\sqrt{6}}, \\ \bar{\Gamma}_3 &= \frac{\Gamma_1 + \Gamma_2 + \Gamma_4}{\sqrt{3}}, & \bar{\Gamma}_4 &= \frac{\Gamma_1 - \Gamma_2 + 2\Gamma_3 - \sqrt{3}\Gamma_5}{3}, & \bar{\Gamma}_5 &= \frac{\Gamma_1 - \Gamma_2 - \Gamma_3}{\sqrt{3}},\end{aligned}\quad (101)$$

such that they satisfy the anticommuting Clifford algebra $\{\bar{\Gamma}_j, \bar{\Gamma}_k\} = 2\delta_{jk}$ for $j, k = 1, \dots, 5$. Then the effective single particle Hamiltonian reads

$$\hat{h}_L(\mathbf{k}) + \frac{|\Delta|}{\sqrt{3}}[\Gamma_1 - \Gamma_2 - \Gamma_3] \operatorname{sgn}(\Delta) \equiv -\frac{1}{2m} \sum_{j=1}^5 d_j(\mathbf{q})\bar{\Gamma}_j + |\Delta| \bar{\Gamma}_5 \operatorname{sgn}(\Delta), \quad (102)$$

which takes the form of Eq. (8.9).

Next we assume the T_{2g} strain applied along the $[\bar{1}\bar{1}\bar{1}]$ direction, such that tensile (compressive) strain corresponds to $\operatorname{sgn}(\Delta_1) = -(+)$, $\operatorname{sgn}(\Delta_2) = +(-)$ and $\operatorname{sgn}(\Delta_3) = -(+)$, yielding $\operatorname{sgn}(\Delta) = +(-)$ [see Eq. (8.5)]. We introduce the following set of momenta

$$q_x = \frac{k_x + k_y}{\sqrt{2}}, \quad q_y = \frac{k_x - k_y - 2k_z}{\sqrt{6}}, \quad q_z = \frac{-k_x + k_y - k_z}{\sqrt{3}},$$

such that $q_z \parallel [\bar{1}\bar{1}\bar{1}]$ and a new set of mutually anticommuting $\bar{\Gamma}$ matrices according to

$$\begin{aligned}\bar{\Gamma}_1 &= -\left[\frac{1}{3\sqrt{2}}(\Gamma_1 - \Gamma_2 - 2\Gamma_3) - \sqrt{\frac{2}{3}}\Gamma_5\right], & \bar{\Gamma}_2 &= -\frac{\Gamma_1 + \Gamma_2 + 2\Gamma_4}{\sqrt{6}}, \\ \bar{\Gamma}_3 &= \frac{-\Gamma_1 - \Gamma_2 + \Gamma_4}{\sqrt{3}}, & \bar{\Gamma}_4 &= \frac{\Gamma_1 - \Gamma_2 - 2\Gamma_3 + \sqrt{3}\Gamma_5}{3}, & \bar{\Gamma}_5 &= \frac{-\Gamma_1 + \Gamma_2 - \Gamma_3}{\sqrt{3}},\end{aligned}\quad (103)$$

such that they satisfy the anticommuting Clifford algebra $\{\bar{\Gamma}_j, \bar{\Gamma}_k\} = 2\delta_{jk}$ for $j, k = 1, \dots, 5$. Then the effective single particle Hamiltonian reads

$$\hat{h}_L(\mathbf{k}) + \frac{|\Delta|}{\sqrt{3}}[-\Gamma_1 + \Gamma_2 - \Gamma_3] \operatorname{sgn}(\Delta) \equiv -\frac{1}{2m} \sum_{j=1}^5 d_j(\mathbf{q})\bar{\Gamma}_j + |\Delta| \bar{\Gamma}_5 \operatorname{sgn}(\Delta), \quad (104)$$

which takes the form of Eq. (8.9).

Finally, we consider the T_{2g} strain applied along the $[\bar{1}\bar{1}1]$ direction, such that tensile (compressive) strain corresponds to $\operatorname{sgn}(\Delta_1) = -(+)$, $\operatorname{sgn}(\Delta_2) = -(+)$ and $\operatorname{sgn}(\Delta_3) = +(-)$, yielding $\operatorname{sgn}(\Delta) = +(-)$ [see Eq. (8.5)]. We introduce the following set of momenta

$$q_x = \frac{k_x - k_y}{\sqrt{2}}, \quad q_y = \frac{k_x + k_y + 2k_z}{\sqrt{6}}, \quad q_z = \frac{-k_x - k_y + k_z}{\sqrt{3}},$$

such that $q_z \parallel [\bar{1}\bar{1}1]$ and a new set of mutually anticommuting $\bar{\Gamma}$ matrices according to

$$\begin{aligned}\bar{\Gamma}_1 &= -\left[\frac{1}{3\sqrt{2}}(\Gamma_1 + \Gamma_2 + 2\Gamma_3) - \sqrt{\frac{2}{3}}\Gamma_5\right], & \bar{\Gamma}_2 &= -\frac{\Gamma_1 - \Gamma_2 + 2\Gamma_4}{\sqrt{6}}, \\ \bar{\Gamma}_3 &= \frac{-\Gamma_1 + \Gamma_2 + \Gamma_4}{\sqrt{3}}, & \bar{\Gamma}_4 &= \frac{\Gamma_1 + \Gamma_2 + 2\Gamma_3 + \sqrt{3}\Gamma_5}{3}, & \bar{\Gamma}_5 &= \frac{-\Gamma_1 - \Gamma_2 + \Gamma_3}{\sqrt{3}},\end{aligned}\quad (105)$$

such that they satisfy the anticommuting Clifford algebra $\{\bar{\Gamma}_j, \bar{\Gamma}_k\} = 2\delta_{jk}$ for $j, k = 1, \dots, 5$. Then the effective single particle Hamiltonian reads

$$\hat{h}_L(\mathbf{k}) + \frac{|\Delta|}{\sqrt{3}}[-\Gamma_1 - \Gamma_2 + \Gamma_3] \operatorname{sgn}(\Delta) \equiv -\frac{1}{2m} \sum_{j=1}^5 d_j(\mathbf{q})\bar{\Gamma}_j + |\Delta| \bar{\Gamma}_5 \operatorname{sgn}(\Delta), \quad (106)$$

which again takes the form of Eq. (8.9).

Therefore, when the external strain is applied along any high symmetry $\langle 001 \rangle$ or $\langle 111 \rangle$ directions, the effective single particle Hamiltonian can always be cast in the form of $\hat{h}_{E_g}^{z,t}$ [see Eq. (8.9)], capturing the effects of an external strain applied along the z or $[001]$ direction. Therefore, analysis of the emergent topology from $\hat{h}_{E_g}^{z,t}$ is sufficient to address the effects of external strain, applied along any high symmetry direction.

D.4.2 Luttinger Hamiltonian in the $k_z = 0$ plane

The Luttinger Hamiltonian in the presence of an external strain in the z direction and on the $k_z = 0$ plane reads

$$\hat{h}_{E_g}^{z,t}(k_z = 0) = \left[|\Delta| \operatorname{sgn}(\Delta) + \frac{k_\perp^2}{4m}\right] \Gamma_5 - \frac{1}{2m} [d_3(\mathbf{k})\Gamma_3 + d_4(\mathbf{k})\Gamma_4]. \quad (107)$$

Recall that $\Gamma_3 = \kappa_2 \otimes \sigma_0$, $\Gamma_4 = \kappa_1 \otimes \sigma_0$ and $\Gamma_5 = \kappa_3 \otimes \sigma_3$. Since the above Hamiltonian involves only three mutually anticommuting matrices, it can be cast in the block diagonal form, where each block is two-dimensional. This can be accomplished by arranging the four-component spinor basis according to $\Psi_{\mathbf{k}}^\top = (c_{\mathbf{k},\frac{3}{2}}, c_{\mathbf{k},-\frac{1}{2}}, c_{\mathbf{k},\frac{1}{2}}, c_{\mathbf{k},-\frac{3}{2}})$. Then we find $\hat{h}_{E_g}^{z,t}(k_z = 0) = H_+ \oplus H_-$, where for $\sigma = \pm$

$$H_\sigma = \left[|\Delta| \operatorname{sgn}(\Delta) + \frac{k_\perp^2}{4m}\right] \sigma\tau_3 - \frac{1}{2m} [d_4(\mathbf{k})\tau_1 + d_3(\mathbf{k})\tau_2], \quad (108)$$

identical to Eq. (8.12).

E.5 Disordered higher order topological Dirac semimetal

In this appendix we present the details of the RG analysis the context of disordered HOTDSM.

E.5.1 Renormalization group analysis

Here we show the RG analysis of disordered HOTDSM from Sec. 9.3 in details. In what follows we focus on one of the Dirac points located at $-\mathbf{K}$ and take $\hat{h}_+(\mathbf{p}) \rightarrow \hat{h}(\mathbf{p})$ in Eq. (9.6) for notational compactness. Such a simplification does not alter any outcome as disorder does not couple two valleys and therefore they can be treated as independent flavors. Moreover, the flavor number does not affect the RG flow equations as the perturbative RG analysis does not involve any Feynman diagram that contains fermion bubble or the flavor number [90]. The low energy Hamiltonian around the Dirac point at $-\mathbf{K}$ reads [see the lattice model in Eq. (8.1)]

$$\hat{h}(\mathbf{p}) = v_{\perp} \sum_{j=1}^2 \Gamma_j p_j + v_3 p_3 \Gamma_3 + b(p_2^2 - p_1^2) \Gamma_4 + b(2p_1 p_2) \Gamma_5, \quad (109)$$

where $\mathbf{K} = [0, 0, \pi/2]$ and $\mathbf{p} = -\mathbf{K} + \mathbf{k}$. Even though in the lattice model we set the bare Fermi velocities to be equal, i.e. $v_{\perp}^{\text{bare}} = v_3^{\text{bare}}$ (by setting $t = t_z$), due to the C_4 symmetry breaking terms (proportional to b) they receive different quantum corrections, as the rotational symmetry between $\mathbf{p}_{\perp} = (p_1, p_2)$ and p_3 is broken when $b \neq 0$. Recall the Euclidean action in the presence of disorder from Eq. (9.7). It reads as

$$S = \int d\tau d^3x \Psi^{\dagger} \left[\partial_{\tau} + \hat{h}(\mathbf{p} \rightarrow -i\nabla) - \Phi \right] \Psi + \frac{1}{2\Delta} \int d^3x \Phi |\nabla|^m \Phi, \quad (110)$$

where Ψ is the fermion field and Φ represents the (bosonic) disorder field. The fermionic and disorder Green's functions are respectively given by

$$G(i\omega, \mathbf{p}) = -\frac{i\omega + \hat{h}(\mathbf{p})}{\omega^2 + v^2 p^2 + b^2 p_{\perp}^4} \quad \text{and} \quad \langle \Phi(\mathbf{p}) \Phi(\mathbf{0}) \rangle = \frac{\Delta}{|\mathbf{p}|^m}. \quad (111)$$

While computing the leading order quantum corrections due to disorder, see Fig. 9.6, we set $v_{\perp} = v_3 = v$ in the fermionic Green's function.

In the Wilsonian RG procedure, we integrate out a thin momentum shell $\Lambda e^{-\ell} < |\mathbf{k}| < \Lambda$, with $0 < \ell \ll 1$, where Λ is the ultraviolet cutoff. Subsequently, we recast the action (S) in its original form, but in terms of the renormalized or scale (ℓ) dependent quantities, leading to their RG flow equations. We begin with determining the engineering dimensions of various quantities in Eq. (110). Since momentum and frequency respectively scale as $[q] = 1$ and $[\omega] = z$, where z is the dynamic scaling exponent, the scaling dimensions for their conjugate variables are respectively $[x] = -1$ and $[\tau] = -z$. The scale invariance of the Euclidean action then implies $[\Psi] = d/2$, $[v] = z - 1$ and $[b] = z - 2$.

Note that the Φ field appears in Eq. (110) exactly as $i\omega$, consequently at the clean fixed point it bears the same scaling dimension as $1/\tau$, so $[\Phi] = z + \eta_\Phi$, where we introduced an anomalous dimension of the disorder field η_Φ , to allow for possible quantum corrections arising at the disorder controlled fixed point. Imposing the above relations on the second term of Eq. (110) we obtain

$$[\Delta] = 2(z + \eta_\Phi) - (d - m). \quad (112)$$

At the clean fixed point (describing a HOTDSM) $z = 1$ for linearly dispersing fermions at sufficiently low energies, yielding $\eta_\Phi = 0$. Notice that the disorder field couples with the fermionic field like a gauge field. Consequently, $\eta_\Phi=0$ always, due to the Ward identity, as we demonstrate below for the leading-order RG analysis. In three dimensions $[\Delta] = m - 1$. As seen in Eq. (9.8) $m = 0$ corresponds to Gaussian white noise distribution, for which disorder is irrelevant in the language of RG. On the other hand, for $m = 1$ disorder becomes marginal, which motivates our ϵ expansion in terms of a small parameter $\epsilon = 1 - m$. Accordingly we define a dimensionless disorder coupling

$$g = \frac{\Delta \Lambda^\epsilon}{2\pi^2 v^2}, \quad (113)$$

which to leading order scales identically as Δ . Having established the scaling of various quantities appearing in the action S , we proceed with evaluating the two relevant one-loop Feynman diagrams in Fig. 9.6, namely the fermionic self energy (left) and the correction to the fermion-disorder vertex (right).

E.5.1.1 Fermionic self energy

First we compute the contribution from the self energy diagram, given by

$$\Sigma(i\omega, \mathbf{k}) = \Delta \int \frac{d^3 \mathbf{q}}{(2\pi)^3} G(i\omega, \mathbf{k} - \mathbf{q}) \frac{1}{|q|^m}. \quad (114)$$

Since to the leading-order the divergences in the spatial and temporal part of the self energy are separated (no overlapping divergences), we evaluate $\Sigma(i\omega, 0)$ and $\Sigma(0, \mathbf{k})$ separately, and $\Sigma(i\omega, \mathbf{k}) = \Sigma(i\omega, 0) + \Sigma(0, \mathbf{k})$. Let us write down the time-like component of self-energy correction as

$$\Sigma(i\omega, 0) = -\Delta(i\omega) \int \frac{d^3 \mathbf{q}}{(2\pi)^3} \frac{|q|^{-m}}{\omega^2 + v^2 q^2 + b^2 q^4 \sin^4 \theta}. \quad (115)$$

Since we compute this contribution within the Wilsonian momentum shell $\Lambda e^{-\ell} < |\mathbf{k}| < \Lambda$, we set $\omega = 0$ in the integrand, leading to

$$\Sigma(i\omega, 0) = -\frac{\Delta(i\omega)}{4\pi^2} \int_{\Lambda e^{-\ell}}^{\Lambda} dq \int_0^{\pi} d\theta \frac{q^{2-m} \sin \theta}{v^2 q^2 + b^2 q^4 \sin^4 \theta} = -(i\omega)gl f_1(x), \quad (116)$$

where $x = \Lambda b/v$ and $f_1(x)$ has been defined in Eq. (9.11).

Next we set $\omega = 0$ and evaluate $\Sigma(0, \mathbf{k})$, that to the k -linear order renormalizes the Fermi velocities v_{\perp} and v_3 , and to the quadratic order in momentum gives corrections to b . By setting $\mathbf{k} = [k_x, 0, 0]$, we collect the renormalization for both v_{\perp} and b , while for $\mathbf{k} = [0, 0, k_z]$ only v_3 gets renormalized. Hence, we evaluate $\Sigma(0, \mathbf{k})$ for these two choices of \mathbf{k} separately. Let us begin by taking $\mathbf{k} = [k_x, 0, 0]$ for which

$$\begin{aligned} \Sigma(0, \mathbf{k}) &= -\Delta \int \frac{d^3 \mathbf{q}}{(2\pi)^3} [v^2(k_x^2 + q^2 - 2k_x q_x) + b^2 [(k_x - q_x)^2 - q_y^2]^2 + 4b^2(k_x - q_x)^2 q_y^2]^{-1} \\ &\times \frac{v [(k_x - q_x)\Gamma_1 - q_y\Gamma_2 - q_z\Gamma_3] + b [(k_x - q_x)^2 - q_y^2] \Gamma_4 - 2b(k_x - q_x)q_y\Gamma_5}{|q|^m}, \end{aligned} \quad (117)$$

and expand the denominator up to (for now) the linear order in k_x , yielding

$$\text{denom}(k_x) = \frac{1}{v^2 q^2 + b^2 q_{\perp}^4} + \frac{2q_x [2b^2 q_{\perp}^2 + v^2] k_x}{[v^2 q^2 + b^2 q_{\perp}^4]^2} + \mathcal{O}(k_x^2). \quad (118)$$

Substituting the above expansion into Eq. (117) and performing the ϕ integral yields

$$\begin{aligned} \Sigma(0, \mathbf{k}) &= -v_{\perp} k_x \Gamma_1 \frac{\Delta}{4\pi^2} \int_{\Lambda e^{-\ell}}^{\Lambda} dq q^2 \int_0^{\pi} d\theta \sin \theta \left(\frac{1}{v^2 q^2 + b^2 q_{\perp}^4} - \frac{v q_{\perp}^2 (v^2 + 2b^2 q_{\perp}^2)}{(v^2 q^2 + b^2 q_{\perp}^4)^2} \right) \\ &= -v_{\perp} gl [f_1(x) - f_{\perp}(x)] \Gamma_1 k_x, \end{aligned} \quad (119)$$

where $f_{\perp}(x)$ is introduced in Eq. (9.11).

Because of the $b(k_x^2 - k_y^2)$ term in Eq. (109), we continue the above expansion to k_x^2 order, which will yield quantum corrections or renormalization to b . For brevity we do not write out the $\mathcal{O}(k_x^2)$ term in the Taylor expansion, rather quote the (significantly simpler) result after the ϕ integration, given by

$$\begin{aligned} &-bk_x^2 \Gamma_4 \frac{\Delta}{4\pi^2} \int_{\Lambda e^{-\ell}}^{\Lambda} dq q^2 \int_0^{\pi} d\theta \sin \theta \frac{1}{|q|^m} \\ &\times \left(\frac{1}{v^2 q^2 + b^2 q_{\perp}^4} - 2 \frac{q_{\perp}^2 (v^2 + 2b^2 q_{\perp}^2)}{(v^2 q^2 + b^2 q_{\perp}^4)^2} + \frac{q_{\perp}^4 [v^4 + 3b^4 q_{\perp}^4 - v^2 b^2 (q^2 - 4q_{\perp}^2)]}{(v^2 q^2 + b^2 q_{\perp}^4)^3} \right) \\ &= -bgl [f_1(x) - 2f_{\perp}(x) + f_b(x)] \Gamma_4 k_x^2, \end{aligned} \quad (120)$$

where we introduce yet another function

$$f_b(x) = \frac{1}{2} \int_0^{\pi} d\theta \frac{1 + 3x^4 \sin^4 \theta - x^2(1 - 4 \sin^2 \theta)}{(1 + x^2 \sin^4 \theta)^3} \sin^5 \theta. \quad (121)$$

If we now take $\mathbf{k} = [0, k_y, 0]$, we obtain the above correction with an overall negative sign, corresponding to the renormalization of $b(k_x^2 - k_y^2)$.

As the next step let us take $\mathbf{k} = [0, 0, k_z]$, after which Eq. (114) becomes

$$\Sigma(0, \mathbf{k}) = \int \frac{d^3 \mathbf{q}}{(2\pi)^3} \frac{v[-q_x \Gamma_1 - q_y \Gamma_2 + (k_z - q_z) \Gamma_3] + b(q_x^2 - q_y^2) \Gamma_4 + 2bq_x q_y \Gamma_5}{v^2(k_z^2 + q^2 - 2k_z q_z) + b^2(q_x^2 - q_y^2)^2 + 4b^2 q_x^2 q_y^2} \frac{\Delta}{|q|^m}, \quad (122)$$

and expand the denominator in k_z to linear order as

$$\text{denom}(k_z) = \frac{1}{v^2 q^2 + b^2 q_\perp^4} + \frac{2v^2 q_z k_z}{[v^2 q^2 + b^2 q_\perp^4]^2} + \mathcal{O}(k_z^2), \quad (123)$$

and like before, substitute it into $\Sigma(0, \mathbf{k})$, which leads to

$$\begin{aligned} \Sigma(0, \mathbf{k}) &= -v_3 k_z \Gamma_3 \frac{\Delta}{4\pi^2} \int_{\Lambda e^{-\ell}}^{\Lambda} dq q^2 \int_0^\pi d\theta \sin \theta \left(\frac{1}{v^2 q^2 + b^2 q_\perp^4} - \frac{2v^3 q_z^2}{(v^2 q^2 + b^2 q_\perp^4)^2} \right) \frac{1}{|q|^m} \\ &= -v_3 g l [f_1(x) - f_3(x)] \Gamma_3 k_z. \end{aligned} \quad (124)$$

Since k_z^2 does not appear in the action we have no reason to proceed to this order in the Taylor expansion.

E.5.1.2 Vertex correction

Next we evaluate the vertex diagram, see Fig. 9.6(b). The leading divergence of this diagram can be extracted by setting the external frequency to zero. Then the contribution reads

$$V(\mathbf{k}) = \int \frac{d^3 \mathbf{q}}{(2\pi)^3} \frac{\Gamma_0 \hat{h}(\mathbf{k} - \mathbf{q}) \Gamma_0 \hat{h}(\mathbf{k} - \mathbf{q}) \Gamma_0}{[v^2(\mathbf{k} - \mathbf{q})^2 + b^2(\mathbf{k}_\perp - \mathbf{q}_\perp)^2]^2} \frac{\Delta}{|q|^m}. \quad (125)$$

We now evaluate the integral for $\mathbf{k} = 0$, and obtain

$$V(0) = \frac{\Delta}{4\pi^2} \int \frac{dq d\theta q^2 \sin \theta}{v^2 q^2 + b^2 q_\perp^4} |q|^{-m} = g f_1(x) l \Gamma_0 \equiv -\Sigma(i\omega, 0). \quad (126)$$

Therefore, the disorder field (Φ) does not receive any anomalous dimension (η_Φ) from quantum corrections, according to the Ward identity. From the self-energy and vertex diagrams, we now derive the RG flow equations for various parameters appearing in the imaginary time Euclidean action.

E.5.1.3 RG flow equations

Let us write the dressed or renormalized fermion propagator as

$$G^{-1}(i\omega, \mathbf{k}) = G_0^{-1}(i\omega, \mathbf{k}) + \Sigma(i\omega, \mathbf{k})$$

$$= Z_\Psi \left[i\omega - Z_{v_\perp} v_\perp \sum_{j=1}^2 \Gamma_j k_j - Z_{v_3} v_3 \Gamma_3 k_3 - Z_b b \left((k_x^2 - k_y^2) \Gamma_4 + 2k_x k_y \Gamma_5 \right) \right], \quad (127)$$

from where we read off the renormalization conditions as

$$Z_\Psi = 1 - g f_1(x) \ell + \mathcal{O}(\ell^2), \quad (128)$$

$$Z_{v_3} = Z_\Psi^{-1} \left[1 + g \left(f_1(x) - f_3(x) \right) \ell \right] \approx 1 + g \left(2f_1(x) - f_3(x) \right) \ell + \mathcal{O}(\ell^2), \quad (129)$$

$$Z_{v_\perp} = Z_\Psi^{-1} \left[1 + g \left(f_1(x) - f_\perp(x) \right) \ell \right] \approx 1 + g \left(2f_1(x) - f_\perp(x) \right) \ell + \mathcal{O}(\ell^2), \quad (130)$$

$$\begin{aligned} Z_b &= Z_\Psi^{-1} \left[1 + g \left(f_1(x) - 2f_\perp(x) + f_b(x) \right) \ell \right] \\ &\approx 1 + g \left(2f_1(x) - 2f_\perp(x) + f_b(x) \right) \ell + \mathcal{O}(\ell^2). \end{aligned} \quad (131)$$

Since Φ appears in Eq. (109) exactly the same way as $i\omega$, we can write analogously

$$Z_\Phi = Z_\Psi^{-1} \left[1 - g f_1(x) \ell \right] = 1. \quad (132)$$

In other words, to the leading order g cancels from the renormalization of the disorder field, and $\eta_\Phi = 0$. From Z_b we can write down the renormalization condition for the corresponding dimensionless quantity $x = b\Lambda/v$ as

$$Z_x = Z_b Z_\Lambda = 1 - \ell + g \left(2f_1(x) - 2f_\perp(x) + f_b(x) \right) \ell + \mathcal{O}(\ell^2), \quad (133)$$

since $Z_\Lambda = (1 - \ell)$, as $\Lambda \rightarrow \Lambda e^{-\ell}$ under rescaling.

The RG flow equations are then given by

$$\frac{dv_\perp}{d\ell} = g v_\perp \left(2f_1(x) - f_\perp(x) \right), \quad (134)$$

$$\frac{dv_3}{d\ell} = g v_3 \left(2f_1(x) - f_3(x) \right), \quad (135)$$

$$\frac{d}{d\ell} \frac{v_\perp}{v_3} = \frac{1}{v_3} \frac{dv_\perp}{d\ell} - \frac{v_\perp}{v_3^2} \frac{dv_3}{d\ell} = g \frac{v_\perp}{v_3} \left(f_3(x) - f_\perp(x) \right), \quad (136)$$

$$\frac{dg}{d\ell} = g \left[-\epsilon + 2(z - 1) \right] \quad (137)$$

$$\frac{dx}{d\ell} = -x \left[1 + g \left(2f_1(x) - 2f_\perp(x) + f_b(x) \right) \right]. \quad (138)$$

Since we are interested in the leading-order corrections to all variables, we only consider the contribution of the first term in the flow equations of x , and neglect the quantum corrections arising from disorder.

In Sec. 9.3 we analyzed the above flow equations by setting

$$\frac{dv_3}{d\ell} = (z - 1)v_3. \quad (139)$$

Alternatively, we can choose

$$\frac{dv_{\perp}}{d\ell} = (z - 1)v_{\perp}. \quad (140)$$

Then

$$z = 1 + g[2f_1(x) - f_{\perp}(x)], \quad (141)$$

and the dirty QCP is located at

$$g = g_* = \epsilon/[2(2f_1(x) - f_{\perp}(x))], \quad (142)$$

where $z = 1 + \epsilon/2$ and $\nu^{-1} = \epsilon$. Therefore, only the location of the dirty QCP g_* changes (however, without altering its variation with x , qualitatively), which is a nonuniversal quantity. But the universal critical exponents, z and ν , are insensitive to these details.

Acknowledgements

This thesis, though bears my name on the cover, depended on much more than myself. Without question, I have to salute Bitan Roy for the years of guidance, teaching, and quite honestly, the relentless grunt work he committed to my betterment.

As any long undertaking, this work also came down to incremental steps taken on countless days. In this regard, I raise my hat in front of the entire staff and leadership of the Max Planck Institute for the Physics of Complex Systems. We are truly spoiled in the environment they create.

Finally, I want to express gratitude to the people that made these years not only possible, but enriching and fun. For my crew of friends at the institute, my training partners that helped me let the steam out, my family giving me support from so far away, and the happy people of Dresden, thank you guys.

Bibliography

- [1] J.-P. Issi, Low temperature transport properties of the group V semimetals, Australian Journal of Physics **32**, 585 (1979).
- [2] J.-P. Issi, *Thermoelectric properties of the group V semimetals*, vol. 7 (2006).
- [3] L. Zhang, Y. Zhang, J. Camacho, M. Khodas and I. Zaliznyak, The experimental observation of quantum Hall effect of $l = 3$ chiral quasiparticles in trilayer graphene, Nature Physics **7**, 953 (2011).
- [4] C. Fang, M. J. Gilbert, X. Dai and B. A. Bernevig, Multi-Weyl topological semimetals stabilized by point group symmetry, Physical review letters **108**, 266802 (2012).
- [5] S.-M. Huang, S.-Y. Xu, I. Belopolski, C.-C. Lee, G. Chang et al., New type of Weyl semimetal with quadratic double Weyl fermions, Proceedings of the National Academy of Sciences **113**, 1180 (2016).
- [6] M. E. Peskin and D. V. Schroeder, *An Introduction to quantum field theory*, Addison-Wesley, Reading, USA (1995).
- [7] K. Gottfried and T.-M. Yan, *Quantum Mechanics : Fundamentals* (2003).
- [8] P. R. Wallace, The band theory of graphite, Phys. Rev. **71**, 622 (1947).
- [9] G. W. Semenoff, Condensed-matter simulation of a three-dimensional anomaly, Phys. Rev. Lett. **53**, 2449 (1984).
- [10] A. H. Castro Neto, F. Guinea, N. M. R. Peres, K. S. Novoselov and A. K. Geim, The electronic properties of graphene, Rev. Mod. Phys. **81**, 109 (2009).
- [11] I. F. Herbut, V. Juričić and B. Roy, Theory of interacting electrons on the honeycomb lattice, Phys. Rev. B **79**, 085116 (2009).
- [12] I. F. Herbut, Interactions and phase transitions on graphene's honeycomb lattice, Phys. Rev. Lett. **97**, 146401 (2006).
- [13] A. L. Szabó and B. Roy, Extended hubbard model in undoped and doped monolayer and bilayer graphene: Selection rules and organizing principle among competing orders, Phys. Rev. B **103**, 205135 (2021).

- [14] S. Hesselmann, D. D. Scherer, M. M. Scherer and S. Wessel, Bond-ordered states and f -wave pairing of spinless fermions on the honeycomb lattice, *Phys. Rev. B* **98**, 045142 (2018).
- [15] F. F. Assaad and I. F. Herbut, Pinning the order: The nature of quantum criticality in the Hubbard model on honeycomb lattice, *Phys. Rev. X* **3**, 031010 (2013).
- [16] Z. Wang, Y. Liu, T. Sato, M. Hohenadler, C. Wang et al., Doping-induced quantum spin Hall insulator to superconductor transition, *Phys. Rev. Lett.* **126**, 205701 (2021).
- [17] C.-Y. Hou, C. Chamon and C. Mudry, Electron fractionalization in two-dimensional graphenelike structures, *Phys. Rev. Lett.* **98**, 186809 (2007).
- [18] O. Vafek, Interacting fermions on the honeycomb bilayer: From weak to strong coupling, *Phys. Rev. B* **82**, 205106 (2010).
- [19] B. Roy, Classification of massive and gapless phases in bilayer graphene, *Phys. Rev. B* **88**, 075415 (2013).
- [20] K. Sun, H. Yao, E. Fradkin and S. A. Kivelson, Topological insulators and nematic phases from spontaneous symmetry breaking in 2d fermi systems with a quadratic band crossing, *Phys. Rev. Lett.* **103**, 046811 (2009).
- [21] M. Z. Hasan and C. L. Kane, Colloquium: Topological insulators, *Rev. Mod. Phys.* **82**, 3045 (2010).
- [22] X.-L. Qi and S.-C. Zhang, Topological insulators and superconductors, *Reviews of Modern Physics* **83**, 1057 (2011).
- [23] A. Burkov and L. Balents, Weyl semimetal in a topological insulator multilayer, *Phys. Rev. Lett.* **107**, 127205 (2011).
- [24] B. Roy, R.-J. Slager and V. Juričić, Global phase diagram of a dirty Weyl liquid and emergent superuniversality, *Phys. Rev. X* **8**, 031076 (2018).
- [25] S.-Y. Xu, I. Belopolski, N. Alidoust, M. Neupane, G. Bian et al., Discovery of a Weyl fermion semimetal and topological Fermi arcs, *Science* **349**, 613 (2015).
- [26] B. Q. Lv, H. M. Weng, B. B. Fu, X. P. Wang, H. Miao et al., Experimental discovery of Weyl semimetal TaAs, *Phys. Rev. X* **5**, 031013 (2015).
- [27] S.-Y. Xu, N. Alidoust, I. Belopolski, Z. Yuan, G. Bian et al., Discovery of a Weyl fermion state with Fermi arcs in niobium arsenide, *Nature Physics* **11**, 748 (2015).
- [28] C. Shekhar, A. Nayak, Y. Sun, M. Schmidt, M. Nicklas et al., Extremely large magnetoresistance and ultrahigh mobility in the topological Weyl semimetal NbP, *Nature Physics* **11** (2015).

- [29] S. Borisenko, D. Evtushinsky, Q. Gibson, A. Yaresko, K. Koepernik et al., Time-reversal symmetry breaking type-II Weyl state in YbMnBi₂, *Nature Communications* **10**, 1 (2019).
- [30] D. Liu, A. Liang, E. Liu, Q. Xu, Y. Li et al., Magnetic Weyl semimetal phase in a Kagomé crystal, *Science* **365**, 1282 (2019).
- [31] Y. Li, T. Oh, J. Son, J. Song, M. K. Kim et al., Correlated magnetic Weyl semimetal state in strained Pr₂Ir₂O₇, *Advanced Materials* 2008528 (2021).
- [32] Z. K. Liu, B. Zhou, Y. Zhang, Z. J. Wang, H. M. Weng et al., Discovery of a three-dimensional topological Dirac semimetal, Na₃Bi, *Science* **343**, 864 (2014).
- [33] M. Neupane, S.-Y. Xu, R. Sankar, N. Alidoust, G. Bian et al., Observation of a three-dimensional topological Dirac semimetal phase in high-mobility Cd₃As₂, *Nature Communications* **5**, 3786 (2014).
- [34] Z. K. Liu, J. Jiang, B. Zhou, Z. J. Wang, Y. Zhang et al., A stable three-dimensional topological Dirac semimetal Cd₃As₂, *Nature Materials* **13**, 677 (2014).
- [35] W. Witczak-Krempa, G. Chen, Y. B. Kim and L. Balents, Correlated quantum phenomena in the strong spin-orbit regime, *Annual Review of Condensed Matter Physics* **5**, 57 (2014).
- [36] W. Witczak-Krempa, A. Go and Y. B. Kim, Pyrochlore electrons under pressure, heat, and field: Shedding light on the iridates, *Phys. Rev. B* **87**, 155101 (2013).
- [37] L. Savary, E.-G. Moon and L. Balents, New type of quantum criticality in the pyrochlore iridates, *Phys. Rev. X* **4**, 041027 (2014).
- [38] H. Shinaoka, S. Hoshino, M. Troyer and P. Werner, Phase diagram of pyrochlore iridates: all-in–all-out magnetic ordering and non-Fermi-liquid properties, *Phys. Rev. Lett.* **115**, 156401 (2015).
- [39] K. Ueda, J. Fujioka, B.-J. Yang, J. Shiogai, A. Tsukazaki et al., Magnetic field-induced insulator-semimetal transition in a pyrochlore Nd₂Ir₂O₇, *Phys. Rev. Lett.* **115**, 056402 (2015).
- [40] W. Witczak-Krempa and Y. B. Kim, Topological and magnetic phases of interacting electrons in the pyrochlore iridates, *Phys. Rev. B* **85**, 045124 (2012).
- [41] Y. Machida, S. Nakatsuji, Y. Maeno, T. Tayama, T. Sakakibara et al., Unconventional anomalous Hall effect enhanced by a noncoplanar spin texture in the frustrated Kondo lattice Pr₂Ir₂O₇, *Phys. Rev. Lett.* **98**, 057203 (2007).

- [42] Y. Machida, S. Nakatsuji, S. Onoda, T. Tayama and T. Sakakibara, Time-reversal symmetry breaking and spontaneous Hall effect without magnetic dipole order, *Nature* **463**, 210 (2010).
- [43] P. Goswami, B. Roy and S. D. Sarma, Competing orders and topology in the global phase diagram of pyrochlore iridates, *Phys. Rev. B* **95**, 085120 (2017).
- [44] X.-P. Yao and G. Chen, $\text{Pr}_2\text{Ir}_2\text{O}_7$: when Luttinger semimetal meets Melko-Hertog-Gingras spin ice state, *Phys. Rev. X* **8**, 041039 (2018).
- [45] R. Dornhaus, G. Nimtz and B. Schlicht, *Narrow-gap semiconductors*, Springer-Verlag Berlin (1983).
- [46] J. Tsidilkovski, *Electron spectrum of gapless semiconductors*, Springer Science & Business Media (2012).
- [47] S. Groves and W. Paul, Band structure of gray tin, *Phys. Rev. Lett.* **11**, 194 (1963).
- [48] B. J. Roman and A. W. Ewald, Stress-induced band gap and related phenomena in gray tin, *Phys. Rev. B* **5**, 3914 (1972).
- [49] E.-G. Moon, C. Xu, Y. B. Kim and L. Balents, Non-Fermi-liquid and topological states with strong spin-orbit coupling, *Phys. Rev. Lett.* **111**, 206401 (2013).
- [50] M. Nakayama, T. Kondo, Z. Tian, J. J. Ishikawa, M. Halim et al., Slater to Mott crossover in the metal to insulator transition of $\text{Nd}_2\text{Ir}_2\text{O}_7$, *Phys. Rev. Lett.* **117**, 056403 (2016).
- [51] T. Kondo, M. Nakayama, R. Chen, J. J. Ishikawa, E. G. Moon et al., Quadratic Fermi node in a 3D strongly correlated semimetal, *Nature Communications* **6**, 10042 (2015).
- [52] B. Cheng, T. Ohtsuki, D. Chaudhuri, S. Nakatsuji, M. Lippmaa et al., Dielectric anomalies and interactions in the three-dimensional quadratic band touching Luttinger semimetal $\text{Pr}_2\text{Ir}_2\text{O}_7$, *Nature Communications* **8**, 2097 (2017).
- [53] H. Lin, L. A. Wray, Y. Xia, S. Xu, S. Jia et al., Half-Heusler ternary compounds as new multifunctional experimental platforms for topological quantum phenomena, *Nature materials* **9**, 546 (2010).
- [54] Z. Liu, L. Yang, S.-C. Wu, C. Shekhar, J. Jiang et al., Observation of unusual topological surface states in half-Heusler compounds InPtBi ($\text{In} = \text{Lu, Y}$), *Nature Communications* **7**, 1 (2016).
- [55] J. Yu, B. Yan and C.-X. Liu, Model hamiltonian and time reversal breaking topological phases of antiferromagnetic half-Heusler materials, *Phys. Rev. B* **95**, 235158 (2017).

- [56] A. Nikitin, Y. Pan, X. Mao, R. Jehee, G. Araizi et al., Magnetic and superconducting phase diagram of the half-Heusler topological semimetal HoPdBi, *Journal of Physics: Condensed Matter* **27**, 275701 (2015).
- [57] Y. Nakajima, R. Hu, K. Kirshenbaum, A. Hughes, P. Syers et al., Topological RPdBi half-Heusler semimetals: A new family of noncentrosymmetric magnetic superconductors, *Science Advances* **1**, e1500242 (2015).
- [58] H. Kim, K. Wang, Y. Nakajima, R. Hu, S. Ziemak et al., Beyond triplet: Unconventional superconductivity in a spin-3/2 topological semimetal, *Science Advances* **4**, eaao4513 (2018).
- [59] H. Xiao, T. Hu, W. Liu, Y. Zhu, P. Li et al., Superconductivity in the half-Heusler compound TbPdBi, *Phys. Rev. B* **97**, 224511 (2018).
- [60] G. Goll, M. Marz, A. Hamann, T. Tomanic, K. Grube et al., Thermodynamic and transport properties of the non-centrosymmetric superconductor LaBiPt, *Physica B: Condensed Matter* **403**, 1065 (2008).
- [61] N. P. Butch, P. Syers, K. Kirshenbaum, A. P. Hope and J. Paglione, Superconductivity in the topological semimetal YPtBi, *Phys. Rev. B* **84**, 220504 (2011).
- [62] T. Bay, T. Naka, Y. Huang and A. De Visser, Superconductivity in noncentrosymmetric YPtBi under pressure, *Phys. Rev. B* **86**, 064515 (2012).
- [63] Y. Pan, A. Nikitin, T. Bay, Y. Huang, C. Paulsen et al., Superconductivity and magnetic order in the noncentrosymmetric half-Heusler compound ErPdBi, *EPL* **104**, 27001 (2013).
- [64] F. Tafti, T. Fujii, A. Juneau-Fecteau, S. R. de Cotret, N. Doiron-Leyraud et al., Superconductivity in the noncentrosymmetric half-Heusler compound LuPtBi: A candidate for topological superconductivity, *Phys. Rev. B* **87**, 184504 (2013).
- [65] G. Xu, W. Wang, X. Zhang, Y. Du, E. Liu et al., Weak antilocalization effect and noncentrosymmetric superconductivity in a topologically nontrivial semimetal LuPdBi, *Scientific reports* **4**, 1 (2014).
- [66] R. Shankar, Renormalization-group approach to interacting fermions, *Reviews of Modern Physics* **66**, 129 (1994).
- [67] B. Roy and I. F. Herbut, Unconventional superconductivity on honeycomb lattice: Theory of Kekule order parameter, *Phys. Rev. B* **82**, 035429 (2010).
- [68] F. K. Kunst, C. Delerue, C. M. Smith and V. Juričić, Kekule versus hidden superconducting order in graphene-like systems: Competition and coexistence, *Phys. Rev. B* **92**, 165423 (2015).

- [69] B. Roy and V. Juričić, Strain-induced time-reversal odd superconductivity in graphene, *Phys. Rev. B* **90**, 041413 (2014).
- [70] C. Honerkamp, Density waves and Cooper pairing on the honeycomb lattice, *Phys. Rev. Lett.* **100**, 146404 (2008).
- [71] B. Guo, L. Fang, B. Zhang and J. R. Gong, Graphene doping: a review, *Insciences J.* **1**, 80 (2011).
- [72] W. Kohn and J. M. Luttinger, New mechanism for superconductivity, *Phys. Rev. Lett.* **15**, 524 (1965).
- [73] M. A. Baranov, A. V. Chubukov and M. Yu. Kagan, Superconductivity and superfluidity in Fermi systems with repulsive interactions, *Int. J. Mod. Phys. B* **06**, 2471 (1992).
- [74] N. Xu, H. M. Weng, B. Q. Lv, C. E. Matt, J. Park et al., Observation of Weyl nodes and Fermi arcs in tantalum phosphide, *Nature Communications* **7**, 11006 (2016).
- [75] S. Borisenko, Q. Gibson, D. Evtushinsky, V. Zabolotnyy, B. Büchner et al., Experimental realization of a three-dimensional Dirac semimetal, *Phys. Rev. Lett.* **113**, 027603 (2014).
- [76] S.-Y. Xu, C. Liu, S. K. Kushwaha, R. Sankar, J. W. Krizan et al., Observation of Fermi arc surface states in a topological metal, *Science* **347**, 294 (2015).
- [77] C.-K. Chiu, J. C. Y. Teo, A. P. Schnyder and S. Ryu, Classification of topological quantum matter with symmetries, *Rev. Mod. Phys.* **88**, 035005 (2016).
- [78] N. P. Armitage, E. J. Mele and A. Vishwanath, Weyl and Dirac semimetals in three-dimensional solids, *Rev. Mod. Phys.* **90**, 015001 (2018).
- [79] W. A. Benalcazar, B. A. Bernevig and T. L. Hughes, Quantized electric multipole insulators, *Science* **357**, 61 (2017).
- [80] F. Schindler, A. M. Cook, M. G. Vergniory, Z. Wang, S. S. Parkin et al., Higher-order topological insulators, *Science Advances* **4**, eaat0346 (2018).
- [81] W. A. Benalcazar, B. A. Bernevig and T. L. Hughes, Electric multipole moments, topological multipole moment pumping, and chiral hinge states in crystalline insulators, *Phys. Rev. B* **96**, 245115 (2017).
- [82] Z. Song, Z. Fang and C. Fang, $(d-2)$ -dimensional edge states of rotation symmetry protected topological states, *Phys. Rev. Lett.* **119**, 246402 (2017).
- [83] D. Călugăru, V. Juričić and B. Roy, Higher-order topological phases: A general principle of construction, *Phys. Rev. B* **99**, 041301 (2019).

- [84] M. Ezawa, Higher-order topological insulators and semimetals on the breathing Kagome and pyrochlore lattices, *Phys. Rev. Lett.* **120**, 026801 (2018).
- [85] F. Schindler, Z. Wang, M. G. Vergniory, A. M. Cook, A. Murani et al., Higher-order topology in bismuth, *Nature Physics* **14**, 918 (2018).
- [86] L. Aggarwal, P. Zhu, T. L. Hughes and V. Madhavan, Evidence for higher order topology in Bi and Bi_{0.92}Sb_{0.08}, *Nature Communications* **12**, 1 (2021).
- [87] Y.-B. Choi, Y. Xie, C.-Z. Chen, J. Park, S.-B. Song et al., Evidence of higher-order topology in multilayer WTe₂ from Josephson coupling through anisotropic hinge states, *Nature Materials* **19**, 974 (2020).
- [88] D. M. Mahler, J.-B. Mayer, P. Leubner, L. Lunczer, D. Di Sante et al., Interplay of Dirac nodes and Volkov-Pankratov surface states in compressively strained HgTe, *Phys. Rev. X* **9**, 031034 (2019).
- [89] J. Pixley, P. Goswami and S. D. Sarma, Anderson localization and the quantum phase diagram of three dimensional disordered Dirac semimetals, *Phys. Rev. Lett.* **115**, 076601 (2015).
- [90] B. Roy and S. D. Sarma, Diffusive quantum criticality in three-dimensional disordered Dirac semimetals, *Phys. Rev. B* **90**, 241112 (2014).
- [91] S. Syzranov, V. Gurarie and L. Radzihovsky, Unconventional localization transition in high dimensions, *Phys. Rev. B* **91**, 035133 (2015).
- [92] J. W. Negele and H. Orland, *Quantum Many-particle Systems*, Westview Press (1998).
- [93] I. Herbut, *A Modern Approach to Critical Phenomena*, Cambridge University Press (2007).
- [94] J. I. Kapusta and C. Gale, *Finite-Temperature Field Theory: Principles and Applications*, Cambridge Monographs on Mathematical Physics, Cambridge University Press, 2 edn. (2006).
- [95] T. R. Kirkpatrick and D. Belitz, Soft modes and nonanalyticities in a clean Dirac metal, *Phys. Rev. B* **99**, 085109 (2019).
- [96] H. Nielsen and M. Ninomiya, A no-go theorem for regularizing chiral fermions, *Physics Letters B* **105**, 219 (1981).
- [97] T. C. Lang and A. M. Läuchli, Quantum monte carlo simulation of the chiral Heisenberg Gross-Neveu-Yukawa phase transition with a single Dirac cone, *Phys. Rev. Lett.* **123**, 137602 (2019).

- [98] Y. Huang, H. Guo, J. Maciejko, R. T. Scalettar and S. Feng, Antiferromagnetic transitions of Dirac fermions in three dimensions, *Phys. Rev. B* **102**, 155152 (2020).
- [99] H. R. Quinn and M. Weinstein, Lattice theories of chiral fermions, *Phys. Rev. D* **34**, 2440 (1986).
- [100] K. G. Wilson, Confinement of quarks, *Phys. Rev. D* **10**, 2445 (1974).
- [101] J. Kogut and L. Susskind, Hamiltonian formulation of Wilson's lattice gauge theories, *Phys. Rev. D* **11**, 395 (1975).
- [102] B. Roy, P. Goswami and J. D. Sau, Continuous and discontinuous topological quantum phase transitions, *Phys. Rev. B* **94**, 041101 (2016).
- [103] A. L. Szabó and B. Roy, Emergent chiral symmetry in a three-dimensional interacting Dirac liquid, *Journal of High Energy Physics* **2021**, 4 (2021).
- [104] P. Nason, The lattice schwinger model with slac fermions, *Nuclear Physics B* **260**, 269 (1985).
- [105] J. P. Costella, A New proposal for the fermion doubling problem, arXiv:hep-lat/0207008 (2002).
- [106] P. Goswami and S. Chakravarty, Quantum criticality between topological and band insulators in 3+1 dimensions, *Phys. Rev. Lett.* **107**, 196803 (2011).
- [107] H. Isobe and N. Nagaosa, Theory of a quantum critical phenomenon in a topological insulator: (3+1)-dimensional quantum electrodynamics in solids, *Phys. Rev. B* **86**, 165127 (2012).
- [108] J. González, Phase diagram of the quantum electrodynamics of two-dimensional and three-dimensional Dirac semimetals, *Phys. Rev. B* **92**, 125115 (2015).
- [109] I. S. Tupitsyn and N. V. Prokof'ev, Stability of Dirac liquids with strong Coulomb interaction, *Phys. Rev. Lett.* **118**, 026403 (2017).
- [110] R. E. Throckmorton, J. Hofmann, E. Barnes and S. Das Sarma, Many-body effects and ultraviolet renormalization in three-dimensional Dirac materials, *Phys. Rev. B* **92**, 115101 (2015).
- [111] V. Juričić, I. F. Herbut and G. W. Semenoff, Coulomb interaction at the metal-insulator critical point in graphene, *Phys. Rev. B* **80**, 081405 (2009).
- [112] J. E. Drut and T. A. Lähde, Is graphene in vacuum an insulator?, *Phys. Rev. Lett.* **102**, 026802 (2009).
- [113] B. Roy and S. Das Sarma, Quantum phases of interacting electrons in three-dimensional dirty Dirac semimetals, *Phys. Rev. B* **94**, 115137 (2016).

- [114] V. V. Braguta, M. I. Katsnelson, A. Y. Kotov and A. A. Nikolaev, Monte carlo study of Dirac semimetals phase diagram, *Phys. Rev. B* **94**, 205147 (2016).
- [115] P.-L. Zhao and A.-M. Wang, Interplay between tilt, disorder, and coulomb interaction in type-I Dirac fermions, *Phys. Rev. B* **100**, 125138 (2019).
- [116] Z.-K. Yang, J.-R. Wang and G.-Z. Liu, Effects of Dirac cone tilt in a two-dimensional Dirac semimetal, *Phys. Rev. B* **98**, 195123 (2018).
- [117] J. Maciejko and R. Nandkishore, Weyl semimetals with short-range interactions, *Phys. Rev. B* **90**, 035126 (2014).
- [118] B. Roy, P. Goswami and V. Juričić, Interacting Weyl fermions: Phases, phase transitions, and global phase diagram, *Phys. Rev. B* **95**, 201102 (2017).
- [119] A. L. Szabó, R. Moessner and B. Roy, Interacting spin-3/2 fermions in a Luttinger semimetal: Competing phases and their selection in the global phase diagram, *Phys. Rev. B* **103**, 165139 (2021).
- [120] J. Zinn-Justin, *Quantum Field Theory and Critical Phenomena*, International series of monographs on physics, Clarendon Press (2002).
- [121] M. Moshe and J. Zinn-Justin, Quantum field theory in the large N limit: a review, *Physics Reports* **385**, 69 (2003).
- [122] B. Roy, S. A. A. Ghorashi, M. S. Foster and A. H. Nevidomskyy, Topological superconductivity of spin-3/2 carriers in a three-dimensional doped Luttinger semimetal, *Phys. Rev. B* **99**, 054505 (2019).
- [123] B. Roy and M. S. Foster, Quantum multicriticality near the Dirac-semimetal to band-insulator critical point in two dimensions: A controlled ascent from one dimension, *Phys. Rev. X* **8**, 011049 (2018).
- [124] C. N. Yang and S. Zhang, SO_4 symmetry in a hubbard model, *Mod. Phys. Lett. B* **04**, 759 (1990).
- [125] A. Auerbach, *Interacting Electrons and Quantum Magnetism*, Graduate texts in contemporary physics, Springer-Verlag New York (1994).
- [126] M. Hermele, $SU(2)$ gauge theory of the Hubbard model and application to the honeycomb lattice, *Phys. Rev. B* **76**, 035125 (2007).
- [127] T. Ohsaku, BCS and generalized BCS superconductivity in relativistic quantum field theory: Formulation, *Phys. Rev. B* **65**, 024512 (2001).
- [128] L. Fu and E. Berg, Odd-parity topological superconductors: Theory and application to $Cu_xBi_2Se_3$, *Phys. Rev. Lett.* **105**, 097001 (2010).

- [129] R. D. Peccei and H. R. Quinn, **CP** conservation in the presence of pseudoparticles, Phys. Rev. Lett. **38**, 1440 (1977).
- [130] S. Weinberg, A new light boson?, Phys. Rev. Lett. **40**, 223 (1978).
- [131] F. Wilczek, Problem of strong **P** and **T** invariance in the presence of instantons, Phys. Rev. Lett. **40**, 279 (1978).
- [132] J. M. Luttinger, Quantum theory of cyclotron resonance in semiconductors: General theory, Phys. Rev. **102**, 1030 (1956).
- [133] S. Murakami, N. Nagosa and S.-C. Zhang, SU(2) non-abelian holonomy and dissipationless spin current in semiconductors, Phys. Rev. B **69**, 235206 (2004).
- [134] X. Wan, A. M. Turner, A. Vishwanath and S. Y. Savrasov, Topological semimetal and Fermi-arc surface states in the electronic structure of pyrochlore iridates, Phys. Rev. B **83**, 205101 (2011).
- [135] K. Ladovrechis, T. Meng and B. Roy, Competing magnetic orders and multipolar Weyl fermions in 227 pyrochlore iridates, Phys. Rev. B **103**, L241116 (2021).
- [136] P. Brydon, L. Wang, M. Weinert and D. Agterberg, Pairing of $j = 3/2$ fermions in half-Heusler superconductors, Phys. Rev. Lett. **116**, 177001 (2016).
- [137] I. Boettcher and I. F. Herbut, Unconventional superconductivity in Luttinger semimetals: Theory of complex tensor order and the emergence of the uniaxial nematic state, Phys. Rev. Lett. **120**, 057002 (2018).
- [138] L. Savary, J. Ruhman, J. W. Venderbos, L. Fu and P. A. Lee, Superconductivity in three-dimensional spin-orbit coupled semimetals, Phys. Rev. B **96**, 214514 (2017).
- [139] I. Boettcher and I. F. Herbut, Anisotropy induces non-fermi-liquid behavior and nematic magnetic order in three-dimensional Luttinger semimetals, Phys. Rev. B **95**, 075149 (2017).
- [140] S. L. Sondhi, S. Girvin, J. Carini and D. Shahar, Continuous quantum phase transitions, Rev. Mod. Phys. **69**, 315 (1997).
- [141] S. Sachdev, *Quantum phase transitions*, Cambridge university press (2011).
- [142] B. Roy and V. Juričić, Unconventional superconductivity in nearly flat bands in twisted bilayer graphene, Phys. Rev. B **99**, 121407 (2019).
- [143] P. Fulde and R. A. Ferrell, Superconductivity in a strong spin-exchange field, Phys. Rev. **135**, A550 (1964).
- [144] A. I. Larkin and Y. N. Ovchinnikov, Nonuniform state of superconductors, Zh. Eksp. Teor. Fiz. **47**, 1136 (1964).

- [145] T. Esslinger, Fermi-Hubbard physics with atoms in an optical lattice, *Annu. Rev. Condens. Matter Phys.* **1**, 129 (2010).
- [146] L. Tarruell, D. Greif, T. Uehlinger, G. Jotzu and T. Esslinger, Creating, moving and merging Dirac points with a Fermi gas in a tunable honeycomb lattice, *Nature* **483**, 302 (2012).
- [147] T. Uehlinger, G. Jotzu, M. Messer, D. Greif, W. Hofstetter et al., Artificial graphene with tunable interactions, *Phys. Rev. Lett.* **111**, 185307 (2013).
- [148] M. Tarnowski, M. Nuske, N. Fläschner, B. Rem, D. Vogel et al., Observation of topological Bloch-state defects and their merging transition, *Phys. Rev. Lett.* **118**, 240403 (2017).
- [149] R. T. Weitz, M. T. Allen, B. E. Feldman, J. Martin and A. Yacoby, Broken-symmetry states in doubly gated suspended bilayer graphene, *Science* **330**, 812 (2010).
- [150] A. S. Mayorov, D. C. Elias, M. Mucha-Kruczynski, R. V. Gorbachev, T. Tudorovskiy et al., Interaction-driven spectrum reconstruction in bilayer graphene, *Science* **333**, 860 (2011).
- [151] F. Freitag, J. Trbovic, M. Weiss and C. Schönenberger, Spontaneously gapped ground state in suspended bilayer graphene, *Phys. Rev. Lett.* **108**, 076602 (2012).
- [152] A. Veligura, H. J. van Elferen, N. Tombros, J. C. Maan, U. Zeitler et al., Transport gap in suspended bilayer graphene at zero magnetic field, *Phys. Rev. B* **85**, 155412 (2012).
- [153] J. Velasco, L. Jing, W. Bao, Y. Lee, P. Kratz et al., Transport spectroscopy of symmetry-broken insulating states in bilayer graphene, *Nature Nanotechnology* **7**, 156 (2012).
- [154] F. Freitag, M. Weiss, R. Maurand, J. Trbovic and C. Schönenberger, Spin symmetry of the bilayer graphene ground state, *Phys. Rev. B* **87**, 161402 (2013).
- [155] Y. Lemonik, I. L. Aleiner, C. Toke and V. I. Fal'ko, Spontaneous symmetry breaking and Lifshitz transition in bilayer graphene, *Phys. Rev. B* **82**, 201408 (2010).
- [156] Y. Lemonik, I. Aleiner and V. I. Fal'ko, Competing nematic, antiferromagnetic, and spin-flux orders in the ground state of bilayer graphene, *Phys. Rev. B* **85**, 245451 (2012).
- [157] O. Vafek, J. M. Murray and V. Cvetkovic, Superconductivity on the brink of spin-charge order in a doped honeycomb bilayer, *Phys. Rev. Lett.* **112**, 147002 (2014).

- [158] V. Cvetkovic, R. E. Throckmorton and O. Vafek, Electronic multicriticality in bi-layer graphene, *Phys. Rev. B* **86**, 075467 (2012).
- [159] A. Giuliani and V. Mastropietro, Rigorous construction of ground state correlations in graphene: Renormalization of the velocities and Ward identities, *Phys. Rev. B* **79**, 201403 (2009).
- [160] A. Bácsi, A. Virosztek, L. Borda and B. Dóra, Mean-field quantum phase transition in graphene and in general gapless systems, *Phys. Rev. B* **82**, 153406 (2010).
- [161] B. Roy, Multicritical behavior of $\mathbb{Z}_2 \times O(2)$ Gross-Neveu-Yukawa theory in graphene, *Phys. Rev. B* **84**, 113404 (2011).
- [162] J.-R. Wang, G.-Z. Liu and S. Kirchner, Nature of the antiferromagnetic quantum phase transition on the honeycomb lattice, arXiv:1110.0093 (2011).
- [163] L. H. C. M. Nunes, R. L. S. Farias and E. C. Marino, Superconducting and excitonic quantum phase transitions in doped Dirac electronic systems, *Physics Letters A* **376**, 779 (2012).
- [164] D. Mesterházy, J. Berges and L. von Smekal, Effect of short-range interactions on the quantum critical behavior of spinless fermions on the honeycomb lattice, *Phys. Rev. B* **86**, 245431 (2012).
- [165] B. Roy and I. F. Herbut, Topological insulators in strained graphene at weak interaction, *Phys. Rev. B* **88**, 045425 (2013).
- [166] M. Daghofer and M. Hohenadler, Phases of correlated spinless fermions on the honeycomb lattice, *Phys. Rev. B* **89**, 035103 (2014).
- [167] T. Đurić, N. Chancellor and I. F. Herbut, Interaction-induced anomalous quantum Hall state on the honeycomb lattice, *Phys. Rev. B* **89**, 165123 (2014).
- [168] W. Wu and A.-M. S. Tremblay, Phase diagram and Fermi liquid properties of the extended Hubbard model on the honeycomb lattice, *Phys. Rev. B* **89**, 205128 (2014).
- [169] L. Wang, P. Corboz and M. Troyer, Fermionic quantum critical point of spinless fermions on a honeycomb lattice, *New Journal of Physics* **16**, 103008 (2014).
- [170] H. Guo and Y. Jia, Interaction-driven phases in a Dirac semimetal: exact diagonalization results, *Journal of Physics Condensed Matter* **26**, 475601 (2014).
- [171] F. Parisen Toldin, M. Hohenadler, F. F. Assaad and I. F. Herbut, Fermionic quantum criticality in honeycomb and π -flux Hubbard models: Finite-size scaling of renormalization-group-invariant observables from quantum Monte Carlo, *Phys. Rev. B* **91**, 165108 (2015).

- [172] Z.-X. Li, Y.-F. Jiang and H. Yao, Fermion-sign-free Majorana-quantum-Monte-Carlo studies of quantum critical phenomena of Dirac fermions in two dimensions, *New Journal of Physics* **17**, 085003 (2015).
- [173] S. Capponi and A. M. Läuchli, Phase diagram of interacting spinless fermions on the honeycomb lattice: A comprehensive exact diagonalization study, *Phys. Rev. B* **92**, 085146 (2015).
- [174] D. D. Scherer, M. M. Scherer and C. Honerkamp, Correlated spinless fermions on the honeycomb lattice revisited, *Phys. Rev. B* **92**, 155137 (2015).
- [175] Y. Otsuka, S. Yunoki and S. Sorella, Universal quantum criticality in the metal-insulator transition of two-dimensional interacting Dirac electrons, *Phys. Rev. X* **6**, 011029 (2016).
- [176] S. Capponi, Phase diagram of interacting spinless fermions on the honeycomb lattice, *Journal of Physics Condensed Matter* **29**, 043002 (2017).
- [177] A. Sharma, V. N. Kotov and A. H. Castro Neto, Excitonic mass gap in uniaxially strained graphene, *Phys. Rev. B* **95**, 235124 (2017).
- [178] K. Seki, Y. Otsuka, S. Yunoki and S. Sorella, Fermi-liquid ground state of interacting Dirac fermions in two dimensions, *Phys. Rev. B* **99**, 125145 (2019).
- [179] R. Boyack, H. Yerzhakov and J. Maciejko, Quantum phase transitions in Dirac fermion systems, *EPJ ST* 1–14 (2021).
- [180] J. Ostmeyer, E. Berkowitz, S. Krieg, T. A. Lähde, T. Luu et al., Semimetal–Mott insulator quantum phase transition of the Hubbard model on the honeycomb lattice, *Phys. Rev. B* **102**, 245105 (2020).
- [181] B. Uchoa and A. H. Castro Neto, Superconducting states of pure and doped graphene, *Phys. Rev. Lett.* **98**, 146801 (2007).
- [182] Y. Qi, L. Fu, K. Sun and Z. Gu, Coexistence of antiferromagnetism and topological superconductivity on the honeycomb lattice Hubbard model, *Phys. Rev. B* **102**, 245140 (2020).
- [183] J. P. L. Faye, M. N. Diarra and D. Sénéchal, Kekulé superconductivity and antiferromagnetism on the graphene lattice, *Phys. Rev. B* **93**, 155149 (2016).
- [184] S. Tsuchiya, J. Goryo, E. Arahata and M. Sgrist, Cooperon condensation and intravalley pairing states in honeycomb Dirac systems, *Phys. Rev. B* **94**, 104508 (2016).
- [185] X. Y. Xu, S. Wessel and Z. Y. Meng, Competing pairing channels in the doped honeycomb lattice Hubbard model, *Phys. Rev. B* **94**, 115105 (2016).

- [186] N. B. Kopnin and E. B. Sonin, BCS superconductivity of Dirac electrons in graphene layers, *Phys. Rev. Lett.* **100**, 246808 (2008).
- [187] J. González, Kohn-Luttinger superconductivity in graphene, *Phys. Rev. B* **78**, 205431 (2008).
- [188] J. Motruk, A. G. Grushin, F. de Juan and F. Pollmann, Interaction-driven phases in the half-filled honeycomb lattice: An infinite density matrix renormalization group study, *Phys. Rev. B* **92**, 085147 (2015).
- [189] L.-K. Lim, A. Lazarides, A. Hemmerich and C. Morais Smith, Strongly interacting two-dimensional Dirac fermions, *EPL* **88**, 36001 (2009).
- [190] S. Raghu, X.-L. Qi, C. Honerkamp and S.-C. Zhang, Topological Mott insulators, *Phys. Rev. Lett.* **100**, 156401 (2008).
- [191] T. Paiva, R. T. Scalettar, W. Zheng, R. R. P. Singh and J. Oitmaa, Ground-state and finite-temperature signatures of quantum phase transitions in the half-filled Hubbard model on a honeycomb lattice, *Phys. Rev. B* **72**, 085123 (2005).
- [192] D. V. Khveshchenko, Magnetic-field-induced insulating behavior in highly oriented pyrolytic graphite, *Phys. Rev. Lett.* **87**, 206401 (2001).
- [193] D. V. Khveshchenko, Ghost excitonic insulator transition in layered graphite, *Phys. Rev. Lett.* **87**, 246802 (2001).
- [194] F. D. M. Haldane, Model for a quantum Hall effect without Landau levels: Condensed-matter realization of the "parity anomaly", *Phys. Rev. Lett.* **61**, 2015 (1988).
- [195] S. Sorella and E. Tosatti, Semi-metal-insulator transition of the Hubbard model in the honeycomb lattice, *EPL* **19**, 699 (1992).
- [196] L. M. Martelo, M. Dzierzawa, L. Siffert and D. Baeriswyl, Mott-Hubbard transition and antiferromagnetism on the honeycomb lattice, *Z. Phys. B* **103**, 335 (1997).
- [197] T. C. Lang, Z. Y. Meng, M. M. Scherer, S. Uebelacker, F. F. Assaad et al., Antiferromagnetism in the Hubbard model on the Bernal-stacked honeycomb bilayer, *Phys. Rev. Lett.* **109**, 126402 (2012).
- [198] F. Zhang, H. Min and A. H. MacDonald, Competing ordered states in bilayer graphene, *Phys. Rev. B* **86**, 155128 (2012).
- [199] F. Zhang, H. Min, M. Polini and A. H. MacDonald, Spontaneous inversion symmetry breaking in graphene bilayers, *Phys. Rev. B* **81**, 041402 (2010).

- [200] R. Nandkishore and L. Levitov, Electron interactions in bilayer graphene: Marginal Fermi liquid and zero-bias anomaly, *Phys. Rev. B* **82**, 115431 (2010).
- [201] R. Nandkishore and L. Levitov, Dynamical screening and excitonic instability in bilayer graphene, *Phys. Rev. Lett.* **104**, 156803 (2010).
- [202] R. E. Throckmorton and S. Das Sarma, Quantum multicriticality in bilayer graphene with a tunable energy gap, *Phys. Rev. B* **90**, 205407 (2014).
- [203] Y.-M. Dong, Y.-H. Zhai, D.-X. Zheng and J. Wang, Stability of two-dimensional asymmetric materials with a quadratic band crossing point under four-fermion interaction and impurity scattering, *Phys. Rev. B* **102**, 134204 (2020).
- [204] I. F. Herbut, Explanation for the isotropy of the Dirac cone in graphene, *Phys. Rev. B* **79**, 193405 (2009).
- [205] J. González, F. Guinea and M. A. H. Vozmediano, Marginal-Fermi-liquid behavior from two-dimensional Coulomb interaction, *Phys. Rev. B* **59**, R2474 (1999).
- [206] D. T. Son, Quantum critical point in graphene approached in the limit of infinitely strong Coulomb interaction, *Phys. Rev. B* **75**, 235423 (2007).
- [207] J. Hofmann, E. Barnes and S. Das Sarma, Why does graphene behave as a weakly interacting system?, *Phys. Rev. Lett.* **113**, 105502 (2014).
- [208] S. Das Sarma and E. H. Hwang, Velocity renormalization and anomalous quasiparticle dispersion in extrinsic graphene, *Phys. Rev. B* **87**, 045425 (2013).
- [209] B. Roy, V. Juričić and I. F. Herbut, Emergent Lorentz symmetry near fermionic quantum critical points in two and three dimensions, *Journal of High Energy Physics* **2016**, 18 (2016).
- [210] P.-L. Zhao, X.-B. Qiang, H.-Z. Lu and X. C. Xie, Coulomb instabilities of 3D higher-order topological insulators, *arXiv:2103.02456* (2021).
- [211] D. C. Elias, R. V. Gorbachev, A. S. Mayorov, S. V. Morozov, A. A. Zhukov et al., Dirac cones reshaped by interaction effects in suspended graphene, *Nature Physics* **7**, 701 (2011).
- [212] S. Chakravarty, B. I. Halperin and D. R. Nelson, Two-dimensional quantum Heisenberg antiferromagnet at low temperatures, *Phys. Rev. B* **39**, 2344 (1989).
- [213] S. Ryu, C. Mudry, C.-Y. Hou and C. Chamon, Masses in graphenelike two-dimensional electronic systems: Topological defects in order parameters and their fractional exchange statistics, *Phys. Rev. B* **80**, 205319 (2009).

- [214] C. L. Kane and E. J. Mele, Quantum spin Hall effect in graphene, *Phys. Rev. Lett.* **95**, 226801 (2005).
- [215] R. Blankenbecler, D. J. Scalapino and R. L. Sugar, Monte Carlo calculations of coupled boson-fermion systems. I, *Phys. Rev. D* **24**, 2278 (1981).
- [216] D. R. Hamann, Path integral theory of magnetic alloys, *Phys. Rev. B* **2**, 1373 (1970).
- [217] Y. Cao, V. Fatemi, S. Fang, K. Watanabe, T. Taniguchi et al., Unconventional superconductivity in magic-angle graphene superlattices, *Nature* **556**, 43 (2018).
- [218] X. Lu, P. Stepanov, W. Yang, M. Xie, M. A. Aamir et al., Superconductors, orbital magnets and correlated states in magic-angle bilayer graphene, *Nature* **574**, 653 (2019).
- [219] E. Codecido, Q. Wang, R. Koester, S. Che, H. Tian et al., Correlated insulating and superconducting states in twisted bilayer graphene below the magic angle, *Science Advances* **5** (2019).
- [220] M. Yankowitz, S. Chen, H. Polshyn, Y. Zhang, K. Watanabe et al., Tuning superconductivity in twisted bilayer graphene, *Science* **363**, 1059 (2019).
- [221] B. Irsigler, T. Grass, J.-H. Zheng, M. Barbier and W. Hofstetter, Topological Mott transition in a Weyl-Hubbard model: Dynamical mean-field theory study, *Phys. Rev. B* **103**, 125132 (2021).
- [222] S. Sur and R. Nandkishore, Instabilities of Weyl loop semimetals, *New Journal of Physics* **18**, 115006 (2016).
- [223] B. Roy, Interacting nodal-line semimetal: Proximity effect and spontaneous symmetry breaking, *Phys. Rev. B* **96**, 041113 (2017).
- [224] J. W. Venderbos, L. Savary, J. Ruhman, P. A. Lee and L. Fu, Pairing states of spin-3/2 fermions: Symmetry-enforced topological gap functions, *Phys. Rev. X* **8**, 011029 (2018).
- [225] G. Sim, A. Mishra, M. J. Park, Y. B. Kim, G. Y. Cho et al., Topological $d+s$ wave superconductors in a multiorbital quadratic band touching system, *Phys. Rev. B* **100**, 064509 (2019).
- [226] J. Luttinger, Fermi surface and some simple equilibrium properties of a system of interacting fermions, *Phys. Rev.* **119**, 1153 (1960).
- [227] A. L. Szabó, R. Moessner and B. Roy, Strain-engineered higher-order topological phases for spin-3/2 Luttinger fermions, *Phys. Rev. B* **101**, 121301 (2020).

- [228] M. Sigrist and K. Ueda, Phenomenological theory of unconventional superconductivity, *Reviews of Modern physics* **63**, 239 (1991).
- [229] C. Timm, A. Schnyder, D. Agterberg and P. Brydon, Inflated nodes and surface states in superconducting half-Heusler compounds, *Phys. Rev. B* **96**, 094526 (2017).
- [230] K. Matsuhira, M. Wakeshima, Y. Hinatsu and S. Takagi, Metal–insulator transitions in pyrochlore oxides $\text{Ln}_2\text{Ir}_2\text{O}_7$, *Journal of the Physical Society of Japan* **80**, 094701 (2011).
- [231] L. Balicas, S. Nakatsuji, Y. Machida and S. Onoda, Anisotropic hysteretic Hall effect and magnetic control of chiral domains in the chiral spin states of $\text{Pr}_2\text{Ir}_2\text{O}_7$, *Phys. Rev. Lett.* **106**, 217204 (2011).
- [232] A. A. Burkov, Topological semimetals, *Nature Materials* **15**, 1145 (2016).
- [233] B. A. Bernevig and T. L. Hughes, *Topological Insulators and Topological Superconductors*, Princeton University Press, Student edn. (2013).
- [234] J. Langbehn, Y. Peng, L. Trifunovic, F. von Oppen and P. W. Brouwer, Reflection-symmetric second-order topological insulators and superconductors, *Phys. Rev. Lett.* **119**, 246401 (2017).
- [235] S. Franca, J. van den Brink and I. Fulga, An anomalous higher-order topological insulator, *Phys. Rev. B* **98**, 201114 (2018).
- [236] Z. Wang, B. J. Wieder, J. Li, B. Yan and B. A. Bernevig, Higher-order topology, monopole nodal lines, and the origin of large Fermi arcs in transition metal dichalcogenides XTe_2 ($\text{X} = \text{Mo}, \text{W}$), *Phys. Rev. Lett.* **123**, 186401 (2019).
- [237] C.-H. Hsu, P. Stano, J. Klinovaja and D. Loss, Majorana Kramers pairs in higher-order topological insulators, *Phys. Rev. Lett.* **121**, 196801 (2018).
- [238] Y. Wang, M. Lin and T. L. Hughes, Weak-pairing higher order topological superconductors, *Phys. Rev. B* **98**, 165144 (2018).
- [239] M. Lin and T. L. Hughes, Topological quadrupolar semimetals, *Phys. Rev. B* **98**, 241103 (2018).
- [240] S. A. A. Ghorashi, X. Hu, T. L. Hughes and E. Rossi, Second-order Dirac superconductors and magnetic field induced Majorana hinge modes, *Phys. Rev. B* **100**, 020509 (2019).
- [241] Y. Volpez, D. Loss and J. Klinovaja, Second-order topological superconductivity in π -junction Rashba layers, *Phys. Rev. Lett.* **122**, 126402 (2019).

- [242] T. Nag, V. Juričić and B. Roy, Out of equilibrium higher-order topological insulator: Floquet engineering and quench dynamics, *Phys. Rev. Res.* **1**, 032045 (2019).
- [243] S. H. Lee, Y. Zhu, Y. Wang, L. Miao, T. Pillsbury et al., Spin scattering and non-collinear spin structure-induced intrinsic anomalous Hall effect in antiferromagnetic topological insulator MnBi_2Te_4 , *Phys. Rev. Res.* **1**, 012011 (2019).
- [244] Z. Yan, Higher-order topological odd-parity superconductors, *Phys. Rev. Lett.* **123**, 177001 (2019).
- [245] B. Roy, Antiunitary symmetry protected higher-order topological phases, *Phys. Rev. Res.* **1**, 032048 (2019).
- [246] B. J. Wieder, Z. Wang, J. Cano, X. Dai, L. M. Schoop et al., Strong and fragile topological Dirac semimetals with higher-order Fermi arcs, *Nature Communications* **11**, 1 (2020).
- [247] H. Hu, B. Huang, E. Zhao and W. V. Liu, Dynamical singularities of Floquet higher-order topological insulators, *Phys. Rev. Lett.* **124**, 057001 (2020).
- [248] R.-X. Zhang, Y.-T. Hsu and S. D. Sarma, Higher-order topological Dirac superconductors, *Phys. Rev. B* **102**, 094503 (2020).
- [249] E. Fradkin, Critical behavior of disordered degenerate semiconductors. II. Spectrum and transport properties in mean-field theory, *Phys. Rev. B* **33**, 3263 (1986).
- [250] Y. Ominato and M. Koshino, Quantum transport in a three-dimensional Weyl electron system, *Phys. Rev. B* **89**, 054202 (2014).
- [251] S. Syzranov, L. Radzihovsky and V. Gurarie, Critical transport in weakly disordered semiconductors and semimetals, *Phys. Rev. Lett.* **114**, 166601 (2015).
- [252] S. V. Syzranov, P. M. Ostrovsky, V. Gurarie and L. Radzihovsky, Critical exponents at the unconventional disorder-driven transition in a Weyl semimetal, *Phys. Rev. B* **93**, 155113 (2016).
- [253] B. Roy, V. Juričić and S. D. Sarma, Universal optical conductivity of a disordered Weyl semimetal, *Scientific reports* **6**, 1 (2016).
- [254] P. Goswami and S. Chakravarty, Superuniversality of topological quantum phase transition and global phase diagram of dirty topological systems in three dimensions, *Phys. Rev. B* **95**, 075131 (2017).
- [255] T. Louvet, D. Carpentier and A. A. Fedorenko, On the disorder-driven quantum transition in three-dimensional relativistic metals, *Phys. Rev. B* **94**, 220201 (2016).

- [256] T. Louvet, D. Carpentier and A. A. Fedorenko, New quantum transition in Weyl semimetals with correlated disorder, *Phys. Rev. B* **95**, 014204 (2017).
- [257] K. Kobayashi, T. Ohtsuki, K.-I. Imura and I. F. Herbut, Density of states scaling at the semimetal to metal transition in three dimensional topological insulators, *Phys. Rev. Lett.* **112**, 016402 (2014).
- [258] B. Sbierski, G. Pohl, E. J. Bergholtz and P. W. Brouwer, Quantum transport of disordered Weyl semimetals at the nodal point, *Phys. Rev. Lett.* **113**, 026602 (2014).
- [259] B. Sbierski, E. J. Bergholtz and P. W. Brouwer, Quantum critical exponents for a disordered three-dimensional Weyl node, *Phys. Rev. B* **92**, 115145 (2015).
- [260] J. Pixley, P. Goswami and S. D. Sarma, Disorder-driven itinerant quantum criticality of three-dimensional massless Dirac fermions, *Phys. Rev. B* **93**, 085103 (2016).
- [261] S. Liu, T. Ohtsuki and R. Shindou, Effect of disorder in a three-dimensional layered Chern insulator, *Phys. Rev. Lett.* **116**, 066401 (2016).
- [262] S. Bera, J. D. Sau and B. Roy, Dirty Weyl semimetals: Stability, phase transition, and quantum criticality, *Phys. Rev. B* **93**, 201302 (2016).
- [263] T. S. Sikkenk and L. Fritz, Disorder in tilted Weyl semimetals from a renormalization group perspective, *Phys. Rev. B* **96**, 155121 (2017).
- [264] I. Balog, D. Carpentier and A. A. Fedorenko, Disorder-driven quantum transition in relativistic semimetals: functional renormalization via the porous medium equation, *Phys. Rev. Lett.* **121**, 166402 (2018).
- [265] J. Klier, I. Gornyi and A. Mirlin, From weak to strong disorder in Weyl semimetals: Self-consistent Born approximation, *Phys. Rev. B* **100**, 125160 (2019).
- [266] E. Brillaux, D. Carpentier and A. A. Fedorenko, Multifractality at the Weyl-semimetal–diffusive-metal transition for generic disorder, *Phys. Rev. B* **100**, 134204 (2019).
- [267] T. Hirose, H. Maebashi and M. Ogata, Nuclear spin relaxation rate near the disorder-driven quantum critical point in Weyl fermion systems, *Phys. Rev. B* **101**, 155103 (2020).
- [268] R. Nandkishore, D. A. Huse and S. L. Sondhi, Rare region effects dominate weakly disordered three-dimensional Dirac points, *Phys. Rev. B* **89**, 245110 (2014).
- [269] J. Pixley, D. A. Huse and S. D. Sarma, Rare-region-induced avoided quantum criticality in disordered three-dimensional Dirac and Weyl semimetals, *Phys. Rev. X* **6**, 021042 (2016).

- [270] M. Buchhold, S. Diehl and A. Altland, Vanishing density of states in weakly disordered Weyl semimetals, *Phys. Rev. Lett.* **121**, 215301 (2018).
- [271] E. Fradkin, S. A. Kivelson, M. J. Lawler, J. P. Eisenstein and A. P. Mackenzie, Nematic Fermi fluids in condensed matter physics, *Annu. Rev. Condens. Matter Phys.* **1**, 153 (2010).
- [272] J.-H. Chu, H.-H. Kuo, J. G. Analytis and I. R. Fisher, Divergent nematic susceptibility in an iron arsenide superconductor, *Science* **337**, 710 (2012).
- [273] M. Polini, F. Guinea, M. Lewenstein, H. C. Manoharan and V. Pellegrini, Artificial honeycomb lattices for electrons, atoms and photons, *Nature nanotechnology* **8**, 625 (2013).
- [274] A. G. Grushin, J. W. Venderbos, A. Vishwanath and R. Ilan, Inhomogeneous Weyl and Dirac semimetals: Transport in axial magnetic fields and Fermi arc surface states from pseudo-Landau levels, *Phys. Rev. X* **6**, 041046 (2016).
- [275] P. Dietl, F. Piéchon and G. Montambaux, New magnetic field dependence of Landau levels in a graphenelike structure, *Phys. Rev. Lett.* **100**, 236405 (2008).
- [276] S. Sur and B. Roy, Unifying interacting nodal semimetals: A new route to strong coupling, *Phys. Rev. Lett.* **123**, 207601 (2019).
- [277] C. W. Hicks, M. E. Barber, S. D. Eddins, D. O. Brodsky and A. P. Mackenzie, Piezoelectric-based apparatus for strain tuning, *Review of Scientific Instruments* **85**, 065003 (2014).
- [278] Y.-S. Li, N. Kikugawa, D. A. Sokolov, F. Jerzembeck, A. S. Gibbs et al., High-sensitivity heat-capacity measurements on Sr_2RuO_4 under uniaxial pressure, *Proceedings of the National Academy of Sciences* **118** (2021).
- [279] T. Ohtsuki, Z. Tian, A. Endo, M. Halim, S. Katsumoto et al., Strain-induced spontaneous Hall effect in an epitaxial thin film of a Luttinger semimetal, *Proceedings of the National Academy of Sciences* **116**, 8803 (2019).
- [280] R. Jackiw and C. Rebbi, Solitons with fermion number $1/2$, *Phys. Rev. D* **13**, 3398 (1976).
- [281] I. F. Herbut and L. Janssen, Topological Mott insulator in three-dimensional systems with quadratic band touching, *Phys. Rev. Lett.* **113**, 106401 (2014).
- [282] H. Huang and F. Liu, Tensile strained gray tin: Dirac semimetal for observing negative magnetoresistance with Shubnikov–de Haas oscillations, *Phys. Rev. B* **95**, 201101 (2017).

Bibliography

- [283] A. Weiße, G. Wellein, A. Alvermann and H. Fehske, The kernel polynomial method, *Rev. Mod. Phys.* **78**, 275 (2006).
- [284] A. L. Szabó and B. Roy, Dirty higher-order Dirac semimetal: Quantum criticality and bulk-boundary correspondence, *Phys. Rev. Research* **2**, 043197 (2020).
- [285] E. M. Stein, *Singular Integrals and Differentiability Properties of Functions (PMS-30)*, vol. 30, Princeton University Press (2016).
- [286] R.-J. Slager, V. Juričić and B. Roy, Dissolution of topological Fermi arcs in a dirty Weyl semimetal, *Phys. Rev. B* **96**, 201401 (2017).
- [287] G. E. Volovik, *The universe in a helium droplet*, vol. 117, Oxford University Press on Demand (2003).
- [288] G. Xu, H. Weng, Z. Wang, X. Dai and Z. Fang, Chern semimetal and the quantized anomalous Hall effect in HgCr_2Se_4 , *Phys. Rev. Lett.* **107**, 186806 (2011).
- [289] P. Goswami and A. H. Nevidomskyy, Topological Weyl superconductor to diffusive thermal Hall metal crossover in the B phase of UPt_3 , *Physical Review B* **92**, 214504 (2015).
- [290] H.-H. Lai, Correlation effects in double-Weyl semimetals, *Physical Review B* **91**, 235131 (2015).
- [291] B. Roy and J. D. Sau, Magnetic catalysis and axionic charge density wave in Weyl semimetals, *Physical Review B* **92**, 125141 (2015).
- [292] S.-K. Jian and H. Yao, Correlated double-Weyl semimetals with Coulomb interactions: Possible applications to HgCr_2Se_4 and SrSi_2 , *Physical Review B* **92**, 045121 (2015).
- [293] Y. Wang and P. Ye, Topological density-wave states in a particle-hole symmetric Weyl metal, *Physical Review B* **94**, 075115 (2016).
- [294] Y. Huh, E.-G. Moon and Y. B. Kim, Long-range Coulomb interaction in nodal-ring semimetals, *Physical Review B* **93**, 035138 (2016).
- [295] A. N. Rudenko, E. A. Stepanov, A. I. Lichtenstein and M. I. Katsnelson, Excitonic instability and pseudogap formation in nodal line semimetal ZrSiS , *Physical review letters* **120**, 216401 (2018).
- [296] M. Krottenmüller, M. Vöst, N. Unglert, J. Ebad-Allah, G. Eickerling et al., Indications for Lifshitz transitions in the nodal-line semimetal ZrSiTe induced by interlayer interaction, *Physical Review B* **101**, 081108 (2020).

- [297] Q. Li, C. He, Y. Wang, E. Liu, M. Wang et al., Proximity-induced superconductivity with subgap anomaly in type II Weyl semi-metal WTe_2 , *Nano Letters* **18**, 7962 (2018).
- [298] Y. Qi, P. G. Naumov, M. N. Ali, C. R. Rajamathi, W. Schnelle et al., Superconductivity in Weyl semimetal candidate $MoTe_2$, *Nature Communications* **7**, 1 (2016).
- [299] D. Kang, Y. Zhou, W. Yi, C. Yang, J. Guo et al., Superconductivity emerging from a suppressed large magnetoresistant state in tungsten ditelluride, *Nature Communications* **6**, 7804 (2015).
- [300] X.-C. Pan, X. Chen, H. Liu, Y. Feng, Z. Wei et al., Pressure-driven dome-shaped superconductivity and electronic structural evolution in tungsten ditelluride, *Nature Communications* **6**, 7805 (2015).
- [301] E. Cheng, W. Xia, X. Shi, Z. Yu, L. Wang et al., Pressure-induced superconductivity and topological phase transitions in the topological nodal-line semimetal $SrAs_3$, *npj Quantum Materials* **5**, 1 (2020).
- [302] A. Ikeda, M. Kawaguchi, S. Koibuchi, T. Hashimoto, T. Kawakami et al., Superconductivity in the nonsymmorphic line-nodal compound $CaSb_2$, *Phys. Rev. Materials* **4**, 041801 (2020).
- [303] S.-Y. Guan, P.-J. Chen, M.-W. Chu, R. Sankar, F. Chou et al., Superconducting topological surface states in the noncentrosymmetric bulk superconductor $PbTaSe_2$, *Science Advances* **2**, e1600894 (2016).
- [304] Y. Li, Z. Wu, J. Zhou, K. Bu, C. Xu et al., Enhanced anisotropic superconductivity in the topological nodal-line semimetal In_xTaS_2 , *Phys. Rev. B* **102**, 224503 (2020).
- [305] Y. Li, Y. Wu, C. Xu, N. Liu, J. Ma et al., Anisotropic gapping of topological Weyl rings in the charge-density-wave superconductor In_xTaSe_2 , *Science Bulletin* **66**, 243 (2021).
- [306] A. L. Szabó and B. Roy, Emergent $SO(5)$ symmetries in the global phase diagram of extended honeycomb Hubbard model, In preparation .

Erklärung

Hiermit versichere ich, dass ich die vorliegende Arbeit ohne unzulässige Hilfe Dritter und ohne Benutzung anderer als der angegebenen Hilfsmittel angefertigt habe; die aus fremden Quellen direkt oder indirekt übernommenen Gedanken sind als solche kenntlich gemacht. Die Arbeit wurde bisher weder im Inland noch im Ausland in gleicher oder ähnlicher Form einer anderen Prüfungsbehörde vorgelegt.

Die vorliegende Dissertation wurde am Max-Planck-Institut für Physik komplexer Systeme unter der wissenschaftlichen Betreuung von Prof. Dr. Bitan Roy angefertigt. Ich erkenne die Promotionsordnung des Bereichs Mathematik und Naturwissenschaften der Technischen Universität Dresden vom 23.02.2011 an.

András László Szabó

Dresden, 5. Oktober 2021